NON-DESTRUCTIVE DETECTION OF PORK INTRAMUSCULAR FAT CONTENT USING HYPERSPECTRAL IMAGING

by

Hui Huang

Department of Bioresource Engineering
McGill University, Montreal
Canada

April, 2013

A Thesis Submitted to McGill University in partial fulfillment of the requirements for the degree of Doctor of Philosophy

ABSTRACT

Intramuscular fat levels of pork affect the flavor of pork meat. In the pork industry, two quality attributes namely intramuscular fat (IMF) content and marbling score (MS) are used to represent intramuscular fat levels of pork meat. Conventional determination methods are not suitable for the current requirements of the pork industry as they are either destructive or subjective. This study investigated the use of hyperspectral imaging in evaluating intramuscular fat content and marbling score of pork. Intramuscular fat distribution along the longissmus muscle and the influences of freezing, thawing, and image pattern analysis on prediction capacity were also considered.

Near infrared (NIR) hyperspectral imaging technique from 900 to 1700 nm was used for prediction of IMF content and MS. Fresh pork at the $3^{rd}/4^{th}$ last rib was imaged. Pattern analysis techniques of Gabor filter, wide line detector (WLD), and an improved grey-level co-occurrence matrix (GLCM) were studied and different image features, i.e. spectral, texture, and line features, were extracted. Key wavelengths were identified. Multiple linear regression (MLR) was used to develop prediction models. For determination of marbling score, the MLR model, using the first derivative of Gabor filtered mean spectra, performed best with a prediction accuracy of 0.90 at wavelengths of 961, 1186 and 1220 nm. For intramuscular fat content, prediction accuracy of 0.85 was obtained using the raw mean spectra at 1207 and 1279 nm. The distribution map of IMF content in pork was developed. The results showed the possibility of rapid and non-destructive evaluation of intramuscular fat level of pork using NIR images.

Regarding marbling as a visual index, a method for objective evaluation of pork marbling score using red-green-blue (RGB) images was developed by applying WLD-based linear models.

The possibility of non-destructive prediction of IMF content and MS using frozen and frozen-thawed pork was studied. Prediction accuracy of 0.90 for MS was achieved for frozen pork. Prediction accuracy of 0.82 for IMF content and accuracy of 0.91 for MS were realized by frozen-thawed pork. The potential of frozen and frozen-thawed pork for assessment of marbling score and frozen-thawed pork for the assessment of intramuscular fat content were demonstrated.

Besides the effects of freezing and thawing, the variation of IMF content and MS across the last seven thoracic longissmus muscle was studied. Relationships between IMF content and MS at the last rib and the corresponding attribute at other ribs and the whole section of the loin were determined. The relationship between NIR images of rib end and the IMF level of pork at the six last thoracic ribs was investigated. Close relationships were indicated, especially between the images of rib end and IMF levels at the 2nd/3rd last ribs and the 2nd last/last ribs.

RÉSUMÉ

La teneur en matières grasses du porc affecte la saveur de la viande de porc. Dans l’industrie porcine, la graisse intramusculaire (GIM) et la cote de persillage (CP) sont deux propriétés qui déterminent la teneur en gras du porc. Les méthodes conventionnelles de détermination ne sont pas adaptées aux besoins actuels de l'industrie car elles sont destructrices ou subjectives. Cette étude porte sur l'utilisation de l'imagerie hyperspectrale dans l'évaluation de la teneur en graisse intramusculaire et du persillage du porc. Les effets de la répartition de la graisse intramusculaire le long du muscle Longissmus, de la congélation, du dégel et de l'analyse de la forme pour le traitement de l’image ont été pris en compte.

Une technique d’imagerie hyperspectrale proche infrarouge (IR) allant de 900 à 1700 nm a été utilisée pour prédire le GIM ou la CP. La viande fraîche au niveau de la $3^{ème}/4^{ème}$ côte du porc a été utilisée pour recueillir les images hyperspectrales. Des analyses de la forme fondée sur les techniques du filtre de Gabor, du détecteur linéaire à large spectre (WLD) et de la matrice de cooccurrence de niveau gris améliorée (GLCM) ont été étudiées et les propriétés de l’image, i.e spectre, texture et propriétés des lignes, ont été extraites. La régression linéaire multiple (RLM) a été utilisée pour développer des modèles de prédiction. Pour la cote persillage, le modèle de RLM utilisant la moyenne de spectre filtrée pour la première dérivée de Gabor a le mieux performé avec une précision de calibration de 0,90 aux longueurs d'onde de 961, 1186 et 1220 nm. Pour le GIM, une précision de calibration de 0.85 a été obtenue avec un spectre moyen de base à 1207 et 1279 nm. La distribution du contenu de GIM a été illustrée. Les résultats démontrent la possibilité d’utiliser les images hyperspectralces proche IR pour évaluer rapidement et de façon non-destructive le taux de gras intramusculaire du porc.

En ce qui concerne le persillage en tant qu’indice visuel, une méthode objective d’évaluation de la cote persillage utilisant des images rouge-vert-bleu (RGB) a été développée en appliquant un WLD basé sur un model linéaire au canal vert.

La possibilité d’un contrôle non-destructif du GIM et de la CP utilisant du porc congelé et décongelé a été étudiée. Une précision de la prédiction de 0.90 pour la CP a été réalisée avec du porc congelé. Une précision de la prédiction de 0.82 pour le GIM découle du porc décongelé. Le potentiel du porc congelé et décongelé pour l'évaluation de la cote de persillage et du porc décongelé pour l'évaluation de la teneur en gras intramusculaire a été démontré.

Outre l'effet du gel et du dégel, la variation du GIM et de la CP à travers les sept derniers muscles thoraciques Longissmus a été étudiée. Les relations entre le GIM et la CP à la dernière côte et les propriétés correspondantes aux autres côtes et au filet ont été déterminées avec précision. La relation entre les images de proche IR à l’extrémité et le niveau de GIM du porc six dernières côtes thoraciques a été étudiée. Des relations étroite ont été déterminées, en particulier entre les images de l’extrémité de la côte et les taux de GIM aux 2eme/3eme dernières côtes et la 2eme dernière côte.

ACKNOWLEDGEMENTS

Foremost, I would like to express my sincere gratitude to my supervisor Prof. Michael O. Ngadi, for his continuous support of my Ph.D study and research and for his patience, constant guidance, motivation, enthusiasm, and immense knowledge. His support helped me throughout the course of this work. I simply cannot imagine a better adviser.

Along with Prof. Michael O. Ngadi, I would like to thank my co-supervisor Prof. Shiv O. Prasher, for his encouragement, insightful comments, and valuable advice.

I am also grateful to Dr. Li Liu for her continued technical assistance and guidance in each part of this work. Her academic direction, scrupulous organization, and valuable advice were instrumental to my completion of this thesis. In addition to our academic cooperation, I greatly value the close personal rapport that Dr. Liu and I have forged.

Also, I would like to thank the members of my comprehensive exam committee for their time and valuable suggestions: Prof. Valérie Orsat, Dr. Claude Gariépy, and Prof. Martin Rochette. I would particularly like to acknowledge Dr. Claude Gariépy for providing samples and comments for parts of this manuscript. I appreciate Prof. Valérie Orsat for her unconditional help.

I appreciate the help of Prof. G.S. Vijaya Raghavan and Prof. Arif F. Mustafa for allowing me access to the necessary equipment. Big thanks to Mr. Yvan Gariépy, Mr. Jamshid Rahimi, Mr. Peter Olusola Adewale and Mrs. Somaia Amer for their help with the operation of the equipments; Mr. Hongyuan Deng for transporting part of the samples;

Ms. Audrey Yank for French translation.

My sincere thanks also go to Prof. Robert Kok, Prof. Roger I. Cue, Prof. Grant Clark, Prof. Mark Lefsrud, and Prof. Viacheslav Adamchuk for their excellent teaching skills and Prof. Benjamin K. Simpson for his help. Special thanks are extended to our departmental administrative staff, Ms. Susan Gregus, Ms. Abida Subhan and Ms. Patricia Singleton for solving problems and processing all the paper work in an efficient and friendly manner.

I would like to say thank you to our entire research group, Dr. Amaka Marian Odenigbo, Mr. Ben Wang, Mr. Akinbode A. Adedeji, Mr. Farzad Saadatian, Mr. Hernan Rey-Sanches, Mrs. Mary Adewale, Mr. Fengle Zhu, Mr. Mohsin Bin Latheef, Mr. Bakari Mohammed, Chijioke Ejebe, Ms. Tina Beigi, and Mr. Ogan Mba. I would also like to thank my friends, Jing Zhang, Qianying Ruan, Luan Pan, Laura Cinquino, Claudine Chartrand, Yashi Huang, Shrikalaa Kannan, Deepika Arumugam, Pratyusha Chennupati, Min Zhou, Shimin Fan, Ning An, Wei Que, Chen Chen, and all others for their help and for all the fun we have had in the last few years. In particular, thanks to Qianying Ruan for the statistical discussions and for being my swimming partner. Also, I am grateful to my former supervisor in China Agricultural University Prof. Yankun Peng and my friend Dr. Jianhu Wu for enlightening me regarding hyperspectral imaging research.

I sincerely acknowledge the support of my motherland-China. I also acknowledge the sample support received from the Canadian Centre for Swine Improvement Inc. (CCSI).

Last but not the least, I wish to express my thanks to my family. Their support and blessing has helped me throughout my life.

PARTS OF THIS THESIS HAVE BEEN SUBMITTED FOR PUBLICATION

1. **Huang, H.**, Liu, L., Ngadi, M.O., & Gariépy, C. Hyperspectral image-assisted non-destructive quantification of intramuscular fat content of intact pork. *Talanta*, Submitted for publication.
2. **Huang, H.**, Liu, L., Ngadi, M.O., Gariépy, C., & Prasher, S.O. Near-infrared spectral image analysis for pork marbling determination. *Applied Spectroscopy*, Submitted for publication.
3. **Huang, H.**, Liu, L., Ngadi, M.O., Gariépy, C., & Prasher, S.O. Predicting intramuscular fat content and marbling score of pork along the longissimus muscle based on the last rib. *International Journal of Food Science and Technology*, Submitted for publication.
4. **Huang, H.**, Liu, L., Ngadi, M.O., & Gariépy, C. Assessment of intramuscular fat content and marbling score of pork using NIR hyperspectral imageries of rib end. *Food Control*, Submitted for publication.
5. **Huang, H.**, Liu, L., Ngadi, M.O., & Gariépy, C. Prediction of intramuscular fat content and marbling score of pork using NIR images of frozen and frozen-thawed pork. *Journal of Food Engineering*, Submitted for publication.

PART OF THIS THESIS HAS BEEN PUBLISHED

1. **Huang, H.**, Liu, L., Ngadi, M.O., & Gariépy, C. (2013). Prediction of pork marbling scores using pattern analysis techniques. *Food Control*, 31(1), 224-229.

PART OF THIS THESIS WAS PRESENTED AT SCIENTIFIC AND TECHNICAL CONFERENCES

1. **Huang, H.**, Liu, L., Ngadi, M.O., & Simpson, B.K. (2011). Hyperspectral evaluation of changes in vacuum-packed cold-smoked salmon during storage. A paper presented at International Conference of Agricultural Engineering. Conference held at France from 14th - 20th April, 2011. Oral Presentation.
2. **Huang, H.**, Ngadi, M.O., & Liu, L. (2011). Hyperspectral imaging: answering challenges in food quality and safety. A paper presented at Northeast Agricultural and Biological Engineering Conference (NABEC). Conference Held at South Burlington, VT, USA from 24th - 27th July, 2011. Oral Presentation.
3. **Huang, H.**, Liu, L., Ngadi, M.O., & Prasher, S.O. (2012). Near-infrared spectral image analysis for pork marbling detection. A paper presented at NABEC conference. Conference Held at Orillia, ON, Canada from 15th - 18th July, 2012. Oral Presentation.

CONTRIBUTION OF AUTHORS

The role and contribution made by different authors are as follows: Hui Huang is the principal author of this work. She is the Ph.D candidate who designed and executed all parts of the experiments, data analysis, manuscript writing and revision for scientific publications. Prof. Michael O. Ngadi is the thesis supervisor, who guided the candidate in the stages of planning, design and execution of experiments, and analysis of data during the entire program. He also corrected, edited, and reviewed all the manuscripts sent for publications.

Dr. Li Liu contributed in giving guidance in the manipulation of equipment, executing some aspects of the experiments, and revising the manuscripts. Dr. Claude Gariépy contributed in providing samples and revising the manuscripts for scientific publications. Prof. Shiv O. Prasher contributed in giving valid suggestions for improvement in the study and revision of the manuscripts.

TABLE OF CONTENTS

LIST OF FIGURES

LIST OF TABLES

NOMENCLATURE

ATP	Adenosine triphosphate
ASM	The angular second moment
ADP	Adenosine diphosphate
a*	The termed opponent color axe
a	Regression coefficients, including model constant
b*	The color-opponent dimension
c	Calibration set
σ	Standard deviation of a Gaussian function
θ	Angle of two pixels (°)
cv	Cross-validation
D	Distance of offset (pixels)
DFD	Dark firm dry
DMR	The first derivative of raw mean spectra
DMG	The first derivative of Gabor filtered mean spectra
f	Frequency of a sinusoidal wave

FL	IMF content at a specific rib
GF	Gabor filter
GI	Texture feature index extracted by GLCM
GLCM	Grey-level co-occurrence matrix
HSI	Hyperspectral imaging
IMF	Intramuscular fat
I	Image
L	Loin
L*	Lightness
ML	Marbling score at a specific rib
MLR	Multiple linear regression
MS	Marbling score
MR	Mean spectra
MG	Gabor filtered mean spectra
P	p-value
PFN	Pale, firm, normal

PLSR	Partial least squares regression
PM	Proportion of marbling
PL	Proportion of lines
PSE	Pale, soft, exudative
R	Correlation coefficient
r	Radius of circular mask of wide line detector
RFN	Red, firm, normal
RGB	Red-green-blue
RSE	Red, soft, exudative
RMSE	Root mean square error
SAS	Statistical analysis software
SE	Square error
theta	Direction of offset (°)
thresh	The global threshold of wide line detector
v	Validation set
WLD	Wide line detector

I. GENERAL INTRODUCTION

1.1 Background

Pork is very popular due to its unique characteristics in terms of nutritional quality, distinct flavor, and palatability. Along with the beef and poultry industries, the pork industry is a multi-billion dollar business worldwide. Global pork production was over 100 million metric tons in 2012, with roughly 2% increase from the previous year (Foreign Agricultural Service, United States Department of Agriculture (USDA), 2012). Pork companies produce different types of pork products ranging from fresh, frozen, smoked, and canned meats to sausage. Pork and pork products comprised about 70% of processed meats in Canada (Agriculture and Agri-Food Canada, 2011). The large amount of pork and pork products did not only go to Canadian markets, but were exported worldwide. Therefore, the quality of pork should meet the requirements and high standards of different markets.

The demand for pork of high quality is increasing dramatically. Together with the current need for improving quality, the pork industry is faced with a number of challenges, including the maintenance of high-quality standards along with a demand of reduction in production costs. Meeting these challenges has become crucial to the development of the pork industry. Intramuscular fat (IMF) content is closely related to pork palatability and thus to pork quality. The intramuscular fat content of pork must be identified and quantified to classify pork. Ineffective fat inspection can lead to lost revenue for the pork industry. Pork companies and suppliers have sought to devise efficient and low-cost quality inspection methods to enable them to meet stricter pork quality standards, thereby raising their competitiveness and expanding their market share.

Either marbling score or intramuscular fat content represents the intramuscular fat level of pork. Conventional determination methods for intramuscular fat content are based on chemical fat extraction, which is tedious, time-consuming, destructive, potentially imprecise, costly, and environmentally harmful. Consequently, the pork industry has sought to implement non-destructive rapid-detection methods and devices to determine the intramuscular fat content of pork. Traditionally, pork marbling is scored subjectively from 1 to 6 and 10 according to National Pork Producers Council (NPPC) charts (NPB, 2002). Besides being unrepeatable and labor-intensive, this conventional method is not suitable for online inspection of pork quality. Therefore, fast, real-time, and non-chemical detection technology is necessary to assist the development of the global pork industry. For this purpose, pork producers and processors are seeking ways in which new technologies, such as hyperspectral imaging, can improve and speed up the fat inspection of pork meat.

To overcome the limitations of regular machine vision techniques and spectroscopic technology, hyperspectral imaging was recently introduced for the quality control of food. Hyperspectral imaging provides a means of visualizing spatial distribution and capturing spectral information of an object over the visible (390-700 nm) and near-infrared (NIR) spectral regions (700-2500 nm) (Bannon, 2009). Recently, the technique has become more and more popular due to its non-destrictive characterstics and the challenges of market segmentation.

Most published studies on hyperspectral imaging of pork have focused on pork qualities such as drip loss, pH, and color, whereas very few studies have reported the application of hyperspectral imaging in assessing the intramuscular fat content of pork. To classify marbling levels, Qiao *et al*. (2007c) analyzed hyperspectral images using grey-level co-occurrence matrix (GLCM) method. Using a type of GLCM measuremen, i.e. angular second moment, the authors were able to determine pork marbling scores ranging from 3.0 to 5.0 (±1), but they were not able to distinguish the score level of 10.0. To assist the analysis of hyperspectral images, and draw on data from Qiao *et al*. (2007c), Liu *et al*. (2012) used wide line detector (WLD) for the objective assessment of pork marbling score. Line pattern analysis was applied in pork quality control for the first time. Predictive accuracy of 99% was achieved. However, this study did not include validation using independent pork samples. Reflecting the valued potential of NIR hyperspectral imaging for prediction of fat levels in meat, Kobayashi *et al.* (2010) applied NIR hyperspectral imaging for intramuscular fat detection in beef.

Research activities have not fully explored the relationship between hyperspectral images and the marbling score or IMF content of pork. Given the success of above-mentioned studies, an investigation of hyperspectral imaging for intramuscular fat levels of pork may be equally successful. Pattern analysis techniques performed well in pork quality detection using hyperspectral images in the 400-1100 nm range (Qiao *et al*., 2007c; Liu *et al.*, 2010; Liu *et al.*, 2012). It is therefore of great interest to study the efficiency of pattern analysis methods, such as Gabor filter, grey-level co-occurrence matrix, and wide line detector in the processing of hyperspectral images.

Since the marbling score is assessed subjectively, the study of digital images of pork has the potential to provide greater convenience for the evaluation of marbling scoreg. For example, if a model using red-green-blue (RGB) images could be developed with good predictive and descriptive ability, a normal RGB camera could be implemented in the real-time inspection systems of pork, and portable detecting instruments could be developed. Therefore, RGB imaging presents an intersting means of determining pork marbling score.

Conventional evaluation of pork marbling is performed on fresh pork at the 3rd/4th last ribs, according to the standard charts of NPPC (NPB, 2002), while determination of IMF content is focused on the five last ribs (Fortin *et al.*, 2005; Rincker *et al.*, 2008; Lo Fiego *et al.*, 2010; Lakshmanan *et al.*, 2012). Different anatomical locations were used due to the large variation of IMF content across the longissimus muscle. Hence, it is of interest to study the variation of IMF content and marbling score along the longissimus muscle and to see if hyperspectral imaging could assist the correlation study. Hyperspectral images of frozen and frozen-thawed pork were collected to study their influence on non-destructive measurements of IMF content and marbling score.

1.2 Hypothesis

Based on the foregoing discussions, the hypothesis in this study is that hyperspectral images of pork could provide accurate information about the intramuscular fat content of pork; application of pattern recognition techniques could elevate the accuracy of prediction results; the intramuscular fat content of pork at several last rib locations could be correlated; pork in different states (namely fresh, frozen and frozen-thawed) could be used for non-destructive determination of pork intramuscular fat content and marbling score using hyperspectral imaging.

1.3 General objective

The general objective of this study was to assess the intramuscular fat content and marbling score of pork using non-destructive hyperspectral image analysis. The outcome is anticipated to enhance the evaluation of intramuscular fat content and support modern pork production. The knowledge will be critical in pork processing resulting in improved pork products and efficient pork production.

1.4 Specific objectives

To contribute to the overall objectives, the specific objectives for this project are:

1. To develop a regression model to determine the marbling score of pork using hyperspectral imaging augmented with pattern recognition techniques.
2. To predict the marbling score of fresh pork using standard RGB images of pork.
3. To quantitatively evaluate intramuscular fat content and describe the distribution map of intramuscular fat content in pork using hyperspectral images.
4. To assess the influence of freezing and thawing on the capacity of NIR hyperspectral images for prediction of intramuscular fat level of pork.
5. To study the correlations between intramuscular fat content and marbling score of pork at the last rib and the corresponding attributes of pork at several ribs anterior to the last rib.
6. To explore the use of hyperspectral images of rib end for non-destructive characterization of intramuscular fat content and marbling score of pork at the several last ribs.

II. GENERAL LITERATURE REVIEW

2.1 Pork and pork quality

Pork is commonly defined as the edible postmortem components of the slaughtered pigs, including tissue, muscle fiber cells, fat and connective tissue, even bones that are originated from hogs (Miller, 2002). Usually pork is considered as a type of red meat due to its level of myoglobin being higher than in poultry or fish. The structure and composition of pork meat determines its unique flavor. For centuries, pork and its derived products including bacon, sausage, pork chops, minced pork, and ham have made or constituted some of the most important foods consumed in many countries worldwide. Hence, pork has been used widely as one of the main food source of the human diet, in ways of raw meat, by-products or an essential ingredient in other food products. Showing worldwide consumption of meat by species, Figure 2.1 indicated that pork is the most popular meat. The specific market of pork varies. In 2012, the greatest pork imports went to China, Russia, the Ukraine and Mexico. China is currently making efforts to upgrade the quantity and quality of their pig production. The United States and Canada are two of the major producers and exporters of pork and pork products. Exports of pork bring in profits of at least $1 billion per year for those two countries. Pork produced in Quebec is famous in the industry for its high quality. Global pork production increased by almost 35 million metric tons from 1996 to 2012 (Figure 2.2, Food and Agriculture Organization of the United Nations, 1996-2012). There is an increasing trend of global pork production is observed despite the current larger market share of pork compared to other meat. World production and consumption of pork is predicted to continue increasing over the next few years (Foreign Agricultural Service, United States Department of Agriculture, 2012).

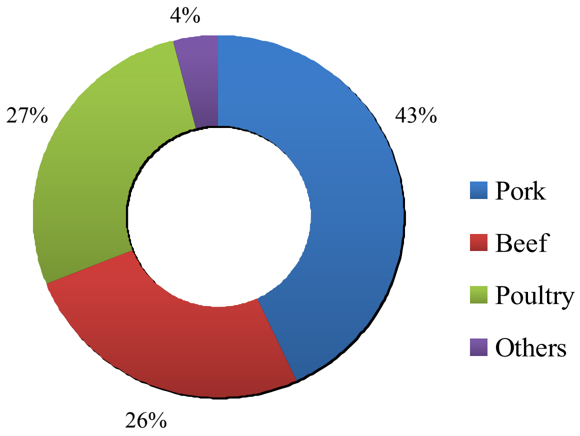

Figure 2.1 Global meat consumption by species (million metric tons, Source: http://www.fas.usda.gov/dlp/pubs.html).

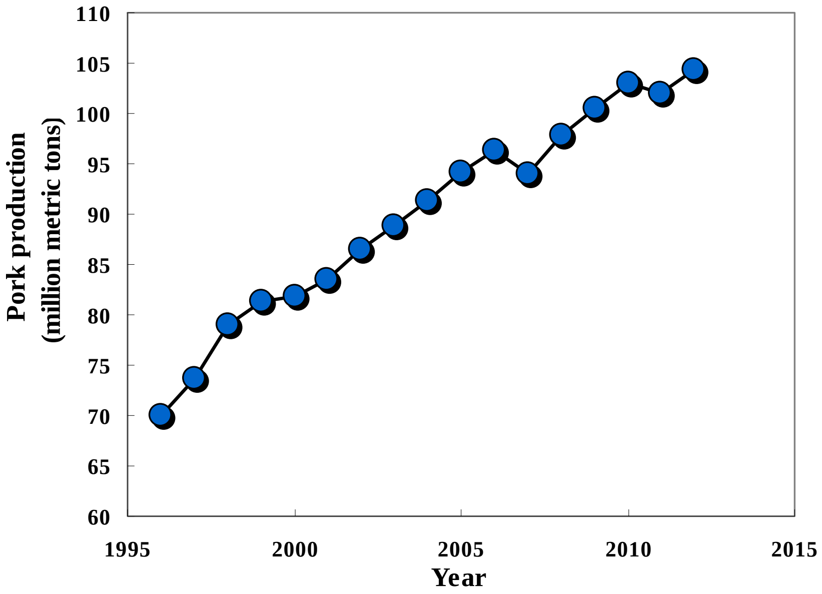

Figure 2.2 Global pork production from 1996 to 2012 (Data obtained from: http://www.fas.usda.gov/dlp/pubs.html).

Along with the growing market and increasing production, keeping or enhancing pork quality is essential for the pork industry to maintain this upward trend. The quality of raw pork covers the distinctive traits, characteristics, capacities, or virtues that make the meat acceptable to consumers. In the market, food quality includes external factors such as appearance (size, shape, color, gloss, juiciness, and consistency), texture, and flavor; and internal factors such as chemical, physical, and microbial activity. In the pork industry, pork quality can be assessed by determining several technological attributes including intramuscular fat content, water holding capacity, marbling score, tenderness, and sensory attributes like flavor, chewiness, and juiciness. Pork quality standards are coordinated with the development of social acceptance of the food.

2.2 Challenges for the pork industry

The pork industry represents one of the major components of the food industry. It includes producers, processors, retailers, packing companies, advertisers, the transporting industry and other segments. The objective of producing pork is to provide a high quality product for consumers. During meat production, the quality and safety of raw pork are evaluated using either objective or subjective techinques. The meats are classified to different levels of quality and are assigned to targeted markets. Along with the development of the world economy, the pork industry is facing several challenges.

Over the past two decades, the pork industry has changed a great deal due to massive hyper-consolidation in terms of merging of players in the pork industry. The number of processors has declined but the scale of operation has exploded (MacDonald and William, 2009). The high concentration of the industry has led to high competitiveness and an expansion of market shares. Therefore, pork related companies are facing a high pressure to make improvements in every possible aspect of meat production. Along with efforts towards enhancement of industrial efficiency, the industry is seeking to lower production costs to the greatest extent. The value of pork production fluctuated within a relatively narrow range from 1970 to 2011 (USDA Economic

Research Service). Hence, the low increase in value has proved to be a challenge for pork producers. More economical and efficient quality control methods should be developed equivalent to support the development of the industry.

On the other hand, consumers today have become more discriminating regarding food quality. People have begun to focus on the nutrition level of pork. Some people even associate pork fat content with chronic diseases such as cancer and heart disease, which is still controversial. The consumers expect meat products that are labeled with fat content, fat compositions, sodium, calories, and cholesterol and other quality attributes. Requirements for meat products are changing as well. Leaner meat is preferred by North American today while fatter meat is preferred by Asian consumers. Therefore, to win in the food market, it is critical that the the pork industry enhance pork quality to meet the demand of consumers. In addition, governments have begun to pay greater attention to food quality and safety control. Standards that are more rigorous are applied to domestic meat production and international meat imports by different governments.

Therefore, to meet these challenges, effective detection methods and technologies would enable the pork industry to tailor pork products for the changing appetite of consumers and the increasing requirements of governments. Features of objective, chemical-free, rapid, non-destructive, and real-time are amongst the most important ones for technologies that will be applied in modern the pork industry.

2.3 Longissimus muscles

Pork muscle is an unpredictable product due to the complex body structures of animals and the various factors that could affect the quality of the meat, such as varieties, feeding resources, time of aging, chilling rate, post-mortem age, way of slaughter, pre-slaughter handling, storing status, and method of dissection. After slaughtering, muscles from animals become meat. Some principal muscles are sold as meat such as muscle from belly, legs, back, shoulder, and legs. These are sold as products such as loins, rib chop, rack joint, leg joint, shoulder joint, and mince. The *Longissimus dorsi* muscle (as shown in Figure 2.3) is one of the most popular and major products selling on the market. The longissimus muscle is part of the erector spinae muscle groups (sacrospinalis) along the back of the pig. The erector spinae muscles run parallel to the spine from the base of the skull to the base of the spine. The longissimus muscle represents approximately 4% of the live animal, 7% of the carcass, 12% of all carcass muscles, and 51% of the back muscles (Kauffman, 2012). These values vary by breed, genetic types, diet, rearing, slaughtering, and other factors.

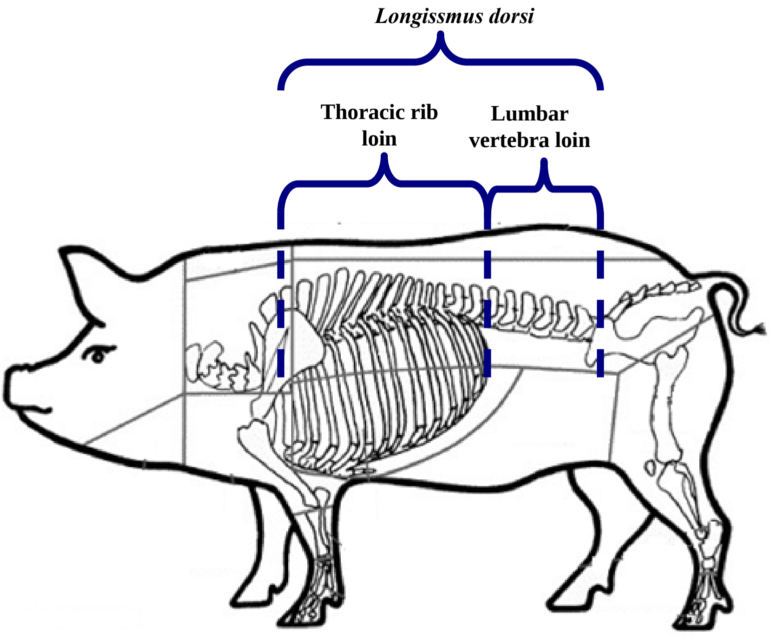

Figure 2.3 Pork cuts (Source: http://www.kristom.com/products.php).

The lumbar loins are the lower of the *Longissimus* muscles, which run along the lumbar vertebra. The thoracic rib chops are the upper portion of the longissimus muscles, which run from the top first to the last thoracic vertebra. Thoracic loins with ribs or without bones, also known as center cut loin, are popular as main constituents of many meals. The thoracic loins are the muscle material studied in this thesis.

2.3.1 Composition

Longissimus muscle usually refers to the meat that is surrounded by connective tissue and surrounding fat. Muscle mainly consists of lean meat and fat droplets (adipocytes) between leans. The constituents of muscle include water, protein, and lipid, along with carbohydrates, non-protein nitrogenous substances [creatine and creatine phosphate, adenosine triphosphate (ATP), adenosine diphosphate (ADP)], free amino acids, anserine, and carnosine), minerals, and vitamins. Water and protein are the two largest constituents of muscle, and are mainly stored in lean (Huff-Lonergan, 2010). In living tissue, water plays an important role in thermoregulation, as a medium of cellular processes, in the transport of cell-related nutrients and in the vascular system. Protein plays a range of functions in living tissue, as there are many types of proteins. Muscle proteins help to maintain the muscle structure, organize the muscle and muscle cells (a bundle of muscle fibers), assist in contractile movement of muscle, regulate the interactions between different classes of proteins, process cellular signals, metabolize enzymes, and assist the protein degradation (Huff-Lonergan, 2010).

Little lipid is found in the lean while most of the lipid is stored in fat droplets between leans. Although there is a small amount of lipid in longissimus muscle, lipids play an important role in living animals. Lipids are involved in energy metabolism, membrane structure, and various other processes such as immune responses and cellular recognition pathways (Huff-Lonergan, 2010). The lipid in connective tissue (cell membranes) inside lean helps in the movement of muscle.

At the postmortem stage, there are many changes in the composition of muscle. As living tissue is converted to meat muscle, energy is gradually depleted. Proteins are oxidized and gradually nitrated (Rowe *et al.*, 2004; Huff-Lonergan, 2010). Metabolism shifts from being aerobic to anaerobic, resulting in a decline of pH value. Ionic strength is raised along with the levels of calcium, sodium, and potassium. Those postmortem changes of composition during the storage of meat have a number of influences on the meat quality, particularly with regard to fat content, fat composition, water holding capacity, and tenderness. Leaner pigs (low lipid content) can exhibit poor capillarization of muscle fibers, and thereby result in pork of reduced quality.

2.3.2 Structure

In the living animal, the longissimus muscle is a type of skeletal muscle, which is connected to bones. Skeletal muscle has a complex structure, which transmits energy in the myofibrils to the entire muscle, perform the actions of the limb, and ultimately affects meat quality. The lean muscle visible to the naked eyes includes many muscle fascicles, which are enclosed and connected by several layers of connective tissue. Fat deposits can be found between groups of muscle fascicles. Each muscle fascicle (bundle of muscle fibers) contains a different number of muscle fibers (muscle cells), which are bound up by a layer of membrane, the sarcolemma. The sarcolemma is connected by continuous connective tissue, the edomysium (Bailey and Light, 1989). The muscle fiber has a cylindrical shape, and can be up to a few centimeters in length. Histochemical and biochemical properties of a muscle fiber, such as fiber type composition, fiber area, oxidative and glycolytic capacities, and lipid contents, are factors that have been found to interactively influence meat quality.

Inside a muscle fiber are sarcoplasma and plentiful myofibrils (Figure 2.4). Sarcoplasma contains the red muscle pigment myoglobin, which absorbs oxygen and reserves oxygen for contraction of muscle myofibrils. Myofibrils make up about 70% of a muscle fiber's volume. Myofibrils are made up of two major types of filaments, thin and thick filaments, whose main components are the proteins actin and myosin, respectively, and a third type of filament composed primarily of the protein titin (Ma *et al.*, 2006; Huff-Lonergan, 2010). Myofibrils have a striated appearance due to the alternation of dark (A band) and light (I band) bands within each myofibril. The bands are created by the alternating hexagonal arrangements of thick and thin filaments. Each hexagon is a

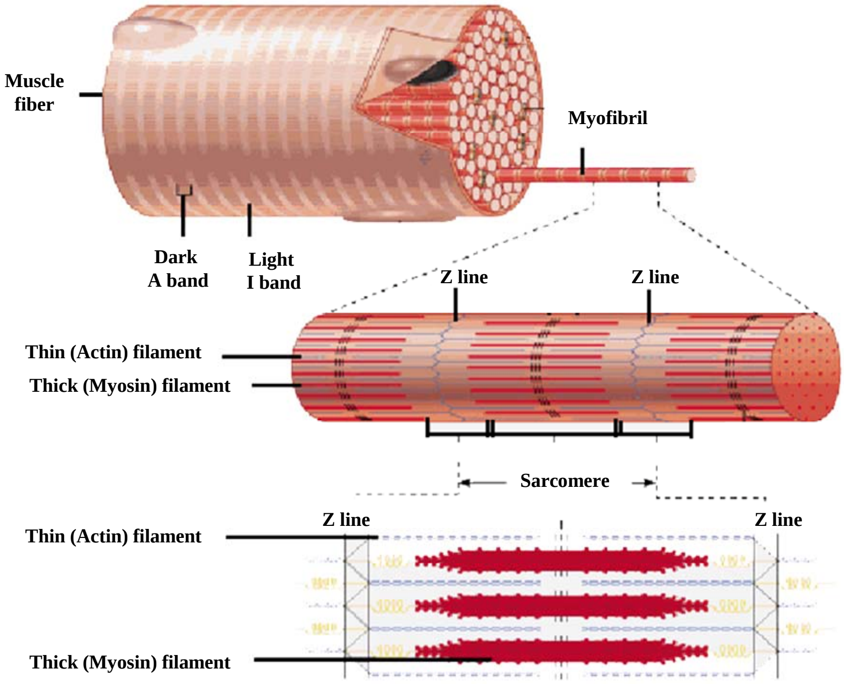

Figure 2.4 Structure of muscle fiber (Source: http://humanbiologylab.pbworks.com/w/page/67318721/How%20Does%20a%20Muscle%20Contract_Kayley%20Mikolajczyk).

functional unit of muscle, i.e. sarcomere. The whole band of thick filament including the overlapping band of thick and thin filaments in a sarcomere results in a dark band, while only thin filaments exist between two sarcomeres, the resultant band is light band. The Z line in the center of a light band is a cytoskeletal disc connecting parallel thin filaments, and the region between two such Z lines is termed a sarcomere. The protein titin acts to stabilize the integrity of the sarcomere and improve the spring of the muscle.

The muscle contraction results from the interaction between thin and thick filaments. In living muscle, when ATP is hydrolyzed, energy is liberated for myosin to pull the thin filaments toward the center of the sarcomere. The myofibril is then shortened, resulting in the contraction of muscle. When a new molecule of ATP is bound to the myosin head, the myosin and actin disassociate, which results in the relaxation of muscle. In the postmortem stage, muscle becomes stiff because the supply of ATP is depleted, resulting the irreversible form of actomyosin (Huff-Lonergan, 2010; Kauffman, 2012).

2.4 Intramuscular fat

2.4.1 Definition of intramuscular fat and marbling

Fat in muscle is an important factor in terms of meat quality. Fat in pork supplies the essential fatty acid linoleic adic (contains 18 carbon atoms and 2 unsaturated bonds), carries fat-soluble vitamins, and provides protection and insulation for the energy molecules. Fat in pigs can be classified to intramuscular fat, intermuscular fat, and subcutaneous fat according to its position (Figure 2.5). Intramuscular fat appears as cellular structure within muscle. In pork muscle, intramuscular fat is stored as droplets not only within intramuscular adipocytes, but also within myofibril and connective tissue within muscle. Intramuscular fat content in longissimus muscle varies according to breeds, individuals, diets, and even cuts of the animal. Intramuscular fat is different to intermuscular fat, which refers to the fat located between different muscles in a same cut. Subcutaneous fat is the fat, which lies immediately under the skin.

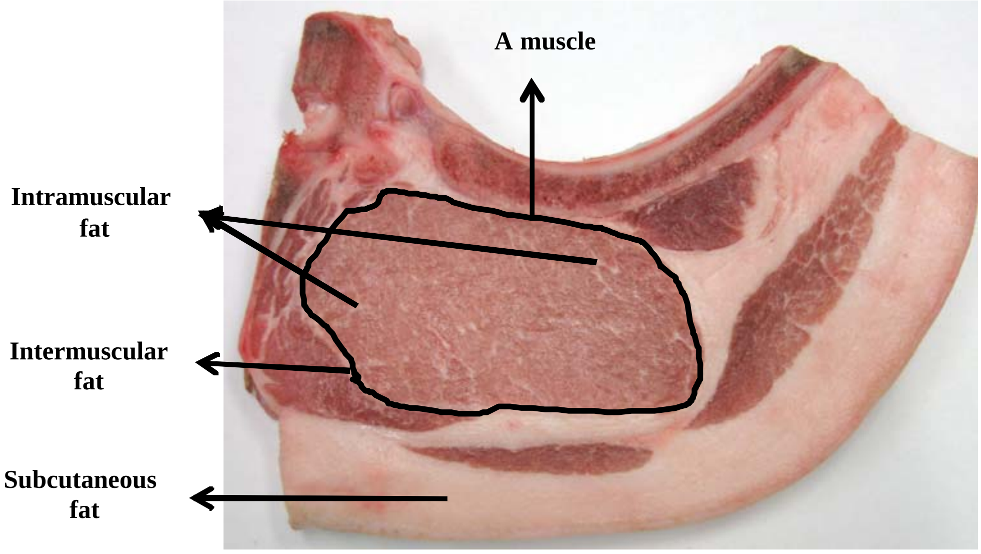

Figure 2.5 Fat in meat.

Triglycerides and phospholipids are the two main kinds of lipid found in intramuscular fat of pork, with triglycerides being around 80% of the total (Huff-Lonergan, 2010). Phospholipids can be found in cell membranes while triglycerides are the main forms of energy reserves. The lipid in intramuscular fat contains a wide variety of saturated and unsaturated fatty acids (Figure 2.6). C-H and C-C are the main chemical bonds in intramuscular fat in pork, while smaller numbers of C-O, C=O, O-H, C=C, and N-H could be found. As a type of complex, fat can change to other substances due to a series of reactions of bonds. The unsaturation levels of the principle fatty acids are correlated to the melting point of a fat. Lipids with more saturated fatty acids have higher melting points. Intramuscular fat is more saturated than intermuscular fat and subcutaneous fat, thus intramuscular fat has a higher melting point (Romans *et al.*, 2001).

The profile of fatty acids is correlated to the quality of pork, such as firmness, color, and health. There is an effort to improve fat quality by changing fatty acids in pork fat, such as reducing saturated fatty acids since they are said to increase the risk of cardiovascular diseases.

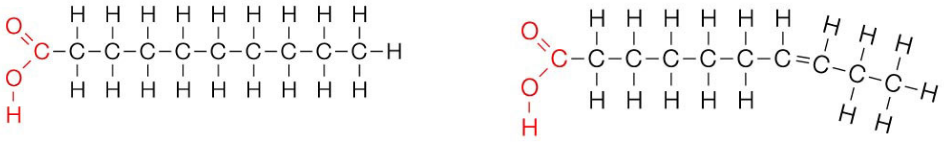

(a) Saturated (b) Unsaturated

Figure 2.6 Typical molecular formulas of fatty acids (Source: http://cccmkc.edu.hk/ ~sbj-chemistry/.htm).

Marbling refers to the visible white flecks of intramuscular fat, i.e. adipocytes among bundles of muscle fibers (muscle fascicle). Marbling only refers to the visible intramuscular fat between muscle cells, while intramuscular fat refers to fat that is distributed not just between muscle cells but in the muscle cell as well. The amount, structure, and distribution of marbling in muscle vary by species, individuals and cuts (Kauffman, 2012). Compared to marbling in beef, marbling in pork is less visible due to the light color of pork lean and the relatively low amount of extractable lipids in pork. However, consumers are still able to distinguish pork with marbling at low (1%), medium (2.3%), and high (3.5%) levels. Since marbling level can reveal the IMF level of pork muscle, some countries such as the United States, include marbling levels in pork grading systems. Marbling levels were even regarded as the same as IMF levels in some laboratory studies (Witte *et al*., 2000; Teye *et al*., 2006; Rincker *et al*., 2008; Hocquette *et al*., 2010).

2.4.2 Development of intramuscular fat

The development of IMF in pork occurs early in the life of hogs and develops during growth of the animal. The ways of either form of adipocytes or accumulation of adipose is linked to uptake, synthesis and degradation of fatty acids. The intramuscular adipocytes are derived from the stem cells of an animal. The postnatal adipocytes are formed along with depot of the budding embryonic cells and fetal adipose cells. During the growing stage of fetal and postnatal, lipids are first stored within muscle fibers. After then, when the energy cannot be metabolized immediately in muscle fiber, they will be stored in adipose tissue for later synthesis of fatty acids, which will be released as a later energy supply (Azain, 2004; Hausman and Richardson, 2004). As a result, the fat is deposited and intramuscular adipocytes grow in size and numbers (Gondret and Lebret, 2002; Hausman *et al*., 2009). Hence, adipocytes are developed at a lower rate than the growth of muscle fiber, resulting in increased concentration in the later life of an animal. Thus, over the life of an animal, IMF develops in three stages: constant, linear increase, and plateau.

2.4.3 Influence of intramuscular fat content on pork quality

Intramuscular fat helps in the organization of muscle structure and contributes to the unique flavor of pork. As the intramuscular fat is deposited in and around the muscle fascicles, the structure of the endomysium is disintegrated, which results in the dissolution of collagen in muscle, the collapse of muscle structure, and the increase of raw meat tenderness and juiciness. When pork is cooked, the melting fat produces oil that lubricates the muscle fibers and increases the juiciness and tenderness of cooked pork. The lipid oxidation products produced by fat give rise to the aroma of cooked pork.

It is accepted that IMF content is correlated to pork quality parameters such as flavor, juiciness, tenderness, and the overall acceptability or palatability of pork. A very low amount of intramuscular fat in muscle leads to an inferior meat, being dry and unpalatable (Warriss *et al*. 1996). A number of studies have revealed that better sensory quality was the result of increased amounts of intramuscular fat in the pork meat (Rhodes, 1970; Kemspter *et al*., 1986; Rincker *et al*., 2008). However, other studies reported that significant enhancements on sensory traits of pork were observed only when a threshold level of intramuscular fat was applied. Levels of 1.5, 2, and 2.5% were suggested by Fortin *et al.* (2005), Fernandez *et al*. (1999), and Barton-Gade and Bejerholm (1985), respectively. Van Laack *et al*. (2001) reported that there was a positive linear relationship between IMF level and tenderness in the high-fat Duroc pig breed, whereas the relationship was not noticeable in the low-fat Landrace and Berkshire breeds. Another study by Lonergan *et al*. (2007) demonstrated that intramuscular fat has limited effect on pork tenderness and texture when the pH value remained the same level.

The perception of pork quality including intramuscular fat level by consumers differs due to their cultural and social background, and even individual health cognition. For instance, Canadians and Americans prefer leaner pork. Due to the preference for low-fat pork, the production system in the US was modified to produce less fat in meat. Furthermore, fatty acid composition of fat is considered to affect pork quality as well as fat quantity (Wood *et al*., 2008). The composition of lipids affects the oxidative stability of lipid during processing. A high level of lipid oxidation would produce rancid odour in meat (Scollan *et al*., 2006). The conjugated linoleic acid (essential polyunsaturated fatty acid) is important to human nutrition, as it must be ingested from food since it cannot be synthesized in the human body. An increase of linoleic acid in pork fat would be beneficial to human health. Some studies have implicated the consumption of fat in health issues such as obesity, cancer, or coronary heart disease (Azevedo *et al.*, 1999; Beauchesne-Rondeau *et al.*, 1999). To meet the demands of different markets, efforts have been made to modify IMF levels, and even compositions.

2.4.4 Modification of intramuscular fat

The swine industry has been making effort to modify IMF content by choosing gene types, choosing gender, changing feed intake amounts, changing compostions of diet and other approaches. Generally, breeds that mature earlier will produce a fatter carcass than breeds that have a later maturation time. Intramuscular fat proportion increases with increasing carcass weight, since the deposited rate of intramuscular fat in earlier maturing breeds is faster than later maturing breeds. The Duroc breed of pig has higher intramuscular fat content than the British Landrace breed (Cameron and Enser, 1991). An increase in intake by pigs or in male pigs generally have higher intramuscular fat content as they have matured earlier than female pigs (Moloney *et al.*, 2002). Feeding pigs with high-energy (high fat and/or low fiber) feed will increase intramuscular fat content. Excess protein in the diet of pigs will result in a muscle with low intramuscular fat content.

Some efforts have been made to modify the composition of intramuscular fat, i.e. fatty acids, by choosing breeds or changing diet. Generally, genotypes with higher IMF content are associated with more monounsaturated fatty acids. However, an exception has been reported by Cameron and Enser (1991) that the Duroc breed, which provides fatter muscle than the British Landrace breed, had higher saturated and monounsaturated fatty acids proportions in intramuscular fat than the British Landrace breed. Dietary fatty acid composition influences the profile of fatty acids in intramuscular fat in meat (Verbeke *et al*., 1999; De Smet *et al*., 2001). Incorporation of oilseeds (e.g. tallow, rapeseed, linseed, safflower, soybean) or increased supply of polyunsaturated fatty acids in the diet of pigs can raise the concentration of polyunsaturated fatty acids in intramuscular fat in meat (Riley *et al*., 2000; Sheard *et al*., 2000; Kouba *et al*., 2003). Eggert *et al*. (2001) demonstrated that inclusion of the linoleic acid in the diet of pigs increased the concentration of the linoleic acid in pork.

Hogs are raised to achieve different levels of fatness and different fatty acid compositions. Variation in IMF content differs substantially between countries, which places pressure on producers to determine IMF rapidly, so as to assist in market allocation.

2.5 Evaluation of the intramuscular fat content of pork

2.5.1 Conventional methods

The IMF level in pork is indicated by two attributes, i.e. intramuscular fat content and marbling score. Marbling, as the visible intramuscular fat in the surface of pork, is traditionally assessed visually by comparing to standard charts. Different countries may use different standards. The most used standards are those launched by the National Pork Board Council (2002), in which there are seven levels of marbling from 1 (low marbling level) to 6 and 10 (high marbling level). To practice subjective evaluation, assessors should be trained by an intensive training program. This would raise the pressure on the pork industry by adding the costs of training and employing graders. In addition, different specialists may give different scores for one sample and one standard since human error is inevitable. As such a method is time consuming, labor intensive, and costly, traditional marbling assessment cannot be applied in real-time inspection systems and will not suit the modern pork producing industry.

Intramuscular fat content is conventionally determined chemically. For this type of method, fat is extracted from raw meat by chemical solvent to determine the amount of fat (AOAC, 1990; AOAC, 2000). The traditional measurement of intramuscular fat content is objective, with no need to consider the type, size, or color of pork. However, the chemical method has the disadvantages of being invasive, environmentally-harmful, labor-intensive, and time-consuming. To overcome the challenges that the pork industry is facing, a better detection method, one that has the advantages of being non-destructive and rapid, should be developed to replace the traditional one.

2.5.2 Computer vision

Recently, novel techniques have been investigated for their usefulness as indicators of IMF level of pork, including computer vision, nuclear magnetic resonance (NMR), spectroscopy, and hyperspectral imaging. NMR offers a non-invasive access to fat distribution and amount of intramuscular fat in pork (Monin, 1998; Brøndum *et al.*, 2000). However, the prohibitive cost of this method would not meet the criterion of low costs in pork production.

Computer vision integrates devices for non-contact optical sensing and data processing to interpret an image automatically by constructing meaningful information from digital images of physical objects (Ballard and Brown, 1982). Computer vision seeks to simulate human vision by electronically perceiving and processing images. Normally, digital images are generated with three channels (red, green, and blue). The core of computer vision is image analysis, which aims to perform a predefined visual task.

Image analyses involve a series of image operations such as region segmentation, edge detection, image re-shaping, and feature extraction. Computer vision generates precise descriptive data of an image objectively, rapidly, consistently, automatically, and easily. The data can be recorded permanently for further analysis. All the benefits of computer vision make it attractive. Computer vision has developed dramatically since its origins in the 1960s and has been applied in diverse fields, including character or fingerprint recognition, product assembly, medical diagnostics, vehicle guidance, and food quality analysis (Gerrard *et al*., 1996; Zhou and Huang, 2003; Brosnan and Sun, 2004; Liu *et al*., 2007; Li and Nigel, 2008; Chen and Qin, 2008).

Recently, computer vision was expanded to pork quality assessment due to the ease of use (Lu *et al*., 2000; Tan *et al*., 2000; O'Sullivan *et al*., 2003; Tan 2004; Faucitano *et al*., 2005; Huang *et al*., 2013). Most studies have focused on color grading. Faucitano *et al.* (2005) applied computer image analysis to measure pork marbling characteristics. Marblings in three genotypes of pigs, namely Large White, a Meishan-derived dam line, and Synthetic Genex 3000, were studied. To enhance the contrast between lean and fat in pork, oil red-O was used to stain pork for several hours to enhance the contrast between lean and fat in the pork image. The analysis demonstrated that marbling fat was finer and better distributed in the Synthetic Genex 3000. Positive effect of marbling on pork tenderness was observed, indicating the contribution of marbling to pork eating quality. In addition, a significant correlationship between IMF content and pork marbling was demonstrated in the same study. Although computer vision is non-destructive, a chemical was involved to enhance the image quality of pork. This study indicated the limits of computer vision for fat detection in pork. Huang *et al.* (2013) successfully applied computer vision for the assessment of marbling score of pork by involving pattern analysis technique of wide line detector.

Normal computer vision is effective when quality attributes are evidently related to the extrinsic characteristics of an object such as color, size, and shape, but it becomes less effective or ineffective when quality attributes are mainly determined by the intrinsic properties of an object, such as IMF content. Due to the low contrast between fat and lean in pork, the limited spectral information (three channels of red, green, and blue) provided by normal computer vision makes it a challenge to detect intramuscular fat and marbling in pork. In addition, the heterogeneous distribution of intramuscular fat and marbling in pork presents another dilemma for normal image analysis.

2.5.3 Near-infrared spectroscopy

Spectroscopic methods here refer to photonic spectroscopy, which provide detailed spectral fingerprints of objects using the interaction between electromagnetic wave and the detected material. The spectral region covered is usually used to characterize the spectroscopic technique, such as visible (VIS) region (350-800 nm), near infrared (NIR) region (800-2500 nm), and mid-infrared (MIR) region (2500-25000 nm). Among types of spectroscopies, NIR spectroscopy has been accepted among researchers as a means for non-destructive sensing of food samples since the 1970s (Blanco *et al.*, 2002). NIR spectroscopy records spectra of samples without sample preparation and the spectra contain both physical and chemical profiles of the matter.

The absorption bands in NIR region mainly correspond to overtones and combinations of fundamental vibrations of molecules. The vibration of molecules could be explained by the electron transitions between different energy levels (ΔE). Eq. 2.1 is usually used to calculate the energy level produced by vibration of molecules (Blanco *et al.*, 2002).

$$E = (\upsilon + \frac{1}{2}) \frac{h}{2\pi} \sqrt{\frac{k}{u}}\,, \tag{2.1}$$

$$\Delta E = hv\,, \tag{2.2}$$

$$\Delta E = hv[1 - (2\upsilon + \Delta\upsilon + 1)y]\,, \tag{2.3}$$

where υ is the vibrational electron number, h is the Planck constant, k is the force constant, u is the reduced mass of the bonding atoms, v is the fundamental vibrational frequency, and y is the anharmonicity factor.

When $\Delta\upsilon = \pm 1$, the electron transition between contiguous energy levels yields absorption bands known as fundamental vibrational frequency, which are mainly located in the MIR region. The fundamental frequency of the bond, i.e. the wavelength of the band, can be calculated by Eq. 2.2 (Blanco *et al.*, 2002). When $\Delta\upsilon \neq \pm 1$, the transition between non-contiguous energy levels yields absorption bands known as overtones, which appear in the range of 780-2000 nm. The absorption band of the bond can be estimated by Eq. 2.3 (Blanco *et al.*, 2002). Interaction of multiple vibrational modes can cause concurrent transitions of energy states, which result in combination bands. The combination bands appear in spectral range of 1900-2500 nm. The NIR bands mainly arise from hydrogen atoms and hydrogen-related bonds of C-H, O-H, N-H, and S-H. Other bonds such as C=O, C-C, and C=C contribute much less in the spectral intensity. With regard to intramuscular fat, the main bands of lipid in the NIR region are located at

1208, 1416, 1724, 1760, 2190, 2304, 2348, and 2380 nm, whereas C-H bonds are mainly responsible for absorption patterns (Shenk *et al*., 1992; Blanco *et al*., 2002). With regard to water, the main bands in NIR region are located in 1400-1500 nm, whereas O-H is mainly responsible for the absorption (Vasko *et al*., 1971). On the other hand, movement of atoms could reflect the information regarding crystal structure, by which the physical properties of samples could be distinguished by NIR spectra.

Due to the close relationship between components in food and NIR spectra, NIR spectroscopy is widely employed for composition analysis of food. The development of instruments has encouraged the expansion of NIR spectroscopy in food quality control, such as the recent application of this technique in pork quality assessment. Several studies have been conducted to evaluate of IMF content in pork using NIR spectroscopy (Forrest *et al*., 1997; Brøndum *et al*., 2000; Prevolnik *et al*., 2005; Barlocco *et al*., 2006; Savenije *et al*., 2006; Prieto *et al*., 2009). Correlation coefficient (R) between measured and predicted values was widely used to evaluate the performance of built models in above studies. Brøndum *et al*. (2000) used NIR spectroscopy to predict the IMF content of pork with predictive linear correlation coefficient of 0.70. Savenije *et al*. (2006) applied reflectance spectrophotometer in determination of the IMF content of pork. Meat from three breeds of pigs was used as samples. The second derivative of reflected spectra was used to build prediction models. Linear correlation coefficients of calibration (*Rc*) between measure and predicted IMF content varied from 0.70 to 0.86, and correlation coefficients of validation (*Rv*) varied from 0.63 to 0.76. The NIR study on IMF content has recently been extended by applying NIR spectrum on both minced and intact pork meat (Prieto *et al*., 2009). Prediction results between 0.84 and 0.99 were obtained, while calibrations were less accurate for intact than for minced meat.

Due to the limited detection field, some studies have indicated that the minced or ground meat produced more accurate results than intact muscle when determing IMF content using NIR spectra (Isaksson *et al.*, 1992; Rodbotten *et al.*, 2000; Prevolnik *et al.*, 2005; Barlocco *et al.*, 2006). Rodbotten *et al.* (2000) suggested higher repeated numbers of NIR scans on intact meat samples to improve the prediction accuracy for intramuscular fat in meat. Research conducted by Wold *et al.* (1999) suggested that NIR spectroscopy in conjunction with imaging indicated better prediction for fat content of meat. These studies implied the limitation of spectroscopic techniques for evaluation of intramuscular fat in intact pork. Intramuscular fat is distributed in pork heterogeneously. However, spectroscopic techniques only measure the light feedback from a specific point of a sample instead of the whole surface. It would expand the ability of NIR spectroscopy and thereby improve the predictive ability of the technique if the detected field of view could be enlarged.

2.5.4 Hyperspectral imaging

With the development of instruments featuring improved spectral and optical components, a hyperspectral imaging (HIS) technique was proposed combining computer vision and spectroscopy. HSI overcomes the limits of spectroscopic techniques and traditional machine vision techniques. It was initially applied in remote sensing. Recently, HSI has received considerable attention for non-destructive inspection of meat quality. Hyperspectral images could provide detailed spectral information covering VIS and NIR spectral regions while providing spectral measurements over the entire surface area of the imaged product. Hence, HSI could be effective in the case of pork quality control, where both extrinsic, like appearance (e.g. size, marbling, color), and intrinsic (e.g. IMF content, drop loss, tenderness) properties could be captured. No specimen preparation is needed for detection using HSI. Multiple constituents in the objects could be measured simultaneously. The data could be stored permanently. As HSI is non-destructive and efficient, it is well suited for potential determination of IMF level of pork.

The use of HSI for rapid prediction of IMF level of pork meat has been successfully demonstrated in a few applications. Qiao *et al.* (2007c) applied VIS/NIR HSI for marbling grading of pork. Image parameters were calculated from images at 661 nm and were used to estimate marbling score of pork. Prediction was moderately successful with a small error between predicted and referenced marbling scores. Liu *et al.* (2009) reported the use of NIR HSI on evaluation of the IMF content of pork. Line features were extracted from NIR images of pork to predict the IMF content of pork. A promising prediction accuracy of 0.91 was obtained in this study. Although limited studies were reported regarding prediction of fat content in meat muscle, the promising results in the studies discussed above indicated the great potential of HSI for determination of pork IMF content.

2.6 Hyperspectral imaging

2.6.1 Fundamentals of hyperspectral imaging

As a combination of spectroscopy and computer vision, the HSI technique is based on the principles of spectroscopy and computer vision. Hyperspectral images consist of numerous spatial images of an object at successive wavelengths. The data cube is achieved through the superimposition of the spatial images at continuous wavelengths, thus creating a three-dimensional data cube called *hypercube*. At each wavelength, the image of the sample is formed from the responsed lights of all points in the surface of the sample. The spectrum of each pixel in the image can be extracted from the *hypercube*. The spectra are derived from the changes of molecular energy levels in the sample. Images of samples are indicative of the physical and external properties of samples, while spectra of samples represent chemical characteristics (Sun, 2008). Spectra or images from the data cube of different samples can be compared. Similarity between the image and spectra of two samples indicates similarity of physical composition or chemical features.

2.6.2 Configuration of hyperspectral imaging system

The *hypercube* usually can be constructed in three ways: *area scanning*, *point scanning*, and *line scanning* (Gowen *et al*., 2007). Due to the presence of conveyor belts (for in-line inspection) in most food processing plants, *line scanning* (or *pushbroom*) is the preferred method of image acquisition. The *hypercube* of line scanning is acquired by composing several whole lines of an image instead of a single pixel at a time, and it is stored in the format of Band Interleaved by Line (BIL). In the BIL format, the current line along with the other previous lines are available and can be composed to form images. HSI system can be operated either in reflectance or transmittance modes. Most studies were conducted in reflectance mode (Gowen *et al*., 2007). In transmittance mode, thin sample sizes are usually used to allow light to travel through the sample. Meat muscles are usually inspected in reflectance mode.

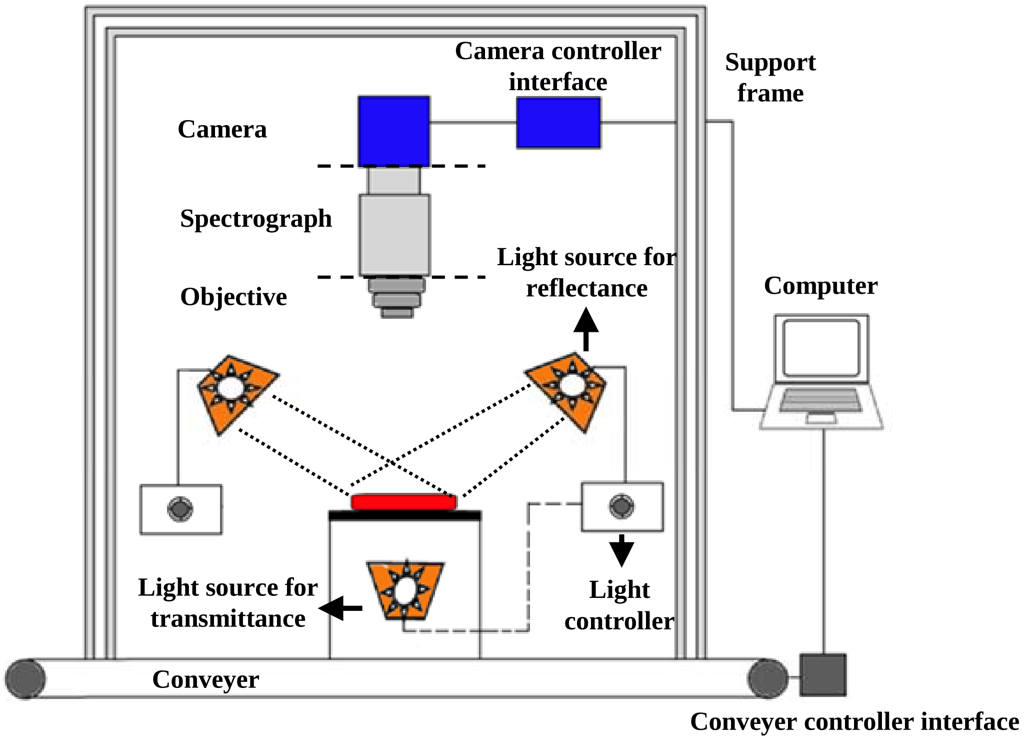

Figure 2.7 Configuration of a hyperspectral imaging system.

A typical hyperspectral imaging system is comprised of hardware and software. The specific configuration varies on the object to be assessed. Most hardware platforms for hyperspectral imaging share common basic components (Figure 2.7): an illumination to provide a light source; light controllers; a camera to collect spatial resolution; a spectrograph to collect spectral resolution; a zoom lens to adjust the field of view; a platform fixed to a conveyer to hold and transport the sample; a support enclosure; and a computer with software to control the camera and the conveyer, and compose and store the *hypercube*. Light sources are placed at different positions according to the used mode. In the reflectance mode, the light source and the camera are placed at the same side of the sample. In the transmittance mode, the light and the camera are placed at two sides of the sample.

For the detector of hyperspectral imaging system, there are three basic choices of cameras, including Silicon (Si) based charge-coupled device (CCD) or Complementary Metal Oxide Semiconductor (CMOS) camera, Indium Gallium Arsenide (InGaAs) camera, and Mercury Cadmium Telluride (HgCdTe) camera. The choice of the camera in hyperspectral imaging system depends on the required wavelength, the quantum efficiency (QE), and the cost. A higher QE of a camera indicates greater sensitivity. Due to limitation of technical development, CCD camera covering 400-1000 nm and InGaAs camera covering 900-1700 nm are those mostly applied systems in practice. The average QE of CCD cameras is around 30% at 400-1000 nm, while the average QE of InGaAs camera is around 60% at 900-1700 nm. An InGaAs camera, i.e. NIR hyperspectral imaging at 900-1700 nm is more recommended than a CCD camera considering the sensitivity. At present, the CCD camera (400-1100 nm) is the most widely used detector in food quality and safety analysis. The development of advanced instrumentation enabled the application of InGaAs cameras in food processing. Increasing interest has been shown in the application of NIR hyperspectral imaging, particularly in meat products due to the strong relationship between NIR spectra and meat quality.

2.6.3 Hyperspectral imaging for pork quality evaluation

The application of hyperspectral imaging in food analysis ranges from contaminant detection, defect identification, constituent analysis, and quality evaluation. The explosive number of scientific articles published on hyperspectral imaging for food quality control since 2005 (Figure 2.8) proves the growing interest in hyperspectral imaging for food quality control.

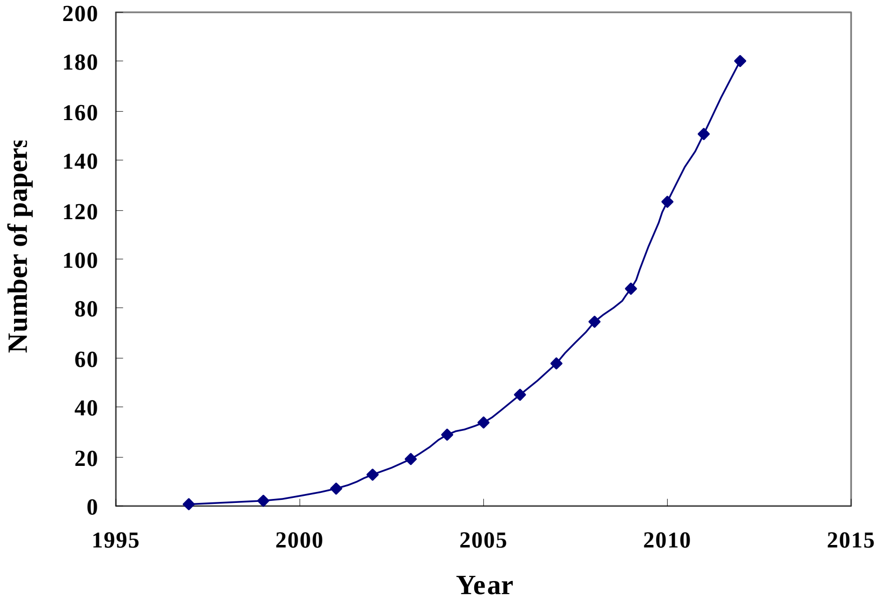

Figure 2.8 Number of papers published on application of HSI in food.

Application of HSI was initially focused on fruit and vegetables, but has recently expanded to meat products (Gowen *et al*., 2007; Sun, 2010; ElMasry *et al*., 2012a). Looking at the many studies published on the use of HSI for pork quality assessment (Table 2.1), more studies have used VIS/NIR hyperspectral imaging (400-1000 nm) than NIR hyperspectral imaging (900-1700 nm). Drip loss, pH, color, quality classification, and total visible count were the main attributes that were studied. The only three studies on prediction of intramuscular fat content and marbling of pork were conducted by Qiao *et al*. (2007c), Liu *et al*. (2009) and Liu *et al*. (2012). According to Liu *et al*. (2012), the low contrast between lean and fat in pork raised the difficulty of detection of marbling score in pork. Application of line pattern analysis technique, wide line detector, solved the problem by producing an accurate prediction result of 0.99. Validation with independent samples was not conducted in this study. Although few studies were reported on assessment of IMF level of pork using hyperspectral imaging, the promising results demonstrated the strong potential of hyperspectral imaging as a powerful detection technique for assessment of the IMF content of pork.

Table 2.1 Summary of wavelength region, analyzed quality attributes, studied image processing techniques employed in papers published on reflectance hyperspectral imaging of raw pork.

Wavelength region (nm)	Quality attributes	Image processing	Author, Year
900-1700	Color, drip loss, pH, sensory characteristics	Thresh holding (TH), averaging spectra (AS)	Barbina *et al.*, 2012a
900-1700	Quality classification	TH, AS	Barbina *et al.*, 2012b
900-1700	Identification of pork, beef, lamb	TH, AS,	Kamruzzaman *et al.*, 2012a
900-1700	Intramuscular fat content	Accumulation of images, Wide line detector (WLD)	Liu *et al.*, 2009
400-1100	Tenderness, Escherichia coli contamination	TH, AS, Lorentzian distribution function	*Tao et al.*, 2012a
400-1100	Total viable counts (TVC)	TH, AS, Gompertz function	*Tao et al.*, 2012b
400-1000	Marbling scores	WLD	Liu *et al.*, 2012
400-1000	Total volatile basic-nitrogen (TVB-N), pH, color	TH, AS, Lorentzian distribution function	Li *et al.*, 2011
400-1000	Quality classification	TH, AS, Gabor filter	Liu *et al.*, 2010
400-1000	TVC	TH, AS	Peng *et al.*, 2008
400-1000	Drip-loss, pH, color	TH, AS	Qiao *et al.*, 2007a
400-1000	Quality classification, color, texture, exudation	TH, AS	Qiao *et al.*, 2007b
430-1000	Quality classification, marbling score	TH, co-occurrence matrix	Qiao *et al.*, 2007c
400-1000	Drip loss, pH	TH, AS	Qiao *et al.*, 2005

Application of NIR spectroscopy on evaluation of intramuscular fat content in pork suggested that NIR hyperspectral imaging has a great potential for detection of intramuscular fat in pork. Due to the deep penetration of NIR illumination, reflectance mode in NIR hyperspectral imaging could be considered as a combination of transmission inside the deeper samples and reflectance on the surface. NIR hyperspectral imaging not only collects surface information of samples but the inside characteristics as well. In addition, the NIR region ranging from 900 to 1700 nm is derived from overtones of hydrogen-bearing moleculars such as C-H and O-H while the main bonds of lipids are C-H (Benson, 1993). This indicated the potential ability of NIR hyperspectral imaging for characterization of intramuscular fat in pork. The successful application of NIR hyperspectral imaging on assessment of marbling and fat content of beef, lamb, and pork also increased the interest on the application of hyperspectral imaging on pork fat (Liu *et al*., 2009; Kobayashi *et al.*, 2010; Kamruzzaman *et al*., 2012a, 2012b, 2012c).

Therefore, NIR hyperspectral imaging was adopted as the main detection technique in this study. Furthermore, nearly all the studies regarding application of hyperspectral imaging in pork quality control were conducted on fresh pork. The inherent features of intramuscular fat would not be modified dramatically by proper processing like freezing and thawing. There are many benefits if frozen or frozen-thawed pork could be used for image acquisition. Determination of IMF content could be expanded to each samples even at the retail stage. Waste of fresh pork could be reduced, by which cost of determination could be reduced evidently.

2.6.4 Pattern analysis techniques in processing of hyperspectral images

After the hyperspectral imageries of objects are acquired, the data are analysed following the procedure illustrated in Figure 2.9, where Io is the raw obtained image, and I_b and I_w are obtained when the camera is covered by a cap and when a standard reference is used as object, respectively, and I is the corrected reflected percentage image. Pre-processing such as threshold segmentation is useful to separate the interested part of the product image from the background and other nonrelevant parts. Post processing is used to remove objects too small to be of interest or to smooth the edge of a selected region of interest (ROI). The main purpose of image pre-processing and post processing is to raise the ratio of signal to noise. After the image pre-processing, different methods can be used to describe the feature of images or spectra (which represents the quality traits of food) from ROI. In most studies, algorithm of averaging spectra was adopted. Pattern analysis techniques including wide line detector, Gabor filter, and co-occurance matrix, were recently applied to extract image features (Devijver and Kittler, 1982). Image or spectral parameters from *hypercube* are obtained to input the model as independent variables. Therefore, the measured/ observed value of quality traits would be the dependent variable of image parameters. By data analysis, a prediction model is built based on the image or spectral index and quality traits of food are measured. During the validation of the built model, statistical indices of the model are calculated and evaluated according to specific criterion. If the performance of the model is not very good, the calibrated images could be re-analyzed to exploit further information and enhance the efficiency of prediction.

Image processing is a key step for data analysis in hyperspectral imaging. The interposition of image analysis techniques capable of effectively processing the information contained in NIR images has facilitated the expansion of hyperspectral imaging in pork quality control. Effective technique helps improve the efficiency of assessment using hyperspectral images. Amongst different methods, pattern recognition techniques of wide line detector, Gabor filter, and co-occurrence matrix were applied successfully on quality control of pork (Table 2.1). In pattern analysis, information about

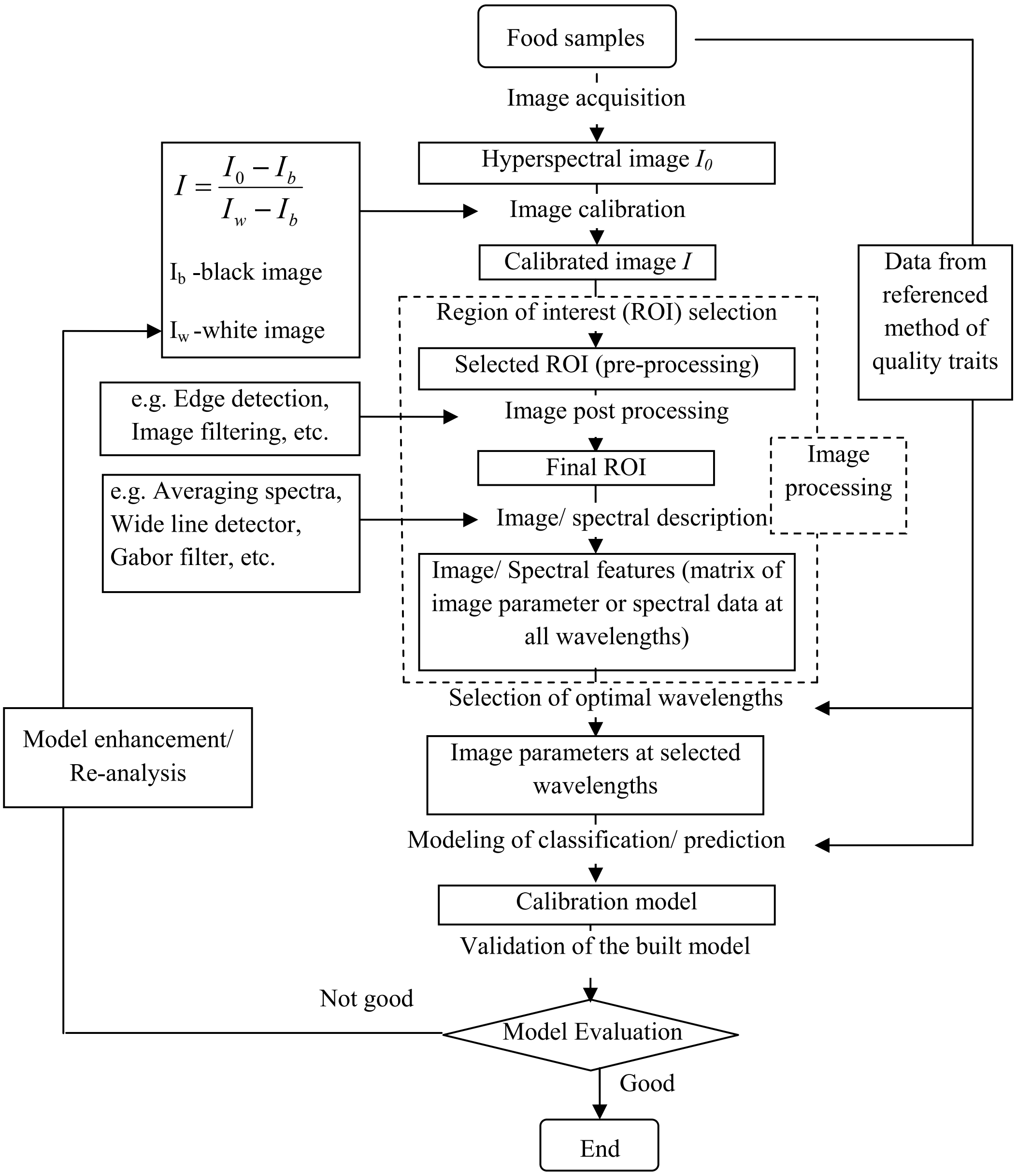

Figure 2.9 Flow chart of application of hyperspectral imaging in food quality control.

intramuscular fat and marbling are considered as texture, line or other features of images. Image features are represented by different statistical values that are derived from processed images using different methods. In a study undertaken by Qiao *et al.* (2007c), the pattern recognition technique of grey-level co-occurrence matrix was used to assess the marbling score of pork. The predicted marbling scores in the study were able to distinguish the marbling scores of standard charts except the score of 10.0. The same group (Liu *et al.*, 2009) applied another pattern recognition technique of wide line detector to process NIR hyperspectral images for evaluation of intramuscular fat content of pork. Prediction model for intramuscular fat content was moderately successful with correlation coefficients of 0.91. In research of Liu *et al.* (2012), wide line detector was extended to assessment of marbling score. Hyperspectral images of pork at red-green-blue channels were used to predict marbling score of pork samples. Seven levels of marbling in NPPC charts were discriminated fully by features extracted using wide line detector. The results implied the potential of wide line detector for marbling detection of RGB images as well. Liu *et al.* (2010) developed a Gabor filter-based hyperspectral imaging system to grade pork sample into the same four classes of quality (red, firm, normal (RFN), pale, soft, exudative (PSE), pale, firm, normal (PFN), and red, soft, exudative (RSE)). By combining principal components from hyperspectral images with combining principal components from Gabor-filtered images, the authors reported classifying accuracy of 84 ± 1%, which was an increase of 4% over the result of Qiao *et al* (2007c). It is of interest to adopt such methods for processing of NIR images for fat assessment of pork.

2.6.4.1 Gabor filter (GF)

Texture analysis is an important branch of image processing. Texture of the image refers to smoothness, roughness, color changes, direction of changes, rotation, scale, translation, and other aspects of an image. For texture extraction of images, several algorithms are applied to images to obtain meaningful statistical terms (Tuceryan and Jain, 2010). These calculated values are used to describe the texture characters of the image. As a type of texture analysis technique, Gabor filter has been promoted for its powerful properties in image processing.

Gabor filter is a transformation of elliptic Gaussian and sinusoidal waves, which are applied on all the receptive fields in the image. It provides tunable orientation and radial frequency bandwidths, tunable center frequency and allows optimal achievement of joint resolution in spatial and frequency domain (Clausi and Jernigan, 2000; Liu *et al.*, 2010). According to Liu *et al.*, (2010), Gabor filter is similar to the recognition pattern of human vision by extracting the important spatial characteristics including spatial localization and frequency simultaneously. Two types of two-dimensional Gabor filters, i.e. isotropic (Eq. 2.4) and oriented (Eq. 2.5, Ma *et al.* 2002) are used. After Gabor filtering, grayscale images are created, from which surface texture expressions are usually calculated for further data analysis.

$$GF1(x, y, f, \sigma) = \frac{1}{2\pi\sigma^2} \exp\left\{-\frac{x^2 + y^2}{2\sigma^2}\right\} \cos\left[2\pi f(\sqrt{x^2 + y^2})\right], \qquad (2.4)$$

$$GF2(x, y, f, \sigma, \theta) = \frac{1}{2\pi\sigma^2} \exp\left\{-\frac{x^2 + y^2}{2\sigma^2}\right\} \cos\left[2\pi f(x\cos\theta + y\sin\theta)\right], \qquad (2.5)$$

where (x, y) is the coordinate of pixel in each NIR image, f represents the frequency of the sinusoidal wave, σ is the standard deviation of the Gaussian function, and θ is a vector which controls the orientation of the filter. Usually the parameters of Gabor filter are defined by trail-to error.

For its superior ability of extracting texture feature, Gabor filter has been applied in various fields including digital signal and image processing, iris and face recognition, textile manufacturing, identification of stem cells, characterization of biological cells, and automatic document processing (Tang *et al.*, 1996; Samantaray *et al.*, 2005; Moon and Javidi, 2007; Bowyer *et al.*, 2008; Ngan *et al.*, 2011; Kurita and Masuda, 2012). Recently, Gabor filter was introduced for the image analysis of food (Zhu *et al.*, 2007; Ngadi and Liu 2010; Liu *et al.*, 2010; Liu and Ngadi, 2012). Ngadi and Liu (2010) and Liu *et al.* (2010) extracted Gabor features of hyperspectral images of pork for quality classification. Pork from four quality groups were well graded. The successful application of Gabor filter on pork by Liu *et al.* (2010) indicated the potential of Gabor filter to facilitate the prediction of pork intramuscular fat content. Extremely limited research regarding Gabor filter-based hyperspectral image analyses was executed for pork quality control, and even for food quality inspection. Therefore, it is of interest to investigate the effectiveness of Gabor filter for evaluation of intramuscular fat level of pork.

2.6.4.2 Wide line detector (WLD)

Wide line detector was proposed by Liu *et al.* (2007) for detection of palm lines. It demonstrated strong ability for detection of lines with pre-defined length, width, and contrast to neighbored pixels.

The procedure of WLD-based segmentation of line features are given as follows:

$$L(x_0,y_0;r,t)=\begin{cases} g-m(x_0,y_0;r,t), & \text{if } \mathrm{m}(x_0,y_0)<g \\ 0, & \text{otherwise} \end{cases}, \tag{2.6}$$

$$m(x_0,y_0;r,t)=\sum\nolimits_{x_0-r\le x\le x_0+r}^{y_0-r\le y\le y_0+r} s(x,y,x_0,y_0;r,t), \tag{2.7}$$

$$s(x,y,x_0,y_0;r,t)=\begin{cases} n(x,y,x_0,y_0;r), & \text{if } I(x_0,y_0)-I(x,y)\le t \\ 0, & \text{if } I(x_0,y_0)-I(x,y)>t \end{cases}, \tag{2.8}$$

$$n(x,y,x_0,y_0;r)=\begin{cases}1/\pi r^2, \text{if } (x-x_0)^2+(y-y_0)^2\le r^2 \\ 0, \quad \text{otherwise}\end{cases}, \qquad (2.9)$$

where (x_0, y_0) is the center of the circular neighborhood, (x, y) is any other point within the neighborhood, *I* is the intensity of the point (x, y), *r* is the radius of circular mask, *t* is the intensity contrast threshold, *L* is the extracted isotropic line by WLD, *s* is the normalized weighting comparison based on the measure of similarity between the center point and any other point in the circular neighborhood, and *m* is the mass of the neighborhood center (x_0, y_0), *g* is the geometric threshold. A global threshold (*l*) was applied on the output of the WLD to segment objects with lower responses. Using the WLD-produced mask, lines with defined width, length, and luminance are obtained.

Wide line detector was introduced to hyperspectral image processing of pork by Liu *et al*. (2012). In the research of Liu *et al*. (2012), classification model was developed from wide line detector processed digital images of seven standard charts. Seven levels of marbling score in standard charts were graded accurately. Wide line detected line features from VIS/NIR hyperspectral images at three channels of red, green, and blue were used to grade pork marbling levels. To our knowledge, no other study has been conducted on wide line detector-based hyperspectral imaging for food quality control. The promising result and lack of application of wide line detector in other studies implied the necessity to investigate the power of wide line detector-based hyperspectral imaging for prediction of intramuscular fat level of pork.

2.6.4.3 Grey-level co-occurrence matrix

Regular grey-level co-occurrence matrix (GLCM) is a commonly used algorithm for texture segmentation. Grey-level co-occurrence matrix is an image analysis technique, which specifies image texture information by accumulating frequencies with two neighboring pixels separated by a distance in the defined window (Haralick, 1979). In the window, a multi-scale GLCM matrix is derived from each image. For instance, Figure 2.10 shows how an 8-level GLCM matrix is calculated from a 6×5 matrix (i.e. 6×5 image). As shown in Figure 2.10, if east (0°) is used as the offset direction and 1 is used as the offset distance of two pixels, there will be two instances that two neighbouring pixels have the values 1 and 3. Hence, the element {1, 3} in the GLCM contains the value 2. The size of the generated GLCM matrix depends on the number of grey scales considered. Usually, eight scales were considered, which means the formed GLCM matrix was an 8× 8 square matrix.

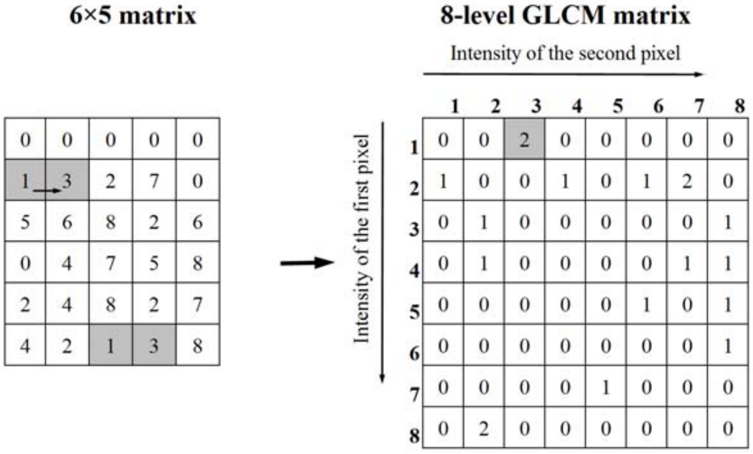

Figure 2.10 Principle of GLCM matrix.

Different sets of scales, offset directions, and offset distances could be applied to form the GLCM matrices. The image texture information could be evaluated by different measurements of GLCM matrix according to Eq. 2.10 to Eq. 2.13. The measurement of the angular second moment was denoted as ASM.

$$Contrast = \sum_{i,j} (i-j)^2 M_{D,\theta}(i,j), \tag{2.10}$$

$$Correlation = \frac{\sum_{i,j} (ij) M_{D,\theta}(i,j) - \mu_i \mu_j}{\sigma_i \sigma_j}, \tag{2.11}$$

$$ASM = \sum_{i,j} \left[M_{D,\theta}(i,j) \right]^2, \tag{2.12}$$

$$Homogeneity = \sum_{i,j} \frac{M_{D,\theta}(i,j)}{1+(i-j)^2}, \tag{2.13}$$

where (i, j) is the coordinates of the pixel of interest, *D* is the given distance between two pixels, θ is the offset direction of the pair of pixels over an image, $M_{D,\theta}$ is the obtained GLCM matrix, $M_{D,\theta}(i,j)$ is the value in element $\{i,j\}$ of $M_{D,\theta}$, (μ_i, μ_j) are the means in the row and column direction in $M_{D,\theta}$ and (σ_i, σ_j) are standard deviations in the row and column direction of $M_{D,\theta}(i,j)$. Besides Gabor filter, the obtained measurements of GLCM could be used as another type of image texture features in understanding of images.

When applying regular GLCM, the subjective selection of a regular shape (e.g. a circle area) is usually used to select the appropriate processed area. However, bias will be introduced by manual interference especially for heterogeneous objectives such as meat products. For practice of GLCM, improvements should be made to avoid the effect of subjective region selection.

Computation of grey-level co-occurrence in hyperspectral image cubes has been conducted for nondestructive determination of prediction of some quality attributes of strawberry, pork, beef, apples, and lamb (ElMasry *et al.*, 2007; Qiao *et al.*, 2007c; Naganathan *et al*., 2008a; Naganathan *et al*., 2008b; Mendoza *et al.*, 2011; Kamruzzaman *et al.*, 2012a, 2012b, 2012c). Qiao *et al.*, (2007c) applied GLCM for pork marbling detection. More work was suggested as there was an error of one between the predicted values and actual values of marbling score. Three beef tenderness categories were classified with a 96.4% accuracy and a 77% accuracy using statistical textural features derived from GLCM of VIS/NIR and NIR hyperspectral imageries, respectively (Naganathan *et al*., 2008a; Naganathan *et al*., 2008b). Kamruzzaman *et al*. (2012b) conducted textural analysis based on GLCM to determine the correlation between textural features and drip loss of lamb. A correlation below 0.30 was obtained. Ability of GLCM for processing of hyperspectral images has not yet been sufficiently studied. Comparatively limited studies of GLCM were conducted with respect to image analysis of pork. More studies of GLCM could be done to assist the assessment of intramuscular fat level of pork using hyperspectral imaging.

CONNECTING TEXT

A comprehensive review of literature showed that marbling is a very important quality attribute, which is visible intramuscular fat in pork. The need for further studies regarding the objective inspection of marbling score of pork was demonstrated. It was noted that inspection of marbling score is challenging because of the low contrast between lean muscle and fat in pork. Chapter 3 addresses the first objective of the thesis, i.e. assessing the marbling score of fresh pork using NIR hyperspectral imaging. The effect of image-processing techniques such as Gabor filter and wide line detector were assessed.

This chapter was presented at Northeast Agricultural and Biological Engineering Conference in 2012. A paper based on this chapter has been submitted to Applied Spectroscopy. The manuscript is co-authored by my supervisors Dr. M.O. Ngadi and Dr. S.O. Prasher, a research associate Dr. L. Liu, and a researcher Dr. C. Gariépy from Agriculture and Agri-Food Canada. The format of the original manuscript has been modified to remain consistent with the thesis format. All the literature cited in this chapter is listed in Chapter 10 (General references).

III. NEAR-INFRARED SPECTRAL IMAGE ANALYSIS FOR PORK MARBLING SCORE DETERMINATION

3.1 Abstract

Marbling is an important quality attribute of pork. Evaluation of pork marbling level usually involves subjective scoring, which raises efficiency costs to the processor. In this study, the ability of near-infrared hyperspectral imaging for measurement of pork marbling and the effective image processing techniques was studied. A hyperspectral imaging system ranging from 900 to 1700 nm was developed to assess pork marbling. Near-infrared images were collected from pork after marbling evaluation according to standard chart. Samples were grouped into calibration and validation sets. Spectral features, i.e. mean spectra of non-filtered images (MR), and image texture features, i.e. mean spectra of Gabor filtered images (MG) were obtained from a segmented region of interest. The corresponding 1st derivatives of spectral features (DMR) and image texture features (DMG) were calculated. Spectra based line features were also extracted from near-infrared images using the wide line detector, a line pattern technique. Wavelength selection was performed on calibration set by stepwise regression procedure. Prediction models of pork marbling score were built using multiple linear regressions based on derivatives of mean spectra and line features at selected wavelengths. The results showed that the derivative of texture features produced best result with calibrated correlation coefficient of 0.91 and validated correlation coefficient of 0.90 at the wavelengths of 961, 1186 and 1220 nm, while the line feature based model produced calibrated correlation coefficient of 0.79 and validated correlation coefficient of 0.77 with wavelengths selection of 961, 1119 and 1162 nm. The results indicated the great potential of Gabor filter-based near-infrared hyperspectral imaging as an effective and efficient objective evaluation technique for pork marbling.

Keywords: Pork; Marbling Score; Near-Infrared Hyperspectral Imaging; Gabor Filter; Wide Line Detector

3.2 Introduction

Pork marbling, which is defined as the amount of the visible fat within the *Longissimus dorsi* (LD) muscle, has a great effect on buyers' acceptance of pork in the market. In the pork industry, marbling is evaluated and graded to different scores to meet the various requirements of different markets. Grading of pork marbling plays a significant role in allocating markets. In practice, evaluation of pork marbling is usually performed subjectively by human inspectors according to grading standard (NPPC) (NPB, 2002). The visual grading of marbling assessment makes it labor consuming and difficult to maintain repeatability. These features make the standard method not suitable for a fast-paced online process. Therefore, efficient objective technology for evaluation of pork marbling would be beneficial to the pork industry.

Among the various objective techniques for food quality inspection, spectroscopic and imaging techniques are two methods with great potential to predict food quality (Vote *et al.*, 2003; Kumar and Mittal, 2010; Quevedo *et al.*, 2010; Pallottino *et al.*, 2010; Ritthiruangdej *et al.*, 2011). The near-infrared (NIR) spectrum cover broad bands from 780 nm to 2500 nm. The NIR spectrum is composed of overtone and combination bands which are mostly generated by stretching vibrations of functional groups like O-H, N-H, and C-H bonds (Osborne and Fearn, 1986). The main components of meat constituents include O-H, N-H, and C-H bonds. On the other hand, the NIR region of electromagnetic waves enables high penetration that leads to good capacity of probing deep and collecting internal characteristics of food (Bellon *et al.*, 1994; Cozzolino and Murray, 2004; Alishahi *et al.*, 2012). Thus, NIR spectroscopy has been widely applied as a rapid and effective tool to determine the concentration of food constituents such as moisture, fat, and protein (Prevolnik *et al*., 2005; Barlocco *et al.*, 2006; Savenije *et al.*, 2006; Prieto *et al*., 2009). Considering that fat is the major constituent of pork marbling, there exists great potential in application of NIR spectroscopy for assessing pork marbling. However, spectroscopic techniques are not able to provide spatial information about the detected object due to the limited spatial field of view of spectroscopy. Considering that meat is a heterogeneous material, adequate spatial information is necessary for effective marbling determination.

Imaging techniques are capable of providing superior spatial information. Imagings techniques have been applied for quality assessment of beef or pork (Shiranita *et al.*, 2000; Yoshikawa *et al.*, 2000; Toraichi *et al.*, 2002; Tan, 2004; Faucitano *et al.*, 2005; Yang *et al.*, 2006; Jackman *et al.*, 2009; Girolami *et al.*, 2012). The combination of simplicity, speediness, and little or no sample preparation makes the imaging technique attractive. However, normal computer vision usually provides images with limited spectral information.

Hyperspectral imaging overcomes the limitation of spectroscopic and imaging techniques. It simultaneously obtains both spectral and spatial information to assess meat quality (Qiao *et al.*, 2007a, 2007c; Liu *et al.*, 2010). Research works related to marbling evaluation of pork using hyperspectral imaging have been reported mainly in VIS/NIR area (400-1100 nm) (Gowen, *et al*., 2007; Qiao *et al.*, 2007a; Liu *et al*., 2012). Qiao *et al.* (2007c) applied VIS/NIR hyperspectral imaging (400-1100 nm) combined with texture pattern technique (grey-level co-occurrence matrix (GLCM)) to assess marbling scores of pork. Results showed that GLCM processed hyperspectral images could distinguish marbling scores of standard charts except the level of 10.0. Meanwhile, there was an error around 1.0 between subjectively obtained and predicted marbling scores of practical samples. Liu *et al.* (2012) applied a line based pattern analysis technique named wide line detector (WLD, Liu *et al.*, 2007) to assess pork marbling automatically and objectively. The proportion of marbling (PM) was obtained from digital images of NPPC standards by WLD and used as indicator of marbling score. The results showed that the built linear regression models could separate the seven levels of NPPC standards accurately. Comparing results of Qiao *et al.* (2007c) and Liu *et al.* (2012), it indicated that effective image processing techniques could lead to a better result for assessment of pork marbling. GLCM is a common pattern recognition technique for image texture feature. Recently, Liu *et al.* (2010) classified pork using another texture based pattern recognition technique, i.e. Gabor filter which was designed to imitate human vision to capture salient visual properties of images. The results showed that a significant improvement was achieved by applying Gabor filter. This strongly indicated that an advanced texture analysis tool like Gabor filter might lead to a better result for prediction of pork marbling.

In addition, NIR images of meat contain less interference from muscle pigments and water (Ritthiruangdej *et al.*, 2011). ElMasry *et al.* (2012b) studied the possibility of predicting colour, pH and tenderness of fresh beef using NIR hyperspectral imaging. Results with coefficients of determination of 0.88, 0.81, 0.73 and 0.83 for CIE color scale lightness (L*) and one color-opponent dimension (b*), pH and tenderness were obtained, respectively. Barbina *et al*. (2012) applied NIR hyperspectral imaging to classify pork to three quality grades (PSE, RFN and dark firm dry (DFD)). An overall classifying accuracy of 96% was achieved. Promising results of studies demonstrated that near-infrared (NIR) hyperspectral imaging could aid in the quality control of meat.

The main motivation of this study was to investigate the potential of NIR hyperspectral imaging (900-1700 nm) for prediction of pork marbling. Gabor filter and WLD were employed to extract image texture features and line features, respectively. The performance of spectral features from hyperspectral images, texture features from Gabor filter, and line features from WLD were compared.

3.3 Materials and methods

3.3.1 Samples and scoring of marbling

A total of 53 fresh boneless pork loins from a commercial packing plant in Quebec, Canada were obtained. At 24 h post-mortem, the muscle *Longissimus dorsi* (LD) was dissected and sliced to chops with thickness of 2 cm. Blooming of the lean color was allowed by exposing the chop to air for a minimum of 15 min. The chops were labeled for subjective assessment of marbling. Marblings of both sides of the labeled chop were then scored by trained panel according to the NPPC marbling standards (NPB, 2002) and the average value was used as the marbling score of the chop. After the subjective assessment of marbling, the slices were vacuum packed and then transported to the Hyperpsectral Imaging Laboratory, McGill University, Montreal, QC, Canada for NIR image collection.

3.3.2 NIR hyperspectral imaging system

The NIR hyperspectral imaging system (Figure 3.1) consisted of a spectrograph (Headwall photonics, USA, 900-1700 nm), an InGaAs camera, a conveyer (Donner Mfg. Corp., USA), two 50 W tungsten halogen lamps, and supporting frame. The system is a line-scan pushbroom system with a spectral resolution of 4.8 nm, which scans the sample line by line and forms a data cube with two spatial axes and one spectral axe. Thus, within the data cube obtained by this NIR hyperspectral imaging system, individual NIR images at spectra from 900 to1700 nm could be obtained as well as spectrum of each pixel corresponding to the specific position of sample characterized by chemical components.

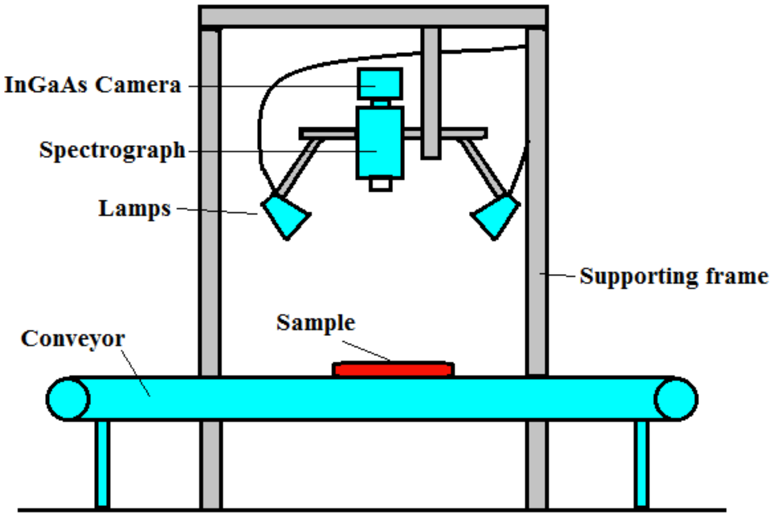

Figure 3.1 Illustration of NIR hyperspectral imaging system (Qiao *et al*., 2007c).

3.3.3 Image acquisition and correction

To correct the camera's dark current error, a dark image (about 0% reflectance) was obtained by covering the lens with a cap. In order to ensure uniform the reflectance, a white image (about 99% reflectance) was obtained by scanning a standard white reference (Spectralon, Labsphere, North Sutton, NH, USA) before the image acquisition of samples. The original images of samples were calibrated using dark and white images according to equation in Liu *et al.* (2010).

One pork chop was unpackaged every time and put on a dark panel to collect the hyperspectral data individually. Both surfaces of each chop were imaged for subsequent analysis. The obtained images were stored in a data cube called a *hypercube*, composed of two spatial coordinates and one spectral coordinate. NIR spectra of each pixel in the image or NIR image at each wavelength could be extracted from the 3D *hypercube*.

3.3.4 Image pre-processing

Figure 3.2 shows the flow chart of image processing and data analysis. In image processing, feature extraction was performed on pre-processed images to extract useful spectral features and image parameters (texture features and line features) for the following data analysis. All operations of image processing and data analysis in this study were performed using MATLAB 7.3.0 (the MathWorks, Inc., Mass., USA).

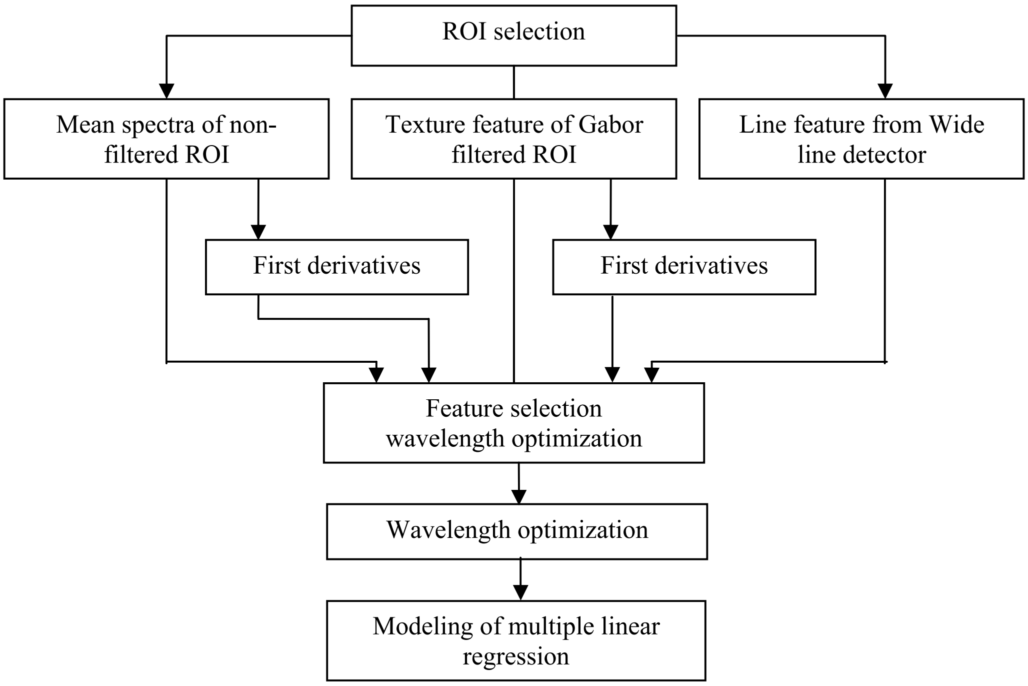

Figure 3.2 Flow chart of data processing.

The loin area in pork images was selected as the region of interest (ROI) from which spectral information and image features were extracted. The ROI was segmented automatically by a method presented in Liu *et al.* (2012) which combined a threshold technique and an edge detection algorithm together. Due to the low signal-to-noise ratio in the two ends of spectral range, only spectral images from 940-1650 nm were used for image analysis.

3.3.5 Spectral features

After image pre-processing, the mean reflectance spectrum of non-filtered ROI (**MR**) were extracted. Spectral responses of two sides of each pork slice were generated and the average spectrum was used as final spectral features. In comparison to NIR spectroscopy, there were over 50,000 pixels in every ROI, which reduced the influence produced by manual selection of detected spot in spectroscopy. The first derivative of the non-filtered mean spectrum (**DMR,** $D(\lambda_i)$) was calculated according to Eq. 3.1.

$$D(\lambda_i) = \frac{M_{i+1} - M_i}{\lambda_{i+1} - \lambda_i} \tag{3.1}$$

where i represents the number of wavelengths, i = 1, 2, 3, … 148 (the wave range/ the spectral resolution of system). The first derivative of mean spectrum was a 1×148 vector. M_{i+1} and M_i represents the value of mean reflectance in **MR** at wavelength λ_{i+1} and λ_i, respectively.

For each sample, the used waveband was 940-1650 nm and the resolution of NIR system was 4.8 nm, thus the mean spectrum of the sample was a 1×149 vector ((1650-940)/4.8+1) and the first derivative of the mean spectrum was a 1×148 vector.

3.3.6 Image analysis

Two different pattern recognition techniques, i.e. the Gabor filter (Liu *et al.*, 2010) and the wide line detector (WLD, Liu *et al.*, 2007), were adopted in this section to extract image features from NIR hyperspectral images.

3.3.6.1 Gabor filters and image texture features

Gabor filter, which is a sinusoidal modulated Gaussian transformation in the spatial domain, is able to extract representative visual characteristics of images including spatial localization and frequency, and orientation selectivity (Clausi and Jernigan, 2000). Considering marbling as texture pattern, an oriented two-dimensional Gabor filter described in Liu *et al.* (2010) was applied to pork images at different wavelengths on the purpose of extracting texture features. The oriented Gabor filter (**G**) was defined as follows (Ma *et al.*, 2002):

$$G(x, y, f, \sigma, \theta) = \frac{1}{2\pi\sigma^2} \exp\left\{-\frac{x^2 + y^2}{2\sigma^2}\right\} \cos[2\pi f(x\cos\theta + y\sin\theta)] \qquad (3.2)$$

where (x, y) is the coordinate of pixel in the image, f is the frequency of the sinusoidal wave, σ is the standard deviation of the Gaussian function, and θ represents the vector of orientation.

The mean reflectance spectra of Gabor filter-based ROI (**MG**) representing the texture features of pork images were extracted. Images of both sides of samples were adopted and the average spectrum was calculated. The first derivatives of the two types of mean spectra (**DMR** and **DMG**) were calculated according to Eq. 3.1.

3.3.6.2 Wide line detector and line features

The image indices called proportion of marblings (**PM**) of pork samples were derived from ROI using wide line detector (WLD) which is able to extract the thickness and distribution of lines in the targeted image (Liu *et al.*, 2012).

There were three parameters involved in the WLD: *r* as the radius of circular mask, *t* as the intensity contrast threshold, and *thresh* as the global threshold. Firstly, lines (marblings) with thickness of *r* and intensity of *t* were detected. After the detection of lines, global thresholding was applied to the detected results to remove the small objects whose areas in pixel were lower than *thresh* (Liu *et al.*, 2012). The *thresh* parameter controls the noise level in the detected marblings. A binary image with same contour of original selected ROI was generated by thresholding. There were open pixels (area of marblings) and closed pixels (area of non-marblings) inside the contour. With the obtained binary image, the image parameter **PM** by WLD was defined as Eq. 3.3. **PM** of images from 940-1650 nm was calculated and a **PM** plot ranging from 940 to 1650 nm could be formed from continuous **PM** values at 940-1650 nm. The algorithm of first derivative was not applied to **PM** plot since it was generated as an image parameter without involvement of mean spectrum.

$$PM = \frac{area(open\ \ pixels)}{area(all\ \ pixels\ inside\ the\ contour)} \tag{3.3}$$

3.3.7 Feature selection and wavelength optimization

The relationship between marbling scores and extracted feature indices (**MG, MR, DMG, DMR,** and **PM**) of pork samples was calculated over the wavebands of 940-1650 nm by

Pearson's correlation. For each feature, the parameter set provided highest correlation coefficient was determined as the best parameters for the corresponding feature. The plots of correlation coefficient between marbling score and the extracted features were performed to decide the features to be used for modeling. The features with maximum absolute correlation coefficient of over 0.6 were selected to do the regression analysis.

Wavelength selection was performed to optimize the obtained features to a lower dimensional linear space and select the wavelengths that were used for establishing prediction models. All pork samples (n = 53) were grouped randomly to calibration set (n = 36) for developing prediction models and the remaining 17 samples were grouped as validation set. The wavelength selection was performed on calibration set. Stepwise regression procedure (Draper and Smith, 1998) was adopted for wavelength selection. Stepwise regression procedure identifies the appropriate wavelength combination by establishing regression models, in which the predictive variables are selected automatically as sequence of F-test. Coefficient of determination (R^2) has been used widely as criterion in F-test. The higher the R^2, the better the model. Firstly, all the wavelengths were used separately to establish regression models, and the single wavelength with the highest R^2 was chosen as the variable providing most information about pork marbling score. Secondly, each remaining wavelengths were in conjunction with the chosen wavelength separately to build regression models, and the wavelength combination with the best R^2 would be used as the best group of wavelengths. The second step was repeated until no significant improvement could be produced by joining of new wavelength. All the chosen wavelengths would be regarded as the optimal combination.

3.3.8 Modeling

The selected features of calibration set were used to build the prediction models of pork marbling scores using the multiple linear regression (MLR) as defined in Eq. 3.4. The extracted features of validation set were then input into the MLR model to evaluate the practical prediction ability for marbling in the case of independent pork samples. The correlation coefficient (*R*) and p-value (*P*) for Pearson's correlation between the predicted and measured marbling scores of the calibration (*Rc, Pc*) and validation (*Rv, Pv*) sets were employed as evaluation of prediction models. The model, which produced best result, i.e. highest *Rc* and *Rv*, *Pc* and *Pv*, was exploited to determine the proper image processing technique for NIR hyperspectral images.

$$Y = a_{.0} + \sum_{i=1}^{i=n} a_i X_i \tag{3.4}$$

where Y is the marbling scores of pork samples, n is the number of selected wavelengths, $a_{.0}, a_i$ are the regression coefficients, X_i is the vector of feature at selected wavelength.

3.4 Results and discussion

3.4.1 Image preprocessing of pork sample

A total of 53 pork loin chops were collected. The description of the quality attributes of samples are listed in Table 3.1. Coefficient of dispersion was calculated by dividing standard deviation by mean value. The high coefficients of dispersion in Table 3.1 indicated that sample in the experiment covered a wide range of quality (a*-one color-opponent dimension).

Table 3.1 Quality of the total samples.

Quality attributes	Mean ± Standard deviation	Minimum	Maximum	Coefficient of dispersion (%)
Marbling score	2.60±0.90	1.00	5.25	35
L*	52.37±2.71	45.68	58.83	5
a*	4.82±1.23	1.90	8.01	26
b*	7.09±1.04	5.07	9.90	15
Drip loss (%)	4.28±2.70	0.33	11.05	63

Obtained NIR hyperspectral images of a pork sample at different wavelengths are shown in the grey-level images in Figure 3.3(1). The shown three wavelengths, 961, 1220,

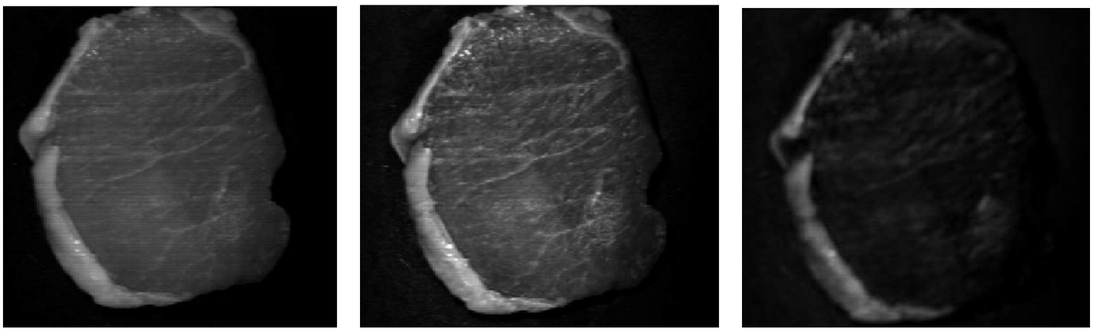

(a) 961 nm (b) 1220 nm (c) 1455 nm

(1) NIR images

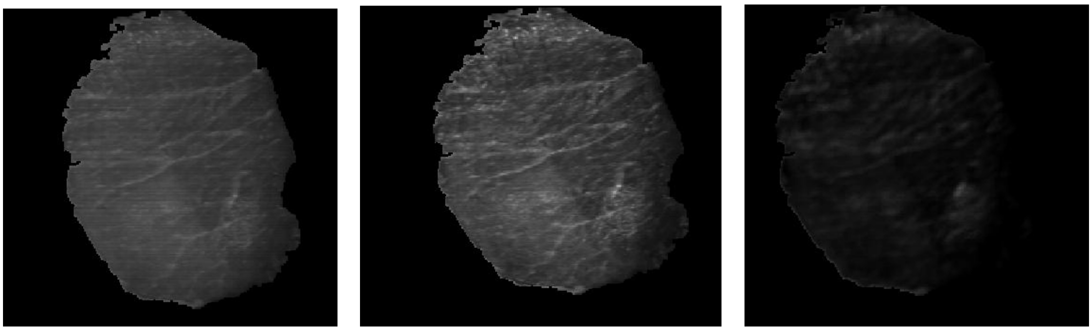

(a) 961 nm (b) 1220 nm (c) 1455 nm

(2) ROI of the NIR images

Figure 3.3 NIR images of a pork sample at different wavelengths and corresponding ROI.

1455 nm were close to water absorption peak at 975 nm and 1460 nm (Burns and Cuirczak, 1992), and fat absorption peak at 1200 nm (Osborne *et al.*, 1993). The absorption peak of water at 975 nm was much lower than the one at 1460 nm (Burns and Cuirczak, 1992). Compared to images at 961 and 1455 nm, the image at 1220 nm showed better contrast between fat and non-fat area. The high absorption of fat and low absorption of water at 1220 nm raised the gap between the reflectance spectrum of fat and lean, which resulted in the high contrast between marbling and lean. Comparing with the image at 961 nm, low clarity of picture was observed at 1455 nm. This could be resulting from the big difference in absorption intensities of water at 961 and 1455 nm. Figure 3.3(2) shows the corresponding segmented ROI, i.e. the representative loin eye areas, using auto selection algorithm. The representative loin eye areas were selected as ROI.

3.4.2 Mean spectra and texture features from Gabor filter

The Gabor filter with parameters of $f = 7$, $\sigma = 10$, and $\theta = \pi/4$ was applied to all the ROI of pork samples at wavelengths from 940 to 1650 nm. The parameter set was determined by trial-to-error. The mean reflectance spectra of non-filtered ROI (**MR**) and filtered ROI (**MG**) were obtained afterwards, as shown in Figure 3.4. The typical derivatives of the two types of mean spectra (**DMG, DMR**) were also calculated and shown in Figure 3.5. The plots of **MR** and **MG** as well as **DMG** and **DMR** showed high similarity in shape. Larger difference in magnitude was observed in overall plots of **MR** and **MG**, while larger difference of **DMG** and **DMR** was observed at 961 and 1220 nm, respectively. **DMG** appeared to be smoother than **DMR**, which may result from filtering.

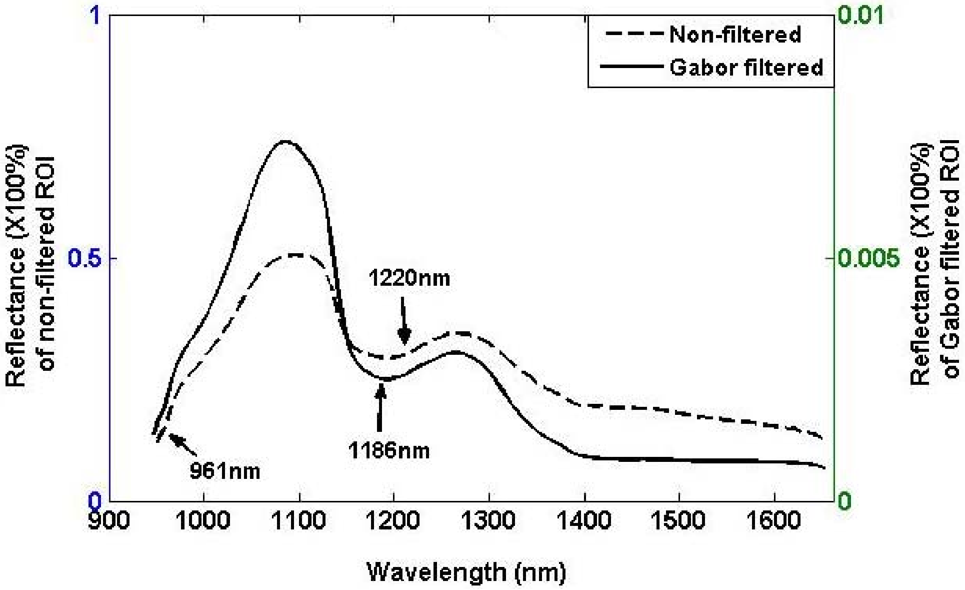

Figure 3.4 Typical mean reflectance spectra of non-filtered ROI (MR) and filtered ROI (MG).

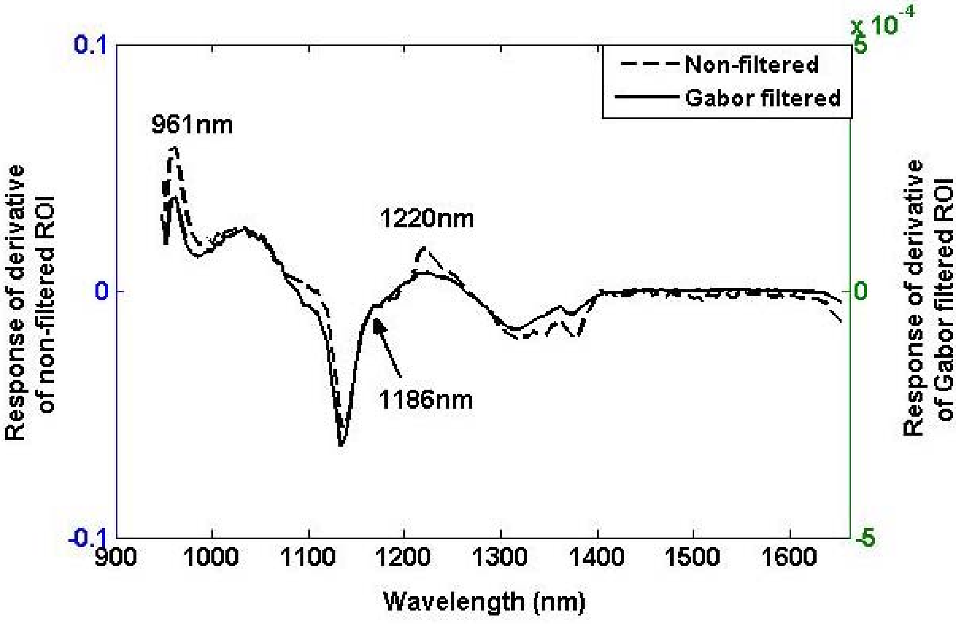

Figure 3.5 Typical first derivatives of mean reflectance spectra of non-filtered ROI (DMR) and filtered ROI (DMG).

3.4.3 Line features from WLD

The WLD (Liu *et al.*, 2012) was applied to all the ROI of pork samples and proportion of marblings (**PM**) was calculated representing the image line features. The parameters used for WLD were set to: *r* = 15, *t* = 4, and *thresh* = 0.3. Figure 3.6 shows the plot of **PM** and referenced marbling score (MS) of all 53 samples at 961 nm where high similarity between PM and MS was observed.

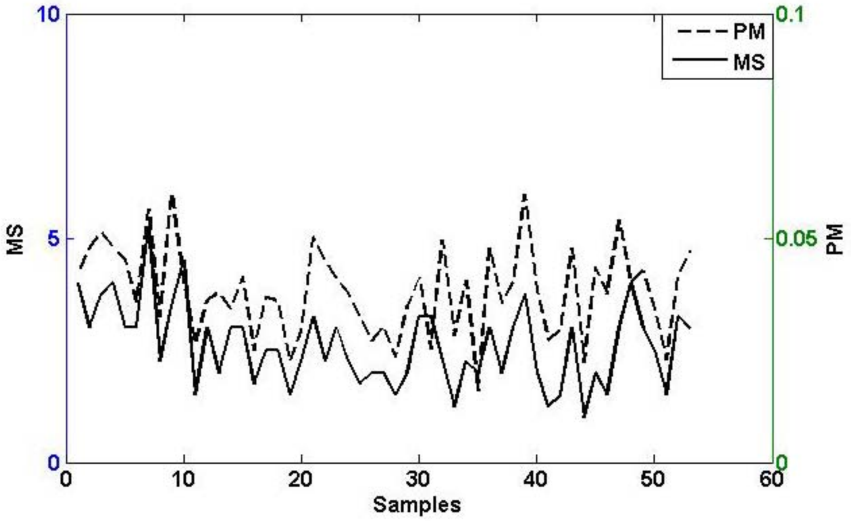

Figure 3.6 Calculated PM and referenced marbling score (MS) at 961 nm.

3.4.4 Spectral and texture features based correlation coefficient

Figure 3.7 shows the correlations between marbling scores and **MR** where all the correlation coefficient was lower than 0.50, with maximum of 0.48 at 1310 nm, while the highest correlation between marbling scores and **MG** is observed with 0.57 at 1315 nm. Similar feature of plots were observed for **MR** and **MG**. Figure 3.8 shows the correlation between marbling scores and **DMG** and **DMR**, where the best correlation of -0.78 at 1186 nm and 0.74 at 1220 nm were found, respectively. The best correlation coefficients between marbling score and **DMR** and **DMG** were 0.21 and 0.26 higher than **MR** and

MG, respectively. It was suggested that the algorithm of first derivative improved the accuracy of marbling quantification. The direct spectra **MR** and **MG** contained interference caused by surface toughness or broad absorbing components like O-H (Owen,

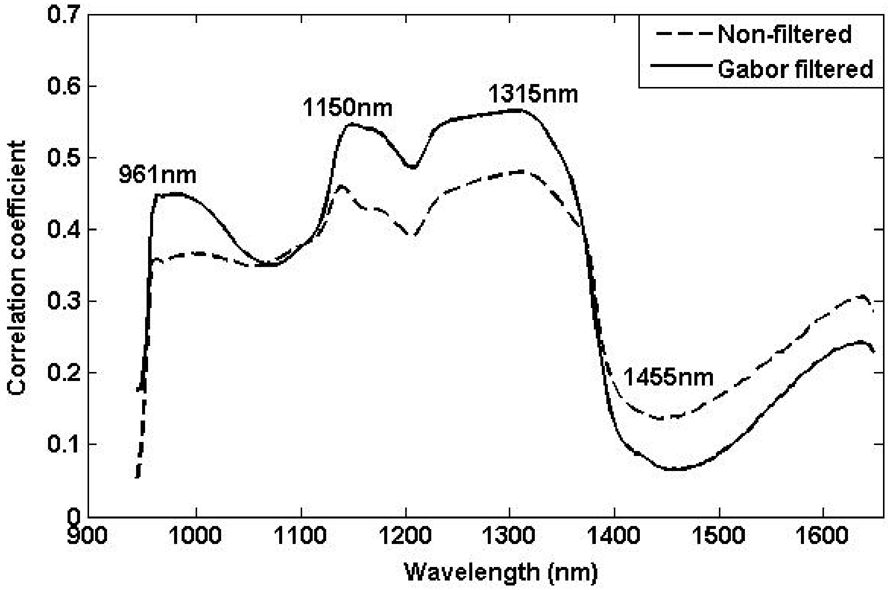

Figure 3.7 The correlations between marbling scores and MR, MG.

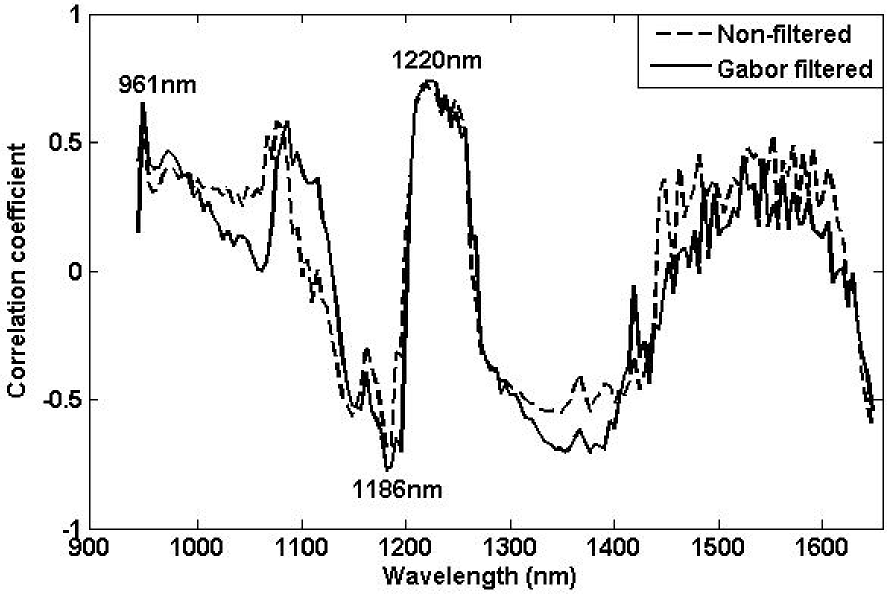

Figure 3.8 The correlations between marbling scores and DMR, DMG.

1995). The derivative analysis presented the direct spectrum in a new way, which reduced the interference and exploited the feature which were implied by the data, hence the result was improved.

Although the maximum absolute values of correlation between marbling and **DMG** and **DMR** were located at different wavelengths, the feature of correlation plots showed high similarity, both having peaks at 1186 and 1220 nm and a lot of overlap in shape. The wavelengths of 1186 and 1220 nm were close to the major absorption band of lipid around 1200 nm (Osborne *et al.*, 1993).

Because of the low correlation coefficients between marbling scores and **MR** and **MG**, the linear regression models were only built based on the **DMR** (denote as MLR-**DMR**) and **DMG** (MLR-**DMG**). According to stepwise procedure, the optimal combination of wavelength for **DMR** based MLR model was 961, 1186, and 1220 nm, as same as the optimal wavelengths for **DMG**. Table 3.2 lists the statistic values for **DMG** and **DMR** at the selected wavelengths. Although the magnitude of **DMG** at 961, 1186, and 1220 nm is lower than **DMR**, the mean value and standard deviation amongst three

Table 3.2 Statistic values of spectral feature (DMG) and texture feature (DMR) at selected wavebands.

Features	Wavelength (nm)	Mean ± Standard deviation
DMR	961	$(2.62\pm 0.58)\times10^{-2}$
	1186	$(2.94\pm 5.79)\times10^{-4}$
	1220	$(6.04\pm 1.90)\times10^{-3}$
DMG	961	$(2.23\pm 0.52)\times10^{-4}$
	1186	$(-4.12\pm 8.29)\times10^{-6}$
	1220	$(7.58\pm 2.58)\times10^{-5}$

wavelengths of **DMG** and **DMR** showed similar changing trends. For both **DMG** and **DMR**, larger variety at 1186 nm and low variety at 961 and 1220 nm are shown.

3.4.5 Line feature based correlation coefficient

The extracted **PM** at different wavelengths was calculated when the line features of images were extracted. Correlation coefficients between **PM** and marbling scores of all the samples are shown in Figure 3.9, with maximum correlation of 0.70 at 961 nm and a relatively high correlation of 0.67 at 1162 nm. The optimal wavebands of 961, 1119 and 1162 nm were selected for data analysis using stepwise regression procedure. The statistic results for **PM** at selected wavelengths are listed in Table 3.3.

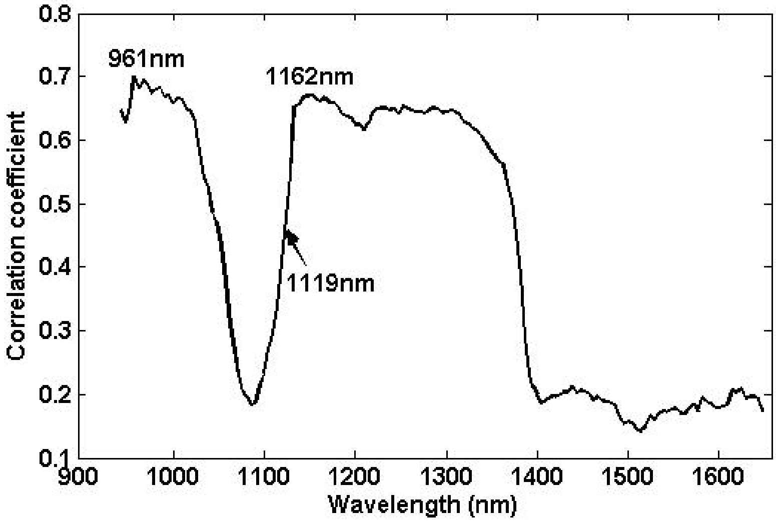

Figure 3.9 The correlation coefficient between marbling scores and PM.

Table 3.3 Statistic values of line feature (PM) at selected wavebands.

Features	Wavelengths (nm)	Mean ± Standard deviation
PM	961	$(3.81\pm 1.00)\times10^{-2}$
	1119	$(6.77\pm 1.23)\times10^{-2}$
	1162	$(7.47\pm 1.17)\times10^{-2}$

3.4.6 MLR models

The data set of 53 samples was divided to calibration and validation sets. For all the features, the range of marbling score in validation set was made sure to be covered by the range of the test set, assuring the appropriate distribution of the samples for modeling.

The regression coefficient of each model and the corresponding prediction results are listed in Table 3.4. It is observed that spectra based and texture feature based models produced better prediction results with at least 9% higher accuracy than line feature based model. In this study, *Rc* of 0.79 and *Rv* of 0.77 were obtained for MLR-**PM**, while in the study of Liu *et al.* (2012), accuracy of 99% was obtained for marbling prediction based on RGB images of standard charts. The WLD was proposed and defined based on visual characteristics of RGB images, which may influence the application of WLD on marbling extraction in NIR images.

Table 3.4 Regression coefficients and prediction results of models based on DMR, DMG, and PM.

Model	Wavebands (nm)	Regression coefficients (a_0, a_1, a_2, a_3)	*Rc*	*Pc*	*Rv*	*Pv*
MLR-**DMR**	961, 1186,& 1220	1.773, -0.367, -1.488, 2.236	0.88	$<1\times10^{-5}$	0.86	$<1\times10^{-5}$
MLR-**DMG**	961, 1186 & 1220	1.114, -15.093, -68.713, 103.918	0.91	$<1\times10^{-6}$	0.90	$<1\times10^{-6}$
MLR-**PM**	961, 1119 & 1162	0.647, 116.386, -43.879, 7.041	0.79	$<1\times10^{-3}$	0.77	$<1\times10^{-3}$

Between MLR-**DMG** and MLR-**DMR,** the Gabor filter-based model of NIR images had slightly higher *Rc* and *Rv* than non-filter based model (MLR-**DMR**). Amongst three models, MLR-**DMG** produced the best prediction results with *Rc* of 0.91 and *Rv* of 0.90. It was indicated that the first derivative of mean spectra of Gabor filtered NIR images were more closely related to pork marbling score. Marbling score was obtained based on human sense of sight and sensation. Gabor filter has good ability of orientation selectivity and efficient reduction of instability in images, which is similar to the human visual and sensory system (Fogel and Sagi, 1989; Fan and Zhang, 2006). The similarity in visual aspect may improve the marbling prediction ability of Gabor filter. In addition, the derivative spectroscopy based on mean spectra of numerous pixels in ROI raised the signal to noise ratio (O'Havers, 1982), which allowed more useful information to be captured by image processing.

Comparing the prediction results of three MLR models, all of the models created good prediction of pork marbling score. It was observed that wavelengths around 1200 nm were covered in all three models. The explanation would be that marbling is visible fat, and the absorption peak of fat was located at 1200 nm (Osborne *et al.*, 1993). These results indicated that hyperspectral images at NIR range had good explanatory power for pork marbling. Meanwhile, Gabor filter-processed NIR hyperspectral images may be more powerful than WLD-processed and direct hyperspectral images. The success of non-destructive detection of pork marbling made it possible to develop a rapid and accurate on-line system to assess pork marbling score.

3.5 Conclusion

This study was conducted to investigate the aptitude of NIR hyperspectral imaging and the proper image processing technique for prediction of pork marbling score. To accomplish this purpose, multiple linear models based on non-filtered NIR images, Gabor filtered images, and WLD-based images at optimal wavelengths were built and compared. The experimental results suggested that Gabor filter-based NIR hyperspectral imaging was efficient as an objective assessment method for pork marbling. The possibility of developing an objective and accurate real-time system to assess pork marbling was demonstrated. Comparing different techniques of feature extraction, the direct mean spectra and Gabor filter showed stronger ability for evaluation of pork marbling than WLD, while the Gabor filter performed better than the first derivative of raw mean spectra. Moreover, in contrast to direct mean spectral response of images, the first derivative transformation of Gabor filtered images enhanced the accuracy of marbling prediction greatly. Prediction result of $Rc = 0.91$ and $Rv = 0.90$ was obtained at 961, 1186, and 1220 nm by the first derivative of Gabor filter-processed hyperspectral images.

Further work will focus on improving the predictive accuracy, building industrial instruments for objective marbling evaluation and exploring the potential of NIR hyperspectral imaging techniques for prediction of intramuscular fat content in pork.

CONNECTING TEXT

In Chapter 3, textural, spectral, and line features of NIR hyperspectral images of pork were extracted. Linear regression models between different image features and pork marbling scores were built and compared. The performance of Gabor filter based model was better than the wide line detector based model. The wide line detector is proposed based on digital pictures from red-green-blue camera. Considering the visual evaluation procedure of pork marbling, it will be prudent to see if wide line detector is capable of overcoming the challenge of low contrast between fat and lean in pork image at visible region. In Chapter 4, line pattern analysis technique of wide line detector was used to predict marbling score using digital red-green-blue images, and the independent effects of red, green, and blue channels were also considered.

This chapter is based on a paper that is published in Food Control. The manuscript is co-authored by my supervisor Dr. M.O. Ngadi, a research associate Dr. L. Liu, and a researcher Dr. C. Gariépy from Agriculture and Agri-Food Canada. The format of the original manuscript has been modified to remain consistent with the thesis format. All the literature cited in this chapter is listed in Chapter 10 (General references).

IV. PREDICTION OF PORK MARBLING SCORES USING PATTERN ANALYSIS TECHNIQUES

4.1 Abstract

Marbling is an important quality attribute of pork. Its assessment usually corresponds to a subjective score being given by trained panelists based on the marbling standards charts. The purpose of this study was to investigate the objective determination of pork marbling using different pattern analysis techniques. A line pattern recognition technique called the wide line detector (WLD) and a texture extraction technique based on an improved grey-level co-occurrence matrix (GLCM) were employed and compared. Fifty three fresh pork loin chops from the *Longissimus dorsi* (LD) muscle were collected and their marbling scores were assessed in a plant. Red-Green-Blue (RGB) images of these chops were acquired using a digital camera. The loin eye area was selected as the region of interest (ROI) of the pork images. Marbling was extracted from the ROI by either GLCM or WLD. Proportion of marbling (**PM**) obtained from WLD or image texture measurement from GLCM (**GI**) was formulated as indices of the marbling score. Linear regressions based on the **PM** and **GI** were carried out at the red, green, and blue channels as well as the combined RGB channels. The results of WLD and GLCM based models showed the effectiveness of pattern analysis techniques for pork marbling assessment. The comparison indicated that the WLD based models had stronger predictive ability for pork marbling score determination than GLCM. The green channel was demonstrated to have the best explanatory power for pork marbling assessment no matter which pattern analysis technique was used. High correlation coefficients of calibration and validation (Rc = 0.94, Rv = 0.94) of the WLD based linear model at the green channel strongly indicated the great potential of pattern analysis techniques especially the line pattern recognition methods for the accurate and real-time evaluation of pork marbling.

Keywords: Pork; Marbling; Wide line detector; Multiple linear regression; Grey-level co-occurrence matrix

4.2 Introduction

Marbling is a visual attribute of meat that influences acceptability and palatability of pork in the market and is defined as the amount and spatial distribution of the visible fat within the *Longissimus dorsi* (LD) muscle. In the pork industry, the evaluation of marbling mainly relies on subjective comparison with pork marbling standards or pictures such as those from the National Pork Producers Council (NPPC) (NPB, 2002) and is carried out by an experienced employee. The NPPC marbling standards comprise seven scores from 1.0 (devoid) to 6.0 and 10.0 (abundant). The visual assessment leads to inconsistencies in pork quality of different companies, increases the labor cost, has low repeatability, and is easily influenced by the environment. Therefore, a more efficient and objective evaluation methods for pork marbling determination would be useful for the the pork industry.

In the past decade, research work related to marbling assessment of either beef or pork using machine vision approaches have been reported (Gerrard *et al.*, 1996; Shiranita *et al.*, 2000; Yoshikawa *et al.*, 2000; Toraichi *et al.*, 2002; Tan, 2004; Faucitano *et al.*, 2005; Yang *et al.*, 2006; Qiao *et al.*, 2007a, 2007c; Chen and Qin, 2008; Liu *et al.*, 2012). In comparison with beef, evaluation of marbling in pork is more challenging not only due to the much more variable color of pork but also due to the paler color of the lean part and the attenuated contrast between lean and fat (Sun, 2008). In order to enhance the color contrast between pork marbling and lean, a chemical pre-treatment was used in Faucitano *et al.* (2005) so that computer image analysis (CIA) was able to be conducted on the digital color pictures (i.e., Red-Green-Blue images) of the pre-processed pork samples. A group of CIA marbling variables was calculated and some of them (such as proportion of marbling fleck area (%), the density of marbling flecks / pieces/cm², the number of marbling flecks / cm², total length of marbling flecks (cm), and total marbling fleck area (cm²)) were significantly correlated with intramuscular fat (IMF) content. Hyperspectral imaging technology was firstly introduced by Qiao *et al.* (2007c) to evaluate pork quality and marbling scores. In the work, a texture pattern analysis technique called grey-level co-occurrence matrix (GLCM) was applied to assess pork marbling levels at the wavelength of 661 nm where a significant contrast image was obtained. A measurement of GLCM named angular second moment (ASM) was exploited as the texture index of marblings. ASM (Energy) gives the sum of squared pixel values in GLCM. Results showed that the sorted marbling score based on the ASM value was about 1.0 higher than the subjective marbling scores. In addition, ASM differentiated samples in the range of marbling scores less than 5.0 but could not segregate samples with scores from 5.0 to 10.0. Liu *et al.* (2012) regarded pork marbling as a line pattern and applied a line pattern recognition technique called the wide line detector (WLD) (Liu *et al.*, 2007) for the marbling extraction. The proportion of marbling (**PM**) was obtained using the WLD on digital color pictures of NPPC standards and formulated as indices of marbling scores by multiple linear regression models. Experimental results demonstrated that the established multiple linear models successfully differentiated the marbling levels of NPPC standards over the entire range. Although leave-one-out cross-validation was used to assess the generalization of the predictive models in practice, model validation on an independent sample set with the reference data from fresh pork samples was absent in the work.

The overall objective of this work was to investigate the applications of different pattern analysis techniques for pork marbling evaluation. The specific objectives were to collect digital RGB images of fresh pork loin samples; to extract different image features, i.e. line pattern and image texture, using the WLD and the improved GLCM, respectively; to establish prediction model based on extracted image features; and to compare the performance of the WLD- and the GLCM-based models for prediction of pork marbling scores.

4.3 Materials and methods

4.3.1 Samples and image acquisition

Fresh boneless pork loins (n = 53) were obtained from a commercial packing plant in Quebec, Canada. A 2 cm thick chop was sliced from the mid portion of the longissimus muscle and was exposed to air for a minimum of 15 min at 10°C to allow blooming of the lean color. Marbling scores of the chop were assessed subjectively by two trained employees of the plant using the NPPC marbling standards (NPB, 2002) and the average value was used as the marbling score of the chop.

Following the subjective assessment of marbling, the RGB digital images of the chops were obtained using a NIKON D5000 digital camera with a predefined condition under a uniform environment. The spatial resolution of the camera was 300 dpi (dots-per-inch) × 300 dpi. Both surfaces of each chop were imaged for subsequent analysis.

4.3.2 Image preprocessing

The main task of image pre-processing was to select the region of interest (ROI), i.e. the loin eye area in this study. The loin eye area of each image was automatically selected by applying the image segmentation method presented in Liu *et al.* (2012). However, reflection points which were produced by the residual water on the chop surface were found in ROI and could affect the analysis results. In order to control the error caused by reflection points and keep the research as a single-factor study, the reflection points were removed from the ROI manually. The final ROI used in this study is the loin eye area without reflection points. All operations of image processing and data analysis in this study were performed using MATLAB 7.3.0 (The MathWorks, Inc., Mass., USA).

4.3.3 Feature extraction

After image preprossessing, image features were extracted from three channels (red, green, and blue) of RGB images for pattern analysis and measurement. In this study, two different feature extraction methods, i.e. the wide line detector (WLD) (Liu *et al.*, 2012) and the grey-level co-occurrence matrix (GLCM) (Qiao *et al.*, 2007c), were employed to detect line patterns and image texture, respectively.

Wide Line Detector. The WLD segmented marblings from ROI in each channel of the RGB image by detecting lines as

$$L(x_0,y_0;r,t)=\begin{cases} g-m(x_0,y_0;r,t), & \text{if } \mathrm{m}(x_0,y_0)<g \\ 0, & \text{otherwise} \end{cases}, \tag{4.1}$$

$$m(x_0,y_0;r,t)=\sum\nolimits_{x_0-r\le x\le x_0+r}^{y_0-r\le y\le y_0+r} s(x,y,x_0,y_0;r,t), \tag{4.2}$$

$$s(x,y,x_0,y_0;r,t)=\begin{cases} n(x,y,x_0,y_0;r), & \text{if } I_c(x_0,y_0)-I_c(x,y)\le t \\ 0, & \text{if } I_c(x_0,y_0)-I_c(x,y)>t \end{cases}, \tag{4.3}$$

$$n(x,y,x_0,y_0;r)=\begin{cases} 1/\pi r^2, & \text{if } (x-x_0)^2+(y-y_0)^2\le r^2 \\ 0, & \text{otherwise} \end{cases}, \tag{4.4}$$

where (x_0, y_0) is the center of the circular neighborhood, (x, y) is any other point within the neighborhood, $I_c(x, y)$ is the intensity of the point (x, y) in the channel *c*, *r* is the radius of circular mask, *t* is the intensity contrast threshold. *s* is the normalized weighting comparison based on the measure of similarity between the center point and any other point in the circular neighborhood, and *m* is the mass of the neighborhood center (x_0, y_0). *g* is the geometric threshold and was set to 0.5 in this study. The output of the WLD was the isotropic line response *L* with the range of 0-0.5. A global threshold was used for image post-processing to remove objects with lower *L*. Therefore, three parameters involved in the WLD based feature extraction, i.e. the radius of circular mask (*r*) which determines the maximum width of marblings that can be detected, the intensity contrast threshold (*t*) which defines the minimum visibility of marblings that can be detected, and the global threshold which controls the noise level in the detected marblings.

The proportion of marblings (**PM**) was used as image feature index to measure marbling scores, which was defined as

$$PM = \frac{area(marblings)}{area(ROI)} \tag{4.5}$$

where *area(marbling)* is the total number of pixels of detected marbling, and *area(ROI)* is the total number of pixels of the corresponding ROI. The principle behind the calculation of PM is comparable to human vision scaling marbling with respect to the lean background.

Improved GLCM. The image texture indices of pork samples were derived from the grey-level co-occurrence matrix (GLCM) which was created from each channel of the RGB image. GLCM is an image analysis technique which specifies image texture information by relative frequencies with two neighbouring pixels separated by a distance in the calculation window (Haralick, 1979). This technique is widely used in food engineering, food quality and safety control to extract image texture characteristics of an object of interest (ElMasry *et al.*, 2007; Naganathan *et al.*, 2008a, 2008b; Mateo *et al.*, 2010). In application, a sub-region with a regular shape (e.g. a rectangle area) is normally selected from the object of interest (such as meat, vegetables and fruits) as the ROI by hand to conduct GLCM texture analysis. However, such manual ROI selection could introduce error to the analysis and result in a biased conclusion.

In order to eliminate the influence of manual selection, an improved GLCM was used in this study to extract image texture features from the irregular-shaped ROI. The improved GLCM, $\mathbf{P}_{D,\theta}$, was defined as a square matrix with elements (i, j) specifying how often the two grey levels i and j occur between two pixels (pixels in the ROI) separated by a distance D along a given direction θ over an image. A total of 8 grey levels were used to scale the gray-scale values in each channel of the pork sample image. The image texture information was evaluated by different measurement of GLCM, i.e.

$$Contrast = \sum_{i,j} (i-j)^2 \mathbf{P}_{D,\theta}(i,j) , \tag{4.6}$$

$$Correlation = \frac{\sum_{i,j} (ij)\mathbf{P}_{D,\theta}(i,j) - \mu_i \mu_j}{\sigma_i \sigma_j} , \tag{4.7}$$

$$ASM = \sum_{i,j} \left[\mathbf{P}_{D,\theta}(i,j)\right]^2 , \tag{4.8}$$

and

$$Homogeneity = \sum_{i,j} \frac{\mathbf{P}_{D,\theta}(i,j)}{1+(i-j)^2}, \tag{4.9}$$

where (μ_i, μ_j) and (σ_i, σ_j) are the means and standard deviations of the value of element (i, j) in the row and column direction in the improved GLCM, respectively. In the GLCM-based feature extraction, the measurement of GLCM obtained by Eq. 4.6-4.9 were used as image texture feature indices (**GI**) to estimate the marbling scores of pork samples.

4.3.3 Modeling and evaluation of models

The relationship between marbling scores and image feature indices (**PM** or **GI**) of pork samples was calculated over three channels by Pearson's correlation coefficients. All pork samples (n = 53) were divided into two sets, the calibration set (36 samples) and the validation set (17 samples). The multiple linear regression (MLR) algorithm was employed on the calibration set to establish the prediction models for pork marbling scores based on different image feature indices derived from each channel of pork sample images. The MLR model was defined as

$$\hat{\mathbf{Y}} = a_0 + \sum_{c=r,g,b} a_c \mathbf{X}_c, \tag{4.10}$$

where $\hat{\mathbf{Y}}$ is the vector of predicted marbling scores, $\mathbf{X}_c$ ($c = r, g, b$) is the vector of image feature indices (**PM** or **GI**) of the calibration or validation set at the channel *C*, a_0 is the constant term and a_c is the regression coefficient on the channel *C*.

The predictive ability of the MLR models was evaluated by four parameters, i.e. the root mean square error of calibration (*RMSEc*), the root mean square error of validation (*RMSEv*), the correlation coefficient between the predicted and measured marbling scores of the calibration (*Rc*) and validation (*Rv*) set. A good model should have low *RMSEc* and *RMSEv*, high *Rc* and *Rv*, and a small difference between *RMSEc* and *RMSEv*.

4.4 Results and discussion

4.4.1 Image of pork sample

Fifty three pork loins were used. The mean marbling score of all samples was 2.60. Minimum and maximum values were 1.00 and 5.25, respectively. All pork loin chops were imaged in RGB format on both sides and the ROI of each image was segmented in image pre-processing. Figure 4.1 shows an example of the RGB images of a pork loin chop on both sides. The segmented ROI of side A (Figure 4.1(a)) is shown in RGB image

(a) Side A (b) Side B

Figure 4.1 Images of pork loin chops at two sides.

in Figure 4.2(a), as well as in grey-level images at the red, green, and blue channels, respectively. In grey-level images, both green and blue channels produced a better contrast between lean and marbling fat than the red channel, since the color of lean is red.

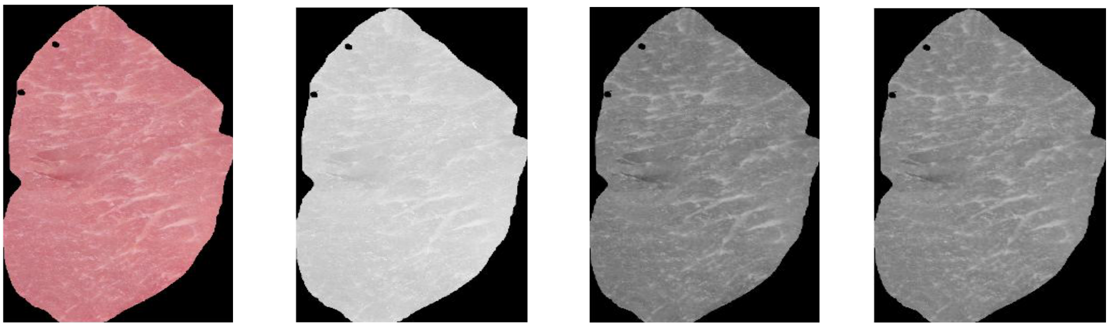

(a) RGB image (b) Red channel (c) Green channel (d) Blue channel

Figure 4.2 ROI (marked as non-black pixels) of pork sample at different channels.

4.4.2 Proportion of marblings based on WLD

The wide line detector defined by Eq. 4.1-4.4 was applied to extract marblings from the ROI at red, green, and blue channels of the digital color image of pork sample. Figure 4.3 shows the marbling detection results of the RGB images at each channel using the WLD where the intensity contrast threshold t is 4, the radius of circular mask r is 30, and the global threshold l is 0.3. The parameters of the WLD were determined based on trial and error (the parameter set providing the highest correlation coefficient to referenced marbling scores was selected as the optimal parameter set) and the same values of parameters were used for all channels.

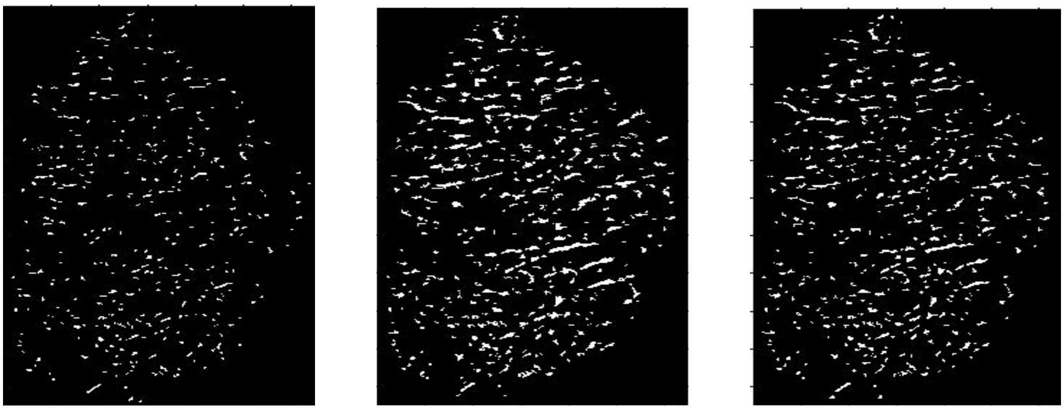

(a) Red channel (b) Green channel (c) Blue channel

Figure 4.3 Extracted marbling of pork at different channel.

Proportion of marblings (**PM**) was calculated for all pork samples according to Eq. 4.5 and the results are listed in Table 4.1. Pearson's correlation coefficients between **PM** and marbling scores of all the samples were 0.90, 0.93, and 0.92 at the red, green, and blue channels, respectively. The high correlations obtained ($R > 0.9$, $P << 0.001$) showed the strong relationship between **PM** and marbling scores This was consistent

Table 4.1 Statistics of PM for all samples and different sets.

Parameter	Set	Channel	Maximum	Minimum	Mean	Standard deviation
PM	All samples	Red	0.055	0.008	0.022	0.010
		Green	0.096	0.029	0.055	0.016
		Blue	0.095	0.032	0.056	0.015
		RGB	0.096	0.008	0.044	0.021
	Calibration	Red	0.055	0.007	0.022	0.011
		Green	0.096	0.030	0.054	0.016
		Blue	0.095	0.033	0.056	0.015
		RGB	0.082	0.023	0.044	0.021
	Validation	Red	0.044	0.009	0.023	0.011
		Green	0.087	0.029	0.055	0.016
		Blue	0.087	0.032	0.056	0.015
		RGB	0.073	0.023	0.044	0.021

with the result obtained by Faucitano *et al.* (2005) where the proportion of marbling fleck area (%) was significantly correlated with marbling score (R = 0.60, $P < 0.001$). The much higher correlation coefficients obtained in this study indicated the effectiveness of the wide line detector for processing of RGB images for the prediction of pork marbling scores.

Three linear regression models, i.e. WLR*r*, WLR*g*, and WLR*b*, were developed using the **PM** values at the red, green, and blue channels, respectively, while one multiple linear regression model WMLR developed based on **PM** of all three channels. The regression coefficients and the corresponding prediction results of each model are listed in Table 4.2. The high correlation coefficients (*Rc* and *Rv*) and low *RMSEc* and *RMSEv* from all established models showed the strong explanatory and predictive capability of **PM** for determination of pork marbling scores, and thereby indicated the effectiveness of the line pattern features for pork marbling prediction. The WLR*g* model established at the green channel outperformed the models at the red (WLR*r*) and the blue (WLR*b*) channels on both calibration and validation sets, which was consistent to the correlation results

Table 4.2 Regression results of the WLD based LR and MLR models, *p* << 0.001 for each *R* value.

Channel	Model	Regression coefficients				Prediction results			
		a_0	a_r	a_g	a_b	*Rc*	*RMSEc*	*Rv*	*RMSEv*
Red	WLR*r*	0.84	80.95	0	0	0.90	0.42	0.94	0.33
Green	WLR*g*	-0.41	0	56.32	0	0.94	0.33	0.94	0.36
Blue	WLR*b*	-0.68	0	0	59.46	0.93	0.34	0.92	0.37
RGB	WMLR	-0.62	-17.63	70.40	-2.91	0.94	0.33	0.93	0.37

between **PM** and marbling scores of all pork samples. The WMLR model based on all three channels produced the same *Rc* as the WLR*g* model (0.94) and a slightly lower *Rv* than the WLR*g* model (0.93 vs. 0.94).

Figure 4.4 shows the plots of measured and predicted marbling scores from **PM** using the two models. The very high similarity between the two plots indicated that the **PM** obtained from the green channel had the most predictive power, and the multiple linear regression model WMLR could be replaced by the simple linear regression model at the green channel (WLR*g*).

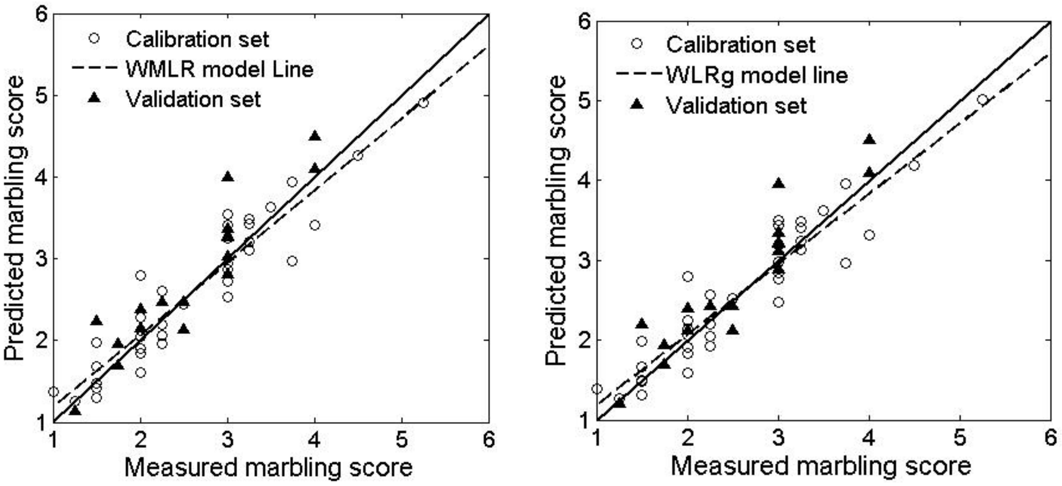

(a) the WMLR model

(b) the WLRg model

Figure 4.4 The measured and predicted marbling scores of calibration and validation sets based on WLD.

4.4.3 Image texture features based on the improved GLCM

The improved GLCM-based image texture feature extraction method was applied on the ROI at all three channels of the pork image to obtain the image texture feature index (**GI**) of pork sample. Four directions ($\theta = [0°,45°,90°,135°]$) and 13 steps ($D = [1,5:5:60]$)

were used to calculate $\mathbf{P}_{D,\theta}$ and four measurements (*Contrast, Correlation, ASM*, and *Homogeneity*) were evaluated for each $\mathbf{P}_{D,\theta}$.

Pearson's correlation coefficients between **GI** and marbling scores of all samples were calculated for all parameter combinations at three channels. The best correlation coefficients along each direction are shown in Table 4.3. The green channel produced the highest correlation coefficient in each direction and the overall best correlation coefficient between **GI** and marbling score (R = 0.69) was obtained in the horizontal direction ($\theta = 0°$) with the distance of 25 pixels when the measurement of *Contrast* was used. The statistics of the corresponding **GI** (denoted as $\mathbf{GI}_0$) are listed in Table 4.4.

Table 4.3 Best correlation coefficients ([R;G;B]) between marbling score and GI along different directions.

Direction	Measurement	Step (pixels)	R ([R;G;B])
0 °	Contrast	25	[0.53;0.69;0.56]
45 °	Contrast	15	[0.50;0.66;0.55]
90 °	Homogeneity	10	[-0.49;-0.60;-0.55]
135 °	Homogeneity	10	[-0.48;-0.59;-0.54]

Linear regression models based on the $\mathbf{GI}_0$ listed in Table 4.4 were developed at the red (GLR*r*), green (GLR*g*), and blue (GLR*b*) channels as well as the combined RGB channels (GMLR). The regression coefficients and the prediction results of the four GLCM based linear regression models are listed in Table 4.5. The multiple linear model based on the combined RGB channels (GMLR) outperformed the three simple linear models (GLR*r*, GLR*g*, and GLR*b*). Among the three simple models, the model at the green channel (GLR*g*) produced the best prediction results which had the same *Rv* as the GMLR model (0.79) and a slightly lower *Rc* than the GMLR model (0.72 vs. 0.73).

Table 4.4 Statistics of $\mathbf{GI_0}$ for all samples and different sets.

Measurement	Set	Channel	Maximum	Minimum	Mean	Standard deviation
Contrast	All samples	Red	1.924	0.869	1.222	0.197
		Green	0.943	0.510	0.661	0.105
		Blue	0.977	0.432	0.649	0.105
		RGB	1.281	0.604	0.844	0.303
	Calibration	Red	1.640	0.890	1.207	0.169
		Green	0.867	0.510	0.648	0.087
		Blue	0.963	0.432	0.643	0.102
		RGB	1.157	0.611	0.833	0.293
	Validation	Red	1.924	0.869	1.255	0.248
		Green	0.943	0.521	0.689	0.134
		Blue	0.977	0.469	0.661	0.115
		RGB	1.281	0.620	0.868	0.326

Table 4.5 Regression results of the GLCM based LR and MLR models, *p* < 0.01 for each *R* value.

Channel	Model	Regression coefficients				Prediction results			
		a_0	a_r	a_g	a_b	*Rc*	*RMSEc*	*Rv*	*RMSEv*
Red	GLR*r*	-1.24	3.06	0	0	0.52	0.84	0.69	0.61
Green	GLR*g*	-2.91	0	8.28	0	0.72	0.68	0.79	0.71
Blue	GLR*b*	-0.93	0	0	5.27	0.54	0.83	0.70	0.56
RGB	GMLR	-2.77	-0.61	9.61	-0.41	0.73	0.68	0.79	0.72

Plots of measured and predicted marbling scores from $\mathbf{GI}_0$ using the models GMLR and GLR*g* are shown in Figure 4.5. A similarity between the two plots was observed, which showed that the $\mathbf{GI}_0$ obtained from the green channel was most explanatory and the simple linear model at the green channel could replace the multiple linear model based on the combined RGB channels.

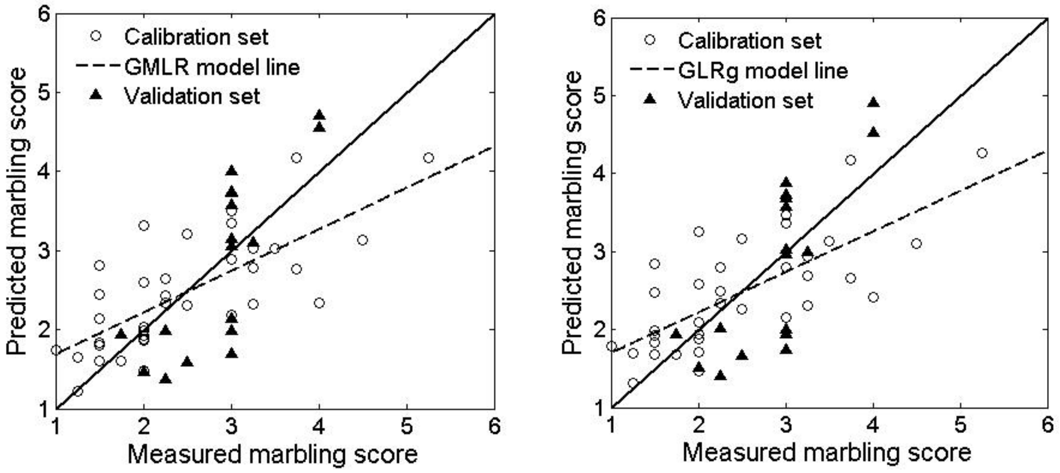

(a) The GMLR model (b) The GLRg model

Figure 4.5 The measured and predicted marbling scores of calibration and validation sets based on the improved GLCM.

4.4.4 Discussion

Both the wide line detector and the grey-level co-occurrence matrix are pattern analysis techniques. In this study, the WLD extracted marbling as line patterns with position and thickness information, while the GLCM measured marbling as the texture of the pork image. Comparing the prediction results based on the two techniques as shown in Table 4.2 and 4.5, the WLD produced much better prediction than the GLCM on both calibration and validation sets for all simple linear and multiple linear models. One possible reason is that image texture features extracted using the improved GLCM included information not only from marblings but also from the lean of the pork, which could limit the ability of GLCM to predict pork marbling scores. This indicated that line pattern appears to be more effective than the image texture for pork marbling prediction.

This study showed the promising potential of the WLD for pork marbling assessment. Regarding marbling as line pattern, the pork sample image with thick lines detected in a few positions could have the same **PM** values as the pork sample image with narrow lines detected in many positions according to Eq. 4.5, which would result in the same predicted marbling scores for both pork samples even though they have different measured marbling scores. This indicates that besides **PM** (the proportion of marbling area), the distribution of marblings (eg. the number of marbling flecks / cm² which was used in Faucitano *et al.* (2005)) should also be taken into account for marbling score assessment. Comparing the prediction results of three simple linear models, both the WLD and the GLCM based models created the best prediction of pork marbling score at the green channel. This indicated that the image feature extracted in the green channel had the best explanatory power no matter which pattern analysis technique used. The prediction results at the green channel are almost same as the results based on all three channels in Table 4.2 and 4.5. This made it possible to develop a rapid and accurate system to assess pork marbling scores.

4.5 Conclusion

In this study, the barriers produced by the low contrast between marbling and lean for objective and fast marbling assessment were overcome by application of effective pattern analysis techniques, i.e. the WLD and the GLCM. The results demonstrated the superior capacity of the WLD for objective assessment of pork marbling even though the predictive accuracy could be further improved. Both WLD and GLCM based models showed the green channel had the strongest prediction ability for pork marbling assessment, which indicated that simple linear model at the green channel, could replace the multiple linear model which was established based on all channels. This made it possible to develop an objective and accurate system to assess pork marblings in a real-time way. Further work will focus on building proper industrial implementations for marbling evaluation and exploring the potential of predicting the intramuscular fat content of pork by applying pattern analysis techniques.

CONNECTING TEXT

In Chapter 4, marbling scores of pork at the 3rd / 4th last rib were evaluated using red-green-blue digital pictures of fresh pork. The effectiveness of wide line detector in the visible light range was demonstrated. Green channel showed the most powerful predictive ability. The success of objective and non-destructive evaluation of pork marbling score using image analysis indicated the possibility of evaluation of total intramuscular fat content of pork using image analysis. Chapter 5 addresses the third objective of the thesis, i.e. investigating the non-destructive measurement of the intramuscular fat content of pork. Hyperspectral imaging was introduced to explore the determination of the intramuscular fat content of pork. Effective image processing techniques were investigated. In addition, the method of mapping the distribution of intramuscular fat content in pork was studied.

The manuscript in this chapter has been submitted for publication to Talanta. This chapter is co-authored by my supervisor Dr. M.O. Ngadi, a research associate Dr. L. Liu, and a researcher Dr. C. Gariépy from Agriculture and Agri-Food Canada. The format of the original manuscript has been modified to remain consistent with the thesis format. All the literature cited in this chapter is listed in Chapter 10 (General references).

V. HYPERSPECTRAL IMAGE-ASSISTED NON-DESTRUCTIVE QUANTIFICATION OF INTRAMUSCULAR FAT CONTENT OF INTACT PORK

5.1 Abstract

Fast and non-invasive assessment of the intramuscular fat (IMF) content of pork chops would benefit the pork industry in terms of saving time and cost of determination. Thus, developing an accurate, non-destructive and rapid method to determine the IMF content of pork would be advantageous to the pork industry. This paper reports on the use of near infrared (NIR) hyperspectral imaging technique for predicting IMF content in intact pork loin and the efficiency of texture pattern techniques for processing of hyperspectral images. Pork samples were collected and their IMF contents were determined using a conventional solvent extraction method. Hyperspectral images of the samples were acquired using an NIR hyperspectral imaging system. After the region of interest (ROI) of each spectral image was segmented, the raw spectral characteristic was obtained by averaging the spectra within the ROI of the non-processed image. Texture-based spectral characteristics were extracted by a pattern recognition technique called Gabor filter (GF), and texture information was extracted by a pattern recognition technique called the improved grey-level co-occurrence matrix (GLCM). The first derivative of the spectral curve was obtained as well. Full waveband partial least squares regression (PLSR) and cross validation were employed to determine the optimal parameters of GF and GLCM, and to select featured wavelengths for IMF prediction. A stepwise procedure was applied to the select wavelengths to optimize the wavelengths again and multiple linear regression (MLR) models were built. Compared to raw spectral information, Gabor filter performed better than GLCM. Averaging ROI and Gabor filter yielded similar predictive ability to IMF content, while the first derivative of Gabor filter showed a slightly better result than the raw mean spectra of ROI. Only the MLR model using raw mean spectra at 1207 and 1279 nm were selected as the final model. A correlation coefficient of calibration (*Rc*) of 0.87, cross validation (*Rcv*) of 0.86, and prediction (*Rp*) of 0.85 were obtained for the raw mean spectra-based model. The model was applied to the spectrum of each pixel in ROI, and the distribution map of IMF content in pork was obtained. These promising results indicated the great potential of non-destructive prediction of IMF content of intact pork using NIR hyperspectral imaging.

Keywords: Pork; Intramuscular Fat content; Gabor filter; Grey-level co-occurrence matrix; Partial least squares regression; Multiple linear regression; Prediction map

5.2 Introduction

Intramuscular fat (IMF) content is defined as the mass of fat within the meat muscle. Pork IMF content influences the cooking quality (flavor and juiciness, etc.), eating satisfaction of consumers, even health issues. Thus, different levels of IMF content lead to different acceptance levels from consumers (Brewer *et al.*, 2001; Bryhni *et al.*, 2003). Non-invasive and rapid determination of IMF content in pork chops would allow commercial cuts to be classified, screened, and assigned to a proper retail spot according to different targets of the markets, thereby enhancing their market allocation and reducing handling costs. Unfortunately, at present, extraction of lipid based on chemicals is involved in the assessment of pork IMF content. Extraction of fat by chemicals is time consuming, labor intensive and harmful to the environment. Since fat extraction-based IMF prediction is not suitable for fast and non-destructive measurement, random sampling are typically used to evaluate the IMF content of pork products, which leads to non-optimal grading of pork cuts. Therefore, it would be beneficial for the pork industry to develop a non-destructive, real-time, rapid, and accurate method for predicting the IMF content of pork.

Some studies have been conducted to detect the IMF content in pork with spectroscopy techniques (Brøndum *et al.*, 2000; Prevolnik *et al.*, 2005; Barlocco *et al.*, 2006; Savenije *et al.*, 2006; Prieto *et al.*, 2009). Savenije e*t al.* (2006) applied a near infrared (NIR) reflectance spectrophotometer to determine the IMF content of pork muscle. The second derivative of the reflected spectra was used to build prediction models. Three breeds of pigs were used as samples. Correlation coefficients of calibration (*Rc*) between the measured and predicted IMF contents were from 0.70 to 0.86, and the correlation coefficients of validation (*Rv*) were from 0.63 to 0.76. Prevolnik *et al.* (2005)

and Barlocco *et al*. (2006) suggested that for IMF measurement by NIR spectroscopy, the minced samples produced more accurate result than intact muscle. This indicated a shortcoming of spectroscopic technique for IMF prediction in pork. Due to the confined detected area of the spectroscopic system and the heterogeneous distribution of fat in pork muscle, limited information was obtained when applying spectroscopic technique to intact muscle. To obtain adequate data from a pork sample, either homogenizing of the sample or enlargement of the field of view of the evaluation system would help.

With development of technology, an advanced technique called hyperspectral imaging was exploited to inspect pork quality (Gowen *et al*., 2007; Qiao *et al*., 2007a, 2007c; Liu *et al*., 2010; Barbina *et al.,* 2012a, 2012b). By integrating both conventional spectroscopy techniques with imaging techniques, hyperspectral imaging overcomes the limitation of spectroscopy. It identifies spectral details of different chemical components at specified spatial locations in a product. The obtained spectral and spatial information is stored in a three-dimensional (two spatial dimensions and one spectral dimension) data cube called a *hypercube*, from which image parameters or spectra can be extracted and analyzed for measurement of chemical attributes or physical properties of tested object. Information of multiple chemical constituents can be extracted from one *hypercube* simultaneously. In addition, no sample preparation is needed to apply hyperspectral imaging. Considering the great potential of the technology, there has been rising interest in application of hyperspectral imaging in pork quality control (ElMasry and Sun, 2010).

Qiao *et al.* (2007c) introduced visible (VIS)/NIR hyperspectral imaging to classify pork quality and assess pork marbling objectively. Grey-level co-occurrence matrix (GLCM) was adopted to evaluate pork marbling. The predicted marbling scores in the study were able to distinguish the marbling scores of standard charts except the score of 10.0. Four classes were involved in the study (Reddish pink, firm and non-exudative (RFN), pale pinkish gray, soft and exudative (PSE), pale, firm and non-exudative (PFN), and reddish, soft and exudative (RSE)). Classification results of 75-80% were reached. Liu *et al.* (2010) developed a Gabor filter-based hyperspectral imaging system to grade pork samples into the same four classes of quality (RFN, PSE, PFN, and RSE). The work reached a classification accuracy of 84 ± 1%, which improved on the earlier result of Qiao *et al* (2007c) by 4%. It was implied that effective pattern recognition techniques would enhance the ability of hyperspectral imaging for inspection of pork quality. Barbina *et al.* (2012a) analyzed NIR hyperspectral images to classify pork quality. Classification accuracy of 96% was obtained with only three quality grades (RFN, PSE, dark purplish red, firm and dry (DFD)) involved. The authors did not consider the PFN and RSE grade which typically tend to be the most difficult grades to classify. Promising results in these studies emphasized the capability of hyperspectral imaging for prediction of pork attributes.

The appearance of NIR spectroscopy for IMF content prediction indicated that NIR hyperspectral imaging might produce better results than the one in VIS area. Furthermore, Kobayashi *et al.* (2010) applied NIR hyperspectral imaging for control of fat content in beef. Compared to beef, the low contrast between fat and lean in pork makes the application of hyperspectral imaging a challenge. Liu *et al.* (2009) reported the use of hyperspectral imaging techniques to predict the IMF of pork. The reflected images in a wavelength interval were accumulated to enhance the contrast between the fat area and the non-fat area. A feature detection method named the wide line detector and a thresholding method were combined to detect fat flecks of pork. A prediction accuracy of 0.91 was obtained by linear regression modeling. This study indicated the possibility of rapid assessment of the intramuscular fat content of pork using NIR hyperspectral imaging. The authors indicated that more samples need to be studied and wavelengths need to be optimized.

The spectra of lipid and water, which are the main constituents of IMF, have many overlaps in the NIR region (Murray and Williams, 1987; Shenk *et al*., 1992), which may cause difficulty for wavelength identification. The processing of large volumes of data provided in a *hypercube* encourages the involvement of effective data mining techniques as well. In the presentation of Liu *et al.* (2009), the application of the image-processing technique of wide line detector enhanced the efficiency of IMF content prediction. It was indicated that an effective image processing technique may help to extract useful information from the data.

The aim of this study was to investigate the potential of NIR hyperspectral imaging (900-1700 nm) for prediction of IMF content in pork. For this purpose, normal averaging of spectra and two texture pattern techniques including Gabor filter and the improved GLCM were investigated for processing of NIR spectral images. The specific objectives were: (1) extract spectral features from raw hyperspectral images and calculate the differential of spectra, (2) extract texture features using Gabor filter and grey-level co-occurrence matrix (GLCM), respectively, (3) identify optimal wavelengths using partial least squares regression (PLSR) and cross validation in the whole wave, (4) identify optimal wavelengths according to the regression coefficient, (5) use stepwise procedure to reduce the dimension of optimal wavelengths further, (6) build multiple linear regression

(MLR) models based on different types of features at key wavelengths, and (7) visualize the distribution maps of the IMF content of pork using the built MLR model.

5.3 Materials and methods

5.3.1 Sample collection and determination of IMF content

In this study, pork samples from longissimus thoracis muscle were collected from 83 pig carcasses raised on a local farm. No differing treatment was applied to the animals. To increase the variability in IMF content in the longissimus muscle, carcasses with big difference in back fat thickness between the 3rd/4th last ribs were selected for dissection.

At 24 h post-mortem, thin pork slices at the 3rd/4th last thoracic rib of the *Longissimus dorsi* (LD) was collected for determination of IMF content. Meanwhile, loin chops with 2 - 2.5 cm thickness were dissected from the same site (the 3rd/4th last thoracic rib), and wrapped in vacuum packs individually and transported to the Hyperspectral Imaging Laboratory, McGill University, Montreal, QC, Canada for image acquisition.

Peripheral fat and surrounding muscle were removed from the thin pork slices. The remaining trimmed muscles were ground. The IMF content of the minced fresh pork was measured using ethanol and dichloromethane-based Soxtec extraction (Association of Official Agricultural Chemists (AOAC), 1990) and the results were used as referenced IMF content. The obtained fat content was based on a wet weight.

5.3.2 NIR hyperspectral imaging system

The NIR hyperspectral imaging system was used to capture NIR images of pork. The system consisted of an InGaAs camera, a spectrograph (Headwall photonics, USA, 900-1700 nm), a conveyer (Donner 2200 series, Donner Mfg. Corp., USA), a real-time control motor (MDIP22314, Intelligent motion system Inc., USA), two 50 W tungsten halogen lamps, supporting frame for the system, and a computer. The incident illumination was placed with an angle of 45° to the sample. Software for data acquisition and control of conveyer was installed on the computer (Hyperspec, Headwall Photonics Inc. USA).

The system is a line-scanning pushbroom system operated in a reflected mode. As the conveyer moves on with a predefined constant speed, the sample was scanned line by line and the reflected light from samples was dispersed into different wavelengths ranging from 900 to 1700 nm by the spectrograph. A three-dimensional *hypercube* was formed by combining spatial information from the InGaAs camera and spectral information from the spectrograph. The spectral resolution for the system was 4.8 nm while the spatial resolution was 0.6 mm. The spectral dimension covered 167 bands. The number of pixels covered by the spatial dimensions was determined by the morphological size of the detected object. The produced *hypercube* was saved in a band-interleaved-by-line (BIL) format, from which NIR images and spectra of each pixel could be extracted easily.

5.3.3 Image acquisition and calibration

Hyperspectral images were obtained from the 2 - 2.5 cm thick loin chops. Before the image collection of samples, dark and white reference images were captured to correct error caused by dark current of the system and to transform the reflected light intensity to reflectance. The dark (**D**, its reflectance is ~0%) image was obtained by covering the lens with an opaque cap. The white reference (**W**, its reflectance is ~99%) was obtained by adopting a reference tile as photographed object. Original NIR images ($\mathbf{N_0}$) of samples were collected by placing sample on a dark board whose reflectance was about 0%. The speed of image acquisition was around four seconds per sample. For each *hypercube*, the minimum interval along spectral dimensions and spatial dimensions were 4.8 nm and 0.6 mm, respectively. Corrected NIR images (**N**) were obtained by algebraic calculus (Eq. 5.1) of the light intensities of each pixel {i, j} in dark (**D**(i, j)), white (**W**(i, j)) and original NIR images (**$\mathbf{N_0}$**(i, j)). The reflectance of pixels in the calibrated NIR images ranges from 0 to 1. Subsequent image analyses and data analyses (As shown in Figure 5.1) were conducted using the corrected *hypercube*.

$$N(i,j) = \frac{N_0(i,j) - D(i,j)}{W(i,j) - D(i,j)}, \tag{5.1}$$

5.3.4 Image processing

Figure 5.1 outlines the whole procedure of spectral averaging-based and pattern technique-assisted image processing, followed by multivariate statistical analysis. Because the images at 900-935 nm and 1655-1700 nm were too noisy, only images from 940-1650 nm were used for image analysis at the stage of image preprocessing. Accordingly, the term ‘whole waveband’ in this study refers to wavelengths from 940 to 1650 nm. All operations of image processing and multivariate statistical analysis in this study were performed using MATLAB 7.3.0 (The MathWorks, Inc., Mass., USA).

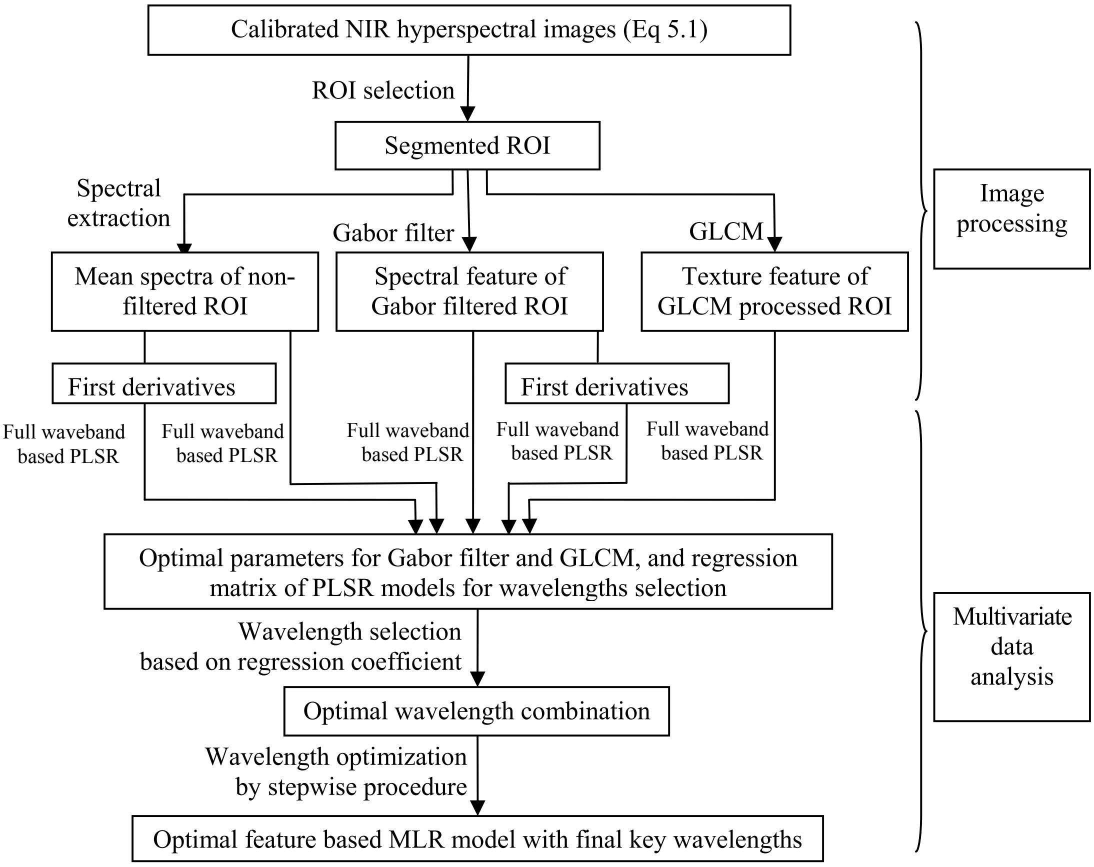

Figure 5.1 Flow chart of data analyses.

5.3.4.1 Image preprocessing

In image preprocessing, the region of interest (ROI) was segmented from which the spectral and texture features were extracted. ROI segmentation with an aim of isolating the targeted lean and IMF part from other portions is an important basis of image processing, as the selected ROI will affect all the analysis afterward. The peripheral fat, surrounding muscle, shadow and other backgrounds were removed and replaced by a homogenous black background. ROI segmentation in this study was conducted according to the method presented in Liu *et al.* (2012). The threshold values of different samples were different. The threshold value was set automatically according to the mean reflectance and standard deviation of each image.

5.3.4.2 Extraction of spectral feature

The mean spectrum of non-filtered ROI (**MR**) was extracted after image preprocessing. **MR** of each sample was a 1×149 (the wave range/ the spectral resolution of system+1) vector. Average spectra of the two sides of each pork sample were used as final spectral features. There were over 40,000 pixels in the selected ROI. Hence, the error introduced by limited area of view was reduced compared to spectroscopy. To raise the ratio of signal to noise, the first derivative (Eq. 5.2) was applied to the obtained non-filtered mean spectra and the first derivative of mean spectra (**DMR**) was obtained for data analysis as well as **MR**. **DMR** of each pork sample was a 1×148 vector (the wave range/ the spectral resolution of system).

$$D_i = \frac{MS_{i+1} - MS_i}{\lambda_{i+1} - \lambda_i}, \tag{5.2}$$

where i represents the number of wavelengths, $i = 1, 2, 3, \ldots 148$. λ_i represents the i^{th} wavelength. There was an interval of 4.8 nm between λ_i and λ_{i+1}. MS_{i+1} and MS_i stand for the value of spectral response at $(i+1)^{th}$ and i^{th} wavelength, respectively. D_i stands for the first differential of mean spectrum at i^{th} wavelength.

5.3.4.3 Extraction of texture spectrum by Gabor filter

A type of texture pattern technique called Gabor filter was applied to extract texture feature of NIR images. The two-dimensional Gabor filter is a transformation of elliptic Gaussian and sinusoidal waves, which are applied on all the receptive fields in the image.

Gabor filter is capable of extracting the important spatial characteristics including spatial localization and frequency from images. It was proposed as an imitation of human visual sense (Clausi and Jernigan, 2000; Liu *et al.*, 2010). Considering IMF as spatial characteristics in pork images, an isotropic Gabor filter (GF1) and an oriented Gabor filter (GF2) was used on the pork images at wavelengths ranging from 940-1650 nm. The functions of Gabor filter were defined as follows (Ma *et al.*, 2002):

$$GF1(x, y, f, \sigma) = \frac{1}{2\pi\sigma^2} \exp\left\{-\frac{x^2 + y^2}{2\sigma^2}\right\} \cos\left[2\pi f(\sqrt{x^2 + y^2})\right], \tag{5.3}$$

$$GF2(x, y, f, \sigma, \theta) = \frac{1}{2\pi\sigma^2} \exp\left\{-\frac{x^2 + y^2}{2\sigma^2}\right\} \cos[2\pi f(x\cos\theta + y\sin\theta)], \tag{5.4}$$

where (x, y) is the coordinate of pixel in each NIR image, f represents the frequency of the sinusoidal wave, σ is the standard deviation of the Gaussian function, and θ is a vector which controls the orientation of the filter (θ = 0°, 45°, 90°, 135°). Since GF1 is an isotropic function, θ was not considered as a parameter for GF1. After filtering, the mean spectral response of the Gabor filtered ROI was obtained. To reduce the influence of heterogeneity of pork sample, the average spectrum from two sides of each sample was obtained and used for following analysis. Mean spectrum from GF1 and GF2 was denoted as **MG1** and **MG2**, respectively. The first derivatives of **MG1** and **MG2** were calculated according to Eq. 5.2 and denoted as **DMG1** and **DMG2**.

5.3.4.4 Extraction of texture features by improved GLCM

Another texture pattern technique call grey-level co-occurrence matrix (GLCM) was investigated for processing of hyperspectral images. GLCM gives the information about how often the pixel intensities occurred between two pixels distributed by a specific distance and direction. Features derived by GLCM were used in texture analysis for food quality and safety control (ElMasry *et al.*, 2007; Naganathan *et al.*, 2008a, 2008b; Mateo *et al.*, 2010). To applying GLCM, subjective selection of a regular shape (e.g. a circle area) is usually used to select the appropriate ROI. To avoid the effect of subjective ROI selection, an advanced GLCM was applied on whole irregular-shaped ROI of pork in this study.

Eight scales, four offset directions (As shown in Figure 5.2, 0°, 45°, 90°, 135°), and 11 offset distances of 1 and 3 to 30 pixels with a stepsize of 3 pixels were applied in this study. The limitation of the scale was defined ranging from the minimum and the maximum of the intensities of the inputted image. The range was divided into eight equal levels. For each image, 52 (4 directions × 13 steps = 52) different matrices were formed. The image texture features (**GI**) including 4 measurements (*Contrast* (**GIt**), *correlation* (**GIn**), *angular second moment* (ASM, **GIa**), and *homogeneity* (**GIh**)) were calculated from obtained GLCM, by which 208 (52 × 4 = 208) plots with different parameters could be obtained for each image. The obtained 4 measurements of GLCM were used as another type of image texture feature indices to estimate the IMF content of pork.

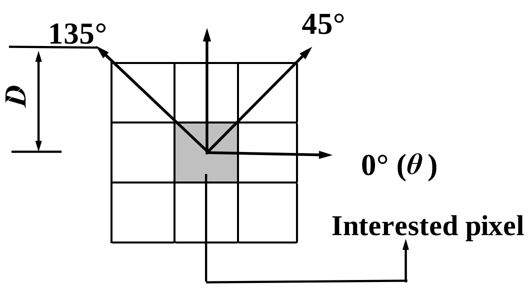

Figure 5.2 Distribution of pixel pair.

5.3.5 Multivariate data analysis

In determination of optimal parameters for GF and GLCM and optimal wavelengths for modeling, partial linear square regression (PLSR) was employed to build full waveband-based calibration models. As a common data analysis method, PLSR is widely used to reduce the dimension of predictor variables and random noise, and it proved to be efficient (Prieto *et al.*, 2009). All the earlier extracted features at the defined whole waveband were used as the predictor variables of PLSR (**X**). The measured IMF content of pork samples was used as the response variable (**Ym**). Eq. 5.5 describes function of PLSR.

$$Ym = X \times B + E, \tag{5.5}$$

where **B** stands for the obtained regression coefficient, and **E** represents the noise term for the model. When **Ym** and **X** are fixed, there will be many models, i.e. many matrix **B** and corresponding **E**, that will match the equation. By getting the solution of matrix **B** when **E** reaches the minimum, the relations between matrices **X** and **Ym** is built. In practice, the essential step of PLSR analysis is selecting the number of the main PLS principal components (PLS-PC) which explain the maximum fundamental relations between **Ym** and **X**. After quantification of PLS-PC, the PLSR model is build. The parameters of GF (f, σ, θ) and GLCM (*D*, θ, measurement), which provided best prediction results, were used as the optimal parameters. The corresponding regression coefficient was used to select optimal wavelengths.

In this study, features at all waveband (940-1650 nm) were used for the PLSR analysis. The total 83 samples were divided into two sets, including calibration sets (56 samples) and prediction sets (27 samples). PLSR models of different features were built using calibration sets. Numbers of PLS-PC were determined when the root mean square error of calibration (*RMSEc*) reached the minimum value. The calibration models with determined PLS-PC were validated by leave-one-out cross validation to check the robustness of the models. Considering the prediction ability of models for real samples as well, data in the prediction sets were input into the calibration models for testing. After the numbers of PLS-PC were determined, parameters of GF-based or GLCM-based models produced best results were shown in results with corresponding optimal parameters of feature extraction. The efficiency of PLSR models were assessed by following statistical values of calibration sets, cross validation sets, and prediction sets, respectively: the correlation coefficient in calibration (*Rc*), cross validation (*Rcv*), and prediction (*Rp*), the root mean square error of calibration (*RMSEc*), cross validation (*RMSEcv*), and prediction (*RMSEp*). Models with greater values of *Rc*, *Rcv*, and *Rp*, and lower values of *RMSEc*, *RMSEcv*, and *RMSEp* would be better than models with opposite values. The smaller the differences between *RMSEc*, *RMSEcv*, and *RMSEp*, the better the model.

The most valuable wavelengths for each feature were selected according to the plot of regression coefficient. The wavelengths with peak coefficients were selected. Stepwise procedure was used to further explain the key wavelengths. The variables at key wavelengths were input into MLR model (Eq. 5.6), the performance of calibration, cross validation, and prediction was compared, and the best and practical model was selected for prediction of IMF content in intact pork.

$$Ym = b_0 + \sum_{i=1}^{i=n} X_i \times b_i , \tag{5.6}$$

where b_0 and b_i are the regression coefficient, X_i is the variable at i^{th} wavelengths, n represents the number of used wavelengths, i.e. variables.

5.3.6 Prediction map of IMF content in pork image

The mapping of IMF distribution would help to analyze the IMF content of pork since pork is an heterogeneous material. One advantage of hyperspectral imaging is that it provides spectral information of each pixel in pork image, which means the IMF content of each pixel could be predicted by inputting the spectrum into a prediction model. The spectral information from hyperspectral imaging includes external information of the objects of interest as well as internal due to the deep penetration ability of NIR spectra, which makes hyperspectral imaging more suitable for prediction of IMF content since the IMF is distributed not just in the surface of pork, but also in the whole pork sample. Application of hyperspectral imaging helps to recognize the IMF distribution in a whole pork sample. Reference data of IMF content of each pixel is required to build an accurate prediction model. However, it is not possible to obtain the IMF content of a pixel. To overcome this challenge, the best MLR model constructed based on mean spectrum or image parameters in previous step was applied to the spectrum of each pixel to predict the corresponding IMF content of each pixel in pork image. By showing the pixel-based IMF content, the prediction map of IMF content in pork was then generated. It would help understanding the IMF distribution in pork and conducting detailed study at pixel level.

5.4 Results and discussion

5.4.1 IMF content and ROI of hyperspectral images

A total of 83 pork loin chops were collected in this study. IMF content of each pork sample was measured and used as the referred IMF content for corresponding sample. Statistical description for IMF content of total pork cutlets, calibration set (n = 56), and prediction set (n = 27) is presented in Table 5.1. Wide variability is observed in total samples, calibration set, and prediction set. The range of prediction was covered by calibration set and the standard deviation (STD) of all three groups was in the same level. This helps to build a stable and reliable calibration model.

Table 5.1 Statistical description for IMF content of all the pork, calibration set and prediction set.

Trait	Total				Calibration				Prediction			
	Mean	STD	Min	Max	Mean	STD	Min	Max	Mean	STD	Min	Max
IMF content (%)	1.86	1.01	0.51	5.8	1.82	1.01	0.51	5.8	1.77	0.85	0.58	3.62

The conformation of *hypercube* (940-1650 nm) obtained by hyperspectral imaging system and corresponding ROI segmentation was described in Figure 5.3(a). A typical NIR image and the spectra of a surrounding fat pixel, an IMF pixel, a lean pixel, and a black board pixel were extracted from *hypercube* as an example. The reflected spectra of fat and lean showed different scales of intensity but similar features: reflected peak around 1100, 1300, and 1650 nm, and valley around 1250 and 1450 nm. The main constituent of fat and lean was lipid and water, whose peak absorption bands have a lot of overlapping (Osborne *et al.*, 1993). Besides, each hyperspectral image was not just

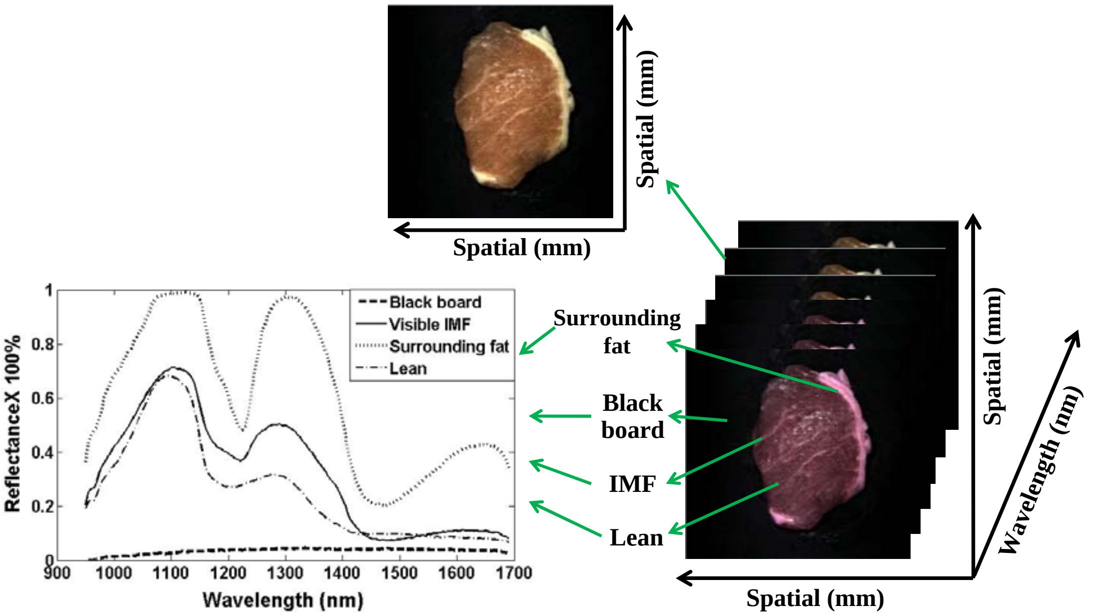

(a) Raw *hypercube*, hyperspectral images, and spectra of black board, visible IMF, surrounding fat, and lean

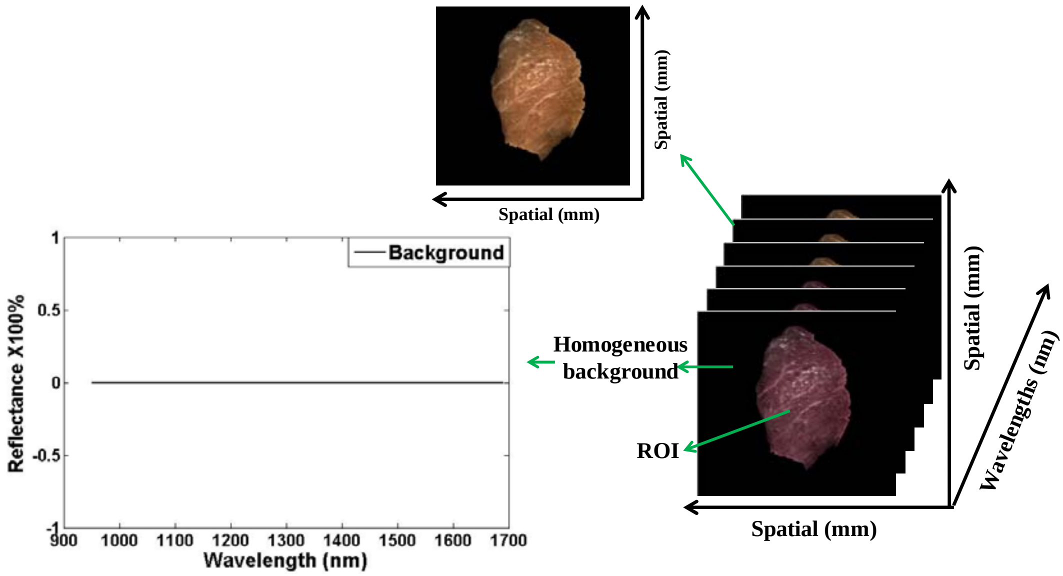

(b) ROI and spectrum of homogeneous background pixel

Figure 5.3 Construction of obtained hypercube and segmentation of ROI.

composed of the external information of sample, but also the internal information. Muscle fibers in pork are structured in lines along the longissmus muscle. Pork was cut cross the grain. Hence, each layer parallel to the cutting surface of pork included information of several muscle fibers. Since pork is a heterogeneous object, spectrum from one pixel may contain information of lean and fat in different layers simultaneously. This would explain the similar spectral characteristics between lean and fat. The spectrum of a black board pixel was shown as well. It is obvious that the reflectance of black board was very close to zero but not totally zero. To screen the board and surrounding fat from the image, automatic ROI segmentation was conducted. A binary mask was obtained and applied to each NIR image at the waveband 940-1650 nm. The resulted data cube was shown in Figure 5.3(b). The reflected values of non-ROI area were set to zero as described by the exampled background pixel.

5.4.2 Spectral response from raw ROI and Gabor filtered ROI

Figure 5.4 illustrated the raw ROI and the corresponding Gabor filtered ROI with parameters of $f = 0.1$, $\sigma = 10$. ROI in each image was filtered by an isotropic GF1 and four oriented GF2 (θ = 0°, 45°, 90°, 135°). The resulting typical mean spectra of raw ROI (**MR**) and Gabor filtered ROI (**MG1** and **MG2**), and the corresponding responses of first derivative of spectra (**DMR, DMG1** and **DMG2**) were shown in Figure 5.5. The mean spectra of raw ROI and filtered ROI showed different magnitude. All types of mean spectra showed similar features: steep peak around 1087 nm, another peak around 1279 nm, and one valley around 1207 nm. In Figure 5.5(a) to (e), the response of first derivative of mean spectra showed similar features as well: gradual peak around 1217 nm, and one steep valley around 1130 nm. **MR, DMR, MG1, MG2, DMG1,** and **DMG2** of samples were used for multivariate data analysis.

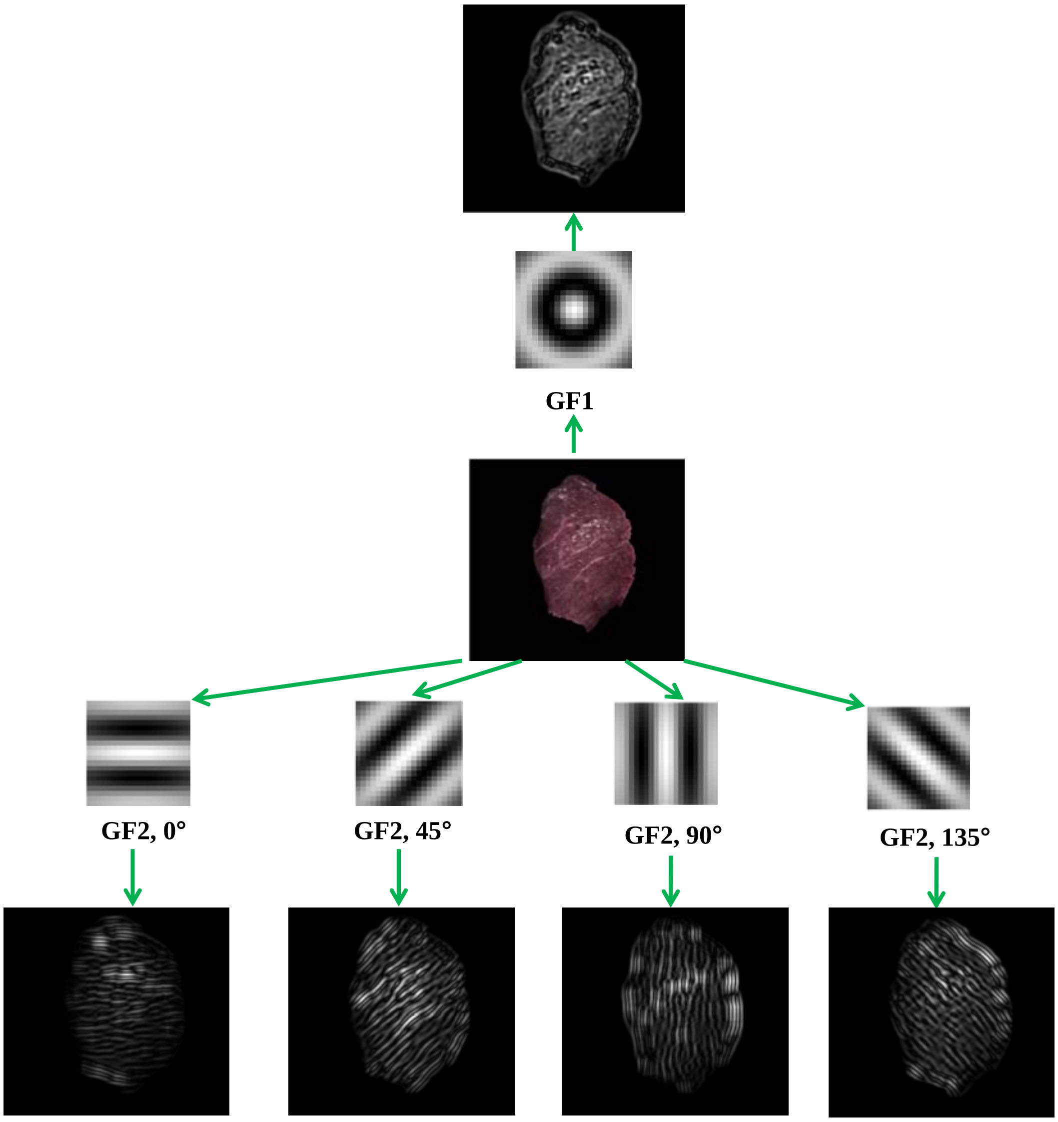

Figure 5.4 The raw ROI, GF1, GF2, and the corresponding Gabor filtered ROI.

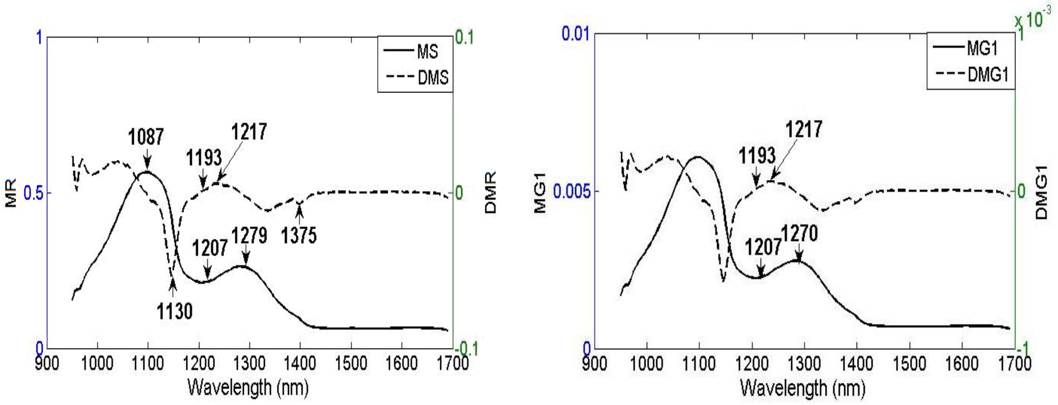

(a) **MR** and **DMR** (b) **MG1** and **DMG1**

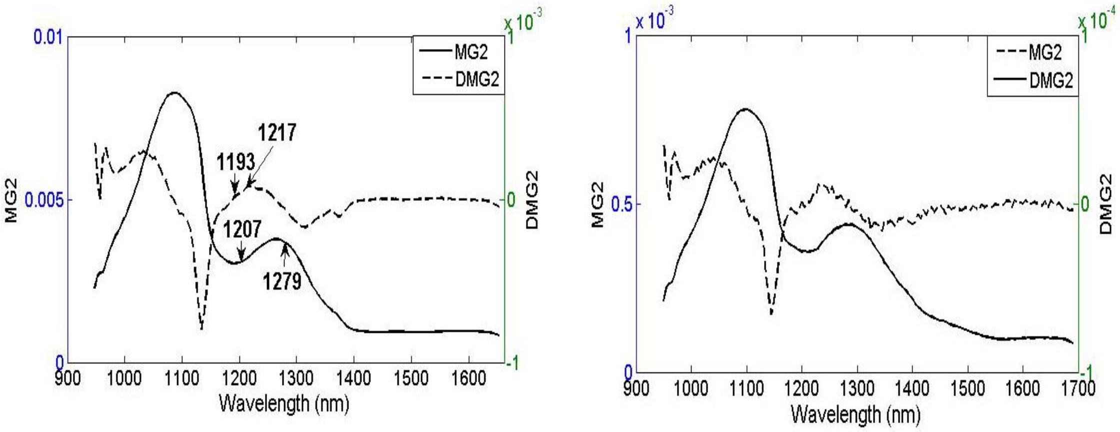

(c) **MG2**, 0° and **DMG2**, 0° (d) **MG2**, 45° and **DMG2**, 45°

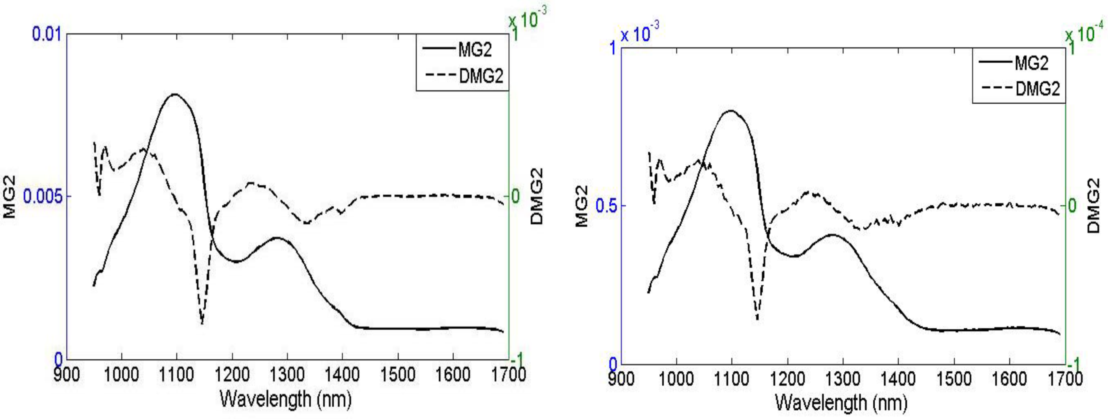

(e) **MG2**, **90**° and **DMG2**, 90° (f) **MG2**, 135° and **DMG2**, 135°

Figure 5.5 Typical mean spectra of raw ROI and Gabor filtered ROI and corresponding response of first derivative.

5.4.3 Texture curve by GLCM

Typical 8-level GLCM matrix of each ROI was formed and the resulted four GLCM measurements (**GIt**, **GIn**, **GIa**, and **GIh**) were obtained as illustrated in Figure 5.6, where offset distance *D* is 9, and direction θ is 0°. The minimum reflectance and maximum reflectance of each ROI were chosen as the first and last level of GLCM matrix. The range was divided into 8 parts, while each portion was regarded as a level. GLCM matrix at each wavelength resulted in 4 measurements (*contrast*, *correlation*, ASM, *homogeneity*). As depicted in Figure 5.6, GLCM index (**GI**) was expressed as curves, which resulted from measurements at different wavelengths. Peaks around 1100 nm is

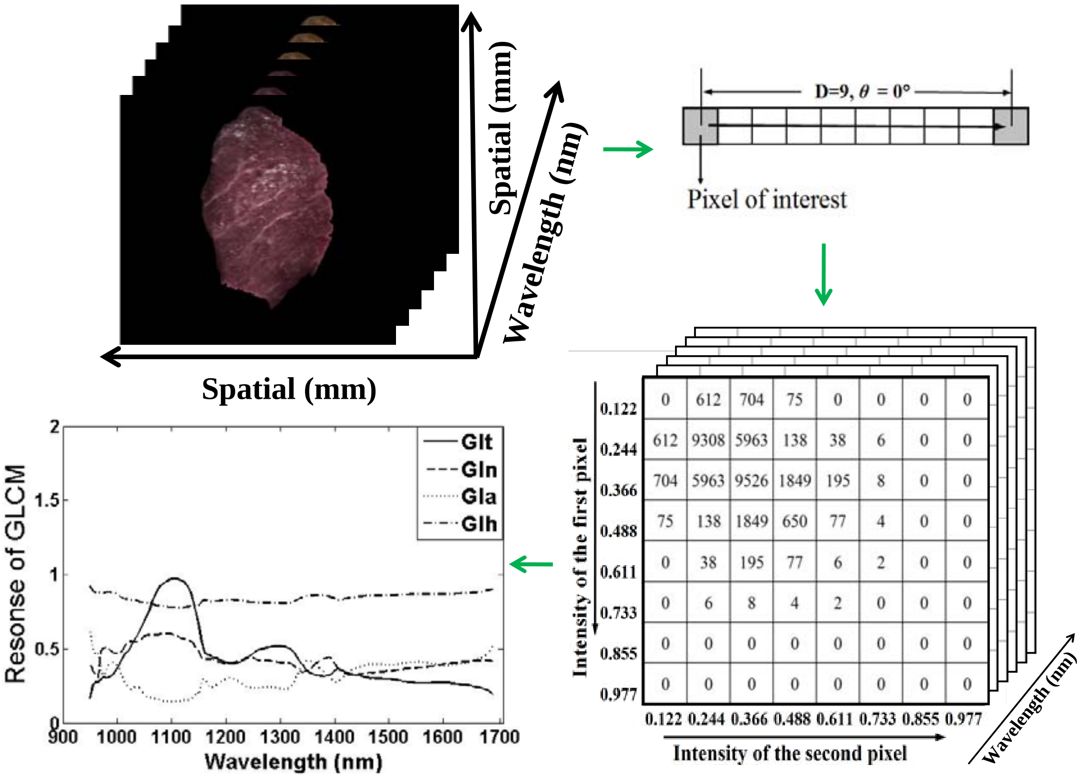

	0.122	0.244	0.366	0.488	0.611	0.733	0.855	0.977
0.122	0	612	704	75	0	0	0	0
0.244	612	9308	5963	138	38	6	0	0
0.366	704	5963	9526	1849	195	8	0	0
0.488	75	138	1849	650	77	4	0	0
0.611	0	38	195	77	6	2	0	0
0.733	0	6	8	4	2	0	0	0
0.855	0	0	0	0	0	0	0	0
0.977	0	0	0	0	0	0	0	0

Figure 5.6 Formation of GLCM matrix and corresponding texture curve.

observed in typical curves of **GIt** and **GIh**, which is similar to features of **MR** and **MG**, while **GIt** and **GIh** showed another peak around 1300 and 1400 nm, respectively. Different measurements were used as variables of multivariate data analysis.

5.4.4 Multivariate data analysis

Features from ROI in calibration set were input into Eq. 5.5 and regression matrices (**B**) were obtained. Models were cross validated and tested by independent samples in prediction set. The results of calibration, cross validation and prediction of all the features are listed in Table 5.2. The optimal parameters of Gabor filters and GLCM were selected based on the performance of PLSR models. When the algorithm-based PLSR models performed the best, the corresponding parameter sets were used as the optimal parameters for the algorithms: $\sigma = 10$, $f = 0.1$ for GF1, $\sigma = 10$, $f = 0.1$, $\theta = 0°$ for GF2, $D = 9$,

Table 5.2 Results of full waveband-based PLSR models using spectral and texture features.

Features	Parameters			Number of latent variables	Calibration		Cross validation		Prediction	
	σ	*f*	*θ*		*Rc*	*RMSEc*	*Rcv*	*RMSEcv*	*Rp*	*RMSEp*
MR				7	0.90	0.44	0.84	0.55	0.81	0.52
DMR				7	0.90	0.44	0.84	0.55	0.82	0.52
MG1	10	0.1		8	0.90	0.43	0.83	0.56	0.82	0.51
DMG1	10	0.1		7	0.90	0.44	0.83	0.56	0.82	0.52
MG2	1	0.5	0°	7	0.90	0.44	0.85	0.55	0.83	0.52
DMG2	1	0.5	0°	7	0.90	0.44	0.84	0.56	0.82	0.53
	Measurement	*D*	*θ*							
GI	Contrast	9	0°	3	0.80	0.65	0.76	0.70	0.79	0.75

$\theta = 0°$, measurement = '*Contrast*' for GLCM. The raw mean spectra and Gabor filtered spectra showed high similarity in PLSR analysis, while **MG2** performed slightly better than the other features. The prediction of IMF content by **GI** was not as strong as mean spectra of raw ROI and Gabor filtered ROI or first derivative of mean spectra.

As shown in Figure 5.7, plots of regression matrices (regression coefficients) for models in Table 5.2 were used to select the optimal wavelengths related to the IMF content of pork. Wavelengths corresponding to the first few peak regression coefficients were selected as potential variables, as listed in Table 5.3. The optimal wavelengths of all the mean spectra covered 986, 1044, 1116, and 1207 nm, while the wavelengths of all the first derivative of mean spectra covered 1025, 1193, and 1217 nm. Wavelengths 1044 and 1400 nm were used for GLCM as well as all types of mean spectra. Wavelengths around 960 and 1200 nm were both used as optimal wavelengths for all types of mean spectra and first derivative of mean spectra. The tight relationship between IMF and NIR spectra at 1200 nm is because of the absorption peak of the C-H bonds for fatty acids (Shenk *et al.,* 1992, Forrest *et al.,* 1997). The absorption peak of water around 960 nm would be the reason that the band was used as optimal wavelength for most of the spectral features (Shenk *et al.,* 1992, Forrest *et al.,* 1997).

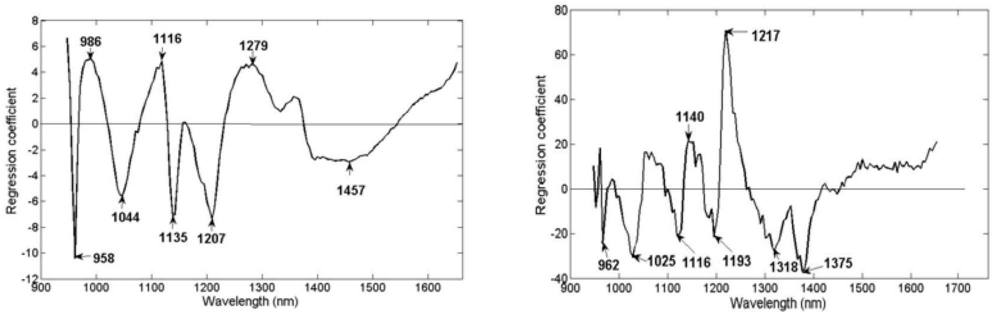

(a) **MR** (b) **DMR**

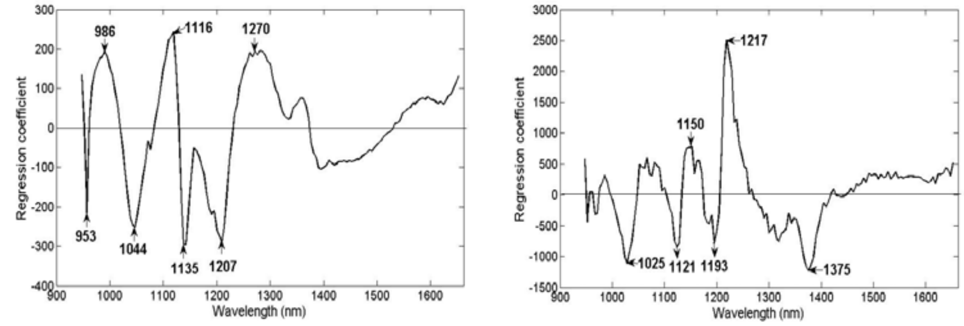

(c) **MG1** (c) **DMG1**

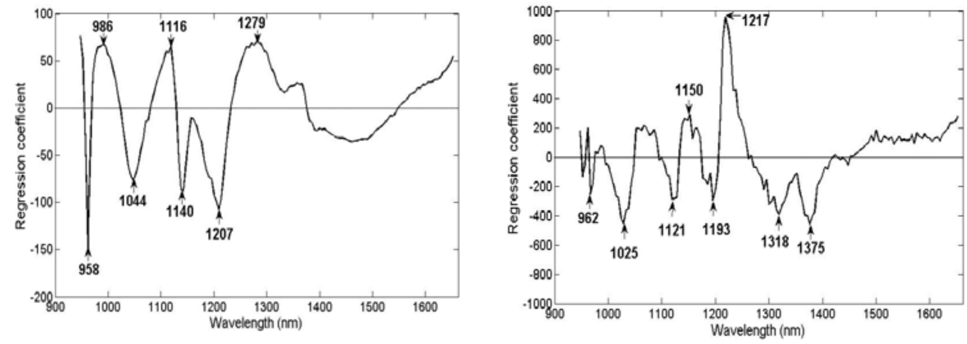

(d) **MG2** (e) **DMG2**

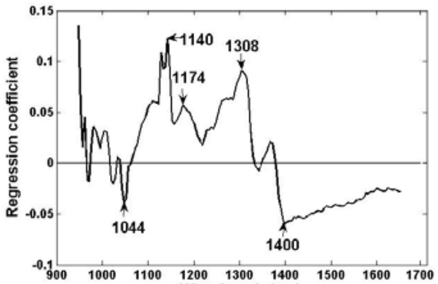

(f) **GI**

Figure 5.7 Regression coefficients from the models with optimal number of PC for all the features.

Table 5.3 Optimal wavelengths selected from PLSR models of spectral and texture features.

Features	Key wavelengths (nm)
MR	958, 986, 1044, 1116, 1135, 1207, 1279, 1457
DMR	962, 1025, 1116, 1140, 1193, 1217, 1318, 1375
MG1	953, 986, 1044, 1116, 1135, 1207, 1270
DMG1	1025, 1121, 1150, 1193, 1217, 1375
MG2	958, 986, 1044, 1116, 1140, 1207, 1279
DMG2	962, 1025, 1121, 1150, 1193, 1217, 1318, 1375
GI	1044, 1140, 1174, 1308, 1400

To reduce the influence of water and lean further, stepwise regression was adopted to simplify the variables at selected wavelengths at Table 5.3 and effective wavelengths were further optimized. The resulting optimal wavelengths, regression coefficients, and results of MLR based on stepwise selected key wavelengths are listed in Table 5.4. Only 2 key wavelengths were selected for most of the features except **DMR**. The few and precise wavelengths would help the development of an online determination system for IMF content in intact pork. Comparing to full waveband-based PLSR, key wavelengths-based MLR of **MR, DMR, MG,** and **DMG** produced similar results, while performance of **DMG1** was the best, with *Rc* of 0.89, *Rcv* of 0.89, and *Rp* of 0.86. The performance of **GIt** was not as good as the other features. However, the MLR model of **GIt** based on key wavelengths performed better than full waveband-based. Considering the complexity of application in practice, mean spectra of raw ROI is suggested as the processing technique of IMF content prediction using hyperspctral imaging. In this study, raw mean spectra-based MLR model produced correlation coefficient of calibration (*Rc*) of 0.87, cross validation (*Rcv*) of 0.86, and prediction (*Rp*) of 0.85, respectively. The prediction result of raw mean spectra-based MLR model is shown in Figure 5.8. It is observed that IMF content of both calibration and prediction set were predicted well. The result is comparable to the result of *Rc* = 0.88 and *Rp* = 0.91 that was reported in presentation of Liu *et al.* (2009).

Table 5.4 Results of MLR models of spectral and texture features.

Features	Key wavelengths (nm)	Regression Coefficient		Calibration		Cross validation		Prediction	
		b_0	b_i	*Rc*	*RMSEc*	*Rcv*	*RMSEcv*	*Rp*	*RMSEp*
MR	1207, 1279	0.408	-84.682, 79.259	0.87	0.52	0.86	0.53	0.85	0.55
DMR	1193, 1217, 1375	-0.063	-405.682, 274.427, -144.927	0.88	0.49	0.88	0.50	0.83	0.58
MG1	1207, 1270	0.538	-3030.206, 2740.172	0.87	0.50	0.86	0.51	0.85	0.53
DMG1	1193, 1217	-0.350	-22904.719, 38033.205	0.89	0.44	0.89	0.44	0.86	0.51
MG2	1207, 1279	0.414	-1210.504, 1125.226	0.87	0.51	0.86	0.51	0.85	0.53
DMG2	1193, 1217	0.376	-6034.862, 5736.390	0.88	0.49	0.88	0.49	0.85	0.52
GIt	1140, 1400	0.787	2.779, -2.998	0.82	0.64	0.81	0.65	0.78	0.76

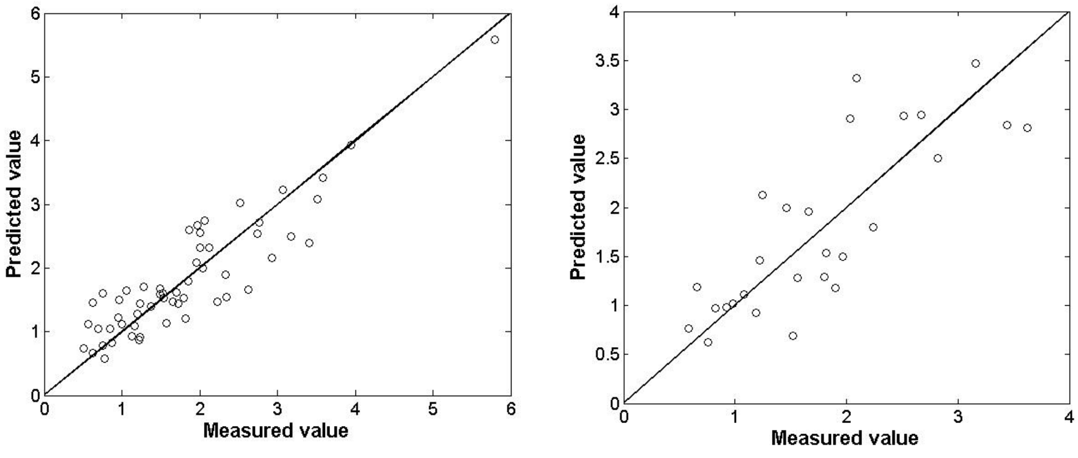

(a) Calibration (b) Prediction

Figure 5.8 Regression result from the MLR model of mean spectra of raw ROI.

5.4.5 Prediction map of IMF content

The MLR model based on raw mean spectra was used to obtain the distribution map of IMF content in pork. For spectrum of each pixel within a selected ROI, only reflectance at 1207 and 1279 nm was input into MLR model to generate IMF content of this pixel, i.e. only images at 1207 and 1279 nm were needed. IMF contents of all the pixels the ROI yield the prediction map of IMF content. Therefore, the loin portion selected by ROI would affect the profile of the prediction map. Images of two sides of one sample were used to generate a prediction map for the sample. Figure 5.9 depicted maps of two sides of two samples with different measured IMF contents. ROI of each side corresponds to one map, which showed how IMF content was distributed in ROI. The prediction maps show how IMF contents vary drastically between different areas of the same sample. Large variation is observed between two ROI of the same sample. Total IMF contents in each image were generated by averaging the IMF contents in each pixel within the relative prediction map. IMF content in ROI of two sides of one sample was used as the IMF content from prediction maps. The comparison of IMF content resulted from raw mean spectrum of ROI, distribution map, and referred IMF content are listed in Table 5.5. The error between IMF content from map and measured value is slightly larger than the one between IMF content from raw mean spectra and measured value. The prediction model for mapping was built using IMF content measured from the intact pork sample. Utilization of referenced IMF content from several small portions of the intact pork sample may help to enhance the prediction accuracy of distribution map of IMF content.

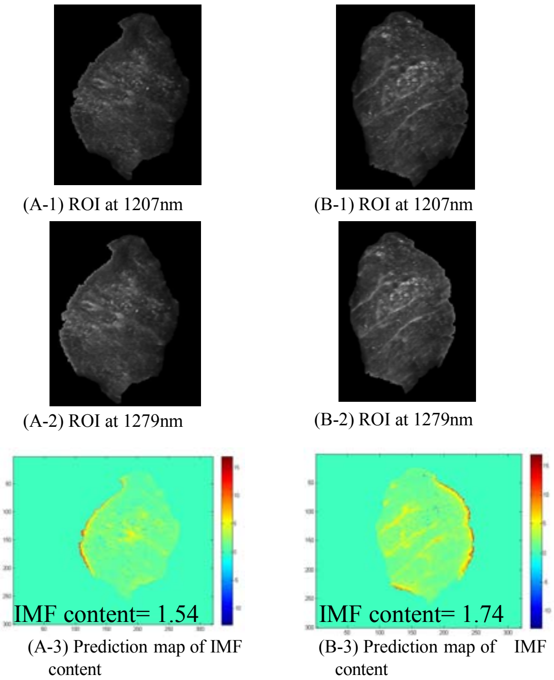

(A-1) ROI at 1207nm

(B-1) ROI at 1207nm

(A-2) ROI at 1279nm

(B-2) ROI at 1279nm

(A-3) Prediction map of IMF content

(B-3) Prediction map of IMF content

(a) Two sides of sample 1, average IMF content from map = 1.64

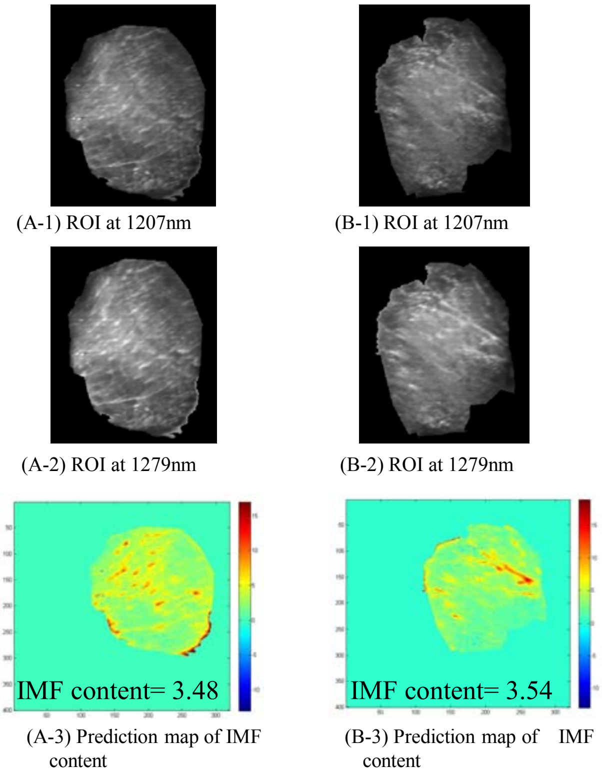

(A-1) ROI at 1207nm

(B-1) ROI at 1207nm

(A-2) ROI at 1279nm

(B-2) ROI at 1279nm

(A-3) Prediction map of IMF content

(B-3) Prediction map of IMF content

(b) Two sides of sample 2, average IMF content from map= 3.51

Figure 5.9 Prediction map of IMF content of two pork samples.

Table 5.5 Measured IMF content and predicted IMF content from map and raw mean spectra.

Trait	Sample ID	Predicted value		Measured value
		From map	From raw mean spectra	
IMF content (%)	1	1.64	1.51	1.25
	2	3.51	3.93	3.95

5.5 Conclusion

This study investigated the potential of NIR hyperspectral imaging technique for non-destructive, fast, and objective prediction of IMF content in intact pork. To exploit features from the numberous data of spectral images, pattern analysis techniques, i.e. the Gabor filter and the GLCM, were applied. Conventional feature extraction including averaging of spectra and first derivative were applied as well. PLSR, stepwise procedure and MLR were combined in a data processing procedure to select effective key wavelengths and establish MLR models. Wavelengths 1207 nm and 1279 nm were selected as featured wavelengths. The spectral dimension of hyperspectral data was reduced drastically from 167 bands to 2 bands. The first derivative of Gabor filtered mean spectra produced best results with little enhancement to the raw mean spectra. GLCM does not appear to be as effective as Gabor filter. Considering availability in practice, raw mean spectra is suggested as the best feature for prediction of IMF content of intact pork, with result of Rc = 0.87, Rcv = 0.86, Rp = 0.85. Prediction map of IMF content using the corresponding MLR model indicated great potential of detailed IMF inspection in the pork industry.

The promising results demonstrated the great value of NIR hyperspectral imaging technique in helping to locate the key wavelengths of IMF content prediction, which would lead to implementation of a detection component in a fast online inspection system of IMF content. More work should be conducted to explore more effective image processing techniques for hyperspectral images and to improve the predictive accuracy for IMF content of intact pork.

CONNECTING TEXT

In Chapter 5, NIR images of fresh pork at the 3rd /4th last ribs were collected and the intramuscular fat content was characterized by spectral features from NIR images. It was established that hyperspectral imaging could be effective in evaluating intramuscular fat content. Chapter 6 focuses on the fourth objective of the thesis, i.e. to investigate the potential of hyperspectral imaging of frozen and frozen-thawed pork for prediction of intramuscular fat content and marbling score of fresh pork. The sampling site was the 3rd /4th last ribs. Fresh pork before freezing and thawing was studied as well to compare with the results of frozen and thawed pork.

This manuscript will be submitted for publication to Journal of Food Engineering. The chapter is co-authored by my supervisor Dr. M.O. Ngadi, a research associate Dr. L. Liu, and a researcher Dr. C. Gariépy from Agriculture and Agri-Food Canada. The format of the original manuscript has been modified to remain consistent with the thesis format. All the literature, cited in this chapter, is listed in Chapter 10 (General references).

VI. PREDICTION OF INTRAMUSCULAR FAT CONTENT AND MARBLING SCORE OF PORK USING NIR IMAGES OF FROZEN AND FROZEN-THAWED PORK

6.1 Abstract

The aim of this study was to evaluate the potential of NIR hyperspectral imaging of fresh, frozen, and frozen-thawed intact pork loin as a fast and non-invasive method for quantifying intramuscular fat content and marbling score of pork loin. Spectral and texture features were obtained by averaging spectral data of raw and Gabor filtered pixels. The algorithm of the first derivative was applied to both raw mean spectra and Gabor filtered mean spectra. Effective wavelengths were selected using stepwise procedure. Multiple linear regression (MLR) models between reference data from fresh pork and image features from NIR images of fresh, frozen, and frozen-thawed intact pork at optimal wavelengths were built, cross-validated and tested with independent data sets, respectively. Predictive results of 0.87 and 0.88 for intramuscular fat content and marbling score were yielded by the first derivative of Gabor filtered mean spectra from images of fresh pork. Predictive results of 0.63 and 0.90 for intramuscular fat content and marbling score were obtained by the first derivative of Gabor filtered mean spectra from NIR images of frozen pork. In the same vein, predictive results of 0.82 and 0.91 for intramuscular fat content and marbling score were obtained using the first derivative of Gabor filtered mean spectra from NIR images of frozen-thawed pork. While there was slight variation but still comparable performance in the MLR models developed from acquired images of frozen and fresh pork samples, the MLR models developed from images of frozen-thawed and fresh pork samples were similar in performance. The current study therefore demonstrated that the NIR images of fresh, frozen and frozen-thawed pork could be utilized to assess intramuscular fat content and marbling score of fresh pork loins.

Keywords: Intramuscular Fat Content; Marbling Score; Gabor Filter; Multiple Linear Regression; Frozen-thawed Pork; Frozen Pork

6.2 Introduction

Pork is considered as one of the most popular red meats. Many quality features influence the acceptance of pork to consumers. Among the quality attributes, the total abundance of intramuscular fat (IMF) in pork, i.e. IMF content, and the visual abundance of marbling, i.e. marbling score (MS), are considerably important due to their perceived influences on eating flavor and therefore acceptance of customers (Brewer *et al.*, 2001; Bryhni *et al.*, 2003; Fortin *et al.*, 2005; Wood *et al.*, 2008). Pork with high IMF content and marbling score can be expected to have improved palatability or flavor (DeVol *et al.*, 1988; Ellis *et al.*, 1996; Resurreccion, 2004). Hence, IMF content and marbling score are used as important indicators of pork quality in the pork industry.

Commonly used method for determination of the IMF content of pork is derived from lipid extraction (AOAC, 1990; AOAC, 2000) in which chemical extraction of lipid taken place. In this method, lipid of pork samples should be extracted using solvent for more than 3.5 hours. Chemical measurement is labor-intensive, time-consuming, non-economical, invasive, and unsuitable for the automatic inspection of pork.

Beside the importance of IMF content, the visual distribution of fat flecks in pork, i.e. marbling, contribute to the eating quality of pork as a type of IMF and affect the judgments of customers more directly (Ferguson, 2004). Marbling in pork is conventionally scored according to standard charts (NPPC, 2002). This method is subjective and labor intensive. Both the subjective assessment of marbling and chemical determination of IMF content are unsuitable for the objective inspection of pork.

A non-destructive, fast and objective method that could evaluate the IMF content and the marbling score of pork would help pork producers to classify pork into different groups and consequently to allocate pork to targeted markets. Hyperspectral imaging, a combination of computer technologies and spectroscopic techniques, was proposed as one such method. This technique has been evaluated for the assessment of pork quality (Gowen *et al*., 2007; Qiao *et al*., 2007c; Liu *et al*., 2010; Barbin *et al*., 2012a; Barbin *et al*., 2012b; Liu *et al*., 2012). Qiao *et al.* (2007c) pioneered the early works using VIS/NIR hyperspectral imaging (400-1100 nm) to quantify the marbling score on the surface of pork chop. The grey-level co-occurrence matrix (GLCM)) of extracting texture features was exploited to distinguish marbling levels of pork. The marbling scores of standard charts were able to be distinguished except the standard level of 10.0. Moreover, an error of around 1.0 between referenced and estimated marbling scores was observed in the testing data set. Liu *et al.* (2012) applied a line pattern analysis technique called the wide line detector for the objective assessment of pork marbling. Hyperspectral images of pork taken at the red-green-blue channels were used to predict the marbling score of pork samples. The seven levels of marbling corresponding to the NPPC standards were discriminated well by the wide line detector. Promising results in previous studies indicated the potential of hyperspectral imaging for fat assessment in pork. Regarding the absorption peaks of lipid in the NIR region, it is of great interest to study the possibility of evaluating the IMF content and the marbling score of pork using NIR hyperspectral imaging.

Fresh pork chops were used in almost all the studies regarding inspection of pork quality using non-destructive assessment technologies. For image analysis, pork loins were imaged right after loins were dissected from 24 h post mortem swine carcass. In case of a large number of pork chops from meat procedures, rapid inspection is required to avoid pork from oxidation or other chemical change. It would be beneficial and much more practical for meat processors if frozen or frozen-thawed pork samples could be used to collect images. The pork could be stored in a freezer. The IMF content of pork could be analyzed later after 24 h post mortem. The successful prediction of fat attributes of fresh pork using frozen or frozen-thawed pork would allow hyperspectral images to be much more valuable for effective fat evaluation of pork.

The aim of this study was to investigate the potential of NIR hyperspectral images of fresh, frozen, and frozen-thawed pork chops for objective assessment of IMF content and marbling score of fresh pork chops. To achieve this goal, specific objectives are to: apply averaging algorithm and Gabor filter to NIR hyperspectral imaging of pork in three different storage conditions; calculate the first derivative of mean spectra; build models using multiple linear regressions (MLR); and compare the performances of models based on fresh, frozen, and frozen-thawed samples.

6.3 Materials and methods

6.3.1 Sample preparation

Forty-eight hogs of the same breed were slaughtered at a local commercial slaughterhouse. A wide range of variation of fat levels along *Longissimus dorsi* was obtained by detecting the thickness of pig back fat using ultrasound. At 24 h post-mortem, forty-eight loins were obtained by excision of *Longissimus dorsi* muscle between the 3rd and 4th last ribs. The obtained loins were further cut into 2.5 cm thick pieces and a thin piece was used for chemical determination of IMF content. The IMF content of the thin pork pieces were analyzed according to modified protocol by AOAC (2000). The marbling of two surfaces of 2.5 thick pork pieces was assessed subjectively according to NPPC (2002). The mean value of marbling measured from two surfaces of each piece was used as the referenced marbling score of the corresponding piece of pork. After marbling assessment, the pork pieces were vacuum-packed, shipped to the Hyperspectral Imaging Laboratory, McGill University, Montreal, QC, Canada and put in a fridge at 4℃ and later a freezer at-80℃ for image acquisition.

6.3.2 NIR hyperspectral imaging system and image acquisition

The hyperspectral system used in this study consisted of a spectrograph (Headwall Photonics Inc. USA), an InGaAs camera with integration time of 2 ms, a conveyer (Donner Mfg. Corp., USA), two tungsten halogen lamps (50 W) as the light source, a sample holder, and an enclosure. The system covers 167 wave bands from 900 to 1700 nm with a spectral resolution of 4.8 nm.

The NIR hyperspectral images of two surfaces of each pork chop were captured on a black background and were saved in a three-dimensional data cube. The same exposure time and focal length were used for all the samples. For each pork chop, a cube of 320 bins ×approximately 300 bins ×167 wave bands was obtained and saved in the image Band Interleaved by Line (BIL) format.

Fresh samples were first frozen, then stored in a freezer at -80℃ for 48 hours. Images of frozen samples were captured. Then samples were thawed in a fridge at 4℃ for another 24 hours, after which images of frozen-thawed samples were acquired.

To remove the effect caused by unevenness of illumination intensity and the intrinsic current of the camera, images in each data cube were calibrated. Values in all pixels were transformed to percent reflectance by dividing the subtraction between reflected light intensity and dark image and the subtraction of referenced light intensity and dark image over whole wave band. Consequently the values in all pixels within each image ranged from 0 (No reflection) to 1 (Full reflection). The corrected images were used for the subsequent image analysis.

6.3.3 Image analysis

It is a challenge to develop a proper image analysis procedure that is capable of automatically extracting the fat information from a NIR hyperspectral data cube. In this study, different image processing methods including image segmentation, spectral averaging, Gabor filter, and the first derivative of raw mean spectra and filtered mean spectra were developed and compared. All operations of image processing and further multivariate analysis in this study were performed using programs implemented with MATLAB R2008a (The MathWorks, Inc., Mass., USA).

6.3.3.1 Image segmentation

Hyperspectral images captured by the system are inevitably subject to background, surrounding fat and connective tissue of pork. The capture of these parts could not be avoided. However, the image analysis is supposed to be based on the loin eye part only. The captured raw images would provide incorrect information if no image pre-processing was applied. In order to improve the quality of pork images and make the proposed method practical in online detection, an automatic operation of region of interest (ROI) selection described in Liu *et al.* (2012) was employed as a tool for non-loin part removal in pork images. In this method, different thresholds were defined according to different data cube, respectively, which suggested high fitness of thresholds for different data cubes. Accordingly, a self-defined binary mask was obtained for each data cube. The segmentation of loin part could be achieved by applying the mask to each NIR image in the original data cube over whole wave band 900-1700 nm. Since there were intensive noises at the two ends of the wave band, which would degrade the image quality, only wave band 940-1650 nm was used for consequent extraction of image features.

6.3.3.2 Characterization of IMF content/ MS

The non-filtered reflected mean spectra (**MR**, 149 ×1) of two surfaces of fresh, frozen, and frozen-thawed pork were obtained by averaging the reflectance value of all pixels in the raw ROI. In total, 48 mean spectra (940-1650 nm) were recorded from each type of samples. The first derivative of the non-filtered mean spectra (**DMR**, 148 ×1) was calculated by subtracting the reflectance values of neighboring wave bands.

To facilitate the evaluation of pork IMF content and MS, texture analysis technique Gabor filter was exploited to extract the texture features of pork images. In this work, an isotropic Gabor filter and an oriented Gabor filter (Ma *et al*. 2002) derived from Gaussian function were used to characterize IMF content and MS in pork. For the isotropic Gabor filter, algorithm parameters of f representing the frequency of the sinusoidal wave, σ representing the standard deviation of the Gaussian function were involved, while parameters of f, σ, and θ controlling the orientation of the filter were involved for the oriented Gabor filter. Different sets of parameters were tried in initial image processing and were optimized by following correlation analysis. The average mean spectra of Gabor filtered ROI of two surfaces from each pork and the first derivative of Gabor filtered mean spectra were calculated and denoted as **MG** (149 ×1) and **DMG** (148 ×1), respectively.

In total, four image features including **MR**, **DMR**, **MG**, and **DMG** characterizing the IMF content and MS were extracted from the masked fresh, frozen, and frozen-thawed NIR images.

6.3.4 Statistical analysis

For imaged samples under different conditions, each group was separated to calibration set (Nc = 36 samples) and prediction set (Np = 12 samples). The Pearson's correlation coefficients between the fat characteristics from fresh, frozen, and frozen-thawed samples in calibration set and the value of IMF content and marbling score assessed by traditional methods were computed. Optimal parameters of algorithm Gabor filter were determined when maximum correlation coefficients were generated. Better image features amongst 4 image features were selected according to the correlation coefficients. Based on the above preliminary results, stepwise procedure was used to narrow broad wave band to several vital wave bands. Multiple linear regression (MLR) technique (Eq. 6.1) was applied in data at selected key wavelengths in calibration set for further analysis to understand and explain the linear relationship between selected image features from images of fresh, frozen, frozen-thawed pork (independent variables) and referenced attributes of IMF content and MS (dependant variables). Leave-one-out cross validation was applied on built calibration MLR models to test the stability of models. To test the predictive ability of built MLR models for independent samples, the data in prediction sets were input to build MLR calibrated models.

$$\hat{Y} = a_{.0} + \sum_{i=1}^{i=n} a_i X_i \,, \tag{6.1}$$

where $\hat{Y}$ is the estimated IMF content or marbling scores of pork, n is the number of selected wave bands, $a_{.0}$ and a_i are the regression coefficients, and X_i is the vector of selected spectral feature at selected wave bands.

The performances of built MLR models were evaluated by statistical values including correlation coefficient (*R*) and root mean square error (*RMSE*) between measured values (Y) and estimated attribute values ($\hat{Y}$) of IMF content or MS. The *R* of calibration (*Rc*), *R* of cross validation (*Rcv*), *R* of prediction (*Rp*), *RMSE* of calibration (*RMSEc*), *RMSE* of cross validation (*RMSEcv*), and *RMSE* of prediction (*RMSEp*) of MLR models based on images of fresh, frozen, and frozen-thawed pork were calculated. The performance of different models was compared. A model is considered to perform well if it produces a high *Rc*, a high *Rcv*, a high *Rp*, a low *RMSEc*, a low *RMSEcv*, a low *RMSEp*, and small differences between *Rc* and *Rcv*, *Rc* and *Rp*, *RMSE*c and *RMSEcv*, and *RMSE*c and *RMSEp*.

6.4 Results and discussion

6.4.1 Referenced IMF content and MS

The description of measured values for IMF content and MS of total 48 samples, calibration and prediction sets are listed in Table 6.1. Coefficient of dispersion was calculated by dividing standard deviation by mean value of the quality attribute. The large variability was indicated by high coefficients of dispersion for three data sets, which implied that samples used in the experiment covered a wide range of quality. Large variability and wide range of referenced attributes would help improve the stability of established predictive models.

Table 6.1 Statistics of IMF content and MS for different data sets.

Parameter	Set	Maximum	Minimum	Mean	Standard deviation	Coefficient of dispersion (%)
IMF content (%)	Total samples	5.80	0.63	2.26	1.05	47
	Calibration set	5.80	0.63	2.23	1.02	45
	Prediction set	5.32	0.82	2.36	1.19	53
MS	Total samples	5.25	1.00	2.49	0.86	35
	Calibration set	5.25	1.25	2.54	0.86	34
	Prediction set	4	1.25	2.46	0.81	33

6.4.2 NIR hyperspectral image analysis

6.4.2.1 Images and ROI of fresh, frozen, and frozen-thawed pork

Figure 6.1 showed the original NIR images and ROI of fresh, frozen, and frozen-thawed pork at 1200 nm and corresponding segmented ROI. High reflectance was observed in frozen sample due to the ice crystals in the frozen pork. Images of fresh and frozen-thawed sample showed high similarity visually at 1200 nm. Automatic selection of ROI was accurately conducted by closing non-loin part (set the reflectance to zero) and keeping loin part open (remain the reflectance values). Background, surrounding fat and connective tissue of pork were removed to enhance the accuracy of further analysis.

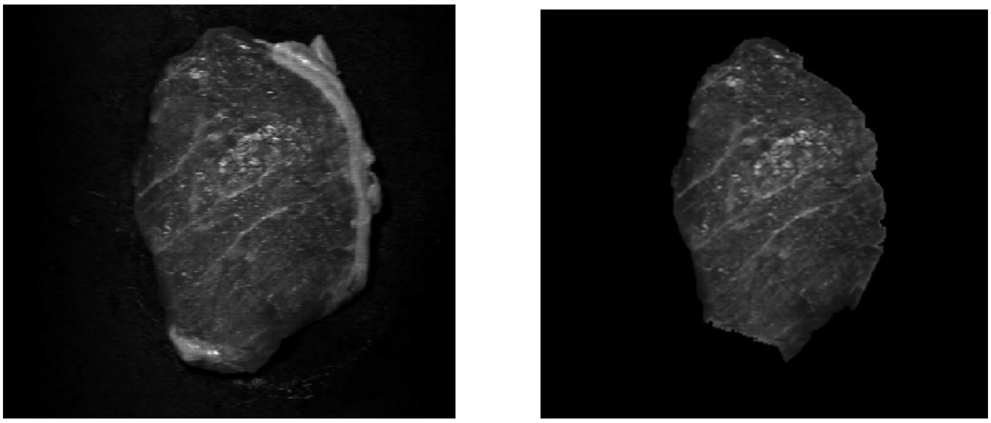

(a-1) NIR image (a-2) ROI

(a) Fresh pork

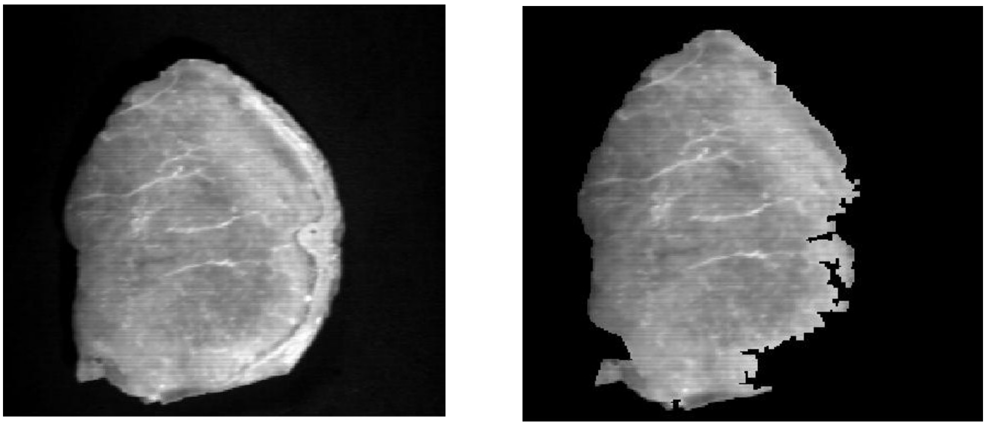

(b-1) NIR image (b-2) ROI

(b) Frozen pork

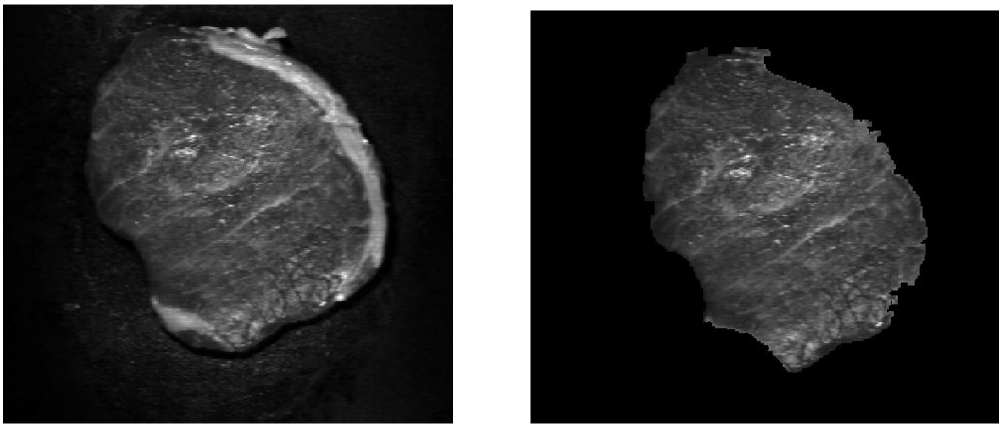

(c-1) NIR image (c-2) ROI

(c) Frozen-thawed pork

Figure 6.1 Typical images of fresh, frozen, and frozen-thawed pork.

6.4.2.2 Mean spectra and the first derivative of mean spectra

The mean **MR**, **DMR**, **MG**, and **DMG** of pork samples at three storage conditions are presented in Figure 6.2, where the oriented Gabor filter with f =10, σ = 0.1, and θ = 0° was adopted. Similar features were observed between **MR**, **MG**, **DMR** and **DMG** of fresh and frozen pork, respectively, with a baseline shift of 30 nm along the wavelengths. Comparing to fresh and frozen-thawed sample, highest reflectance was observed for both **MR** and **MG** of frozen pork, which is corresponding to high reflection of frozen water in samples. Relatively lower reflectance was observed for both **MR** and **MG** of frozen-thawed pork comparing to fresh sample. Lowest changes were observed for **DMR** and **DMG** of frozen samples. Almost same features were observed between **MR**, **MG**, **DMR** and **DMG** of fresh and frozen-thawed pork, respectively. The reflection of water crystal may be the reason of the inflexion in mean spectra of frozen pork. The loss of drip juice in frozen-thawed sample caused the loosening of pork tissue and the alteration of water distribution, which resulted in the different mean spectra of fresh and frozen-thawed pork samples (Ballin and Lametsch, 2008). The amount of enzymes was increased in pork after freeze and thawing due to damage of cell compartments especially for mitochondria and lysosomes, which may result in the difference of mean spectra of frozen-thawed pork and fresh pork (Ballin and Lametsch, 2008). Correlation analysis was further performed to study the difference of mean spectra of samples at three statuses. The changes of **DMR** and **DMG** of fresh samples along wavelengths were similar to the one of frozen-thawed samples. Slight differences of **DMR** and **DMG** of fresh and frozen-thawed pork were observed around 1040 and 1140 nm.

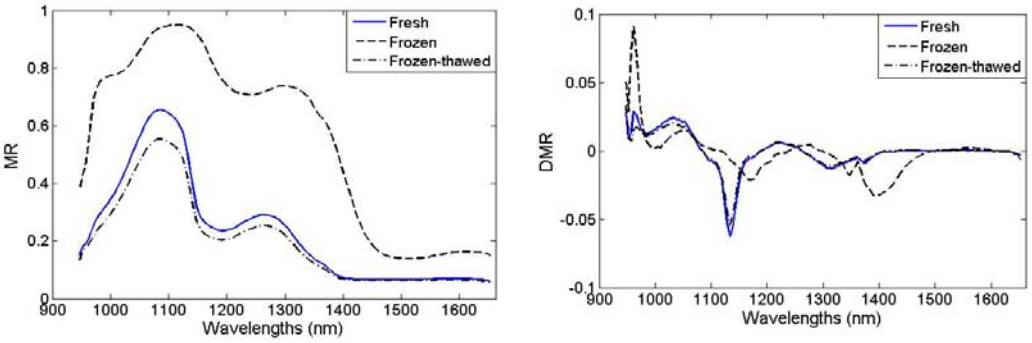

(a) **MR** (b) **DMR**

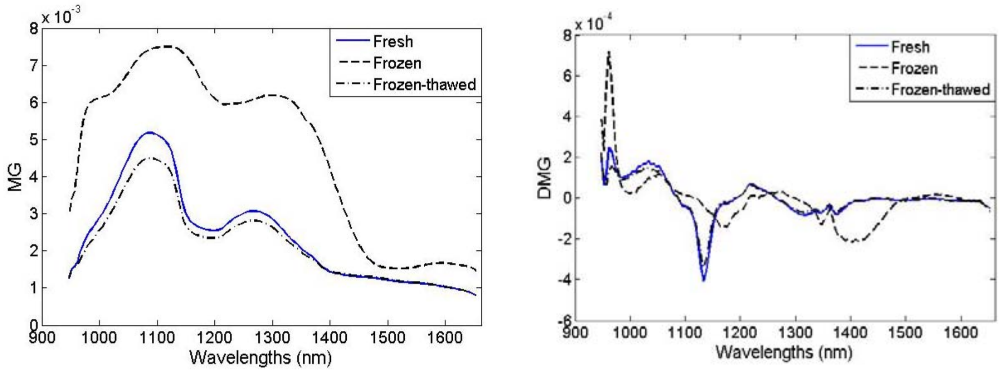

(c) **MG** (d) **DMG**

Figure 6.2 MR, DMR, MG, and DMG of fresh, frozen, and frozen-thawed pork.

The correlation coefficients between **MR**, **MG**, **DMR** and **DMG** of fresh and frozen pork, and the correlation coefficients between **MR**, **MG**, **DMR** and **DMG** of fresh and frozen-thawed pork along wavelengths are depicted in Figure 6.3. Comparing to fresh and frozen-thawed samples, tighter correlation between means spectra, i.e. **MR** and **MG** of fresh and frozen pork was indicated by Figure 6.3(a) and Figure 6.3(c). Low correlation coefficients of mean spectra of fresh and frozen-thawed pork were observed over the whole wave band. In Figure 6.3(b) and Figure 6.3(d), the first derivative of mean spectra, i.e. **DMR** and **DMG** of fresh and frozen pork showed similar maximum correlation coefficient to the first derivative of mean spectra of fresh and frozen-thawed pork. However, the peak correlation coefficients were observed at different wavelengths including 1050, 1100, and 1190 nm. In frozen pork, biochemical reactions were very slow, but became active again during freeze-thawing, which may cause the difference between fresh and frozen or frozen-thawed pork (Downey and Beauchene, 1997). The low correlation coefficients between fresh and frozen-thawed pork indicated the potential of hyperspectral imaging for discrimination of fresh and frozen-thawed meat.

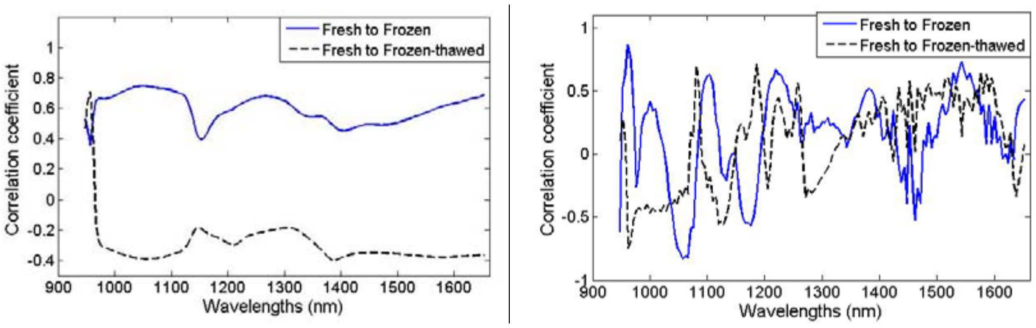

(a) **MR** (b) **DMR**

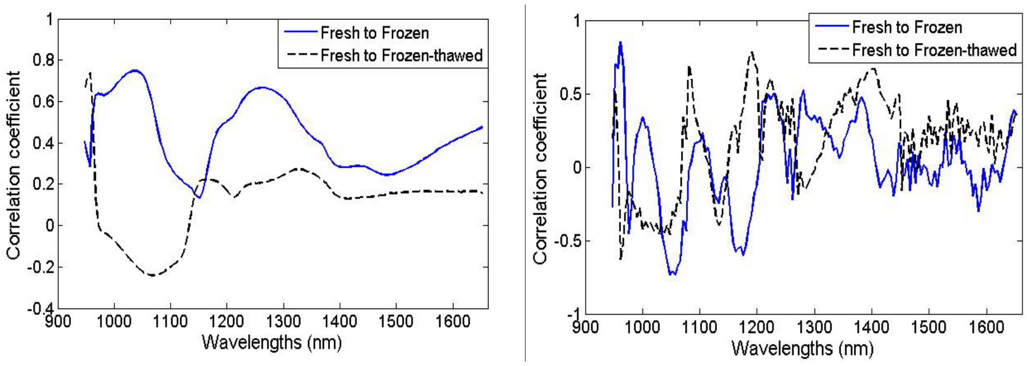

(c) **MG** (d) **DMG**

Figure 6.3 Correlation coefficients between MR, DMR, MG, and DMG of fresh and frozen, and fresh and frozen-thawed pork along wavelength, respectively.

6.4.3 Statistical analysis

6.4.3.1 Correlation coefficients

Based on trial and error, the oriented Gabor filter was used for both **MG** and **DMG** due to its better performance than the isotropic Gabor filter. The parameter sets of Gabor filter used for different status of pork and different attributes are listed in Table 6.2. It is distinct that parameter set of σ = 10, f = 0.1, and θ = 0° were used mostly. The low frequent Gabor filter using this parameter set captured more useful information and at the same time extracted extract less noise.

Table 6.2 Parameters used for MG and DMG for prediction of IMF content and MS.

(a) IMF content

	MG			**DMG**		
	σ	f	θ	σ	f	θ
Fresh	10	0.1	0°	10	0.1	0°
Frozen	15	0.1	0°	10	0.1	0°
Frozen-thawed	15	0.1	135°	15	0.1	0°

(b) MS

	MG			**DMG**		
	σ	f	θ	σ	f	θ
Fresh	10	0.1	0°	10	0.1	0°
Frozen	10	0.25	135°	10	0.1	45°
Frozen-thawed	10	0.1	0°	10	0.1	0°

Figure 6.4 shows the correlation coefficients between different image features of fresh, frozen, and frozen-thawed pork and IMF content/ MS. In Figure 6.4(a) to (d), for all four-image features, fresh samples indicated highest correlation to IMF content comparing to frozen and frozen-thawed samples. **MR** and **MG** of frozen samples indicated tighter correlationship to IMF content than frozen-thawed samples, while **DMR** and **DMG** of frozen samples indicated poorer correlationship to IMF content than frozen-thawed samples. In Figure 6.4(a) and (c), plots of correlation coefficients in between IMF content and **MR** and **MG** of three types of pork show similar features with peaks at 960, 1150, and 1300 nm. As shown in Figure 6.4(b) and (d), plots of correlation coefficients between IMF content and **DMR** and **DMG** of fresh pork show features with peaks at 970,

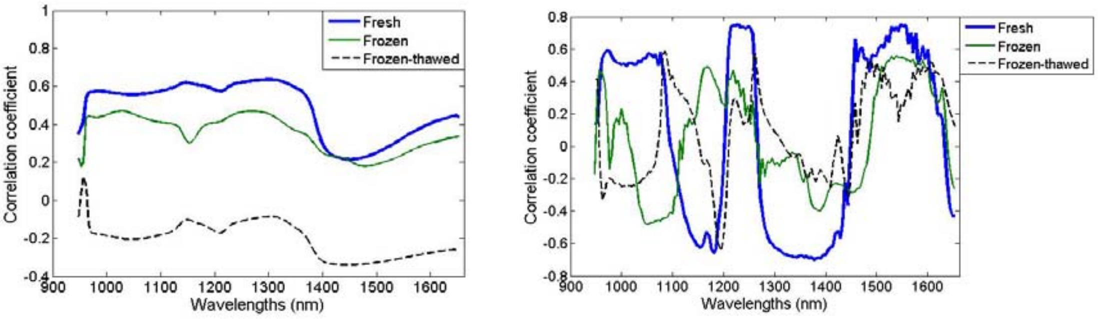

(a) **MR-**IMF (b) **DMR**-IMF

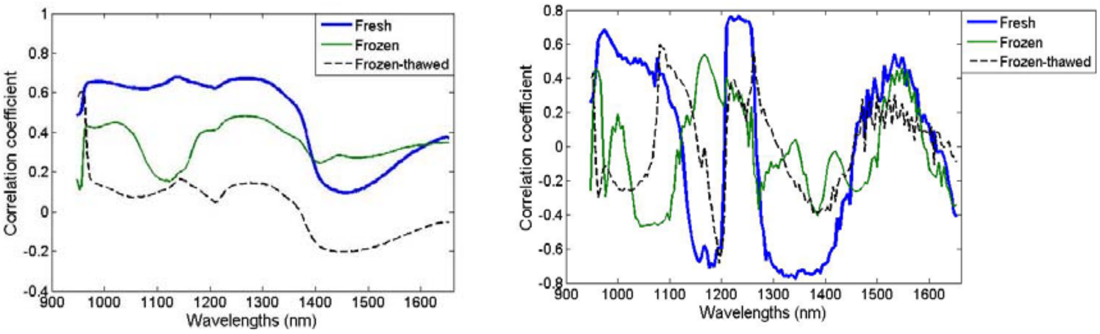

(c) **MG-**IMF (d) **DMG-**IMF

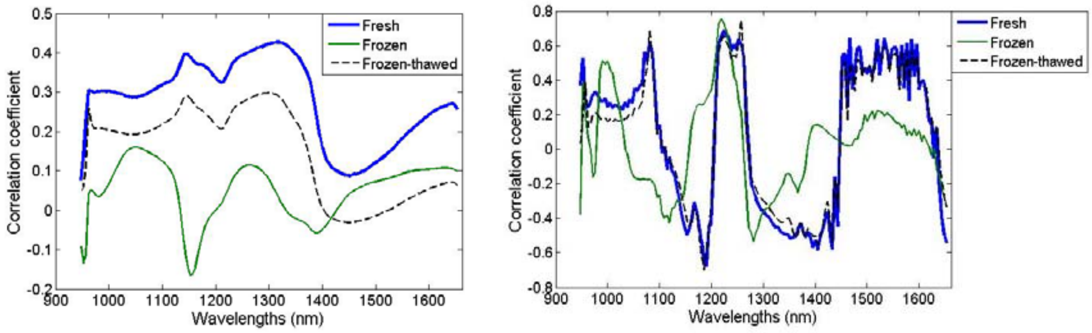

(e) **MR-**MS (f) **DMR**-MS

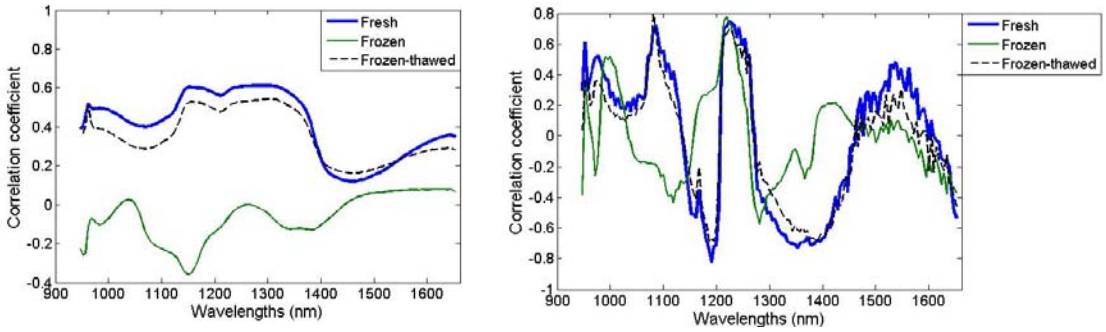

(g) **MG-**MS (h) **DMG-**MS

Figure 6.4 Correlation coefficients between image features of fresh, frozen, and frozen-thawed pork with IMF content/ MS.

1190, and 1220 nm, and broad peak around 1300-1400 nm, while plots of **DMR** and **DMG** of frozen pork show features with peaks at 1050 and 1150 nm. Peaks at 1090, 1200, and 1250 nm were observed for correlation coefficient plots between IMF content and **DMR** and **DMG** of frozen-thawed pork.

In Figure 6.4(e) and (g), **MR** and **MG** of fresh pork implied best correlationship to MS, followed by frozen-thawed pork and frozen pork. Peaks at 1150 and 1300 nm were observed for all six plots. In Figure 6.4(e) and (g), correlation coefficient plots between MS and **DMR** and **DMG** of fresh and frozen-thawed pork show peaks at 1090, 1190, 1210, and 1350 nm, while utmost at 1220 and 1290 nm was observed in plots between MS and **DMR** and **DMG** of frozen pork. Wave band around 1200 nm indicated strong potential for prediction of IMF content and MS for all three types of pork. It is due to the energy absorption or release of chemical bond C-H, which is the main bond of lipid (Murray and Williams, 1987).

The maximum values of correlation coefficients between **MR**/ **MG** of all three types of pork and attributes were obviously lower than the one between **DMR**/ **DMG** and attributes. Hence, **DMR**/ **DMG** of fresh, frozen, and frozen-thawed samples were used for following MLR analysis.

6.4.3.2 Models and performance

To reduce the dimensions of hyperspectral data cube and eliminate redundant wavelengths, stepwise regression was employed to reduce the 149 wave bands to several key wavelengths. The selected wavelengths that were used for **DMR** and **DMG** of fresh, frozen, and frozen-thawed samples for prediction of IMF content and MS are listed in

Table 6.3. Among several different key wavelengths used in Table 6.3(a), wavelengths of 1212 and 1217 nm and wavelengths in range of 1300-1400 nm were used in almost all the MLR models for prediction of IMF content. Reflections around 1200 nm are due to C-H second overtone in lipid. Reflections in 1300-1400 nm are due to C-H combination in protein, and reflections in 1400-1500 nm are due to O-H first overtone in water (Osborne and Fearn, 1988; Kim *et al.,* 2007). Since the compositions of intramuscular fat are lipid, protein, and water, it is reasonable to use related key wavelengths to build prediction

Table 6.3 Key wavelengths selected by stepwise for MLR modeling.

(a) IMF content

Samples	Image features	Key wavelengths (nm)
Fresh	**DMR**	1198, 1212, 1366, 1548
	DMG	1217, 1342,1486,1514
Frozen	**DMR**	1006, 1178, 1217, 1366, 1548
	DMG	1054, 1159, 1193, 1212, 1236, 1370, 1548
Frozen-thawed	**DMR**	1082, 1207, 1217, 1241, 1313, 1342
	DMG	958, 1082, 1193, 1217, 1236, 1318

(b) MS

Samples	Image features	Key wavelengths (nm)
Fresh	**DMR**	1082, 1188, 1217, 1236, 1452
	DMG	1082, 1188, 1236, 1346, 1380
Frozen	**DMR**	1217, 1236
	DMG	1217, 1236
Frozen-thawed	**DMR**	1169, 1255
	DMG	1078, 1174, 1226, 1346, 1433

MLR models of IMF content in pork. Comparing to fresh and frozen pork, wavelengths over 1500 nm were not used for frozen-thawed sample. In Table 6.3(b), wavelengths around 1200 nm were used for MS assessment, due to the relationship between NIR spectra and C-H bonds in fat. The results are reasonable since fat is the major constituent of pork marbling. The models of **DMR**, **DMG** of frozen pork and **DMR** of frozen-thawed pork did not use wavelengths over 1300 nm. One explanation could be that the frozen status of water and the change of water holding capacity had a positive influence on evaluation of MS.

Samples were ranked according to actual values of IMF content and MS. For each four samples, three samples were used for calibration, while the fourth sample was used for prediction. Based on the obtained explanatory matrixes and dependent vectors, MLR was implemented to analyze the linear relationships between the image characteristics, i.e. **DMR** and **DMG** and IMF content or MS. The formulated MLR models were built and cross-validated. The predictive ability of built MLR models was tested using independent data in prediction set. The built 12 MLR models and results of calibration, cross validation, and independent validation are listed in Table 6.4.

In Table 6.4(a) and Figure 6.5(a), MLR models using **DMG** of three status of pork produced better results for prediction of IMF content than models using **DMR**. MLR model using **DMG** of fresh pork performed best with *Rc* of 0.85, *RMSEc* of 0.52, *Rcv* of 0.83, *RMSEcv* of 0.65, *Rp* of 0.87, and *RMSEp* of 0.57. The performance of MLR models for prediction of IMF content using frozen-thawed pork was comparable to the performance of fresh pork, followed by MLR models of frozen pork. More work is

Table 6.4 MLR models based on key wavelengths and performance of MLR models.

(a) IMF content

Samples	Image features	Regression coefficients	Calibration		Cross validation		Prediction	
			Rc	*RMSEc*	*Rcv*	*RMSEcv*	*Rp*	*RMSEp*
Fresh	**DMR**	-0.0146, 123.957, 321.225, 324.994, 4959	0.82	0.63	0.79	0.70	0.65	0.87
	DMG	0.287, 22488, -6515, -117400, 129100	0.85	0.52	0.83	0.65	0.87	0.57
Frozen	**DMR**	1.003, -285.049, -50.038, 379.648, -73.052, 464.904	0.76	0.64	0.72	0.78	0.55	0.99
	DMG	2.704, -7920, 4540, -13558, 84698, -150660, -6336, 43711	0.82	0.56	0.78	0.75	0.63	0.98
Frozen-thawed	**DMR**	3.183, -121.764, -1302, 1914, -2475, 530.123, -1239	0.81	0.58	0.77	0.72	0.81	0.67
	DMG	0.363, -7639, -34807, -40226, 39652, 104150, 35289	0.82	0.57	0.78	0.71	0.82	0.67

(b) MS

Samples	Image features	Regression coefficients	Calibration		Cross validation		Prediction	
			Rc	*RMSEc*	*Rcv*	*RMSEcv*	*Rp*	*RMSEp*
Fresh	**DMR**	2.435, -12.666, -665.906, 629.310, -846.691, 5765	0.85	0.43	0.83	0.55	0.91	0.39
	DMG	1.806, 36012, -70524, -761.786, -21492, 17545	0.88	0.40	0.86	0.50	0.88	0.43
Frozen	**DMR**	3.416, 500.663, -456.432	0.84	0.45	0.83	0.50	0.90	0.35
	DMG	2.958, 47348, -41573	0.86	0.43	0.85	0.47	0.90	0.33
Frozen-thawed	**DMR**	1.025, 502.546, 3121	0.82	0.47	0.81	0.53	0.89	0.40
	DMG	0.722, 84052, 10017, 48846, 32699, -48129	0.89	0.38	0.87	0.49	0.91	0.36

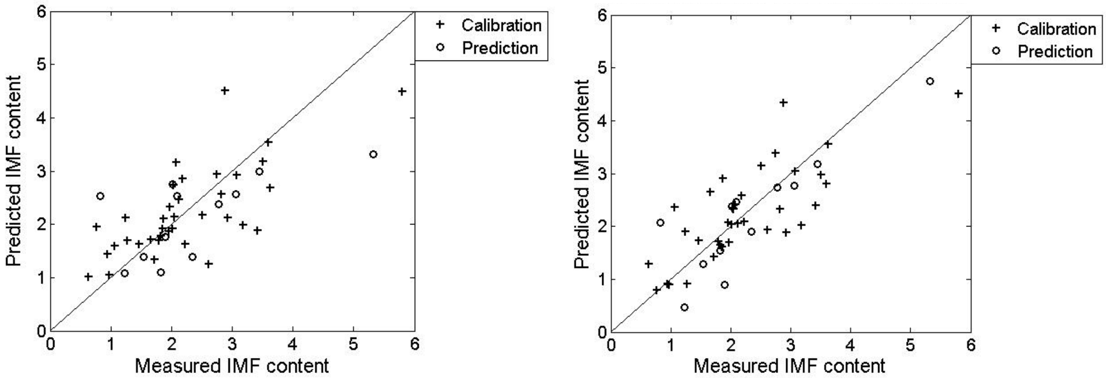

(a-1) **DMR** of fresh pork (a-2) **DMG** of fresh pork

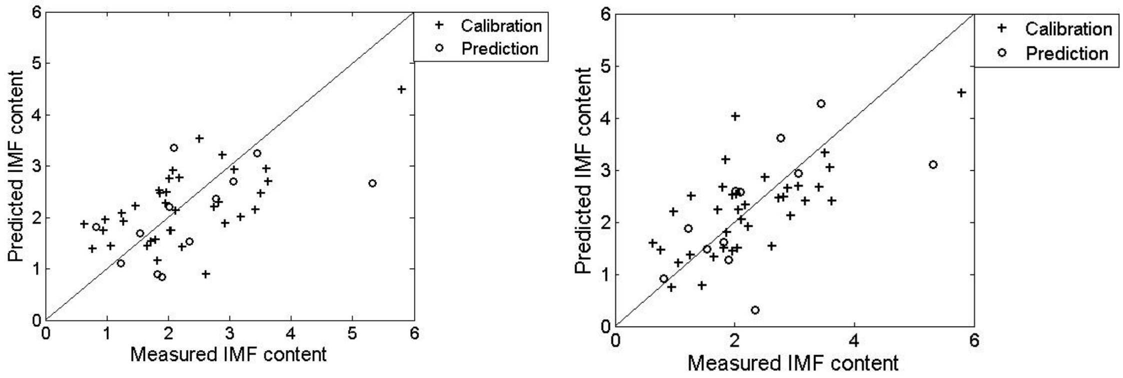

(a-3) **DMR** of frozen pork (a-4) **DMG** of frozen pork

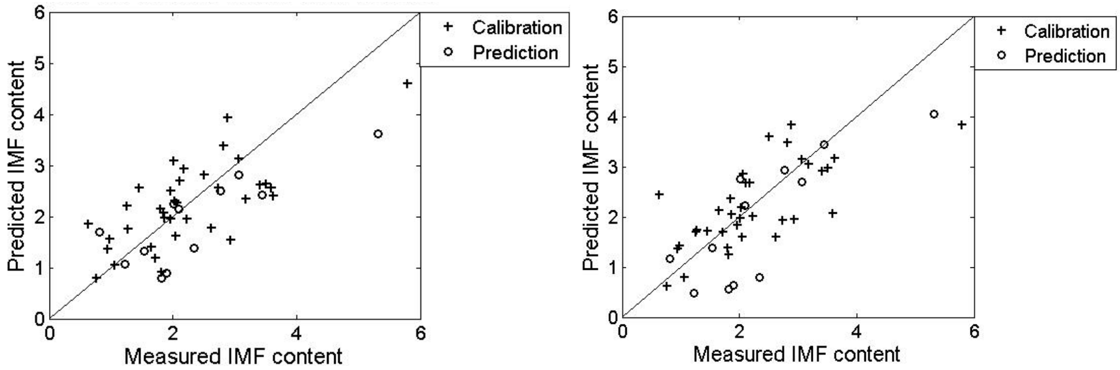

(a-5) **DMR** of frozen-thawed pork (a-6) **DMG** of frozen-thawed pork

(a) IMF content

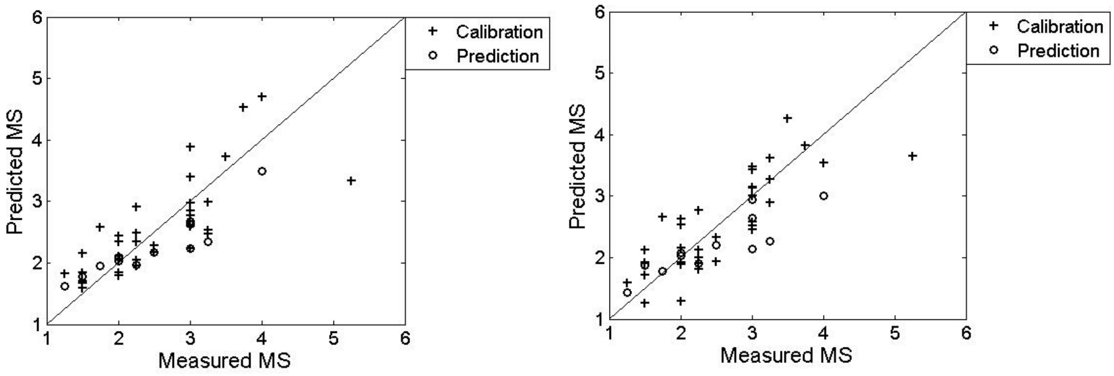

(b-1) **DMR** of fresh pork (b-2) **DMG** of fresh pork

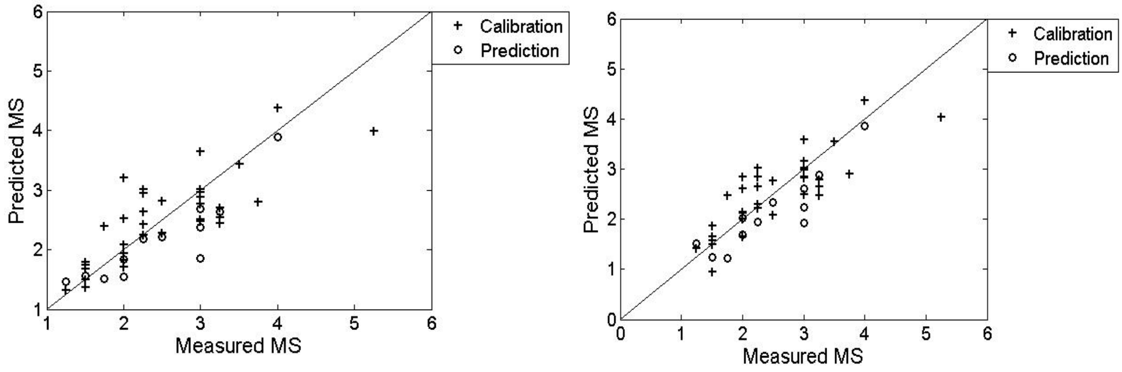

(b-3) **DMR** of frozen pork (b-4) **DMG** of frozen pork

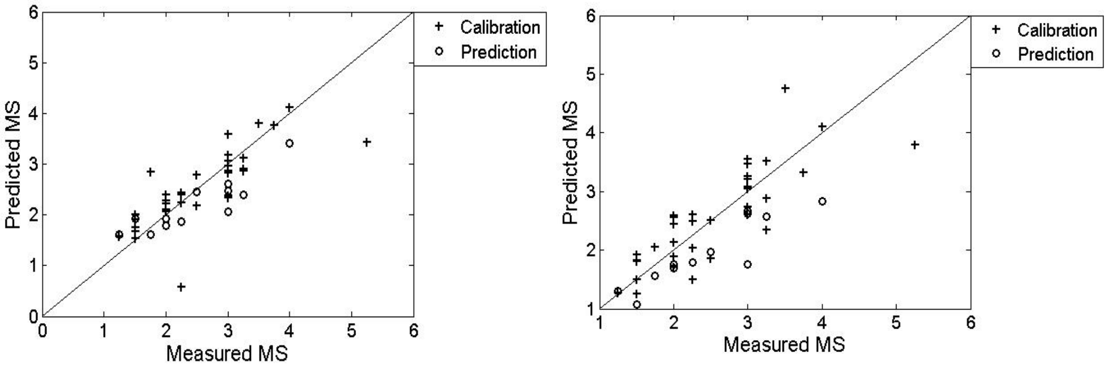

(b-5) **DMR** of frozen-thawed pork (b-6) **DMG** of frozen-thawed pork

(b) MS

Figure 6.5 Performance of fresh, frozen, and frozen-thawed pork-derived MLR models for prediction of IMF content/ MS.

necessary to enhance the predictive accuracy of model using frozen pork. Image characteristics from three status of pork were linearly correlated with measured IMF content, especially image feature **DMG**. It was indicated that NIR images of fresh, frozen, and frozen-thawed pork have great potential to predict IMF content of fresh pork.

In Table 6.4(b) and Figure 6.5(b), MLR models using **DMG** of three status of pork implied slightly stronger explanatory ability for MS than models using **DMR** by performing better than the models using **DMR**. MLR model using **DMG** of frozen-thawed pork performed best with *Rc* of 0.89, *RMSEc* of 0.38, *Rcv* of 0.87, *RMSEcv* of 0.49, *Rp* of 0.91, and *RMSEp* of 0.36, followed by **DMG** of fresh pork with *Rc* of 0.88, *RMSEc* of 0.40, *Rcv* of 0.86, *RMSEcv* of 0.50, *Rp* of 0.88, and *RMSEp* of 0.43. The performance of MLR models for MS assessment using frozen or frozen-thawed pork was comparable to the performance of fresh pork. It was implied that MS characteristics from all three kinds of pork were linearly correlated with measured MS. NIR images of fresh, frozen, and frozen-thawed pork revealed great potential to predict MS of fresh pork.

6.5 Conclusion

By correlation and MLR analysis, promising relationships were found between the image characteristics captured by hyperspectral imaging from fresh, frozen and frozen-thawed pork and chemically extracted intramuscular fat content and subjectively measured marbling score. For all three types of pork, the first derivative of Gabor filtered mean spectra from hyperspectral images revealed strongest predictive potential for non-destructive and rapid evaluation of IMF content and MS. It can be concluded that the first derivative of Gabor filtered mean spectra from hyperspectral images of fresh, frozen and frozen-thawed pork could be used to predict the IMF content and MS. The results confirmed that the Gabor filter technique could extract the features of IMF and MS automatically and objectively. More samples should be investigated to improve the predictive accuracy using image features of fresh, frozen, and frozen-thawed pork. Quantifying IMF content and MS of fresh loin cuts using frozen and frozen-thawed pork would enhance economic opportunities for pork producers and processors dramatically.

CONNECTING TEXT

In Chapter 6, the possibility of using frozen and frozen-thawed pork for determination of intramuscular fat content and marbling score of pork was studied. The relationship between textural and spectral information of frozen and fresh pork, and frozen-thawed and fresh pork was presented. Predictive ability of hyperspectral measurement of frozen-thawed pork was found to be comparable with ability of fresh pork. In Chapter 7, effect of anatomical location was considered for prediction of pork fat attributes. There is large variation of intramuscular fat content and marbling score along the thoracic longissmus muscle. Conventional methods were used to assess intramuscular fat content and marbling score of pork at the seven last ribs. The distribution of intramuscular fat content and marbling score along the longissmus muscle was thus obtained. The fat attributes at the last ribs was used as a predictive site to predict the corresponding attributes at the anterior ribs along the thoracic longissmus muscle.

The manuscript of this chapter will be submitted for publication to International Journal of Food Science and Technology. The chapter is co-authored by my supervisors Dr. M.O. Ngadi and Dr. S.O. Prasher, a research associate Dr. L. Liu, and a researcher Dr. C. Gariépy from Agriculture and Agri-Food Canada. The format of the original manuscript has been modified to remain consistent with the thesis format. All the literature cited in this chapter is listed in Chapter 10 (General references).

VII. PREDICTING INTRAMUSCULAR FAT CONTENT AND MARBLING SCORE OF PORK ALONG THE LONGISSIMUS MUSCLE BASED ON THE LAST RIB

7.1 Abstract

Intramuscular fat (IMF) and marbling are widely regarded as two important quality attributes indicating the fat level of pork. Pork loins at the five last thoracic ribs were usually collected as studied samples representing IMF content and marbling score (MS) of the whole loin. Uniformity is necessary for determination of pork intramuscular fat content. For this purpose, loin chops at 7 sampling sites along posterior side of the thoracic *Longissimus dorsi* were collected. Linear and quadratic regression models were built to predict IMF content/ MS of each loin chop from the 2nd last to the 7th last thoracic rib and the mean of IMF content/ MS of the 7 sites using IMF content/ MS at the last rib, respectively. Cross validation was adopted to analyze the efficiency of models. The IMF content/ MS of loin between the 2nd last and the 7th last rib and the mean value of the whole loin were regarded as the dependent variables, while the IMF content and MS at the last rib were regarded as independent variables of regression models. Random dataset were used for analysis of variance (ANOVA). The results of cross validation implied that IMF content and MS at the last rib showed good predictive ability for IMF content and MS at the other ribs and the whole section of loin, respectively. For both IMF and MS, linear regression and quadratic regression had similar performance. The best mean correlation coefficient of calibration (*Rc*) of 0.91 and validation (*Rv*) of 0.88 were obtained for linear regression model of IMF content of the whole loin, while *Rc* of 0.90 and *Rv* of 0.88 were obtained for quadratic regression model of MS of the whole loin. For IMF content at each rib from the 2nd last to the 7th last separately, the IMF content at the 4th last rib was more related to the IMF content of the last rib, i.e. linear regression with mean *Rc* of 0.90 and *Rv* of 0.88. MS at the 6th last rib was more related to MS of the last rib than MS at other ribs, i.e. quadratic regression with mean *Rc* of 0.90 and *Rv* of 0.84. The results indicated that IMF content and MS at the last rib had great potential for prediction of IMF content and MS at the other ribs and the mean value of the whole loin.

Keywords: Pork; Intramuscular Fat Content; Marbling score; Located sites; Cross validation; Regression analysis

7.2 Introduction

Fat levels of pork include the visible fat (e.g. Marbling) and non-visible fat (e.g. Intramuscular fat, IMF). Intramuscular fat (IMF) content, which is defined as the total concentration of intramuscular fat in meat, is regarded as one of the most important quality traits of meat (Wood *et al.*, 2008; Suzuki *et al.*, 2005a). Marbling is defined as the visible fat in loin. Fat proportion of pork influences the consumer liking for pork (Brewer *et al.*, 2001; Bryhni *et al.*, 2003), which affects the consumption frequency. Pork with the same levels of IMF content and marbling may receive different acceptance in different markets due to the different perception of fat level. Wood (1990) suggested a minimum of 1% (Fresh weight basis) IMF fitted the UK market. For Canada market, Fortin *et al.* (2005) proposed IMF content of 1.5% as a thresholding level to ensure the eating quality of Canadian pork. In the American market, the National Pork Board of US recommended IMF content of 2% ~ 4% to the pork industry in US (Meisinger, 2002). It is important for the pork industry to assess IMF content and marbling levels efficiently in order to classify pork to meet the targeted quality levels of different markets.

For determination of IMF content, samples were generally collected along the longissimus muscle. There are usually around fourteen pairs of ribs along the longissimus muscle of the pig, i.e. there are around fourteen different sampling sites available for determination of IMF content for each pig. Different sampling locations including the last rib (Fernandez *et al.*, 1999; Bahelka *et al.*, 2009; Lo Fiego *et al.*, 2010), the 10th rib (Witte *et al.*, 2000; Lonergan *et al.*, 2007; Rincker *et al.*, 2008), the 3rd /4th last ribs (Sather *et al.*, 1996; Suzuki *et al.*, 2005b; Fortin *et al.*, 2005), and the 2nd /3rd last ribs (Lakshmanan *et al.*, 2012) have been adopted in different studies. It is readily obvious that different sampling sites were adopted in studies and most sampling sites located amongst the five last ribs. The non-uniformity of sampling site could cause discrepancy in results of pork quality studies. Different sites were adopted in different studies since standardization of the representative anatomic site on the *Longissimus dorsi* is still going on. On the other hand, labor work was necessary to count the number of ribs from the sections anterior to the last rib. Comparing to the other anatomical locations, the sampling sites at the last rib of the *Longissimus dorsi* could lower the labor depletion. Hence, it is of interest to study the relations between the IMF content at the last rib and the IMF content measured at the other ribs, including the mean IMF content of the whole loin. The establishment of this relation will assist in provision of IMF content at a demanded location and will help to reconcile the IMF assessments for both laboratories and the pork industry.

As a type of visible IMF, marbling was closely associated to IMF content (Van der Wal *et al*., 1992). For marbling, an evaluation of the marbling indicated by marbling score (MS) was usually performed subjectively according to NPPC (NPB, 2002). The sampling site at the 3rd / 4th last ribs is representative in commercial application. Same as IMF content, the sampling sites at the last rib of the *Longissimus dorsi* could reduce labor counting. It is of interest to study the variation of MS along the longissimus muscle, and establish the relationship between MS at the last rib and the other ribs.

Carpenter *et al.* (1961) observed extreme variation of IMF content and marbling at different loci of thoracic ribs from pig carcasses. Faucitano *et al.* (2004) studied the distribution of IMF content and marbling at different ribs along longissimus muscle and reported a high variability of IMF content and marbling as well. The IMF content and marbling score from the 3rd last lumbar vertebra to the 5th thoracic rib was correlated to the average total IMF content/ marbling score of the whole longissimus muscle. The IMF content and marbling score at or near the 3rd /4th last rib were suggested as prediction site for mean IMF content and marbling score because of the high coefficient determination with mean IMF content and marbling score of the whole thoracic loin and lumbar.

To our knowledge, no quantitative relationship between IMF content/ marbling score of loins at different ribs and the last rib or the average IMF content/ marbling score of the whole loin and the last rib was studied in other researches. The objectives of this study were to examine the quantitative distribution of pork IMF content and marbling score at different ribs; to investigate the possibility of using IMF content and marbling score at the last rib of pig to predict the IMF content and marbling score from the 2nd last to the 7th last ribs and the average IMF and marbling score of each *Longissimus dorsi*.

7.3 Materials and methods

7.3.1 Sample collection and assessment of marbling

In this study, 24 pigs composed of both female and male were raised and slaughtered at a local commercial abattoir. The pigs of the same genetic background were fed with different levels of flax seeds to obtain a large variation in IMF content and marbling levels of the loin along the longissimus muscle. At 24 h post-mortem, the *Longissimus dorsi* (LD) in the same sides of thoracic region were removed from pig carcasses, packed in refrigerated boxes and transported to Hyperspectral Imaging Laboratory, McGill University, Montreal, QC, Canada for further assessment and analysis of IMF content and marbling scores.

Considering that previous studies were on the 7 last ribs, the wider range of the 7 last ribs were used in this study. The loins chops at the 7 last ribs were removed starting from the posterior end of *Longissimus dorsi* and were sliced to 7 pieces along the ribs. Each piece is 2 cm thick approximately. The cutting was conducted perpendicular to the longitudinal axis of the loin chop (Faucitano *et al.*, 2004). Table 7.1 shows the dissection scheme of the cut loin chop from the last thoracic rib (L1) to the 7th last thoracic rib (L7), the assigned name of loin slices, and the corresponding symbols for IMF content and MS. In total, 167 loin samples (Only six loins were obtained from one pig, 24×7-1 = 167) were collected. Samples was classified to 7 sets (L*i*, *i* = 1, 2, 3 …7) according to 7 sampling sites, with 24 samples in each groups (23 samples in one group). The average value of IMF content/ MS from loin joint (L1 to L7) was grouped as a set (L*i*, *i* = 0). In total, 8 groups were obtained. The adhering fat as well as the connective tissue was carefully removed from each loin slice. The trimmed loin samples were then assessed by a technician according to the NPPC charts (NPB, 2002) and establish marbling scored from 1 (Devoid) to 6 and 10 (Abundant). Thus, marbling scores (MS) of two sides of each slice were obtained and averaged. The mean value of MS at two sides (i.e. **ML*i***, ***i*** = 1, 2, 3 … 7) was used as the referenced value of MS for corresponding analysis. The average

Table 7.1 Dissection scheme of the *Longissimus dorsi*.

	Thoracic (rib number)							
Actual rib number	The last - 7th last	The 7th last	The 6th last	The 5th last	The 4th last	The 3rd last	The 2nd last	The last
Assigned ID of loin	L0	L 7	L 6	L 5	L 4	L 3	L 2	L1
Assigned ID of IMF content	**FL0**	**FL7**	**FL6**	**FL5**	**FL4**	**FL3**	**FL2**	**FL1**
Assigned ID of MS	**ML0**	**ML7**	**ML6**	**ML5**	**ML4**	**ML3**	**ML2**	**ML1**

of MS at all 7 ribs was calculated and used as the MS of each whole loin chop (**ML0**). The assessed samples were then packed and stored in the deep-freezer at -80℃ for 24 hours for the subsequent IMF content determination.

7.3.2 Determination of IMF content

IMF content of each loin from the last to the 7th last rib (**FL*i***, ***i*** = 1, 2 … 7) was measured and the mean value of IMF content of the whole loin chop was calculated (**FL0**).

Frozen samples were freeze-dried prior to fat extraction, using a laboratory freeze-dryer (Thermo Savant Modulyod-115, NY, USA) for 96 hours with drying temperature of -50℃ and operating pressure of 120 MPa. Freeze-drying removed moisture from fat by transferring frozen water molecules to vapor directly as well as keeping the characteristics of fat as much as possible.

Dried pork samples were ground using a coffee grinder (Bodum 5678-57, C-MFLl, USA). IMF content (Dry weight basis) of freeze-dried samples was then determined following the protocol of Soxhlet extraction (Association of Official Agricultural Chemists, 2000). Samples of 3 g were measured as initial dry mass (Wi). Crude fat (Regarded as intramuscular fat) of ground samples were extracted by Solvent Extractor (SER148, Velp Scientifica, Usmate, Italy) using petroleum ether as the solvent for intramuscular fat. The samples were immersed in the solvent for 40 minutes, and then washed for 60 minutes recirculating by solvent. The dissolved fat in the resultant fluid was allowed to be detached from solvent for 30 minutes. The extracted fat was weighed (Wf) and the percentage of IMF content was determined as the fraction of fat to the initial dry mass (i.e. Wf/Wi×100%). The whole process of fat extraction took approximately three hours for each set of samples. There were four samples in one set. Two replicates of intramuscular fat extraction was performed and the average value was used.

7.3.3 Data analysis

Regression models including linear regression (Eq. 7.1 and Eq. 7.2, linear model of **FL1-FL*i*** and **ML1-ML*i***) and quadratic regression (Eq. 7.3 and Eq. 7.4, quadratic model of **FL1-FL*i*** and **ML1-ML*i***) were proposed to explain the relationship between the IMF content and MS of L1 and L0 and L2 to L7. Cross validation was applied to explore the possibility of using linear regression model and quadratic model. Cross validation analysis was performed on MATLAB 7.3.0 (The MathWorks, Inc., Mass., USA).

$$FLi = a_0 + a_1 \times FL1, \boldsymbol{i} = 0, 2, 3 \ldots 7, \tag{7.1}$$

$$MLi = a_0 + a_1 \times ML1, \boldsymbol{i} = 0, 2, 3 \ldots 7, \tag{7.2}$$

$$FLi = a_0 + a_1 \times FL1 + a_2 \times FL1^2, \boldsymbol{i} = 0, 2, 3 \ldots 7, \tag{7.3}$$

$$MLi = a_0 + a_1 \times ML1 + a_2 \times ML1^2, \boldsymbol{i} = 0, 2, 3 \ldots 7, \tag{7.4}$$

For each model, the 24 samples were separated to two subsets: calibration set (16 samples) and validation set (8 samples, there was 7 samples for L7 since only the six last loins were obtained from one pig). There were C_{24}^{16} (735471 = $\frac{24!}{16! \times 8!}$ = 24×23×22×21×20×19×18×17/(8×7×6×5×4×3×2×1), note: C_{23}^{16} = 245157 for L7) unrepeated subsets available for cross calibration sets. Ten thousand subsets of data were selected randomly for cross validation of linear and quadratic regression models. The efficiency of models was assessed by the following criteria: correlation coefficient (*Rc*) and *p*-value (*pc*) of calibration, standard deviation (STD) of *Rc* and *pc*, correlation coefficient (*Rv*) and *p*-value (*pv*) of validation, and standard deviation of *Rv* and *pv*. The higher the *Rc* and *Rv*, the lower the *pc* and *pv*, and the lower the standard deviation of *Rc, pc* and *Rv, pv*, the better the model.

After models were identified, subsets of data were chosen randomly to build models for statistical analysis. The IMF or MS at L1 was used as independent effect in the regression models, while the IMF or MS at L*i* (*i* = 0, *2* … 7) was used as the independent variable, respectively. The regression analysis of variance (ANOVA) test was performed in order to check the effectiveness of the built models. ANOVA tests were carried out at the 5% probability on SAS Version 9.2 (SAS, Institute Inc., Cary, USA).

7.4 Results and discussion

7.4.1 IMF content and marbling score

Measured values for IMF content and MS of pork cutlets are presented in Table 7.2. Coefficient of dispersion (unit: %) was calculated by dividing mean value by STD. It is shown that the samples provided data with a great variation. Distribution of IMF content (i.e. **FL*i***, ***i*** = 1, 2, 3 … 7) and MS (i.e. **ML*i***, ***i*** = 1, 2, 3 … 7) along the *Longissimus dorsi* is shown in Figure 7.1. High variation of IMF content along the *Longissimus dorsi* was observed, while MS showed variation which was not as great as IMF content. Both IMF content and MS showed increasing trend from L1 to L7, while graph of IMF content showed steeper slope than MS. The highest value of IMF content was located at L7 with **FL7** = 9.48%, while the lowest IMF content was located at L2 with **FL2** = 5.89%. The trend of IMF content agrees with the finding of Faucitano *et al.* (2004), who recommended that IMF content and MS increased from the last rib (end) of longissimus muscle to the anterior sites. High IMF content was recorded at L6 and L7, which was included in the middle section of the thoracic muscle as of study of Faucitano *et al.* (2004). Low IMF content was recorded around L1 and L2, while Faucitano *et al*. (2004) identified similar section of near the end of the thoracic section. On the other hand, the highest MS was located at L6 of **ML6** = 3.22, while the lowest MS was recorded in L1 of **ML1** = 2.79. This agrees with the result of Faucitano *et al.* (2004) as well, who suggested that the high MS located in the middle of the *Longissimus dorsi* which includes L7 in this study, while low MS located near the end of the *Longissimus dorsi* (Faucitano *et al.*, 2004) which corresponded to the L1 to L3 in this study.

Table 7.2 Statistics for IMF content and MS of loin slices are presented.

Trait	Mean	STD	Minimum	Maximum	Coefficient of dispersion (%)
IMF content (%)	7.38	3.48	3.06	21.84	47.15
Marbling score	3.01	0.98	1.00	6.25	32.58

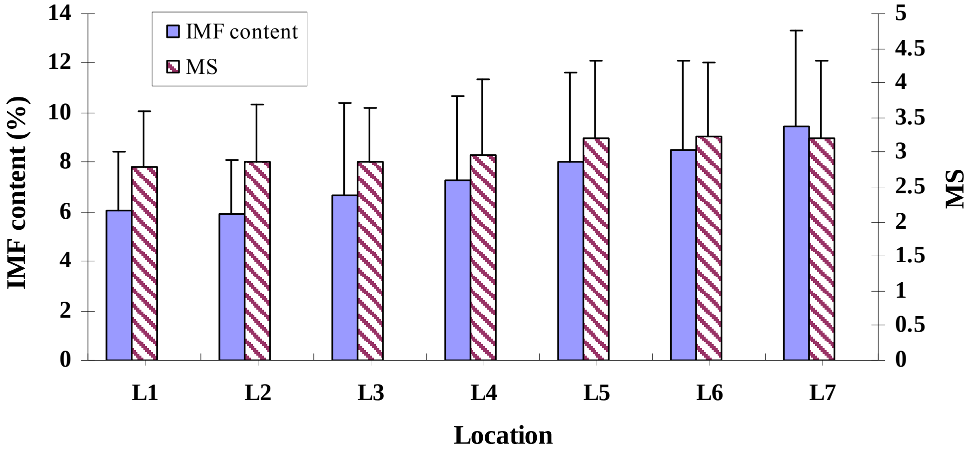

Figure 7.1 Distribution of IMF content and MS along the *Longissimus dorsi*.

7.4.2 Correlation coefficient between FL1 and FL*i*, ML1 and ML*i*

The correlation coefficients (*R*) between IMF content or MS at L1 and L*i* (*i* = 0, 2, 3 … 7) are shown in Table 7.3. The IMF content and MS at the last rib showed a tightest correlation (*R*(**FL1**, **FL0**) = 0.91, **R**(**ML1**, **ML**) = 0.88) with the average IMF content (**FL0**) and MS (**ML0**) of the whole measured loin chop, respectively. Thus, the locations L1 could be exploited as a possible predictive site for its reasonable correlation with the mean IMF content and MS. From location L2 to L7, tight correlation was observed between **FL1** and IMF content of loins at other ribs**,** while highest correlation was obtained between IMF content at L1 (**FL1**) and L4 (**FL4**), as well as L1 (**FL1**) and L5 (**FL5**). The best correlation for marbling score was found between **ML1** and **ML6**, while other high correlation coefficient was found between **ML1** and **ML5**, and **ML1** and **ML7**.

Table 7.3 Correlation coefficients between IMF content or MS of loin at the last rib and other ribs and the average value of whole loin joint.

Trait	L1-L2	L1-L3	L1-L4	L1-L5	L1-L6	L1-L7	L1-L0
IMF content (%), **FL**	0.85	0.84	0.90	0.90	0.85	0.83	0.91
Marbling score, **ML**	0.76	0.64	0.75	0.83	0.85	0.82	0.88

7.4.3 Cross validation of linear and quadratic models

The results of cross validation based on 10000 different subsets were listed in Table 7.4 and Table 7.5 in terms of mean, standard deviation, minimum (min), and maximum (max) of *Rc* and *Rv*, respectively.

Table 7.4 Cross validation of regression model based on IMF content (FL1-FL*i*, *i* = 0, 2, 3 …7).

(a) Linear regression model

Model	Trait	Mean	STD	Min	Max
FL1-FL0	*Rc*	0.91	0.05	0.63	0.98
	pc	<0.0001	<0.001	<<0.0001	<0.01
	Rv	0.88	0.10	0.04	1.00
	pv	<0.05	<0.05	<<0.0001	<0.5
FL1-FL2	*Rc*	0.87	0.12	0.01	0.98
	pc	<0.01	<0.05	<<0.0001	<1.00
	Rv	0.86	0.14	0.07	1.00
	pv	<0.05	<0.5	<<0.0001	1.00E+00
FL1-FL3	*Rc*	0.88	0.07	0.60	0.98
	pc	<0.001	<0.001	<<0.0001	<0.05
	Rv	0.81	0.14	0.02	1.00
	pv	<0.05	<0.1	<<0.0001	<0.5
FL1-FL4	*Rc*	0.90	0.04	0.69	0.98
	pc	<0.0001	<0.001	<<0.0001	<0.01
	Rv	0.88	0.09	0.17	1.00
	pv	<0.05	<0.05	<<0.0001	<1.00
FL1-FL5	*Rc*	0.89	0.06	0.54	0.97
	pc	<0.001	<0.001	<<0.0001	<0.05
	Rv	0.86	0.12	0.02	1.00
	pv	<0.05	<0.1	<<0.0001	<1.00
FL1-FL6	*Rc*	0.83	0.09	0.25	0.97
	pc	<0.01	<0.05	<<0.0001	<0.5
	Rv	0.81	0.16	0.20	1.00
	pv	<0.05	<0.1	<<0.0001	<1.00
FL1-FL7	*Rc*	0.84	0.11	0.25	0.94
	pc	<0.01	<0.05	<<0.0001	<0.5
	Rv	0.76	0.19	0.02	1.00
	pv	<0.05	<0.5	<<0.0001	<1.00

(b) Quadratic regression model

Model	Trait	Mean	STD	Min	Max
FL1-FL0	*Rc*	0.93	0.05	0.64	0.99
	pc	<0.0001	<0.001	<<0.0001	<0.01
	Rv	0.86	0.13	0.02	1.00
	pv	<0.05	<0.05	<<0.0001	<0.5
FL1-FL2	*Rc*	0.87	0.13	0.32	0.98
	pc	<0.01	<0.05	<<0.0001	<0.5
	Rv	0.87	0.14	0.01	1.00
	pv	<0.05	<0.05	<<0.0001	<0.5
FL1-FL3	*Rc*	0.82	0.08	0.45	0.97
	pc	<0.01	<0.01	<<0.0001	<0.1
	Rv	0.78	0.17	0.01	1.00
	pv	<0.05	<0.5	<<0.0001	<1.00
FL1-FL4	*Rc*	0.90	0.04	0.67	0.98
	pc	<<0.0001	<0.0001	<<0.0001	<0.01
	Rv	0.81	0.16	0.18	1.00
	pv	<0.05	<0.5	<<0.0001	<1.00
FL1-FL5	*Rc*	0.91	0.05	0.53	0.98
	pc	<0.0001	<0.0001	<<0.0001	<0.01
	Rv	0.81	0.16	0.03	1.00
	pv	<0.05	<0.5	<<0.0001	<1.00
FL1-FL6	*Rc*	0.86	0.09	0.32	0.98
	pc	<0.01	<0.01	<<0.0001	<0.5
	Rv	0.79	0.16	0.21	1.00
	pv	<0.05	<0.1	<0.0001	<0.5
FL1-FL7	*Rc*	0.84	0.11	0.30	0.98
	pc	<0.01	<0.05	<<0.0001	<0.5
	Rv	0.75	0.21	0.01	1.00
	pv	<0.5	<0.5	<<0.0001	<1.00

Table 7.5 Cross validation of regression model based on MS (ML1-ML*i*, *i* = 0, 2, 3 …7).

(a) Linear regression model

Model	Trait	Mean	STD	Min	Max
ML1-ML0	*Rc*	0.88	0.04	0.62	0.98
	pc	<0.0001	<0.001	<<0.0001	<0.05
	Rv	0.87	0.10	0.01	1.00
	pv	<0.05	<0.1	<<0.0001	<1.00
ML1-ML2	*Rc*	0.75	0.08	0.32	0.94
	pc	<0.01	<0.05	<<0.0001	<0.5
	Rv	0.73	0.17	0.01	0.99
	pv	<0.1	<0.5	<<0.0001	1.00
ML1-ML3	*Rc*	0.63	0.08	0.22	0.87
	pc	<0.05	<0.05	<0.0001	<0.5
	Rv	0.66	0.15	0.02	0.99
	pv	<0.5	<0.5	<<0.0001	<1.00
ML1-ML4	*Rc*	0.73	0.08	0.03	0.92
	pc	<0.01	<0.05	<<0.0001	<1.00
	Rv	0.74	0.16	0.01	0.98
	pv	<0.1	<0.5	<0.0001	<1.00
ML1-ML5	*Rc*	0.83	0.05	0.52	0.94
	pc	<0.001	<0.01	<<0.0001	<0.05
	Rv	0.82	0.12	0.24	0.99
	pv	<0.05	<0.1	<<0.0001	<1.00
ML1-ML6	*Rc*	0.84	0.05	0.49	0.96
	pc	<0.001	<0.01	<<0.0001	<0.1
	Rv	0.83	0.12	0.21	0.99
	pv	<0.05	<0.05	<<0.0001	<1.00
ML1-ML7	*Rc*	0.81	0.05	0.54	0.92
	pc	<0.001	<0.01	<<0.0001	3.08E-02
	Rv	0.80	0.12	0.03	1.00
	pv	<0.05	<0.1	<<0.0001	<1.00

(b) Quadratic regression model

Model	Trait	Mean	STD	Min	Max
ML1-ML0	*Rc*	0.90	0.04	0.61	0.98
	pc	<0.0001	<0.001	<<0.0001	<0.05
	Rv	0.88	0.10	0.01	1.00
	pv	<0.05	<0.1	<<0.0001	<1.00
ML1-ML2	*Rc*	0.77	0.08	0.37	0.95
	pc	<0.01	<0.01	<<0.0001	<0.5
	Rv	0.72	0.17	0.01	0.99
	pv	<0.1	<0.5	<<0.0001	<1.00
ML1-ML3	*Rc*	0.66	0.08	0.23	0.90
	pc	<0.05	<0.05	<<0.0001	<0.5
	Rv	0.65	0.15	0.04	0.98
	pv	<0.5	<0.5	<0.0001	<1.00
ML1-ML4	*Rc*	0.79	0.08	0.09	0.93
	pc	<0.01	<0.05	<<0.0001	<1.00
	Rv	0.76	0.16	0.01	0.99
	pv	<0.1	<0.5	<<0.0001	<1.00
ML1-ML5	*Rc*	0.86	0.05	0.52	0.96
	pc	<0.001	<0.01	<<0.0001	<0.05
	Rv	0.83	0.13	0.30	1.00
	pv	<0.05	<0.1	<<0.0001	<1.00
ML1-ML6	*Rc*	0.90	0.05	0.57	0.98
	pc	<0.001	<0.001	<<0.0001	<0.05
	Rv	0.84	0.13	0.30	1.00
	pv	<0.05	<0.05	<<0.0001	<1.00
ML1-ML7	*Rc*	0.83	0.05	0.57	0.94
	pc	<0.001	<0.01	<<0.0001	<0.05
	Rv	0.79	0.12	0.30	0.99
	pv	<0.05	<0.1	<0.0001	<1.00

7.4.3.1 Cross validation based on IMF content

In Table 7.4(a), all the mean of *Rc* for linear model was equal to or higher than 0.83, and almost all of the mean of *Rv* was higher than 0.80 except *Rv* in model of **FL1-FL7**, which was between 0.75 and 0.80. The linear model between **FL1** and **FL0** produced the best result in cross validation, with *Rc* of 0.91 and *Rv* of 0.88, which indicated the strong predictive ability of **FL1** for the mean IMF content of the whole loin. Linear models of **FL1-FL0**, **FL1-FL2**, **FL1-FL4**, and **FL1-FL5** gave good results with both *Rc* and *Rv* higher than 0.85, while linear models of **FL1-FL3** and **FL1-FL6** produced results with *Rc* and *Rv* higher than 0.81. All the mean of *pc* and *pv* for linear model was lower than the confidence level of 0.05, which implied that the built linear models **FL1-FL*i*** (***i*** = 0, 2, 3 …7) were significant in confidence level of 0.05. This demonstrated that the IMF content at the 2nd last to the 7th last ribs and the average of IMF content of the whole loin chop could be predicted from the IMF content at the last rib by linear regression. **FL0**, **FL2**, **FL3**, **FL4, FL5** and **FL6** could be explained well by **FL1**.

STD of all the models was lower than 0.15, while most of the models gave STD of *Rc* lower than 0.10, except model **FL1-FL2** (STD (*Rc*) = 0.12) and **FL1-FL7** (STD (*Rc*) = 0.11). The STD of *Rv* in linear models of **FL1-FL0**, **FL1-FL2**, **FL1-FL3**, **FL1-FL4**, and **FL1-FL5** was lower than 0.15. The results of STD (*Rc*) and STD (*Rv*) suggested that linear models **FL1-FL0**, **FL1-FL2**, **FL1-FL3**, **FL1-FL4**, and **FL1-FL5** showed good robustness, amongst which model **FL1-FL0** and **FL1-FL4** had the best robustness. The STDs of *Rv* in models of **FL1-FL6** (STD (*Rv*) = 0.16) and **FL1-FL7** (STD (*Rv*) = 0.19) suggested that the repeatability of linear model for **FL6** and **FL7** should be improved.

In Table 7.4(b), the mean of *Rc* for all the quadratic models was higher than 0.80 as well as linear model, while the *Rv* for models **FL1-FL0**, **FL1-FL2**, **FL1-FL4** and **FL1-FL5** was higher than 0.80, the *Rv* of models of **FL1-FL3**, **FL1-FL6**, and **FL1-FL7** scattered between 0.75 and 0.80. The quadratic model of **FL1-FL0** presented best result in cross validation of quadratic models, with mean *Rc* of 0.93 and mean *Rv* of 0.86, while model of **FL1-FL2** performed well following with both *Rc* and *Rv* equaled to 0.87. All the mean *pc* and *pv* for quadratic model was lower than 0.05, which indicated that the established quadratic models were appropriate in confidence level of 0.05. These results implied the possibility of using **FL1** to predict **FL0** and **FL2** to **FL7** based on quadratic model. **FL1** showed strong explanation ability for **FL0**, **FL2**, **FL4**, and **FL5** in quadratic model as well as in linear model.

The STD of *Rc* in quadratic models was not larger than 0.08 with exception of **FL1-FL2** (STD (*Rc*) = 0.13) and **FL1-FL7** (STD (*Rc*) = 0.11). The STDs of *Rv* in quadratic models of **FL1-FL3**, **FL1-FL4**, **FL1-FL5**, **FL1-FL6** and **FL1-FL7** were higher than 0.15. It was suggested that quadratic models of **FL1-FL0** and **FL1-FL2** showed good robustness, while the stability of other models need to be improved.

Both linear model and quadratic models performed well. As shown in Table 7.4(a) and (b), the IMF content in the grading sites L1 and L2 showed the best and the most stable correlation coefficient with the mean IMF content of the whole loin in both types of models. In addition, **FL4** was more related to **FL1**. These results indicated that the IMF content at the last rib could be considered as reliable predictor for mean IMF content of the whole loin. The IMF content at the last rib could be considered as possible predictive sites for the IMF content at the other ribs. In the study of Faucitano *et al.* (2004), IMF content at the 3rd /4th last rib was recommended for predicting sites for the average IMF content of loin from the 5th thoracic to the 4th lumbar ribs.

Comparing linear models to quadratic models (Table 7.4(a) and (b)), the overall differences between mean *Rc* and corresponding *Rv* of most models in Table 7.4(b) were similar to the one in Table 7.4(a). This implied that the linear model had similar stability with quadratic model. The robustness of models suggested that linear model has better repeatability than quadratic model especially at L3, L4, and L5. The quadratic model **FL1-FL2** was slightly better than linear model **FL1-FL2**. Because the linear model is more practical, the linear model was recommended.

7.4.3.2 Cross validation based on MS

In Table 7.5(a), the linear models of **ML1-ML0**, **ML1-ML5**, **ML1-ML6**, and **ML1-ML7** performed well with both mean *Rc* and *Rv* higher than 0.80. All the mean *pc* of linear models was lower than 0.05, while the mean *pv* of models of **ML1-ML2** and **ML1-ML4** was slightly higher than 0.05, and *pv* of **ML1-ML3** was higher than 0.10. This indicated that the linear models of **ML1-ML0**, **ML1-ML5**, **ML1-ML6**, and **ML1-ML7** were appropriate considering the results of cross validation. The STDs of *Rc* in linear models of **ML1-ML0**, **ML1-ML5**, **ML1-ML6** and **ML1-ML7** were lower than or equal to 0.05, while the STD of mean *Rv* was lower than or equal to 0.12. This indicated that the linear models of **ML1-ML0**, **ML1-ML5**, **ML1-ML6**, and **ML1-ML7** had good repeatability. It was indicated that there was linear relationship between **ML1** and **ML0**, **ML5**, **ML6**, and **ML7**. More work is needed to improve the predicting ability of **ML1 for ML2**, **ML3**, and **ML4**.

In Table 7.5(b), the quadratic models of **ML1-ML0**, **ML1-ML4**, **ML1-ML5**, **ML1-ML6**, and **ML1-ML7** performed well with both *Rc* and *Rv* higher than or equal to 0.79. All the mean *pc* of quadratic models was lower than 0.05, while the mean *pv* of models of **ML1**-**ML4** was slightly higher than 0.05, and *pv* of **ML1**-**ML2** and **ML1**-**ML3** was around 0.10. This suggested that the quadratic models of **ML1**-**ML2**, **ML1**-**ML3**, and **ML1**-**ML4** were not stable. All the STDs of *Rc* in quadratic models were lower than or equal to 0.08, while the STD of *Rv* in models of **ML1**-**ML0**, **ML1**-**ML5**, **ML1**-**ML6**, and **ML1**-**ML7** was not larger than 0.13. Considering the significance and robustness, the quadratic models of **ML1**-**ML0**, **ML1**-**ML5**, **ML1**-**ML6**, and **ML1**-**ML7** were appropriate for MS prediction at different ribs.

As shown in Table 7.5 (a) and (b), both linear model and quadratic models based on **ML1** performed well for prediction of **ML0**, **ML5**, **ML6**, and **ML7**. Besides **ML0**, **ML6** showed stronger relationship to **ML1**. This indicated that the MS at the last rib could be used for prediction of mean MS of the whole loin and MS at L5, L6, and L7. Both linear and quadratic regression models of **ML1** for **ML2**, **ML3**, and **ML4** need to be improved to get better accuracy and stability especially for **ML3** and **ML4**. L3 and L4 are the main sites that are used to assess marbling. In the study of Faucitano *et al.* (2004), the correlation coefficient between MS at different ribs and the mean MS of the whole longissimus muscle from the 5th thoracic to the 4th lumbar ribs was lower than the coefficient for IMF content as well as in this study. It was revealed that the MS at the 3rd /4th last rib was proper as a predicting site for the average MS of the whole loin.

Comparing each pair of *Rc* and *Rv* in linear and corresponding quadratic regression model at the same rib sets (Table 7.5 (a) and (b)), both *Rc* and *Rv* in quadratic model were higher than corresponding linear model for **ML1**-**ML0**, **ML1**-**ML4**, **ML1**-**ML5**, and **ML1**-**ML6**. Increase of ≥ 0.02 of *Rc* and decline of 0.01 of *Rv* were obtained in quadratic models to linear models of **ML1**-**ML2**, **ML1**-**ML3**, **ML1**-**ML4**. Almost all the mean *pc* and mean *pv* of quadratic models were lower than the ones of corresponding linear models. It was implied that for **ML5** to **ML7** and **ML0**, quadratic model performed better than linear model for prediction of marbling score using **ML1**.

7.4.4 Regression analysis

Both linear and quadratic regression models for prediction of IMF content and MS were tested by ANOVA. The subsets for calibration and validation were selected randomly from the 10000 sets of cross validation. Table 7.6 shows the result of ANOVA of the

Table 7.6 ANOVA test of regression models based on IMF content of loin at the last rib (FL1-FL*i*, *i* = 0, 2, 3 …7).

(a) Linear model

Depandant variable	*a0*	*a1*	Rc^2	Rv^2	Source	Pr > F (*p*-value)	Significance
FL0	-0.535	1.293	0.85	0.84	**FL1**	<0.0001	Significant (S.S.)
FL2	1.662	0.753	0.81	0.83	**FL1**	<0.0001	S.S.
FL3	-3.171	1.815	0.91	0.84	**FL1**	<0.0001	S.S.
FL4	-1.114	1.427	0.86	0.84	**FL1**	<0.0001	S.S.
FL5	-1.105	1.535	0.83	0.81	**FL1**	<0.0001	S.S.
FL6	0.901	1.389	0.87	0.82	**FL1**	<0.0001	S.S.
FL7	-0.478	1.478	0.83	0.75	**FL1**	<0.0001	S.S.

(b) Quadratic model

Depandant variable	*a0*	*a1*	*a2*	Rc^2	Rv^2	Source	Pr > F (*p*-value)	Significance
FL0	6.72	-0.862	0.135	0.93	0.80	**FL1×FL1**	<0.01	S.S.
FL2	7.382	-1.091	0.126	0.81	0.89	**FL1×FL1**	<0.01	S.S.
FL3	2.611	0.085	0.108	0.95	0.90	**FL1×FL1**	<0.05	S.S.
FL4	4.108	-0.223	0.111	0.91	0.92	**FL1×FL1**	<0.05	S.S.
FL5	6.367	-0.567	0.120	0.88	0.85	**FL1×FL1**	<0.05	S.S.
FL6	9.943	-1.622	0.186	0.87	0.87	**FL1×FL1**	<0.01	S.S.
FL7	12.000	-2.137	0.229	0.84	0.83	**FL1×FL1**	<0.01	S.S.

linear (Eq. 7.1) and quadratic (Eq. 7.3) regression models of IMF content at 2nd to 7th rib and the whole loin chop. Determination coefficients of calibration (Rc^2) and validation (Rv^2) were listed. It was indicated that the built linear models of IMF content at L0 and L2 to L7 based on IMF content at L1 were significant.

Terms of proposed linear (Eq. 7.2) and quadratic models of MS (Eq. 7.4) prediction at 2nd to 7th rib and the whole loin chop were analyzed by ANOVA and the results were listed in Table 7.7. Table 7.7(a) showed that the **ML1** significantly ($P < 0.05$) affected the variation of **ML2** to **ML7** and **ML0**, i.e. the **ML*i*** (***i*** = 0, 2, 3 …7) could be predicted by **ML1** and the built model was appropriate. The models of **ML1**-**ML2** and

Table 7.7 ANOVA test of regression models based on MS of loin at the last rib (ML1-ML*i*, *i* = 0, 2, 3 …7).

(a) Linear model

Dependant variable	*a0*	*a1*	Rc^2	Rv^2	Source	Pr > F (*p*-value)	Significance
ML0	0.172	1.049	0.83	0.74	**ML1**	<0.0001	S.S.
ML2	0.631	0.885	0.77	0.70	**ML1**	<0.0001	S.S.
ML3	1.425	0.61	0.62	0.57	**ML1**	<0.0005	S.S.
ML4	0.068	1.153	0.74	0.70	**ML1**	<0.0001	S.S.
ML5	-0.068	1.268	0.83	0.78	**ML1**	<0.0001	S.S.
ML6	-1.192	1.308	0.82	0.82	**ML1**	<0.0001	S.S.
ML7	0.177	1.171	0.81	0.76	**ML1**	<0.0001	S.S.

(b) Quadratic model

Dependant variable	*a0*	*a1*	*a2*	Rc^2	Rv^2	Source	Pr > F (*p*-value)	Significance
ML0	2.502	-0.531	0.258	0.91	0.80	**ML1×ML1**	<0.05	S.S.
ML2	2.622	-0.582	0.248	0.68	0.64	**ML1×ML1**	<0.5	N.S.S.
ML3	-0.956	1.527	-0.092	0.66	0.45	**ML1×ML1**	<0.5	N.S.S.
ML4	4.968	-2.848	0.634	0.86	0.85	**ML1×ML1**	<0.05	S.S.
ML5	3.752	-1.663	0.527	0.84	0.83	**ML1×ML1**	<0.05	S.S.
ML6	3.213	-1.269	0.410	0.83	0.83	**ML1×ML1**	<0.05	S.S.
ML7	4.535	-2.305	0.570	0.82	0.78	**ML1×ML1**	<0.05	S.S.

ML1-ML3 showed lower accuracy than other models. In Table 7.7(b), the quadratic models of **ML1-ML2** and **ML1-ML3** were not significant in confidence level of 5%, i.e. the predictive ability of these two models was not strong. Significant quadratic models of **ML1-ML2** and **ML1-ML3** could be obtained with low accuracy of *Rc* and *Rv* around 0.58 could be obtained. More work should be conducted to establish models of **ML1-ML2** and **ML1-ML3** with better predictive ability.

7.5 Conclusion

In this study, the aptitude of intramuscular fat content or marbling score of the loin at the last rib for prediction of corresponding attributes of loins at the other located sites, and the whole section of loin was investigated. The linear and quadratic regression analysis and cross validation were conducted on prediction of IMF content as well as MS. The results indicated that both linear regression and quadratic regression based on IMF content at the last rib showed strong explanation for IMF content at the 2nd last to the 7th last rib and the whole loin, while both linear regression and quadratic models performed well for all the measured sites. It was indicated that intramuscular fat content of the loin at the last thoracic rib of pig was efficient as a predictor for IMF content of the whole loin chop and loin at other ribs, ranging from the 2nd last to the 7th last. For prediction based on the MS at the last rib, both linear and quadratic models performed well for prediction of MS at the 5th last, the 6th last, the 7th last rib and the whole loin. Both linear and quadratic regression models based on the MS at the last rib did not show strong explanation ability for MS at the 2nd last, the 3rd last, and the 4th last rib. The explanation accuracy and repeatability for MS at the 2nd last, the 3rd last, and the 4th last rib need to be improved. It was concluded that marbling score of the loin at the last thoracic rib of pig was efficient as a predictor for marbling score of the whole loin chop and loin at the 5th last, the 6th last, and the 7th last rib.

Although there was a great variation of intramuscular fat content and marbling score along the *Longissimus dorsi* of pigs, there is great potential to predict the IMF content and MS of the whole loin and the ones at specific location using the IMF content and MS of the loin at the last rib.

Further work will focus on improving the predictive accuracy for MS at the 2nd last, the 3rd last, and the 4th last rib, exploring efficient and non-destructive method for evaluation of IMF and marbling of the loin at the different ribs in pigs.

CONNECTING TEXT

The results in Chapter 7 indicated that intramuscular fat content and marbling score of pork at the last rib was closely correlated to the fat attributes of pork at the anterior ribs, including the 3rd /4th last ribs. The intramuscular fat content and marbling score in Chapter 7 were determined using conventional methods. The potential of hyperspectral imaging for non-destructive detection of fat attributes of pork was demonstrated in Chapters 3, 5, and 6. It is of interest to study the variation of intramuscular fat content and marbling score of pork using NIR images of rib end instead of the conventional methods. Chapter 8, which serves as an extension to Chapter 7, deals with the sixth objective of the thesis: to investigate the possibility of using NIR images of rib end to non-destructively evaluate intramuscular fat content and marbling score of pork loins at different ribs along the longissimus muscle.

This manuscript has been submitted for publication to Food Control. This chapter is co-authored by my supervisor Dr. M.O. Ngadi, a research associate Dr. L. Liu, and a researcher Dr. C. Gariépy from Agriculture and Agri-Food Canada. The format of the original manuscript has been modified to remain consistent with the thesis format. All the literature cited in this chapter is listed in Chapter 10.

VIII. ASSESSMENT OF INTRAMUSCULAR FAT CONTENT AND MARBLING SCORE OF PORK USING NIR HYPERSPECTRAL IMAGERIES OF RIB END

8.1 Abstract

The purpose of this study was to investigate the possibility of rapid and non-destructive determination of intramuscular fat (IMF) content and marbling score (MS) of pork of the 6 last ribs using hyperspectral images of rib end. Near infrared (NIR) hyperspectral imaging system (900-1700 nm) was used for image acquisition of rib ends. NIR image of round rib-end of the loin was acquired. Pattern analysis techniques including Gabor filter, grey-level co-occurrence matrix (GLCM), and wide line detector (WLD) were applied to process hyperspectral images. Image features including spectral feature, texture-spectral feature, texture feature, and line feature were extracted. The first derivative of raw mean spectra and Gabor filtered mean spectra was studied as well. The first derivative of Gabor filtered mean spectra from image of rib end showed strongest predictive potential for attributes at all 6 ribs. The first derivative of Gabor filtered mean spectra was selected as the optimal feature for prediction of both IMF content and MS at different ribs. Multiple linear regression (MLR) was exploited to build prediction models. Leave-one-out cross validation was used to test the robustness of established models. All the 12 MLR models showed good performance with correlation coefficient of calibration (*Rc*) $\geq$ 0.90, correlation coefficient of cross validation (*Rcv*) $\geq$ 0.87, correlation coefficient of prediction (*Rp*) ≥ 0.81 for IMF content at all 6 ribs and *Rc* ≥ 0.94, *Rcv* ≥ 0.88, *Rp* ≥ 0.89 for the marbling score at all 6 ribs. The model for IMF content at the 2^{nd}/ 3^{rd} last rib led to the best prediction result with *Rc* of 0.96, of *Rcv* of 0.95, *Rp* of 0.83, and with root mean square error of calibration (*RMSEc*) of 0.65%, root mean square error by cross validation (*RMSEcv*) of 0.93%, and with root mean square error of prediction (*RMSEp*) of 0.79%. The model for marbling score at the last/ 2^{nd} last rib led to the best prediction result with *Rc* of 0.99, *Rcv* of 0.99, *Rp* of 0.96, *RMSEc* of 0.08, *RMSEcv* of 0.18, and *RMSEp* of 0.04. These promising results indicated the powerful potential of pattern analysis technique-processed hyperspectral images of rib ends for detection of IMF content and marbling score of pork of the 6 last ribs.

Keywords: Rib end; Intramuscular Fat Content; Marbling Score; Sampling Locations; Pattern Analysis Technique; Gabor Filter; Multiple Linear Regression

8.2 Introduction

The fat level in fresh pork mainly refers to technological quality attributes of intramuscular fat (IMF) content and marbling score (MS). Intramuscular fat (IMF) content is defined as the total amount of scattered flecks of fat within the meat muscle. Marbling is the visible intermingling of fat with lean in a muscle (Qiao *et al.*, 2007c). Fat level of pork influences the cooking quality of pork (flavor and juiciness, etc.) and eating satisfaction of consumers, even health issue. Different levels of IMF content and MS of fresh pork lead to different acceptance from consumers in specific destinations (Brewer *et al.*, 2001; Bryhni *et al.*, 2003; Fortin *et al.*, 2005). Non-invasive and rapid detection of fat levels in pork would allow commercial cuts to be classified and assigned to the retailers or further processors exactly according to the specific markets, by which handling costs could be saved.

Unfortunately, the conventional measurement of pork IMF content involved extraction of lipid using chemical solvent, which is time consuming and harmful to environment. Since fat extraction-based IMF prediction is not suitable for fast and non-destructive detection, random sampling would be necessary to evaluate the average intramuscular fat level of pork products, which makes it impossible to measure large amount of samples. An efficient and non-destructive assessment system is urgently needed for the pork industry to determine the IMF content effectively.

Marbling of pork is normally scored subjectively by visual assessment of size, number and distribution of fat flecks and it is parameterized as marbling score (MS) (Jeremiah, 1998).The traditional assessment of marbling score is carried out with marbling standards from National Pork Producers Council (NPPC) (NPB, 2002). Subjective evaluation of MS is labor intensive and not suitable for real-time detection. It would be beneficial for the pork industry to develop an objective, accurate and economical method for predicting MS of pork.

Previous studies have emphasized the capability of near-infrared (NIR) spectroscopic methods for prediction of IMF content/ MS of pork (Prevolnik *et al.*, 2005; Barlocco *et al.*, 2006; Savenije *et al.*, 2006; Wang and Paliwal, 2007; Prieto *et al.*, 2009). However, the limited spatial field of view provided by spectroscopic technique would affect the result easily by the selection of detected areas, especially when IMF is scattered in the whole piece of pork heterogeneously. As an upgrading of spectroscopic method, hyperspectral imaging technique can provide spectral information of each pixel within an image as well as spatial information of the pictured objects (Gowen *et al.*, 2007). Promising results in previous studies (Gowen *et al.*, 2007; Qiao *et al.*, 2007c; Liu *et al.*, 2010; Barbin *et al.*, 2012a; Barbin *et al.*, 2012b) indicated the potential of hyperspectral imaging to replace conventional determination method of pork quality. Due to the closed relation between fat and NIR spectra (Murray and Williams, 1987; Shenk *et al.*, 1992), it is advantageous to use NIR images as they offers information that is more detailed compared to images in the visible range.

The sampling location of referenced IMF content/ MS and collection site of hyperspectral image are the prerequisites in prediction of IMF content/ MS using NIR images. The 3rd /4th last ribs was suggested by Faucitano *et al.* (2004) as a representative grading site as of analytical determination of IMF content in pork and was adopted in several studies (Sather *et al.*, 1996; Suzuki *et al.*, 2005a; Fortin *et al.*, 2005). However, besides the 3rd /4th last ribs ribs, other sites amongst the 5 last ribs, including the last rib (Fernandez *et al*., 1999; Bahelka *et al*., 2009; Lo Fiego *et al*., 2010), the 2nd /3rd last ribs (Lakshmanan *et al*., 2012), and the 10th rib (Witte *et al*., 2000; Lonergan *et al*., 2007; Rincker *et al.*, 2008), were used in previous studies as well. The large variation of IMF content along the *Longissimus dorsi* makes it necessary to investigate the non-invasive assessment of IMF content at the 5 last ribs. For image analysis, the 5 last ribs along the *Longissimus dorsi* should be used as the imaging site for IMF content prediction. However, the dissection of loin joint for determination of IMF content would increase labor requirement in the process With contrast to the other anatomical sites, imaging using rib end of the *Longissimus dorsi* would be easier, and increase the labor work of counting, therefore increases the practicality of image-based assessment of IMF content. Hence, to evaluate IMF content along the *Longissimus dorsi* using hyperspectral image of rib end is indeed a big step towards real-time quality control of pork.

As of marbling score, the sampling site of subjective marbling assessment is confined to be the 3rd / 4th last ribs by NPPC (NPB, 2002). Huang *et al.* (2012) exploited pattern analysis techniques to analyze digital RGB images to predict MS at the 3rd / 4th last ribs. Technique wide line detector (WLD) obtained determination accuracy over 0.90. However, the loss of the loin at the 3rd / 4th last ribs in practice will still introduce waste for the pork industry even the evaluation was conducted by non-destructive RGB photographing. The success prediction of MS at the different last ribs using image of rib end will make it possible to render individual determination for each loin. On the other hand, aligning with the pork industry's current processing practices, the assessment of

IMF content and MS could be carried out simultaneously using only NIR images of one rib end, which would raise the efficiency of quality inspection of pork dramatically.

Despite the comprehensive potential of hyperspectral imaging for food quality control, proper image processing technique should be applied to extract useful information as enormous data is provided by hyperspectral images (Geladi *et al*., 2004; Gowen *et al*., 2007; Williams *et al*., 2009; Prats-Montalbán *et al*., 2011). Recently, pattern analysis techniques become more and more popular in analysis of hyperspectral image and were demonstrated to be effective for application in pork quality control (Qiao *et al.,* 2007c; Liu *et al.,* 2010; Liu *et al.,* 2012; Barbin *et al*., 2012a). Texture pattern recognition techniques including grey-level co-occurrence matrix (GLCM) and Gabor filter were used for marbling assessment (Qiao *et al.,* 2007c) and pork quality classification (Liu *et al.,* 2010), respectively. Liu *et al.* (2012) applied line pattern recognition technique wide line detector (WLD) in pork marbling evaluation. Different levels of marbling were classified successfully. Effective image processing techniques could enhance the prediction ability of hyperspectral images (Grahn and Geladi, 2007).

Based on the introduction above, the aim of the present study was to study whether pattern analysis techniques-processed hyperspectral images of rib ends could be used to determine IMF content and MS at the several last ribs. Specific objectives are to:

(1) study which pattern analysis techniques amongst GLCM, Gabor filter, and WLD is the most effective technique for analysis of NIR hyperspectral images (900-1700 nm) for prediction of IMF content and MS at the 6 last ribs along the *Longissimus dorsi*,

(2) identify the key wavelengths linked to IMF content and MS at different sampling locations,

(3) build multiple linear regression (MLR) models for quantified determination of IMF content and MS at different ribs using hyperspectral image of rib ends.

8.3 Materials and methods

8.3.1 Sample preparation

In this study, 24 pigs were slaughtered at a local commercial slaughterhouse. A wide range of variation for IMF content and marbling levels along *Longissimus dorsi* was approached by feeding pigs with different levels of fat resources. The loin joint of *Longissimus dorsi* at 24 h post-mortem was dissected from pigs, packed in refrigerated boxes and transported to laboratory of Hyperspectral Imaging, McGill University, Montreal, QC, Canada. To cover the interested location of the 5 last thoracic ribs as mentioned in above, the whole loin joint numbered from the 7th last thoracic rib to posterior (rib end) (Figure 8.1(a)) was sliced along ribs to six rib chops as shown in Figure 8.1(b). Each loin was then fabricated into boneless pork loins. The trimmed loin was packed in vacuum plastic bag right away for image acquisition and analytical measurement. Pork chops at different sampling sites were denoted as L1, L2, L3, L4, L5, and L6 correspondingly as described in Figure 8.1. In total, 144 loin samples (24 pigs×6 chops = 144 loins) were collected. There were 6 groups (L*i*, *i* = 1, 2, 3 …6) of samples with 24 samples in each group.

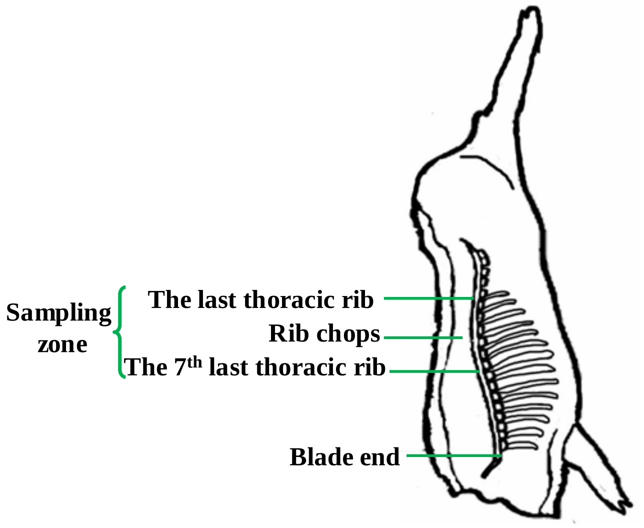

(a) Sampling zone

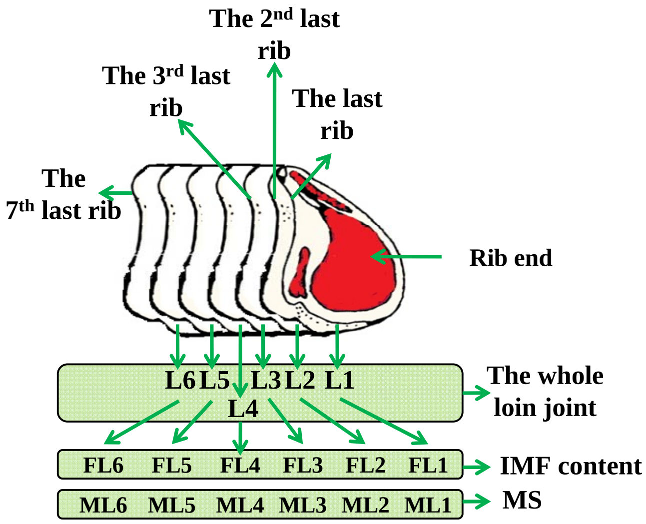

(b) Dissection scheme of the rib chops

Figure 8.1 Dissection scheme of the *Longissimus dorsi*.

8.3.2 Hyperspectral imaging system and image acquisition

A hyperspectral line scanning system was built, which is composed of following components: (1) a spectrograph (Headwall Photonics Inc. USA), (2) a cooled InGaAs camera with extremely short integration time of 2 ms, (3) a conveyer (Donner Mfg. Corp., USA), (4) two tungsten halogen lamps (50 W) which were placed at angle of 45° to provide illumination, (5) a sample holder with a wood board above, (6) and an enclosure. The system covers wavelengths from 900 to 1700 nm with a spectral resolution of 4.8 nm. Hence, 167 wave bands ((1700-900)/ 4.8 = 167) were obtained for each sample.

Pork sample at L1 was placed on the wood board with rib end upward toward the camera. The object distance between the lens and rib end being imaged was set at 21 cm. When the conveyer moved on with a trial-to-error defined speed, the pork entered the camera's field of view, i.e. frame, and rib end was scanned line by line. The captured lines were dispersed into the spectral and spatial matrices and then were projected onto InGaAs camera. Images of every 8 frames were averaged for calculating the output signal. After scanning on a rib end, an output *hypercube* of 350 pixels× 320 pixels× 167 wave bands (spatial dimension (x) × spatial dimension (y) × spectral dimension (λ)) was constructed. From this *hypercube*, NIR image at wave band 900-1700 nm or NIR spectrum of each pixel within the image could be obtained.

Image correction using a bright field reference and a dark image was applied on raw hyperspectral images. The dark image was used to remove the effect of dark current produced by the InGaAs camera. The reference image and dark image were used to transform the raw reflected light intensity to percent reflectance so that the difference of light intensity could be eliminated. Thus, the pixel values within each image range from 0 to 1. The calibrated images were the basis for the subsequent image analysis.

8.3.3 Analytical determination of IMF content/ MS

Marbling scores (MS) of pork chops were assessed by technicians using NPPC standard charts (NPB, 2002). The assessment was held at room temperature (19-24 ℃). MS of two surfaces of each pork slice was evaluated. The average MS value of two surfaces was used as the referenced MS value of the corresponding loin. MS at six different slice locations (L*i*, *i* = 1, 2, 3 …6) from one loin joint were denoted as **ML*i***, ***i*** = 1, 2, 3 … 6.

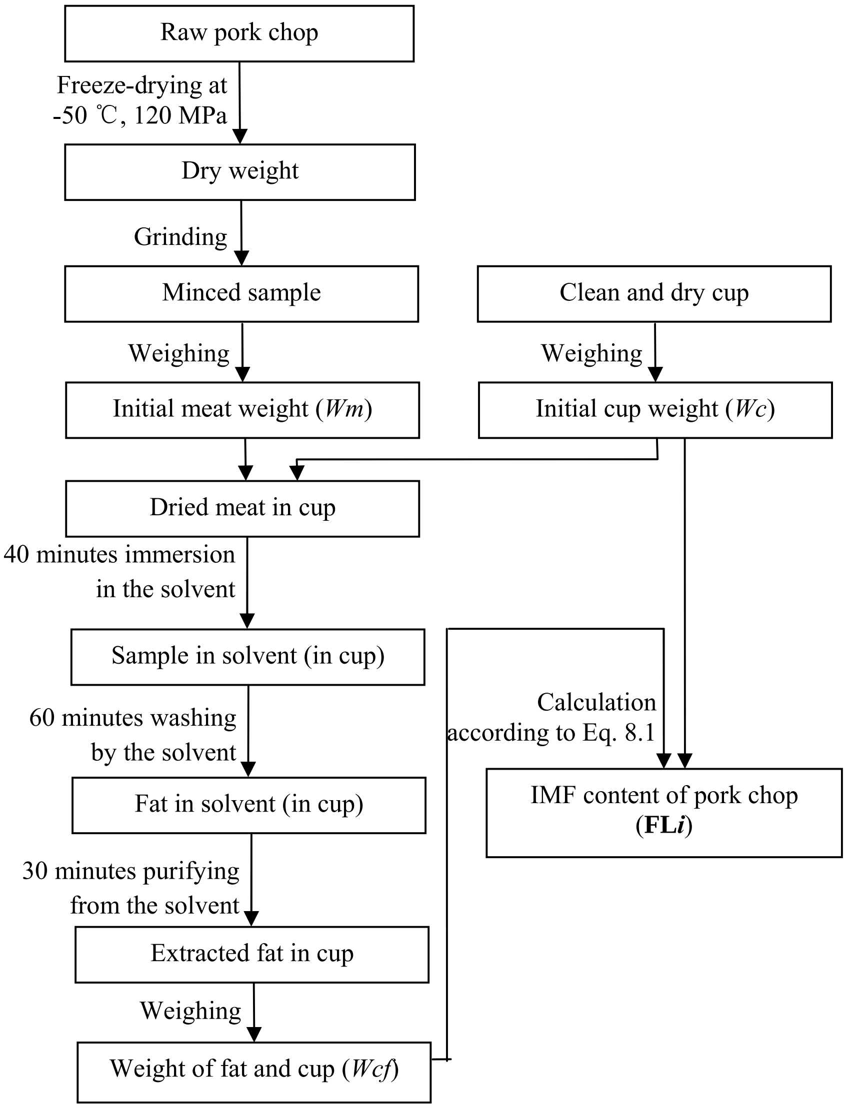

Figure 8.2 Protocol of conventional determination of IMF content.

Right after evaluation of MS, the samples were then packed and stored in the deep-freezer at -80 ℃ for 24 hours for the determination of IMF content. Total lipid of each rib end was extracted and purified with petroleum ether (solvent) following the procedure illustrated in Figure 8.2. IMF content of each rib site (**FL*i***, ***i*** = 1, 2, 3 … 6) was expressed as percentages of total crude fat content in dry weighted potk (Eq. 8.1).

$$FLi(\%) = \frac{Wcf(g) - Wc(g)}{Wm(g)} \times 100\%, \qquad (8.1)$$

8.3.4 Pattern analysis technique-assisted image processing

The corrected images were used for image processing and multivariate analysis (Figure 8.3). All operations of image processing and multivariate analysis in this study were performed using programs written and run in MATLAB 7.3.0 (The MathWorks, Inc., Mass., USA).

8.3.4.1 Image segmentation

The precision of image segmentation would affect the subsequent data analysis, as it is the basis of image processing. The main purpose of image segmentation was to isolate the interested meat part from the background and the residual adhering fat as well as the connective tissue after bone removal. The selected loin part was defined as the region of interest (ROI). In this study, ROI segmentation was operated automatically using the method described in Liu *et al.* (2012). For each *hypercube*, a binary mask was produced, in which value 1 corresponds to interested meat area, while value 0 corresponds to the abandoned other parts. By multiplying each pixel in the mask and corresponding pixel in NIR image in *hypercube*, the ROI of each rib end was isolated from original image. There were over 50,000 pixels in every ROI, which reduced the random error caused by limited field of view in contrast to normal spectroscopic detection. In the selected ROI, the relative reflectance of each pixel was recorded at wavelength from 900 to 1700 nm. Only

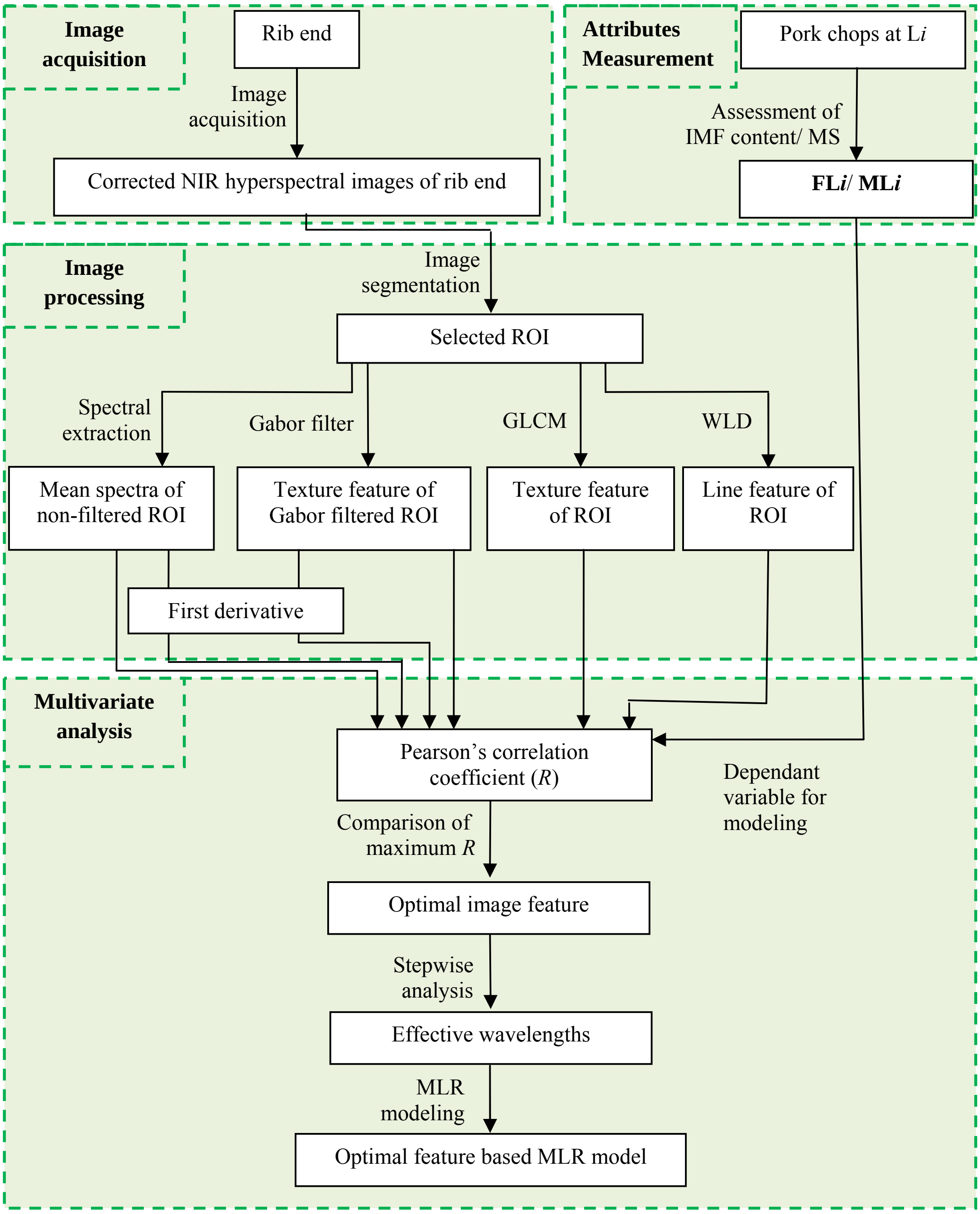

Figure 8.3 Procedure of data processing.

spectral images from 940-1650 nm were used for image processing, because of the low signal-to-noise ratio in the two ends of spectral range. Spectral properties, texture properties, and line properties of each rib end were extracted from ROI by following image processing.

8.3.4.2 Mean spectrum and the first derivative of non-filtered mean spectrum

The non-filtered reflectance mean spectrum (**MR**) was determined by averaging the reflectance value of all pixels in the raw ROI of rib end. The mean spectrum of each rib end was a 149 ×1 vector (Wave range/ spectral resolution + 1 = (1650-940 nm)/ (4.8 nm) + 1 = 149). In total, 144 mean spectra (940-1650 nm) representing all the imaged rib ends were recorded for attributes prediction.

The first derivative of non-filtered mean spectrum (**DMR**) was calculated according to Eq. 8.2.

$$DMR = \frac{MR_{i+1} - MR_i}{(i+1) - i} = MR_{i+1} - MR_i, \tag{8.2}$$

where i represents the i^{th} wave band, i = 1, 2, 3, … 148 (the wave range/ the spectral resolution of hyperspectral imaging system). MR_{i+1} and MR_i represents the value of mean reflectance in **MR** at $(i+1)^{th}$ and i^{th} wave band, respectively. The first derivative of mean spectrum was a 148×1 vector.

8.3.4.3 Gabor filter (GF) and first derivative of filtered mean spectra

Surface texture of rib ends refers to smoothness, roughness, bumpiness, tenderness, and color changes, etc. In the context of grey level images of rib end, texture is defined as the spatial variation in pixel intensities in grey level, which is represented by several statistics

(Tuceryan and Jain, 2010). Texture analysis has been used for measurement of the sensory, physical or chemical properties of pork using hyperspectral imaging (Qiao *et al.*, 2007c; Singh *et al.*, 2008; Liu *et al.*, 2010; Elmasry *et al.*, 2012a). In this case, an isotropic Gabor filter (GF1, Ma *et al.* 2002) and an oriented Gabor filter (GF2, Ma *et al.* 2002) modulated by Gaussian function were used to extract useful texture information to facilitate the prediction of pork IMF content and MS. Mean spectra from GF1-processed and GF2-processed ROI were recorded and denoted as **MG1** and **MG2**, respectively. The first derivatives of **MG1** and **MG2**, i.e. **DMG1** and **DMG2**, were calculated according to Eq. 8.2. For GF1, parameters f representing the frequency of the sinusoidal wave, σ representing the standard deviation of the Gaussian function were involved, while f, σ, and θ controlling the orientation of the filter were involved. **MG1**, **MG2**, **DMG1** and **DMG2** include texture and spectral information of images simultaneously.

8.3.4.4 Advanced grey-level co-occurrence matrix (GLCM)

Another widely used texture analyze tool is GLCM (Haralick, 1979). Normally GLCM is applied in regular-shaped processing area, in which limited information could be used and manual error would be introduced. To overcome this barrier, an improved GLCM was applied on the whole irregular-shaped ROI of rib end in this study. Texture index (**GM**) including *contrast*, *correlation*, *energy*, and *homogeneity* (Eq. 8.3-8.6) are derived from the advanced GLCM-produced co-occurrence matrix. This matrix is an eight-level square matrix, in which each entry ($P(i, j)$) corresponds to the occurrence frequency of the pixel pairs with offset of a certain direction (θ = 0°, 45°, 90°, or 135°) at a given distance (D).

$$Contrast = \sum_{i,j} (i-j)^2 P_{D,\theta}(i,j), \tag{8.3}$$

$$Correlation = \frac{\sum_{i,j} (ij) P_{D,\theta}(i,j) - \mu_i \mu_j}{\sigma_i \sigma_j}, \tag{8.4}$$

$$ASM = \sum_{i,j} \left[P_{D,\theta}(i,j) \right]^2, \tag{8.5}$$

$$Homogeneity = \sum_{i,j} \frac{P_{D,\theta}(i,j)}{1+(i-j)^2}, \tag{8.6}$$

where (i, j) is the coordination of the interested pixel in yield co-occurrence matrix $P_{D,\theta}$, μ_i, μ_j, σ_i, σ_j are the means and standard deviations, respectively, along the rows and columns in $P_{D,\theta}$. The determined **GM**s were used to express image texture for estimation of pork IMF content and marbling score.

8.3.4.5 Wide line detector (WLD)

WLD described in Liu *et al.* (2012) was applied to the ROI of hyperspectral images. The aim of WLD was to extract useful and helpful image line information from images of rib ends. There were three parameters of *r*, *t*, and *thresh* to define line features in ROI. Firstly, initial flerks with width under parameter r , and contrast to neighbor pixels above t were detected. Then, pixels in initial lines with value under $thresh$ were set to 1 and the others were set to 0. A binary mask was generated finally, in which channel 1 represented detected lines, while channel 0 represents other parts. The proportion of lines (**PL**) in the image was defined by Eq. 8.7.

$$PL = \frac{area(lines)}{area(ROI)}, \tag{8.7}$$

where *area(lines)* is the total number of pixels in detected lines in a rib end image, and *area(ROI)* is the total number of pixels in the corresponding ROI.

8.3.5 Multivariate analysis

To develop prediction models between extracted image features (149 wave bands, i.e. 149 variables) and measured IMF content/ MS at different ribs (**FL*i***, **ML*i***, ***i*** = 1, 2, 3 … 6), multivariate regression analysis was applied to select optimal image feature and vital wavelengths for modeling and to build the calibration model and validate the built calibration model. For each rib, 24 samples were separated to calibration set (Nc = 18 samples) and prediction set (Np = 6 samples).

Since four types of image features, i.e. spectral, texture-spectral, texture, line features, were extracted from NIR image of rib ends, selection of optimal image feature is necessary to determine the best feature for establishment of prediction models. Pearson's correlation coefficient described in Eq. 8.8 was applied to evaluate the linear dependence, i.e. correlation between different image features (X, 149×Nc matrix) and IMF content/ MS (Y, 1×Nc vector) at each rib (Rodgers and Nicewander, 1988). The calculated correlation coefficients (R, 149×1 vector, or 148×1 for first derivative of mean spectra) range from -1 to 1. It is redundancy and not practical to compare each single plot of R to select the optimal features and corresponding parameters of algorithms. Hence, maximum value of absolute correlation coefficient was adopted as a criterion of feature selection. For each feature, different parameter sets resulted different maximum values. Firstly, the peak of absolute correlation coefficient over 940-1650 nm between each feature and an attribute at each rib was calculated for each parameter sets ($max(|R|_{rib,\ feature,\ parameter})$). Following, the maximum value of correlation coefficient between each feature and the attribute at each rib ($max(|R|_{rib,\ feature})$) were selected to represent the feature for the corresponding rib. The corresponding parameter set of the feature was used. Finally, for each rib, the maximum value of each feature was used to compare with maximum values produced by other features at each rib. The feature produced the highest value ($max(|R|_{rib})$) was selected as the optimal feature for prediction of IMF content/ MS at the corresponding rib.

$$R(\lambda)=\frac{\sum_{i=1}^{n}(X_i(\lambda)-\overline{X(\lambda)})(Y_i-\overline{Y})}{\sqrt{\sum_{i=1}^{n}(X_i(\lambda)-\overline{X(\lambda)})^2}\sqrt{\sum_{i=1}^{n}(Y_i-\overline{Y})^2}}, \tag{8.8}$$

where λ is wavelength, $R(\lambda)$ is the calculated correlation coefficient at wavelength λ, X_i is a type of image feature for i^{th} sample, i.e. a 149×1 vector, $X_i(\lambda)$ is the image feature value at wavelength λ, Y_i is the measured IMF content/ MS of i^{th} sample. $\overline{X(\lambda)}$ is the average value of image feature of all n samples at λ, and $\overline{Y}$ is the mean value of IMF content/MS of all n samples.

After features and corresponding parameter sets were decided for prediction of **FL*i*/ ML*i*** (***i*** = 1, 2, 3 … 6), regression analysis should be applied to build prediction model. However, there were 149 variables available for modeling. The high dimensional data space from hyperspectral imaging may include influences of noise and useless wavelengths with no or little contribution in prediction, while prevent the application of the regression models from implement in multispectral imaging systems of pork. Thereby, to find several key wavelengths that are most essential on the attribute prediction, stepwise regression procedure described in Draper and Smith (1998) was carried out to identify optimal wavelengths.

Only features at the selected effective wavelengths (XK) were used for subsequent multiple linear regression (MLR) modeling (Eq. 8.9). MLR models were built using data from calibration sets. Leave-one-out cross validation was applied to fitted calibration models to test the robustness of built models. Once the regression model was determined, i.e. regression coefficients, were determined, the equation was used to evaluate data in corresponding prediction set.

$$\hat{Y} = a_0 + \sum_{i=1}^{i=k} a_i \times XK_i \text{ ,} \tag{8.9}$$

where k is the number of identified wavelengths, a_0 and a_i are the regression coefficients, and $\hat{Y}$ is the predicted IMF content/ MS at a specific rib.

To quantify the predictive ability of the models, statistical values including correlation coefficient (*R*) and root mean square error (*RMSE*) between measured values (Y) and estimated attribute values ($\hat{Y}$) of IMF content/ MS were calculated. The performance of MLR models were evaluated by following statistical values: *R* of calibration (*Rc*), *R* of cross validation (*Rcv*), *R* of prediction (*Rp*), *RMSE* of calibration (*RMSEc*), *RMSE* of cross validation (*RMSEcv*), and *RMSE* of prediction (*RMSEp*). A good model should have a high *Rc*, a high *Rcv*, a high *Rp*, a low *RMSEc*, a low *RMSEcv*, a low *RMSEp*, and small differences between *Rc* and *Rp*, and *RMSE*c and *RMSEp*.

For a set of images from rib ends, there were 6 sets of IMF content/ MS (Y) which can be explained, i.e. 12 models could be built simultaneously. The success establishment of linear relations between image feature from rib ends and IMF content/ MS at different ribs would enhance the efficiency of assessment of pork fat level effectively.

8.4 Results and discussion

8.4.1 Measured IMF content and MS

Measured values for IMF content (i.e. **FL*i***, ***i*** = 1, 2, 3 … 6) and MS (i.e. **ML*i***, ***i*** = 1, 2, 3 … 6) of total 24 pork loins at each rib location are depicted in Figure 8.4. Both IMF content and MS along the *Longissimus dorsi* showed increasing trend from L1 to L6 variation, while IMF content showed greater changes along the *Longissimus dorsi*. The range of values was wide for both IMF content and MS at each rib. The L3 showed widest range for IMF content while L5 showed widest range for MS. Larger variability presented in the reference data affect the robustness and stability of predictive models positively.

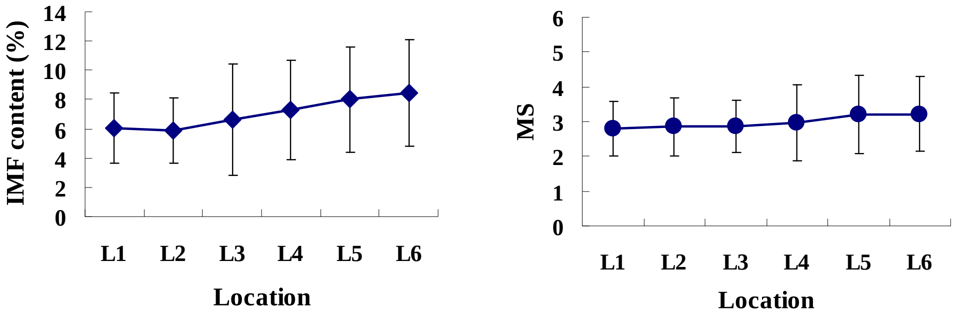

(a) IMF content (b) MS

Figure 8.4 Description of measured intramuscular fat (IMF) content and MS along the *Longissimus dorsi*.

8.4.2 Spectral features

The typical image of rib end, defined mask and corresponding ROI are shown in Figure 8.5. Surrounding fat and connective tissue were removed to insure the interested loin part was selected. Values in pixels in Figure 8.5(a) remains unchanged if the corresponding pixel in Figure 8.5(b) is marked white; otherwise, it is set to zero. By opening useful pixels and closing other pixels, the ROI of each image in *hypercube* was obtained as depicted in Figure 8.5(c).

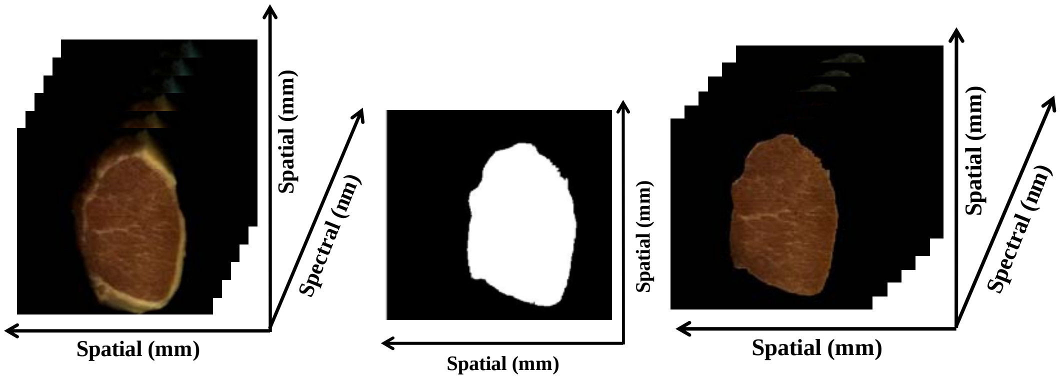

(a) Hyperspectral images (b) Mask for ROI (c) ROI

Figure 8.5 The hyperspectral images, mask and ROI of a rib end.

Each ROI was filtered by isotropic GF1 and four oriented GF2 along 0°, 45°, 90°, and 135°. Different parameters would be selected for IMF content/MS at different ribs by subsequent data analysis. Therefore, only one set of parameters of $f = 0.01$, $\sigma = 10$ was used to show typical figures of filtered ROI (Figure 8.6). Typical curves of spectral reflectance characteristics and the first derivative of mean spectra from raw ROI and Gabor filtered ROI, i.e. **MR**, **MG1**, **MG2**, **DMR**, **DMG1**, and **DMG2**, were depicted in Figure 8.7. The extracted reflectance curves and first derivatives of mean spectra of rib end were rather smooth across the entire spectral region. Both non-filtered and Gabor filtered spectra had one small reflectance peak around 1270 nm in addition to two high reflectance peak around 960 and 1060 nm. A small reflectance valley around 1200 nm is observed as well. Gabor filtered spectra had smaller scale than raw spectra. All the first derivatives of mean spectra had a small peak around 1040 nm and a large peak around 1140 nm. Inflections were observed at 1100 nm for all the plots of first derivatives of mean spectra, which were the results of reflectance peaks in plots of mean spectra.

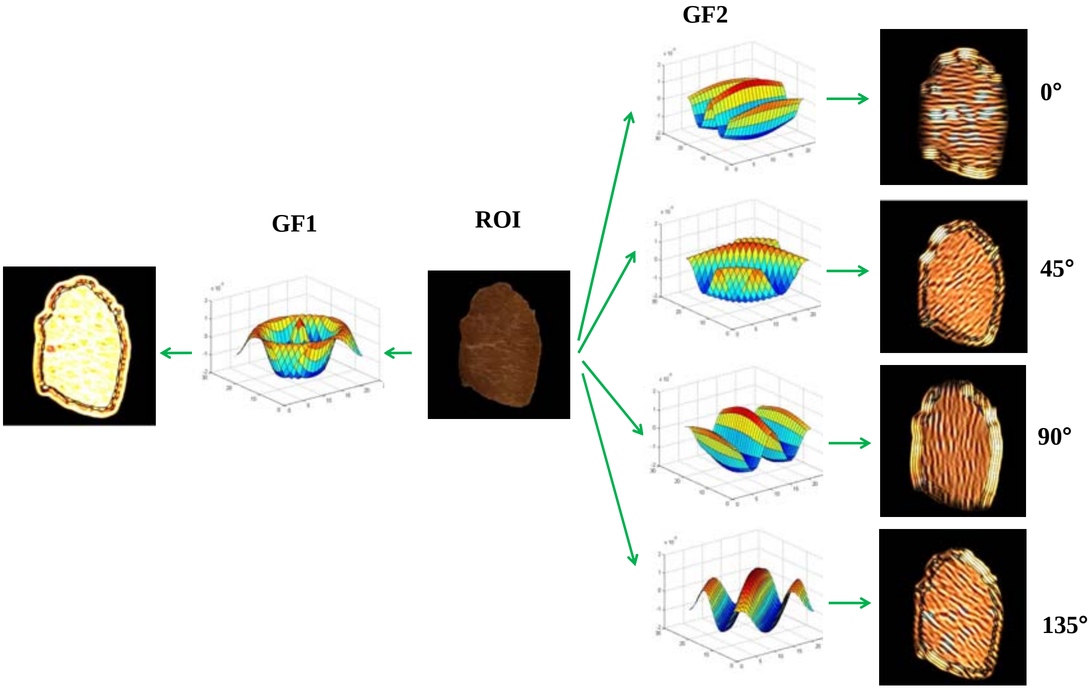

Figure 8.6 The ROI and Gabor filtered images.

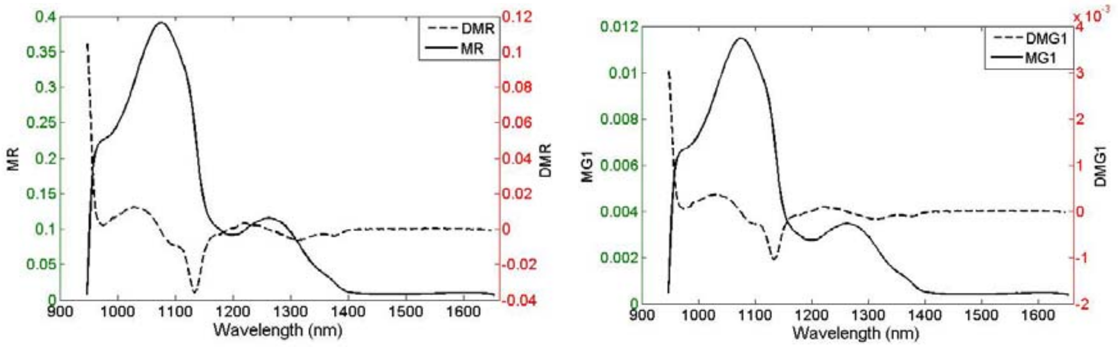

(a) **MR** and **DMR**

(b) **MG1** and **DMG1**

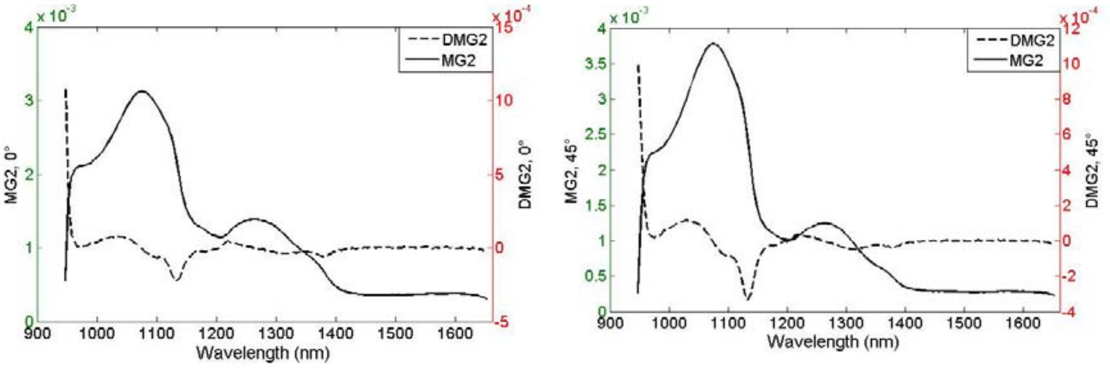

(c) **MG2** and **DMG2**, 0°

(d) **MG2** and **DMG2**, 45°

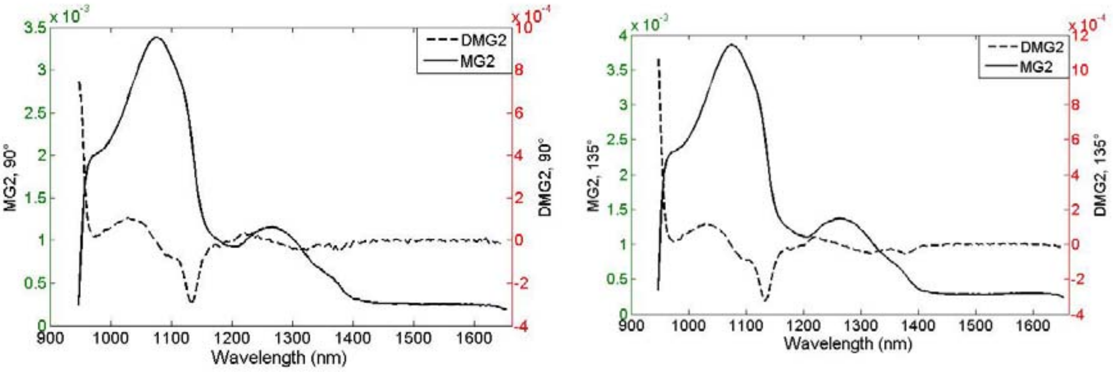

(e) **MG2** and **DMG2**, 90°

(f) **MG2** and **DMG2**, 135°

Figure 8.7 Typical curves of mean spectra and the first derivatives of mean spectra.

8.4.3 Texture features from GLCM

Since different parameters of GLCM were used for different ribs, only result by offset of D = 3 and θ = 45° is shown in Figure 8.8(a). The 8-level matrix was generated from image at 1230 nm of one rib end. The format of this image is 8-bit unsigned integer, i.e. the values in all pixels in the image were amongst 0 and 255. The range between the minimum and the maximum values was divided by eight. Each element in the GLCM matrix indicated the number of pairs of pixels in ROI existing amongst the corresponding two orthotropic levels. The mean values of four statistical measurements in different directions are depicted in Figure 8.8(b). Higher variation is observed for measurements *contrast* and *correlation* than *energy* and *homogeneity* along 4 directions. This could be explained by intrinsic characteristics of heterogeneity of pork meat. Mean *contrast* and *correlation* of rib ends were lower than the other two measurements, which indicated that measurement *contrast* contains low local variations in all directions and the tested rib ends had rough texture.

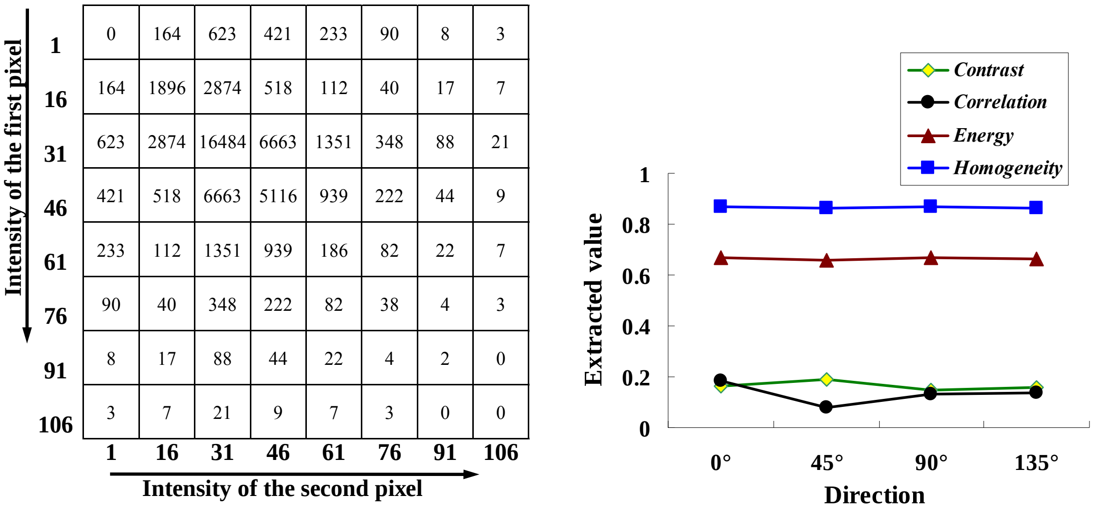

Intensity of the first pixel \ Intensity of the second pixel	1	16	31	46	61	76	91	106
1	0	164	623	421	233	90	8	3
16	164	1896	2874	518	112	40	17	7
31	623	2874	16484	6663	1351	348	88	21
46	421	518	6663	5116	939	222	44	9
61	233	112	1351	939	186	82	22	7
76	90	40	348	222	82	38	4	3
91	8	17	88	44	22	4	2	0
106	3	7	21	9	7	3	0	0

(a) GLCM matrix

(b) Mean values of four measurements along different directions

Figure 8.8 An example of GLCM matrix and mean values of four measurements along different directions.

8.4.4 Line features from WLD

The WLD was applied to all the ROI of rib ends and proportion of lines (**PL**) was calculated representing the line features of rib ends. Typical WLD response with $r = 15$, $t = 2$, and $thresh = 0.3$ of one rib end is shown in Figure 8.9. Low variation amongst wave band 945-1380 nm is observed, while high variation amongst wave band 1380-1650 nm is observed. The WLD was proposed for VIS image, which may affect its ability of extracting line features in NIR image. Larger differences between extracted line features in NIR images may be obtained by improving WLD to NIR region in future, which would affect predictive ability positively.

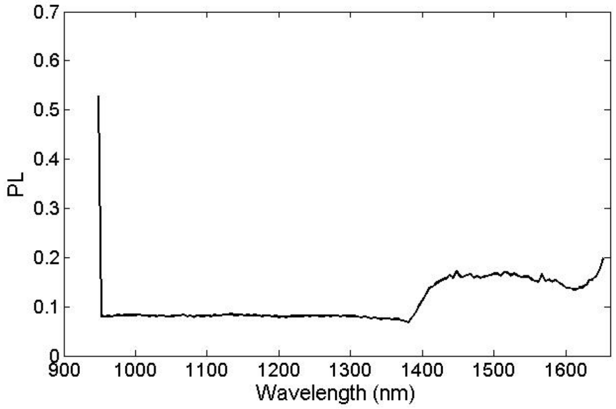

Figure 8.9 Typical calculated PL of one rib end.

8.4.5 Feature selection

For each rib, Pearson's correlation coefficients (R) between IMF content/ MS and different features from rib ends over whole wave band were calculated. Maximum values of correlation coefficient between IMF content/ MS and different features from rib ends are listed in Table 8.1. In Table 8.1(a), maximum correlation coefficients ($max(|R|_{rib, feature})$) between **FL*i*** (***i*** = 1, 2, 3 … 6) and feature **DMG2** obtained good result with minimum value of 0.87 and average value of 0.905. **DMR**, and **DMG1** indicated promising prediction ability with $max(|R|_{rib, feature}) > 0.80$ for **FL*i*** (***i*** = 1, 2, 3 … 6). **MR**, **MG1**, and **MG2** indicated lower predictive ability for **FL*i*** (***i*** = 1, 2, 3 … 6) with $max(|R|_{rib, feature}) <0.80$. **GM** of rib ends revealed good prediction ability for **FL*i*** at L3-L5 with $max(|R|_{rib, feature}) > 0.80$, while **PL** at L3 and L4 produced $max(|R|_{rib, feature}) > 0.80$. The result of **PL** indicated improvement of WLD for NIR image. It was indicated that **DMG2** extracted from rib ends has the best prediction ability for **FL*i*** (***i*** = 1, 2, 3 … 6).

In Table 8.1(b), possibility of prediction of **ML*i*** (***i*** = 1, 2, 3 … 6) using rib end image was revealed only by **DMG2** (Minimum $max(|R|_{rib, feature}) = 0.68$), while all the other feature gave correlation coefficient to **ML*i*** lower than 0.60. Considering the results in Table 8.1, **DMG2** was determined as the optimal image feature for prediction of IMF content/ MS at different ribs.

Typical plots of correlation coefficients between **FL*i***/ **ML*i*** (***i*** = 1, 2, 3 … 6) and feature **DMG2** are shown in Figure 8.10. Smooth plots were obtained for *R* between **FL*i*** (***i*** = 1, 2, 3 … 6) and **DMG2** in 940-1300 nm, while few noise is observed in 1300-1650 nm. Similar pattern is observed for all correlation coefficient between **FL*i*** (***i*** = 1, 2, 3 … 6) and **DMG2** with highest correlation coefficient around 1220 nm ($R \approx 0.90$) at all 6 ribs and correlation coefficient around 0.60 at 1120, 1200, and 1300-1400 nm. For *R* between **ML*i*** (***i*** = 1, 2, 3 … 6) and **DMG2**, peaks are observed around 970, 1070, and 1250 nm for all 5 ribs except **ML3**. Peaks around 1070, 1250, and 1480 nm are observed. Tough plots of *R* between **ML*i*** (***i*** = 1, 2, 3 … 6) and **DMG2** are observed which suggested that image preprocessing techniques could be applied for MS prediction in future.

Table 8.1 Maximum values of correlation coefficients between different features and IMF value/ MS at different ribs.

(a) IMF content

Feature / IMF content	MR	DMR	MG1	DMG1	MG2	DMG2	GM	PL
FL1	0.62	0.88	0.64	0.89	0.68	0.92	0.77	0.62
FL2	0.60	0.90	0.62	0.90	0.68	0.92	0.77	0.70
FL3	0.63	0.86	0.67	0.87	0.75	0.90	0.91	0.85
FL4	0.64	0.90	0.68	0.90	0.75	0.92	0.90	0.82
FL5	0.51	0.84	0.58	0.86	0.66	0.90	0.81	0.70
FL6	0.55	0.80	0.61	0.83	0.69	0.87	0.77	0.68

(b) MS

Feature / IMF content	MR	DMR	MG1	DMG1	MG2	DMG2	GM	PL
ML1	0.26	0.38	0.22	0.48	0.33	0.76	0.53	0.42
ML2	0.29	0.36	0.18	0.62	0.35	0.71	0.58	0.39
ML3	0.25	0.40	0.23	0.61	0.34	0.68	0.56	0.44
ML4	0.18	0.37	0.31	0.57	0.48	0.72	0.51	0.48
ML5	0.29	0.29	0.22	0.54	0.40	0.75	0.56	0.42
ML6	0.24	0.32	0.32	0.49	0.48	0.69	0.53	0.45

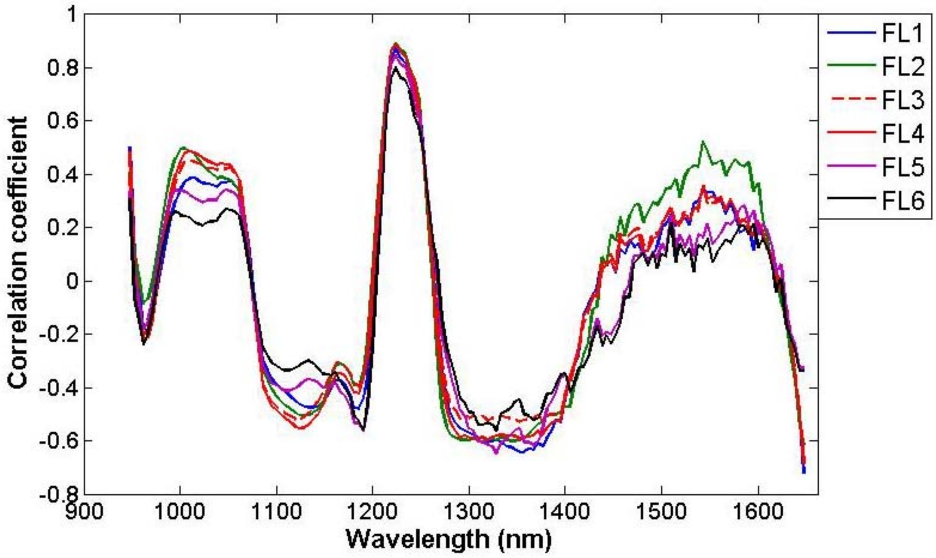

(a) IMF content

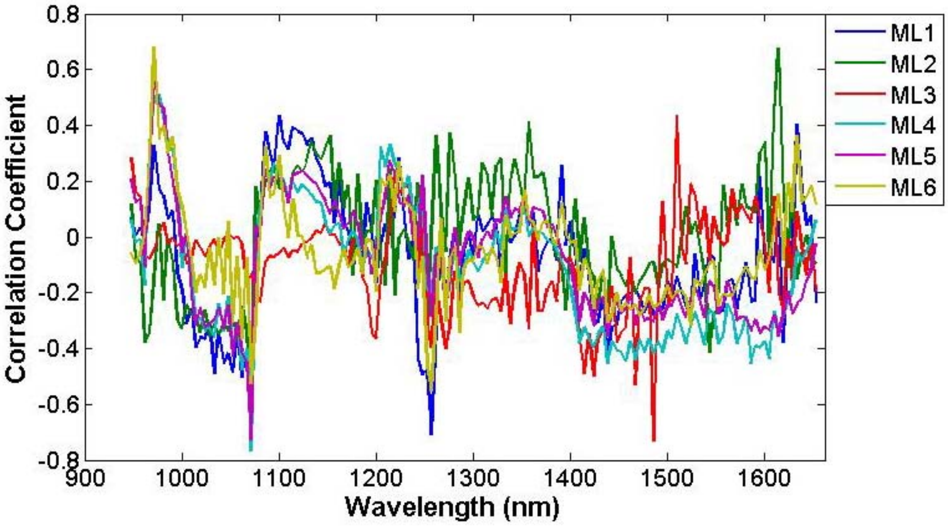

(b) MS

Figure 8.10 The correlation coefficients between IMF content/ MS at different ribs and DMG2 extracted from rib ends.

8.4.6 MLR models

8.4.6.1 Key wavelengths

For each rib, the texture-spectral feature **DMG2** which provided highest correlation coefficient to IMF content/ MS were used as the variables for prediction of corresponding attributes. Stepwise procedure was applied to the feature using optimal parameter set to simplify the independent variables to several vial wavelengths. The used key wavelengths for prediction of **FL*i*** and **ML*i*** (***i*** = 1, 2, 3 … 6) are listed in Table 8.2.

The ability of the NIR spectra-based feature for predicting fat levels in pork is based on the vibrational responses of chemical bonds including in the NIR region. Since composition of IMF in pork is lipid, the NIR spectra produced by the C-H stretch second overtones for fatty acids in 1100-1400 nm would explain the adoption of wavelengths in this range (1164, 1178, 1198, 1212, 1217, 1222, 1231, 1279, 1289, 1298, 1313, and 1346 nm) in Table 8.2(a) (Shenk *et al.,* 1992, Forrest *et al.,* 1997). Wavelengths around 1200 nm were used for prediction of IMF content at different ribs, i.e. 1217 nm was used for prediction of **FL1** by **DMG2**, 1212 nm was used for prediction of **FL2** by **DMG2**, and 1222 nm was used for prediction of **FL3** to **FL6** by **DMG2**. Wavelengths around 1600 nm including 1596, 1610, and 1625 nm were used as key wavelengths for **FL2**, **FL3**, **FL4**, and **FL5**. The characteristically spectra around 1600 nm region include main affect from the first overtone of C-H bonds, which are the main bonds in lipid molecule (Murray, 1986; Miller, 2001).

The main composition of marbling is lipid. The wavelengths selected around 1200 nm (1164, 1183, 1198, 1236, 1246 nm) in Table 8.2(b) could be explained by the tight relationship between lipid and NIR spectra. More wavelengths were selected for prediction of MS at most ribs comparing to IMF content. It is observed that wavelengths around 1400 nm were identified for all 6 ribs. Wavelengths 986 and 982 nm was used for **ML2** and **ML5**, respectively, which is due to the major absorbance bands of O-H bond at 970 nm (Murray and Williams, 1987).

Table 8.2 Optimal parameter sets of DMG2 and selected key wavelengths by stepwise.

(a) IMF content

FL*i*	Parameters			Key wavelengths (nm)
	σ	*f*	*θ*	
FL1	5	0.1	0°	1178, 1217, 1514
FL2	15	0.25	90°	1010, 1212, 1447, 1596
FL3	3	0.1	0°	1198, 1222, 1289, 1610
FL4	10	0.2	90°	1222, 1289, 1298, 1313, 1529, 1625
FL5	10	0.1	135°	1164, 1217, 1222, 1610
FL6	10	0.125	135°	1222, 1231, 1279, 1346, 1462

(b) MS

ML*i*	Parameters			Key wavelengths (nm)
	σ	*f*	*θ*	
ML1	15	0.125	45°	1044, 1087, 1102, 1198, 1370, 1375, 1433, 1442
ML2	10	0.2	45°	986, 1006, 1140, 1183, 1294, 1322, 1346, 1500
ML3	15	0.125	90°	1164, 1246, 1414, 1519, 962
ML4	15	0.125	0°	1260, 1294, 1423, 1505, 1620, 1625, 1644
ML5	15	0.125	135°	982, 1073, 1102, 1270, 1433, 1462, 1524, 1577
ML6	15	0.1	45°	1058, 1236, 1246, 1418, 1538

Different wavelengths were identified for IMF content and MS. The differences could be attributed to the basic differences between the conventional measurements of the two quality attributes (i.e. more chemical and more visual based).

8.4.6.2 Models and performance

The selected key wavelengths in Table 8.2 were used to build MLR models between the first derivative of Gabor filtered mean spectra at these wavelengths (*XK*) and the actual values of the attributes (*Y*). The training sets were used to develop the MLR models, after which the built models were cross validated. The predictive ability of models on independent samples were test by data in the prediction sets. Twelve optimal MLR models were obtained for evaluation of IMF content/ MS at the 6 last ribs. The built models and the corresponding performance of models are listed in Table 8.3. The accuracy of the MLR models are shown in Figure 8.11.

In Table 8.3(a), high correlation coefficients between predicted IMF content and measured IMF content in calibration set with *Rc* not lower than 0.90 are observed for all 6 ribs. Models for **FL2** and **FL6** performed well in training comparing to the other ribs, with *Rc* of 0.96 and 0.98, and *RMSEc* of 0.65% and 0.67%, respectively. Models for **FL3** and **FL4** produced good calibration results with *Rc* of 0.97 and 0.97, and *RMSEc* of 0.89% and 0.85%, respectively. The good robustness of calibration models for **FL*i*** (***i*** = 1, 2, 3 … 6) was demonstrated by the good results of cross validation with *Rcv* ≥ 0.87 for all 6 ribs. Best cross validation result is observed for **FL2** with a high *Rcv* of 0.95 and a low *RMSEcv* of 0.93%. The test results by prediction sets, i.e. *Rp* ≥ 0.81 for all 6 ribs, indicated that built MLR models have great potential to predict IMF content of future independent samples. MLR model for prediction of **FL3** produced best validation result with a high *Rp* of 0.90 and a low *RMSEp* of 0.92%, while MLR model for prediction of **FL2** showed good accuracy with a low *RMSEp* of 0.97%.

As indicated by both Table 8.3(a) and Figure 8.11(a), IMF content at all 6 ribs could be predicted accurately and rapidly by the first derivative of Gabor filtered mean spectra which were extracted from the NIR hyperspectral image of rib ends. Considering the results of both correlation coefficient and root mean square error, MLR models for prediction of **FL2** and **FL3** showed best predictive ability and stability, while cross validation result of **FL2**-predicted model indicated best repeatability. This is attributed to the effective wavelength identification and the alleviation of colinearity and overfitting in MLR models. Considering that sampling sites of the 5 last ribs were used in previous study, the successful prediction of IMF content at the 6 last ribs using image of rib end indicated the promising future of Gabor filter-assisted NIR image of rib end for real time and economical detection of pork IMF content in practice.

In Table 8.3(b), minimum valued and maximum value of 0.88 and 0.99 are observed in range of *Rc*, *Rcv*, and *Rp*, which suggested the great predictive ability of **DMG2**-based MLR models for prediction of MS at different ribs. Stable MLR model with best predictive ability and best robustness is observed for prediction of **ML1** with high *Rc*, *Rcv*, *Rp* of 0.99, 0.99, 0.96, and low *RMSEc*, *RMSEcv*, *RMSEp* of 0.08, 0.18, 0.04, followed by **ML3**, with *Rc*, *Rcv*, *Rp* of 0.95, 0.94, 0.97, and *RMSEc*, *RMSEcv*, *RMSEp* of 0.18, 0.25, 0.13. As shown in Figure 8.11 (b), all the models showed high predictive accuracy as the estimated MS value and actual MS value scattered along the ideal prediction lines compactly. The promising result of **ML3** suggested the great potential of using Gabor filter-processed image of rib end to measure MS of pork instead of using the pork at the 3rd / 4th last rib. In addition, MS at the other sampling locations beside L3 could be assessed rapidly and non-destructively as well if there is a need in practice.

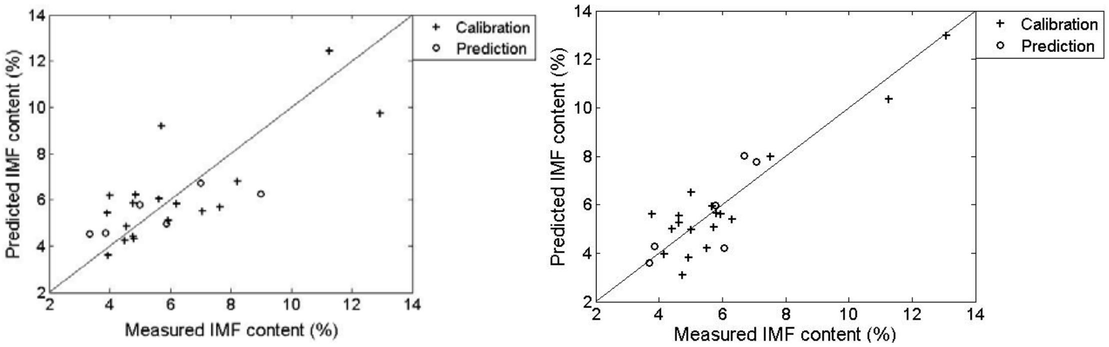

(a-1) **FL1** (a-2) **FL2**

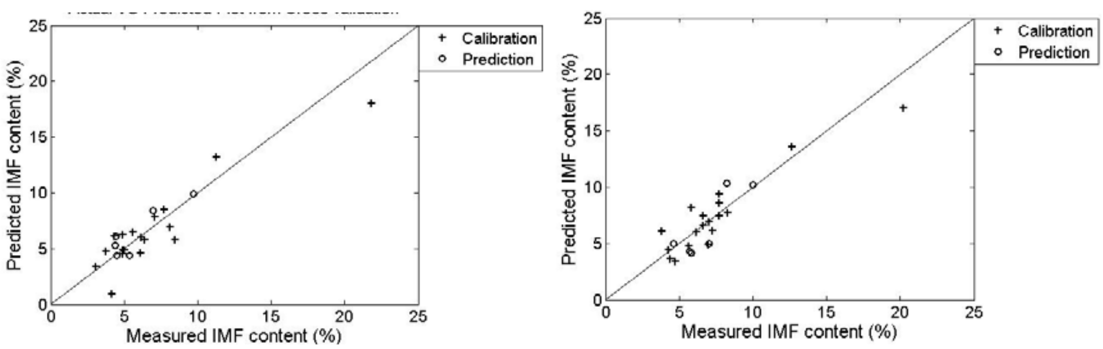

(a-3) **FL3** (a-4) **FL4**

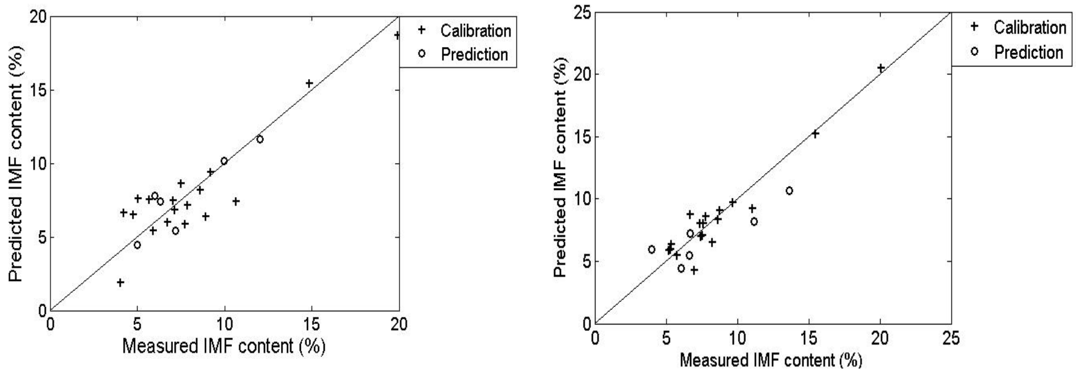

(a-5) **FL5** (a-6) **FL6**

(a) IMF content

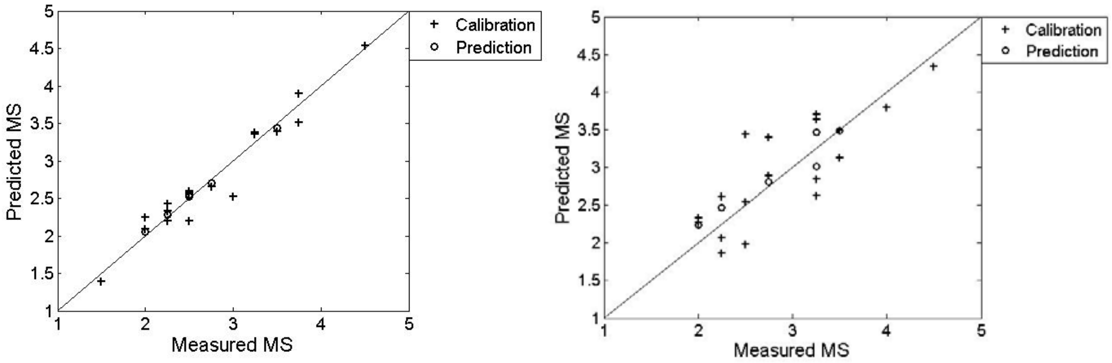

(b-1) **ML1** (b-2) **ML2**

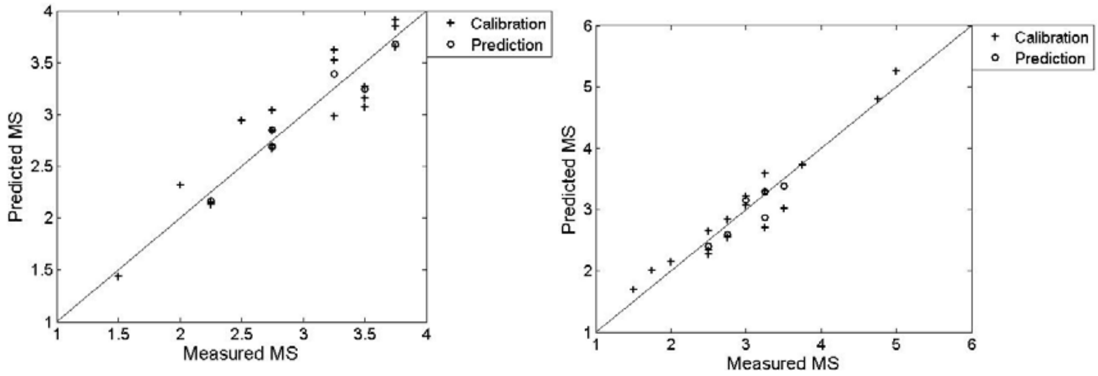

(b-3) **ML3** (b-4) **ML4**

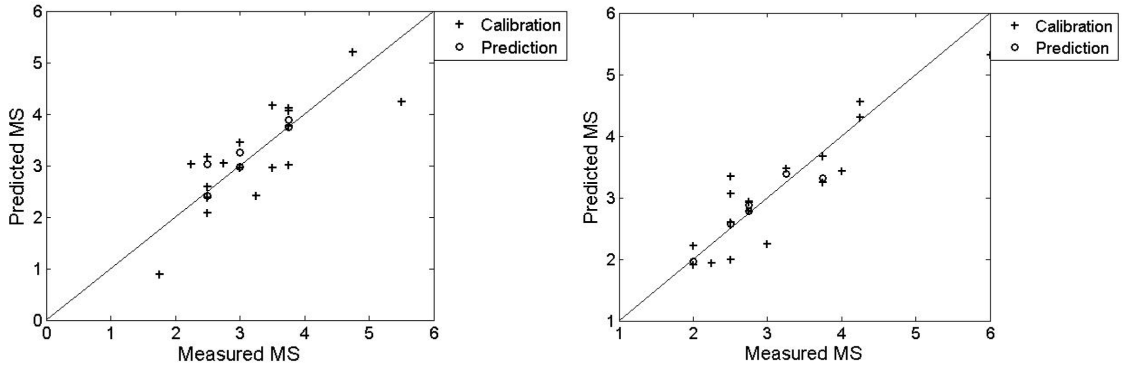

(b-5) **ML5** (b-6) **ML6**

(b) MS

Figure 8.11 Measured and predicted IMF content/ MS for calibration and prediction sets at different ribs.

Table 8.3 MLR models and performance for predicting IMF content/ MS at different ribs.

(a) IMF content

FL*i* (%)	Regression coefficients	Calibration		Cross validation		Prediction	
		Rc	*RMSEc*	*Rcv*	*RMSEcv*	*Rp*	*RMSEp*
FL1	1.644, -3546.759, 121452.949, 104983.968	0.90	1.10	0.87	1.56	0.81	1.32
FL2	3.239, -49717.124, 377044.241, 324159.829, 70668.465	0.96	0.65	0.95	0.93	0.83	0.97
FL3	5.127, 24306.020, 30441.751, 21282.249, 134283.443	0.97	0.89	0.97	1.64	0.90	0.92
FL4	2.021, 674650.929, 396847.337, -5995.125, -105822.737, -775471.098, 249241.775	0.97	0.85	0.96	1.41	0.87	1.45
FL5	2.402, 181417.035, 88613.303, 399690.64361794, -598401.836	0.95	1.21	0.93	1.65	0.90	1.16
FL6	7.686, 384278.539, 200272.139, 435340.141, 184927.366, -209025.877	0.98	0.67	0.97	1.09	0.88	1.78

(b) MS

ML*i*	Regression coefficients	Calibration		Cross validation		Prediction	
		Rc	*RMSEc*	*Rcv*	*RMSEcv*	*Rp*	*RMSEp*
ML1	5.963, -320465.293, -135753.453, -52484.877, 235174.305, 95137.834, -106568.543, 174179.817, -97110.456	0.99	0.08	0.99	0.18	0.96	0.04
ML2	3.268, -174998.243, -71824.478, -46859.179, 163841.090, 81380.519, 98142.759, -89884.792, -27562.161	0.96	0.19	0.92	0.42	0.96	0.17
ML3	1.115, 25008.233, 107444.322, -205818.339, -149799.576, -123895.113	0.95	0.18	0.94	0.25	0.97	0.13
ML4	2.625,163123.945, -26289.098,172041.651, 196623.896, -270188.539, -384056.000, 118384.726	0.98	0.14	0.98	0.25	0.89	0.17
ML5	2.561, 74522.337, 118505.930, 25947.971, 53611.476, -111959.963, 110308.529, -487133.034, -104220.799	0.94	0.30	0.88	0.59	0.91	0.21
ML6	3.841, -161129.006, 104052.211, -154670.725, -191408.998, -96293.245	0.95	0.30	0.93	0.43	0.94	0.20

In both Table 8.3 and Figure 8.11, the MLR models produced promising performance for prediction of both IMF content and MS at the 6 last ribs, i.e. 2 attributes at 6 different sampling locations along the *Longissimus dorsi* could be evaluated by several NIR images of one rib end.

8.5 Conclusion

This study investigated the possibility of using pattern analysis technique-processed NIR hyperspectral images of pig rib end for non-destructive and fast prediction of IMF content and marbling score at the 6 last ribs. Pattern techniques Gabor filter, GLCM, and WLD were applied and compared. The first derivative of Gabor filtered mean spectra of rib end was suggested as the optimal feature for prediction of both IMF content and MS at different ribs. MLR models were established between the first derivative of Gabor filtered mean spectra at selected key wavelengths and the measured IMF content/ MS at different sampling sites amongst the 6 last ribs along *Longissimus dorsi*. All MLR models showed good performance with $Rc \geq 0.90$, $Rcv \geq 0.87$, $Rp \geq 0.81$ for IMF content at all 6 ribs and $Rc \geq 0.94$, $Rcv \geq 0.88$, $Rp \geq 0.89$ for MS at all 6 ribs. The first derivative of Gabor filtered mean spectra of rib end showed strongest predictive ability for IMF content at the 2nd/3rd last rib, while it showed strongest predictive ability for MS at the last/ 2nd last rib. The MLR models demonstrated big potential for prediction of both IMF content and MS at the last 3rd/4th rib, which was suggested as the sampling location for conventional determination of corresponding attributes.

The promising results in this study make it possible to identify fat levels of pork using the images of rib end instead of pork chops along *Longissimus dorsi*. More samples would be studied to validate the predictive accuracy for IMF content and marbling score at different ribs using Gabor filter-processed NIR images of rib end.

IX. GENERAL SUMMARY AND CONCLUSIONS

9.1 General summary and conclusions

Research conducted previously demonstrated the promising potential of hyperspectral imaging in inspection of quality and safety of food. However, as for the intramuscular fat level of pork, limited research work was found. In this thesis, two fat attributes of pork, i.e. intramuscular fat content and marbling score were evaluated using hyperspectral and digital image analysis. The variation of intramuscular fat content along the longissimus ribs was studied. The effect of freezing and thawing on image-based prediction of intramuscular fat level of pork were also investigated. The studies demonstrated the potential of measuring pork fat level non-invasively and rapidly through image analysis.

The near-infrared spectral image analysis of pork at the 3rd / 4th last rib was conducted for pork marbling detection. Comparing to wide line detector, image-processing technique Gabor filter appeared to be more effective in characterizing marbling score from NIR images of pork. The application of wide line detector in NIR area was indicated to be limited.

An extended study was conducted to predict marbling scores of pork by extracting representative textural or line features from RGB images. The performance of wide line detector in RGB images was drastically enhanced compared to NIR images. It was concluded that pork marbling could be detected successfully as a line pattern from RGB images.

The NIR hyperspectral image-assisted quantification of intramuscular fat content of intact pork at the 3rd /4th last ribs indicated that algorithm of averaging spectra was effective as Gabor filter on the evaluation of the intramuscular fat content of pork. Based on the conclusion, the distribution map of intramuscular fat content in pork was developed using mean spectrum of each pixel in NIR image of pork.

In another study, determination of intramuscular fat content and marbling score of pork using hyperspectral images of frozen and frozen-thawed pork was executed. The following conclusion was drawn from this study: the reflective images of frozen-thawed pork had comparable predictive ability as fresh pork, while more work should be conducted to reduce the effect of freezing on NIR images of pork. Frozen-thawed pork was implied to be applicable in the determination of fat level of pork.

The variation study of intramuscular fat content and marbling score or pork along the longissimus muscle indicated the uniformity of the fat assessment procedure. The last rib on the longissimus muscle was identified as a predictive site for intramuscular fat levels of pork at anterior ribs.

Furthermore, a study assessed the potential of NIR images of rib end to evaluate intramuscular fat level of pork at different ribs along longissmus muscle. The Gabor filtered hyperspectral images of rib end were found to be more effective in determination of marbling score and intramuscular fat, making it possible to measure the fat level of different portions of the thoracic loin without slicing the thoracic loin chunk into pieces.

9.2 Contributions to Knowledge

This study of the non-destructive evaluation of the intramuscular fat content of pork using hyperspectral imaging has resulted in the following original contributions to knowledge:

1. To the author’s knowledge, this study represents the first attempt to apply different novel pattern recognition approaches, i.e. Gabor filter, wide line detector, and grey-level co-occurrence matrix to NIR images of pork to characterize the intramuscular fat content and the marbling score of pork;
2. The marbling scores of pork were predicted by line features from digital RGB images of pork;
3. For the first time, image features of frozen and frozen-thawed pork were determined to characterize intramuscular fat content and marbling of pork, and compared to a similar analysis of fresh pork. The results can be scaled up for application in the rapid detection of quality attributes of meat in the meat industry;
4. A protocol for mapping the distribution of intramuscular fat content in pork was designed, which provides a visual image of the variation of intramuscular fat content in a piece of pork;
5. The variation of intramuscular fat level of pork along the longissmus muscle was evaluated by NIR hyperspectral images. Rib end was indicated to be effective as a sampling site for the determination of the IMF content in pork.

9.3 Recommendations for future work

There is a need for further investigation into how rib end of frozen loin can be used for non-invasive evaluation of the intramuscular fat content of pork, how RGB images could be implemented in online detection system for pork marbling assessment, and if distribution maps of marbling score and intramuscular fat content of frozen and frozen-thawed pork could be generated.

X. GENERAL REFERENCES

Alishahi, A., Farahmand, H., Prieto, N., & Cozzolino, D. (2012). Identification of transgenic foods using NIR spectroscopy: A review. *Spectrochimica Acta Part A*, 75, 1-7.

Association of Official Agricultural Chemists. (1990). Official methods of analysis. 15th ed. AOAC, Washington, DC.

Association of Official Agricultural Chemists. (2000). Official methods of analysis. 17th ed., AOAC, Arlington, VA.

Azevedo, L.F., Salgueiro, L.F., Claro, R., Teixeira-pinto, A., & Costa-pereira, A. (1999). Diet and gastric cancer in Portugal-a multivariate model. *European Journal of Cancer Prevention*, 8, 41-48.

Azain, M.J. (2004). Role of fatty acids in adipocyte growth and development. *Journal of Animal Science*, 82, 916-924.

Bahelka, I., Oravcova, M., Peskovicova, D., Tomka, J., Hanusova, E., Lahucky, R., & Demo, P. (2009). Comparison of accuracy of intramuscular fat prediction in live pigs using five different ultrasound intensity levels. *Animal*, 3(8), 1205-1211.

Bailey, A.J., & Light, N.D. (1989). Connective tissue in meat and meat products. Elsevier Applied Science, Barking, UK.

Ballard, D.A., & Brown, C.M. (1982). Computer vision. Prentice-Hall, Englewood Cliffs, NJ, USA.

Ballin, N.Z., & Lametsch, R. (2008). Analytical methods for authentication of fresh vs. thawed meat-A review. *Meat Science*, 80, 151-158.

Barlocco, N., Vadell, A., Ballesteros, F., Galietta, G., & Cozzolino, D. (2006). Predicting intramuscular fat, moisture and Warner-Bratzler shear force in pork muscle using near infrared reflectance spectroscopy. *Animal Science*, 82, 111-116.

Barbin, D., ElMasry, G., Sun, D.W., & Allen, P. (2012a). Near-infrared hyperspectral imaging for grading and classification of pork. *Meat Science*, 90(1), 259-268.

Barbin, D.F., ElMasry, G., Sun, D.W., & Allen, P. (2012b). Predicting quality and sensory attributes of pork using near-infrared hyperspectral imaging. *Analytica Chimica Acta*, 719, 30-42.

Barton-Gade, P., & Bejerholm, A.C. (1985). Eating quality in pork. *Pig Farming*, 33, 56.

Benson, I.B. (1993). Compositional analysis using near infrared absorbtion spectroscopy, In: Instruments and sensors for the food industr*y*. Kress-Rogers, E. Ed., Woodhead publishing. 121-166.

Bellon, V., Vigneau, J.L., & SCvila, F. (1994). Infrared and near infrared technology for the food industry and agricultural users: on-line applications. *Food Control*, 5, 2-27.

Beauchesne-rondeau, E., Gascon, A., Bergeron, J., & Jacques, H. (1999). Lean beef in lipid lowering diet: effects on Plasma Cholesterol and Liporotein B in Hypercholesterolaemic Men. *Canadian Journal of Dietetic Practice and Research*, 60 June Supplement.

Blanco, M., & Villarroya, I. (2002). NIR spectroscopy: a rapid-response analytical tool.

Trends in Analytical Chemistry, 21(4), 240-250.

Bowyer, K.W., Hollingsworth, K., & Flynn, P.J. (2008). Image understanding for iris biometrics: A survey. *Vision and Image Understanding*, 110(2), 281-307.

Brewer, M.S., Zhu, L.G., & McKeith, F.K. (2001). Marbling effects on quality characteristics of pork loin chops: consumer purchase intent visual and sensory characteristics. *Meat Science*, 59, 153-163.

Bryhni, E.A., Byrne, D.V., Rødbotten, M., Møller, S., Claudi-Magnussen, C., Karlsson, A., Agerhem, H., Johansson, M., & Martens, M. (2003). Consumer and sensory investigations in relation to physical/chemical aspects of cooked pork in Scandinavia. *Meat Science*, 65, 737-748.

Brøndum, J., Munck, L., Henckel, P., Karlsson, A., Tornberg, E., & Engelsen, S.B. (2000). Prediction of water-holding capacity and composition of porcine meat by comparative spectroscopy. *Meat Science*, 55, 177-185.

Brosnan, T., & Sun, D.W. (2004). Improving quality inspection of food products by computer vision-a review. *Journal of Food Engineering*, 61(1), 3-16.

Burns, D.A., & Cuirczak, E.W. (1992). Handbook of Near-Infrared Analysis, Marcel Dekker, New York, 396-403.

Cameron, N.D., & Enser, M. (1991). Fattey acid composition of lipid in *longissimus dorsi* muscle of Duroc and British Landrace pigs and its realtionship with lipid quality. *Meat Science*, 29, 295-307.

Carpenter, Z.L., Bray, R.W., Briskey, E.J. & Traeder, D.H. (1961). Intramuscular fat distribution in the *Longissimus dorsi* of paired pork loins. *Journal of Animal*

Science, 20, 603-605.

Chen, K., & Qin, C. (2008). Segmentation of beef marbling based on vision threshold. *Computers and Electronics in Agriculture*, 62(2), 223-230.

Clausi, D.A., & Jernigan, M. (2000). Designing Gabor filters for optimal texture separability. *Pattern Recognition*, 33(1), 1835-1849.

Cozzolino, D., & Murray, I. (2004). Identification of animal meat muscles by visible and near infrared reflectance spectroscopy. *Lebensmittel-Wissenschaft und Technologie*, 37, 447-452.

Devijver, P.A., & Kittler, J. (1982). Pattern Recognition: A Statistical Approach, Prentice-Hall, London, GB, 1982.

De Smet, S., Raes, K., & Demeyer, D. (2001). Meat fatty acid composition as affected by genetics. *Proceediings Belgian Association for Meat Science and Technology*, 44-53.

DeVol, D.L., McKeith, F.K., Bechtel, P.J., Novakofski, J., Shanks, R.D., & Carr, T.R. (1988). Variation in composition and palatability traits and relationships between muscle characteristics and palatability in a random sample of pork carcasses. *Journal of Animal Science*, 66, 385-395.

Downey, G., & Beauchene, D. (1997). Discrimination between fresh and frozen-then-thawed beef M. longissimus dorsi by combined visible-near infrared reflectance spectroscopy: A feasibility study. *Meat Science*, 45(3), 353-363.

Draper, N. R., & Smith, H. (1998). Applied Regression Analysis. Hoboken, NJ: Wiley-Interscience. 307-312.

Eggert, J.M., Belury, M.A., Kempa-Steczko, A., Mills, S.E., & Schinckel, A.P. (2001). Effects of conjugated linoleic acid on the belly firmness and fatty acid composition of genetically lean pigs. *Journal of Animal Science*, 71, 2079-2088.

Ellis, M., Webb, A.J., Avery, P.J., & Brown, I. (1996). The influence of terminal sire genotype, sex, slaughter weight, feeding regimen and slaughter house on growth performance, and carcass and meat quality in pigs and on the organoleptic properties of fresh pork. *Journal of Animal Science*, 74, 521-530.

ElMasry, G., Wang, N., ElSayed, A., & Ngadi, M. (2007). Hyperspectral imaging for nondestructive determination of some quality attributes for strawberry. *Journal of Food Engineering*, 81(1), 98-107.

ElMasry, G., & Sun, D.W. (2010). Meat quality assessment using a hyperspectral imaging system. In: Hyperspectral Imaging for Food Quality Analysis and Control, Academic Press/Elsevier, California, USA, 273-294.

ElMasry, G., Barbin, D.F., Sun, D.W., & Allen, P. (2012a). Meat quality evaluation by hyperspectral imaging technique: an overview. *Critical Reviews in Food Science and Nutrition*, 52(8), 689-711.

ElMasry, G., Sun, D.W., & Allen, P. (2012b). Near-infrared hyperspectral imaging for predicting colour, pH and tenderness of fresh beef. *Journal of Food Engineering*, 110(1), 127-140.

Fan, Y., & Zhang, H. (2006). Application of Gabor filter and multi-class SVM in baking bread quality classification. In: Proceedings of the 2006 IEEE International Conference on Mechatronics and Automation, Luoyang, China.

Faucitano, L., Rivest, J., Daigle, J.P., Levesque, J., & Gariepy, C. (2004). Distribution of intramuscular fat content and marbling within the longissimus muscle of pigs. *Canadian Journal of Animal Science*, 84(1), 57-61.

Faucitano, L., Huff, P., Teuscher, F., Gariepy, C., & Wegner, J. (2005). Application of computer image analysis to measure pork marbling characteristics. *Meat Science*, 69, 537-543.

Fernandez, X., Monin, G., Talmant, A., Mourot, J., & Lebret, B. (1999). Influence of intramuscular fat content on the quality of pig meat-1. Composition of the lipid fraction and sensory characteristics of m. longissimus lumborum. *Meat Science*, 53(1), 59-65.

Ferguson, D.M. (2004). Objective on-line assessment of marbling: A brief review. *Australian Journal of Experimental Agriculture*, 44, 681-685.

Fogel, I., & Sagi, D. (1989). Gabor filters as texture discriminators. *Biol Cybern*, 61, 103-113.

Fortin, A., Robertson, W.M., & Tong, A.K.W. (2005). The eating quality of Canadian pork and its relationship with intramuscular fat. *Meat Science*, 69(2), 297-305.

Forrest, J.C., Sheiss, E.B., Morgan, M., & Gerrard, D.E. (1997). Pork quality measurement tools-now and in the future. In: NPPC pork quality summit proceedings. Des Moines, IA. 79-96.

Garcia, P.T., Pensel, N.A., Margaria, C.A., Pueyrredon, S. & Durselen, G. (1997). Effect of pig diet restriction on ham lipids. International Congress of Meat Science and Technology Auckland, New Zealand, C-20, 290-291.

Geladi, P., Burger, J., & Lestander, T. (2004). Hyperspectral imaging: calibration problems and solutions. *Chemometrics and Intelligent Laboratory Systems*, 72(2), 209-217.

Gerrard, D.E., Gao, X., & Tan, J. (1996). Beef marbling and color score determination by imaging processing. *Journal of Food Science*, 61(1), 145-148.

Girolami, A., Napolitano, F., Faraone, D., & Braghieri, A. (2012). Measurement of meat color using a computervision system. *Meat Science*, 93(1), 111-118.

Gondret, F., & Lebret, B. (2002). Feeding intensity and dietary protein level affect adipocyte cellularity and lipogenic capacity of muscle homogenates in growing pigs, without modification of the expression of sterol regulatory element binding protein. *Journal of Animal Science*, 80, 3184-3193.

Gowen, A.A., O'Donnell, C.P., Cullen, P.J., Downey, G., & Frias, J.M. (2007). Hyperspectral imaging-an emerging process analytical tool for food quality and safety control. *Trends in Food Science & Technology*, 18(12), 590-598.

Grahn, H.F., & Geladi, P. (2007). Techniques and Applications of Hyperspectral Image Analysis. John Wiley & Sons, Ltd. Chichester, England.

Hausman, G.J., & Richardson, R.L. (2004). Adipose tissue angiogenesis. *Journal of Animal Science*, 82, 925-934.

Hausman, G.J., Dodson, M.V., Ajuwon, K., Azain, M., Barnes, K.M., Guan, L.L., Jiang, Z., Poulos, S.P., Sainz, R.D., Smith, S., Spurlock, M., Novakofski, J., Fernyhough, M.E., & Bergen, W.G. (2009). Board-invited review: the biology and regulation of preadipocytes and adipocytes in meat animals. *Journal of Animal Science*, 87,

1218-1246.

Haralick, R.M. (1979). Statistical and structural approaches to texture. *Proceedings of IEEE*, 67(5), 786-804.

Hocquette, J.F., Gondret, F., Baéza, E., Médale, F., Jurie, C., & Pethick, D.W. (2010). Intramuscular fat content in meat-producing animals: development, genetic and nutritional control, and identification of putative markers. *Animal*, 4(2), 303-319.

Huang, H., Liu, L., Ngadi, M.O., & Gariépy, C. (2013) Prediction of pork marbling scores using pattern analysis techniques. *Food Control*, 31(1), 224-229.

Huff-Lonergan, E. (2010). Chemistry and biochemistry of meat. In Handbook of meat processing. Toldra, F. Ed., Blackwell Publishing.

Isaksson, T., Miller, C.E., & NÆS, T. (1992). Nondestructive NIR and NIT determination of protein, fat and water in plastic wrapped, homogenized meat. *Applied Spectroscopy*, 42, 1685-1694.

Jackman, P., Sun, D.W., & Allen, P. (2009). Automatic segmentation of beef longissimus dorsi muscle and marbling by an adaptable algorithm. *Meat science*, 83(2), 187-194.

Jeremiah, L. E. (1998). Marbling and pork tenderness. Pork Fact Sheet. Des Moines, IA: National Pork Producers Council and American Meat Science Association.

Kauffman, R.G. (2012). Meat composition. In: Handbook of meat and meat processing. Hui, Y.H. Ed., Boca Raton, FL: CRC Press.

Kamruzzaman, M., Barbin, D., ElMasry, G., Sun, D.W., & Allen, P. (2012a). Potential of hyperspectral imaging and pattern recognition for categorization and authentication of red meat. *Innovative Food Science and Emerging Technologies*, 16, 316-325.

Kamruzzaman, M., ElMasry, G., Sun, D.W., & Allen, P. (2012b). Prediction of some quality attributes of lamb meat using near-infrared hyperspectral imaging and multivariate analysis. A*nalytica chimica acta*, 714, 57-67.

Kamruzzaman, M., ElMasry, G., Sun, D.W., & Allen, P. (2012c). Non-destructive prediction and visualization of chemical composition in lamb meat using NIR hyperspectral imaging and multivariate regression. *Innovative Food Science and Emerging Technologies*, 16, 218-226.

Kemspter, A.J., Dilworth, A.W., Evans, D.G., & Fisher, K.D. (1986). The effects of fat thickness and gender on pig meat quality with special reference to the problems associated with overleanness. 1. Butcher and consumer panel results. *Animal Production*, 43, 517-533.

Kipfmuller, H., Bodis, K., Peschke, W., & Eichinger, H.M. (2000). Qualitat von Schweinefleisch. *Ernahrung-Umschau*, 47, 416-422.

Kim, M.S., Chen, Y.R., Cho, B.K., Chao, K., Yang, C.C., Lefcourt, A.M., & Chan, D. (2007). Hyperspectral reflectance and fluorescence line-scan imaging for online defect and fecal contamination inspection of apples. *Sensing and Instrumentation for Food Quality and Safety*, 1(3), 151-159.

Kobayashi, K., Matsui, Y., Maebuchi, Y., Toyota, T., & Nakauchi, S. (2010). Near infrared spectroscopy and hyperspectral imaging for prediction and visualisation of fat and fatty acid content in intact raw beef cuts. *Journal of Near Infrared Spectroscopy*, 18(5), 301-315.

Kouba, M., Enser, M., Whittington, F.M., Nute, G.R., & Wood, J.D. (2003). Effect of a high-linolenic acid diet on lipogenic enzyme activities, fatty acid composition and meat quality in the growing pig. *Journal of Animal Science*, 81, 1967-1979.

Kumar, S., & Mittal, G.S. (2010). Rapid detection of microorganisms using image processing parameters and neural network. *Food and Bioprocess Technology*, 3(5), 741-751.

Kurita, H., & Masuda, R. (2012). Application of The Gabor Filters and K-means Method for Characterization of Geometerial Properties of Paranchyma Cell Walls. *Journal of Texture Studies*, 43(5), 339-349.

Lakshmanan, S., Koch, T., Brand, S., Mannicke, N., Wicke, M., Morlein, D., & Raum, K. (2012). Prediction of the intramuscular fat content in loin muscle of pig carcasses by quantitative time-resolved ultrasound. *Meat Science*, 96(1), 216-225.

Li, J., & Nigel, M.A. (2008). A comprehensive review of current local features for computer vision. *Neurocomputing*, 71(10-12), 1771-1787.

Li, Y.Y., Zhang, L.L, Peng, Y.K., Tang, X.Y., Chao, K.L., & Dhakal, S. (2011). Hyperspectral imaging technique for determination of pork freshness attributes. *Proceedings of SPIE*, Vol. 8027, Paper no. 80270H.

Liu, L., Zhang, D., & You, J. (2007). Detecting wide lines using isotropic nonlinear filtering. *IEEE Trans. Image Processing,* 16(6), 1584-1595.

Liu, L., Ngadi, M.O., Prasher, S.O., & Gariépy, C. (2009). Predicting the intramuscular fat content of pork using hyperspectral imaging technique. The Institute of Food

Technologists (IFT) Annual Meeting & Food Expo.

Liu, L., Ngadi, M.O., Prasher, S.O., & Gariépy, C. (2010). Categorization of pork quality using Gabor filter-based hyperspectral imaging technology. *Journal of Food Engineering*, 99(3), 284-293.

Liu, L., Ngadi, M.O., Prasher, S.O., & Gariépy, C. (2012). Objective determination of pork marbling scores using the wide line detector. *Journal of Food Engineering,* 110(3): 497-504.

Liu, L., & Ngadi, M.O. (2012). Detecting Fertility and Early Embryo Development of Chicken Eggs Using Near-Infrared Hyperspectral Imaging. *Food and Bioprocess Technology*, DOI 10.1007/s11947-012-0933-3.

Lo Fiego, D.P., Macchioni, P., Minelli, G., & Santoro, P. (2010). Lipid composition of covering and intramuscular fat in pigs at different slaughter age. *Italian Journal of Animal Science*, 9(2), 200-205.

Lonergan, S.M., Stalder, K.J., Huff-Lonergan, E., Knight, T.J., Goodwin, R.N., Prusa, K.J., & Beitz, D.C. (2007). Influence of lipid content on pork sensory quality within pH classification. *Journal of Animal Science*, 85(4), 1074-1079.

Lu, J., Tan, J., Shatadal, P., & Gerrard, D.E. (2000). Evaluation of pork color by using computer vision. *Meat Science*, 56, 57-60.

Ma, L., Tan, T., Wang, Y., & Zhang, D. (2002). Personal identification based on iris texture analysis. *IEEE Transactions of the Pattern Recognition and Machine Intelligence*, 25(12), 1519-1533.

Ma, K., Forbes, J.G., Gutierrez-Cruz, G., & Wang, K. (2006). Titin as a giant scaffold for integrating stressand srchomology domain 3-mediated signaling pathways-the clustering of novel overlap ligand motifs in the elastic pevk segment. *Journal of Biological Chemistry*, 281, 27539-27556.

MacDonald, J.M., & William, D.M. (2009). The Transformation of U.S. livestock agriculture: scale, efficiency, and risks. USDA EIB-43.

Mateo, M.J., O'Callaghan, D.J., Gowen, A.A., & O'Donnell, C.P. (2010). Evaluation of a vat wall-mounted image capture system using image processing techniques to monitor curd moisture during syneresis with temperature treatments. *Journal of Food Engineering*, 99(3): 257-262.

Mendoza, F., Lu, R., Ariana, D., Cen, H., & Bailey, B. (2011). Integrated spectral and image analysis of hyperspectral scattering data for prediction of apple fruit firmness and soluble solids content. *Postharvest Biology and Technology*, 62, 149-160.

Meat Price Spreads, Data Set for Historical Monthly Price Spread Data for Beef, Pork, Broilers, Turkeys, and Eggs, U.S. Department of Agriculture, Economic Research Service, http://www.ers.usda.gov/Data/meatpricespreads/.

Meisinger, D.J. (2002). A system for assuring pork quality. Des Moines, IA, USA: National Pork Board.

Miller, Ch.E. (2001). Chemical principles of near infrared technology. Near infrared technology in the agricultural and food industries. Second Edition. Williams, P.C., & Norris, K.H. Eds., American Association of Cereal Chemist, Minnesota, USA. 19-39.

Miller, R.K. (2002). Factors affecting the quality of raw meat. In: Meat Processing: Improving Quality. Kerry, J., Kerry. J., & Ledward, D. Eds., CRC Press LLC. USA.

Moloney, A.P., Teagasc, Dunsany. (2002). The fat content of meat and meat products. In Meat Processing: Improving Quality. Kerry, J., Kerry. J., & Ledward, D. Eds., CRC Press LLC. USA.

Monin, G. (1998). Recent methods for predicting quality of whole meat. *Meat Science*, 49(1), 231-243.

Moon, I., & Javidi, B. (2007). Three-dimensional identification of stem cells by computational holographic imaging. *Journal of The Royal Society Interface*, 4(13), 305-313.

Murray, I. (1986). The NIR spectra of homologous series of organic compounds. Hollo, J., Kaftka, K.J., & Gonczy, J.L. Eds., Proceedings of the International NIR/NIT Conference. Akademiai Kiado, Budapest, Hungary. 13-28.

Murray, I., & Williams, P.C. (1987). Chemical principles of near-infrared technology. In: Near infrared technology in the agricultural and food industries, American Association of Cereal Chemists, Inc., St. Paul, Minnesota, USA. 17-34.

Naganathan, G.K., Grimes, L.M., Subbiah, J., Calkins, C.R., Samal, A., & Meyer, G.E. (2008a). Partial least squares analysis of near-infrared hyperspectral images for beef tenderness prediction. *Sensing and Instrumentation for Food Quality and Safety*, 2, 178-188.

Naganathan, G.K., Grimes, L.M., Subbiah, J., Calkins, C.R., Samal, A., & Meyer, G.E.

(2008b). Visible/near-infrared hyperspectral imaging for beef tenderness prediction. *Computers and Electronics in Agriculture*, 64, 225-233.

Ngadi, M.O., & Liu, L. (2010). Hyperspectral image processing techniques. In: Hyperspectral imaging for food quality analysis and control. Sun, D.W. Ed., Academic Press, Elsevier, London, Burlington, San Diego, 99-127.

Ngan, H.Y.T., Pang, G.K.H., & Yung, N.H.C. (2011). Automated fabric defect detection-A review. *Image and Vision Computing*, 29(7), 442-458.

NPB (National pork board). (2002). *Pork quality standards.* Des Moines, IA USA.

Osborne, B.G., & Fearn, T. (1986). Near-Infrared Spectroscopy in Food Analysis. Longman Scientific and Technical, London.

Osborne, B. G., & Fearn, T. (1988). Near-Infrared Spectroscopy in Food Analysis. Wiley: New York.

Osborne, B.G., Fearn, T., & Hindle, P.H. (1993). Applications of near infrared spectroscopy in food and beverage analysis. Browning, D. Ed., Practical NIR spectroscopy with applications in food and beverage analysis, Longman Scientific & Technical, London, 145-159.

Owen, A.J. (1995). Uses of derivative spectroscopy. Application Note. Hewlett Packard Waldbronn, Germany.

O'Havers, T.C. (1982). Derivative Spectroscopy and its applications in analysis: derivative spectroscopy: theoretical aspects, Plenary lecture. *Analytical Proceedings*, 54, 22-28.

O’Sullivan, M.G., Byrne, D.V., Martens, H., Gidskehaug, G.H., Andersen, H.J., &

Martens, M. (2003). Evaluation of pork colour: Prediction of visual sensory quality of meat from instrumental and computer vision methods of colour analysis. *Meat Science*, 65(2), 909-918.

Pallottino, F., Menesatti, P., Costa, C., Paglia, G., De Salvador, F.R., & Lolletti, D. (2010). Image analysis techniques for automated hazelnut peeling determination. *Food and Bioprocess Technology*, 3(1), 155-159.

Peng, Y.K, & Wang, W. (2008). Prediction of pork meat total viable bacteria count using hyperspectral imaging system and support vector machines. In: Food Processing Automation Conference Proceedings, Michigan, Paper no. 701P0508cd.

Prats-Montalbán, J.M., De Juan, A., & Ferrer, A. (2011). Multivariate image analysis: a review with applications. *Chemometrics and Intelligent Laboratory Systems*, 107(1), 1-23.

Prevolnik, M., Čandek-Potokar, M., Škorjanc, D., Velikonja-Bolta, Š., Škrlep, M., Znidaršič, T., & Babnik, D. (2005). Predicting intramuscular fat content in pork and beef by near infrared spectroscopy. *Journal of Near Infrared Spectroscopy*, 13, 77-86.

Prieto, N., Roehe, R., Lavín, P., Batten, G., & Andrés, S. (2009). Application of near infrared reflectance spectroscopy to predict meat and meat products quality: A review. *Meat Science*, 83(2), 175-186.

Qiao, J., Ngadi, M.O., Wang, N., & Gunenc, A. (2005). Determination of pork quality attributes using hyperspectral imaging technique. In: Optical Sensors and Sensing Systems for Natural Resources and Food Safety and Quality. Chen, Y.R., Meyer, G.E., Tu, S.I., Eds., *Proceedings of SPIE*, Vol. 5996, 59960M.

Qiao, J., Wang, N., Ngadi, M. O., Gunenc, A, Monroy, M., Gariepy, C., & Prasher, S.O. (2007a). Prediction of drip-loss, pH, and color for pork using a hyperspectral imaging technique. *Meat Science*, 76(1),1-8.

Qiao, J., Ngadi, M. O., Wang, N., Gunenc, A, Monroy, M., Gariepy, C., & Prasher, S.O. (2007b). Pork quality classification using a hyperspectral imaging system and neural network. *International Journal of Food Engineering*, 3(1), 1556-3758.

Qiao, J., Ngadi, M.O., Wang, N., Gariepy, C., & Prasher, S.O. (2007c). Pork quality and marbling level assessment using a hyperspectral imaging system. *Journal of Food Engineering*, 83, 10-16.

Quevedo, R., & Aguilera, J.M. (2010). Computer vision and stereoscopy for estimating firmness in the Salmon (*Salmon salar*) Fillets. *Food and Bioprocess Technology*, 3(4), 561-567.

Resurreccion, A.V.A. (2004). Sensory aspects of consumer choices for meat and meat products. *Meat Science*, 66, 11-20.

Riley, P.A., Enser, M., Nute, G.R., & Wood, J.D. (2000). Effects of dietary linseed on nutritional value and other quality aspects of pig muscle and adipose tissue. *Animal Science*, 71, 483-500.

Rincker, P.J., Killefer, J., Ellis, M., Brewer, M.S., & McKeith, F.K. (2008). Intramuscular fat content has little influence on the eating quality of fresh pork loin chops. *Journal of Animal Science*, 86(3), 730-737.

Ritthiruangdej, P., Ritthiron, R., Shinzawa, H., & Ozaki, Y. (2011). Non-destructive and rapid analysis of chemical compositions in Thai steamed pork sausages by near-infrared spectroscopy. *Food Chemistry*, 129(2), 684-692.

Rhodes, D.N. (1970). Meat quality: influence of fatness of pigs on the eating quality of pork. *Journal of the Science of Food and Agriculture*, 21, 572-575.

Rodbotten, R., Nilsen, B.N., & Hildrum, K.I. (2000). Prediction of beef quality attributes from post mortem near infared reflectance spectra. *Food Chemistry*, 69(4), 427-436.

Rodgers, J.L., & Nicewander, W.A. (1988). Thirteen ways to look at the correlation coefficient. *American Statistician*, 32, 59-66.

Romans, J.R., Costello, W.J., Carlson, C.W., Greaser, M.L., & Jones, K.W. (2001). Meat as a food. In: The meat we eat. Interstate publishers, Inc. USA.

Rowe, L.J., Maddock, K.R., Lonergan, S.M., & Huff-Lonergan, E. (2004). Influence of early postmortem protein oxidation on beef quality. *Journal of Animal Science*, 82, 785-793.

Sather, A.P., Bailey, D.R.C., & Jones, S.D.M. (1996). Real-time ultrasound image analysis for the estimation of carcass yield and pork quality. *Canadian Journal of Animal Science*, 76(1), 55-62.

Savenije, B., Geesink, G.H., Van der Palen, J.G.P., Hemke, G. (2006). Prediction of pork quality using visible/near-infrared reflectance spectroscopy. *Meat Science*, 73(1), 181-184.

Samantaray, L., Dash, M., & Panda, P. (2005). A review on time-frequency, time-scale and scale-frequency domain signal analysis. *IETE Journal of Research*, 51(4),

287-293.

Scollan, N.D., Hocquette, J-F., Nuernberg, K., Dannenberger, D., Richardson, R.I., & Maloney, A. (2006). Innovations in beef production systems that enhance the nutritional and health value of beef lipids and their relationship with meat quality. *Meat Science*, 74, 17-33.

Sheard, P.R., Enser, M., Wood, J.D., Nute, G.R., Gill, B.P., & Richardson, R.I. (2000). Shelf life and quality of pork and pork products with raised n-3 PUFA. *Meat Science*, 55, 213-221.

Shenk, J.S., Westerhaus, M.O., & Workman, J.J. (1992). Application of NIR spectroscopy to agricultural products. In: Handbook of near infrared analysis, practical spectroscopy series, New York, USA. 383-431

Shiranita, K., Hayashi, K., Otsubo, A., Miyajima, T., & Takiyama, R. (2000). Grading meat quality by image processing. *Pattern Recognition,* 33, 97-104.

Singh, C.B., Choudhary, R., Jayas, D.S., & Paliwal, J. (2008). Wavelet analysis of signals in agriculture and food quality inspection. *Food Bioprocess Technology*, 3(1), 2-12.

Sun, D.W. (2008). Computer vision technology for food quality evaluation. Elsevier/Academic Press, Amsterdam, Boston. 126-128.

Sun, D.W. (2010). Hyperspectral Imaging for Food Quality Analysis and Control. Elsevier Science, London.

Suzuki, K., Irie, M., Kadowaki, H., Shibata, T., Kumagai, M., & Nishida, A. (2005a). Genetic parameter estimates of meat quality traits in Duroc pigs selected for average daily gain, longissimus muscle area, backfat thickness, and intramuscular fat content. *Journal of Animal Science*, 83, 2058-2065.

Suzuki, K., Kadowaki, H., Shibata, T., Uchida, H., & Nishida, A. (2005b). Selection for daily gain, loin-eye area, backfat thickness and intramuscular fat based on desired gains over seven generations of Duroc pigs. *Livestock Production Science*, 97(2-3), 193-202.

Tan, F.J., Morgan, M.T., Ludas, L.I., Forrest, J.C., & Gerrard, D.C. (2000). Assessment of fresh pork colour with colour machine vision. *Journal of Animal Science*, 78(12), 3078-3085.

Tan, J.L. (2004). Meat quality evaluation by computer vision. *Journal of Food Engineering*, 61(1), 27-35.

Tang, Y.Y., Lee, S.W., & Suen, C.Y. (1996). Automatic document processing: A survey. *Pattern Recognition*, 29(12), 1931-1952.

Tao, F.F., Peng, Y.K., Li, Y.Y., Chao, K.L., & Dhakal, S. (2012a). Simultaneous determination of tenderness and Escherichia coli contamination of pork using hyperspectral scattering technique. *Meat Science*, 90(3), 851-857.

Tao, F.F., Peng, Y.K., Song, Y.L., Guo, H., & Chao, K.L. (2012b). Improving prediction of total viable counts in pork based on hyperspectral scattering technique. *Proceedings of SPIE*, Vol. 8369, Paper no. 83690A.

Teye, G.A., Sheard, P.R., Whittington, F.M., Nute, G.R., Stewart, A., & Wood, J.D. (2006). Influence of dietary oils and protein level on pork quality. 1. Effects on muscle fatty acid composition, carcass, meat and eating quality. *Meat Science*, 73(1),

157-165.

Toraichi, K., Kwan, P.W.H., Katagishi, K., Sugiyama, T., Wada, K., Mitsumoto, M., Nakai, H., & Yoshikawa, F. (2002). On a fluency image coding system for beef marbling evaluation. *Pattern Recognition Letters,* 23, 1277-1291.

Tuceryan, M., & Jain, A.K. (2010). Texture analysis. In: The Handbook of Pattern Recognition and Computer Vision, 4th ed. Chen, C.H. Ed., World Scientific Publishing Co., 207-248.

Van der Wal, P.G., Olsman, W.J., Garssen, G.J., & Engel, B. (1992). Marbling, intramuscular fat and meat colour of Dutch pork. *Meat Science*, 32, 351-355.

Van Laack, R., Stevens, S.G., & Stalder, K.J. (2001). The influence of ultimate pH and intramuscular fat content on pork tenderness and tenderization. *Journal of Animal Science*, 79, 392-397.

Vasko, P.D., Blackwell, J., & Koenig, J.L. (1971). Infrared and Raman spectroscopy of carbohydrates. Part 1. Identifi cation of O-H and C-H related vibrational modes for D-glucose, maltose, cellobiose and dextran by deuterium-substitution methods. *Carbohydrate Research*, 19, 297-310.

Verbeke, W., Oeckel, M.J., Van Warrants, N., Viaene, J., & Boucque, C.V. (1999). Consumer perception, facts and possibilities to improve acceptability of health and sensory characteristics of pork. *Meat Science*, 53, 77-99.

Vote, D.J., Belk, K.E., Tatum, J.D., Scanga, J.A., & Smith, G.C. (2003). Online prediction of beef tenderness using a computer vision system equipped with a BeefCam module. *Journal of Animal Science*, 81(2), 457-465.

Wang, W.B., & Paliwal, J. (2007). Near-infrared spectroscopy and imaging in food quality and safety. *Sensing and Instrumentation for Food Quality and Safety*, 1(4), 193-207.

Warriss, P.D., Kestin, S.C., Brown, S.N., & Nute, G.R. (1996). The quality of pork from traditional pig breeds. *Meat Focus Int.*, 5/6, 179-182.

Williams, P., Geladi, P., Fox, G., & Manley, M. (2009). Maize kernel hardness classification by near infrared (NIR) hyperspectral imaging and multivariate data analysis. *Analytica Chimica Acta*, 653, 121-130.

Witte, D.P., Ellis, M., McKeith, F.K., & Wilson, E.R. (2000). Effect of dietary lysine level and environmental temperature during the finishing phase on the intramuscular fat content of pork. *Journal of Animal Science*, 78(5), 1272-1276.

Wood, J.D. (1990). Consequences for meat quality of reducing carcass fatness. In: Reducing fat in meat animals. Wood, J.D., & Enser, M. Eds., London: Elsevier Applied Science. 344-397.

Wold, J.P., Kvaal, K., & Egelandsdal, B. (1999). Quantification of intramuscular fat content in beef by combining autofluoresence spectra and autofluorescence images. *Applied Spectroscopy*, 53(4), 448-456.

Wood, J.D., Enser, M., Fisher, A.V., Nute, G.R., Sheard, P.R., & Richardson, R.I. (2008). Fat deposition, fatty acid composition and meat quality: A review. *Meat Science*, 78, 343-358.

Wold, J.P., O'Farrell, M., Hoy, M., & Tschudi, J. (2011). On-line determination and control of fat content in batches of beef trimmings by NIR imaging spectroscopy.

Meat Science, 89(3), 317-324.

Yang, X.J., Albrecht, E., Ender, K., Zhao, R.Q., & Wegner, J. (2006). Computer image analysis of intramuscular adipocytes and marbling in the longissimus muscle of cattle. *Journal of Animal Science*, 84, 3251-3258.

Yoshikawa, F., Toraichi, K., Wada, K., Otsu, O., Nakai, H., Mitsumoto, M., & Katagishi, K. (2000). On a grading system for beef marbling. *Pattern Recognition Letters*, 21, 1037-1050.

Zhou, X.S., & Huang, T.S. (2003). Relevance feedback in image retrieval: A comprehensive review. *Multimedia Systems*, 8(6), 536-544.

Zhu, B., Jiang, L., Luo, Y., & Tao, Y. (2007). Gabor feature-based apple quality inspection using kernel principal component analysis. *Journal of Food Engineering*, 81, 741-749.